Modulating Proteostatic Stress in Human Motor Neurons to Identify Neuroprotective Targets

Citation

Watts, Michelle Elizabeth. 2020. Modulating Proteostatic Stress in Human Motor Neurons to Identify Neuroprotective Targets. Doctoral dissertation, Harvard University Graduate School of Arts and Sciences.

Permanent link

https://nrs.harvard.edu/URN-3:HUL.INSTREPOS:37369444

Terms of Use

Share Your Story

HARVARD UNIVERSITY
Graduate School of Arts and Sciences

DISSERTATION ACCEPTANCE CERTIFICATE

The undersigned, appointed by the

Division of Medical Sciences

in the subject of Biological and Biomedical Sciences

have examined a dissertation entitled

*Modulating proteostatic stress in human motor neurons to identify
neuroprotective targets*

presented by Michelle Elizabeth Watts

candidate for the degree of Doctor of Philosophy and hereby
certify that it is worthy of acceptance.

Signature: _____

Typed Name: Dr. Dennis Selkoe

Signature: _____

Typed Name: Dr. Brian Wainger

Signature: _____

Typed Name: Dr. Tracy Young-Pearse

Signature: _____

Typed Name: Dr. Hynek Wichterle

Date: November 12, 2020

Modulating Proteostatic Stress in Human Motor Neurons to Identify Neuroprotective Targets

A dissertation presented

by

Michelle Elizabeth Watts

to

The Division of Medical Sciences

in partial fulfillment of the requirements

for the degree of

Doctor of Philosophy

in the subject of

Biological and Biomedical Sciences

Harvard University

Cambridge, Massachusetts

November 2020

Modulating Proteostatic Stress in Human Motor Neurons to Identify Neuroprotective Targets

Abstract

Amyotrophic lateral sclerosis (ALS) is a paralyzing and fatal motor neuron (MN) disease with few therapeutic options. The ability to produce MNs from ALS patients using induced pluripotent stem cell (iPSC) technologies and neuronal differentiation protocols has improved therapeutic identification by allowing, for the first time, mechanistic studies and drug screening within the correct human cellular context. In this thesis, we investigate how modulating protein homeostasis (proteostasis), a core process dysregulated in ALS, affects both healthy and ALS patient MNs. We demonstrate that proteostatic stressors targeting the endoplasmic reticulum (ER) are preferentially more toxic to MNs than non-MNs, in healthy and ALS patient cultures, without inducing insoluble proteins. In contrast, proteostatic stressors targeting the ubiquitin-proteasome machinery induce insoluble proteins associated with ALS, yet do not uniformly trigger cell-type-specific degeneration. These experiments demonstrate, for the first time, a fundamental vulnerability of iPSC-derived MNs to ER stress, with distinctly differential effects to other proteostatic stressors. These studies additionally define assay conditions necessary to induce ALS MN degenerative phenotypes in a synchronous and scalable manner amenable for drug screening.

We demonstrate that these assays can accurately predict and identify drugs with neuroprotective potential by showing that kenpaullone, a well-established MN protective agent, is able to preserve ALS patient MN viability in proteostatic stressor conditions. We further demonstrate, for the first time, that a small molecule inhibitor to one of kenpaullone's targets, MAP4K4, is also able to maintain ALS patient MN viability in all conditions of proteostatic stress. As with kenpaullone, this preserved viability includes the maintenance of healthy neurites and is independent of a direct reduction in UPR induction or insoluble protein buildup. Finally, we utilize global phosphoproteomic remodeling analyses to discover a core proteome that is changed with kenpaullone and MAP4K4 inhibition and identify several new compounds that preserve MN viability. These studies cumulatively outline a network of vulnerability points and protective pathways in human MNs, highlighting the value of modulating

proteostatic stress in patient MNs to gain insights into degenerative disease mechanisms and to identify new

neuroprotective targets.

Table of Contents

Chapter 1- Introduction

List of Figures and Tables

Acknowledgements

First and foremost, I would like to thank my dissertation advisor, Dr. Lee Rubin. The work in this thesis would not have been possible without his expert guidance and support. Lee helped me gain independence and confidence as a scientist, and never once failed to show positivity and encouragement, even when viruses were failing, stem cells were "not cooperating", and robots were malfunctioning. For his wisdom, his inspiration, his kindness, and his mentorship, I will be forever grateful.

Thank you also to my dissertation advisory committee members and defense committee members- Dr. Dan Finley, Dr. Dennis Selkoe, Dr. Clifford Woolf, Dr. Brian Wainger, Dr. Tracy Young-Pearse, and Dr. Hynek Wichterle. Their expert advice, critical comments, and continuous support during my PhD education has been invaluable. Extra thanks also to Nam Che, my undergraduate research mentor. His dedication to teaching and training is truly admirable, and I am so thankful to have learned from him.

Special thanks to my friends and Rubin lab members, past and present, who have gone through this journey with me, providing knowledge, commiseration, laughs, and support, in times when they were needed most. Specifically- Silvia Piccinotti, Ceren Ozek, Sean Buchanan, Chen Wu, Jenny Pena, Ursula Beattie, Juhi Narula, Becca Gibbs, Brittany Mayweather, Tobi Grass, Jack Blank, Samara Santiago, Erin O'Connor, Kiwi Florido, Mark Matyas, Xiaoyu Hu, Francesca Rapino, Rich Krolewski, Jane Lalonde, Kathy Pfaff, Susie Slepian, Erica Wolin, and Erika Norabuena.

Finally, deep thanks and appreciation to my family for their unwavering support and love. To my Dad, Aunt and Uncle- thank you for inspiring me with your science. To my Sister, Stephanie, thank you for showing me strength. And most important, to my Mom, Ann Watts. Your unconditional love and support truly have no limits, and I could not have done this without you. This is for you.

Chapter 1

Introduction

From Mice to MNs- A Review of ALS Biology and Drug Discovery

1.1 Abstract

Amyotrophic lateral sclerosis (ALS) is a fatal and incurable neurodegenerative disorder characterized by the selective deterioration of motor neurons (MNs). Investigating disease processes and discovering effective therapeutics for ALS has been particularly challenging due to the heterogeneous nature of this disease as well as the lack of clinically predictive research models. In this chapter, we provide a comprehensive overview of the complex clinical presentations of ALS, the underlying neuropathology, and the disease mechanisms identified from genetic and mouse studies. We describe how the recent development of induced pluripotent stem cell (iPSC) technologies and directed neuronal differentiation protocols have improved mechanistic studies and drug discovery by enabling, for the first time, the generation of MNs from ALS patients. We compile and critically review published studies using MNs derived from ALS patient iPSCs for their ability to recapitulate hallmark ALS phenotypes of preferential MN degeneration and insoluble protein accumulation, phenotypes which usually manifest in patients over several decades. We ultimately identify a need to better understand the mechanisms initiating selective MN degeneration in patient derived cultures, and the cellular conditions required to robustly observe these hallmark ALS phenotypes in vitro. We conclude with the hypothesis that pharmacological stressors perturbing protein homeostasis (proteostasis) at the endoplasmic reticulum (ER) may mimic ALS cellular dysfunctions to accelerate preferential MN degeneration in vitro, which we investigate alongside a proteasome inhibitor in Chapters 2-4 for an improved understanding of human MN vulnerability and neuroprotective targets.

1.2 Amyotrophic Lateral Sclerosis

Amyotrophic lateral sclerosis (ALS) is a fatal neurological disorder characterized by the degeneration of motor neurons (MNs) controlling movement[1]. First reported in the 1800's[2–8], ALS is now the most common MN disease of adults, with an annual incidence of 1-2 individuals per 100,000 people, and a prevalence of about 5 cases per 100,000 people[9–11]. Disease onset is usually later in life, occurring in individuals between the ages of 54-67 years old[12,13], and morbidity and mortality are high. Symptoms progress rapidly from localized muscle weakness to near complete paralysis, respiratory failure and death approximately 1-5 years after diagnosis[14]. This devastating health prognosis is also associated with a large financial burden. The annual cost per patient is as high as $69,475 in the United States[15], with a total disease cost up to $1,433,992[16]. This corresponds to a national economic burden between $279-472 million dollars annually, and an even higher global economic impact[15,17].

With an aging world population, these individual health and economic burdens are projected to increase substantially[18], fueling large-scale efforts to identify disease-modifying therapeutics. To date, over 70 drugs have been investigated as potential treatments for ALS[19], yet only 2 have been approved by the U.S. Food and Drug Administration (FDA). The anti-glutamatergic agent Riluzole was the first approved drug in 1994, prolonging patient survival by 3 months[20–22]. Over 2 decades later, in 2017 the antioxidant Edaravone was the next approved treatment, modestly improving disease progression and muscle function in a subset of patients[23]. The lack of truly effective treatment options means that current patient care is primarily weighted towards symptom management, ranging from dietary changes and physical therapy, to enteral feeding by insertion of a gastrostomy tube and noninvasive ventilation for maintained respiratory function and prolonged survival[24]. There is thus a clear and critical unmet need for new ALS treatments, which have been incredibly difficult to identify due to the complex clinical, pathological, and genetic features underlying this disease.

1.3 Clinical presentation of ALS

ALS is defined by movement dysfunction caused by MN damage. This includes damage to upper motor neurons (UMNs) residing in the motor cortex of the brain and projecting to the spinal cord, as well as lower motor neurons (LMNs) residing in the brainstem and spinal cord and innervating skeletal muscle (Figure 1.1A)[12].
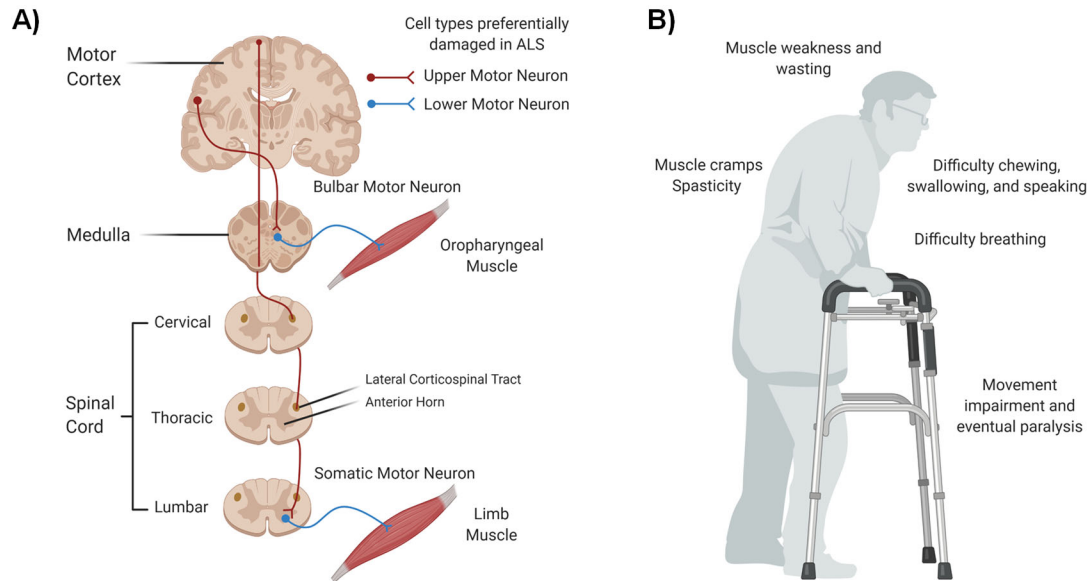
Figure 1.1. The motor system and ALS clinical presentations.
  A) The motor system is composed of upper motor neurons (UMNs) in the motor cortex of the brain and lower motor neurons (LMNs) in the brainstem and spinal cord that innervate skeletal muscle. Figure adapted from Brown, R., and Al-Chalabi, A., 2017[1].
  B) The progressive damage to UMNs and LMNs in ALS patients results in symptoms of muscle weakness and wasting, cramps, spasticity, difficulty chewing, speaking, and swallowing, with eventual paralysis and respiratory failure.

The majority of patients (~98%) present with symptoms of muscle weakness and wasting in one discrete body region due to this MN damage[25], with considerable variability in the degree of UMN and LMN degeneration observed and the body region affected first[12]. Most patients (~2/3) experience initial symptoms in the arms or legs[12]. Less commonly, ~1/3 of patients will have initial difficulties in the bulbar regions responsible for speech, chewing and swallowing[1,12]. Rarely, in the most aggressive forms of disease, patients will have respiratory difficulties first. Motor dysfunction then progresses uniformly from the focal point of onset, propagating to nearby neuroanatomy and circuitry. Patients experience loss of muscle strength and size, spasticity, fasciculations (twitching), cramps, dysarthria (speech impairment), and dysphagia (difficulty swallowing) until paralysis of almost all skeletal muscles and a complete loss of independent movement and activity (Figure 1.1B)[24]. Only MNs in the oculomotor region and Onuf's nuclei resist disease, allowing patients to retain normal visual, bladder and sexual function until disease end stage[26]. Non-motor comorbidities additionally occur[27–31], with as many as 50% of ALS patients experiencing cognitive impairments and about 20% concurrently diagnosed with frontotemporal dementia (FTD)[32–34]. Along with variable comorbidities, distinct sites of onset, and degree of UMN and LMN involvement, the rate of disease

progression is also highly variable, with some patients succumbing to ALS within a year while others live longer than 10 years. Eventually however, MNs innervating the muscles of the diaphragm are affected, resulting in final respiratory failure and death.

These vast clinical presentations of ALS have ultimately led clinicians and researchers to propose that ALS is part of a disease spectrum, with a complex array of human genetics and environmental factors affecting the central nervous system (CNS) at initial vulnerability points to converge onto final disease mechanisms and MN death[12]. Paths to successful new therapeutics may therefore involve either a patient stratification methodology comparable to the precision medicine efforts spear-headed by the field of oncology (reviewed in Gibbs et al., 2018)[35], or alternatively involve targeting convergent features shared by all forms of disease.

1.4 Pathological features of ALS

The core neuropathological feature of ALS is the degeneration of MNs. This includes (1) extensive depletion (≥50%) of LMNs (anterior horn cells) in the spinal cord and lower cranial motor nuclei in the brain stem; (2) axonal loss and scarring (sclerosis) of the descending axons of UMNs (the lateral columns of the spinal cord); and (3) loss of UMNs (large pyramidal neurons known as giant cells of Betz in the layer V of the primary motor cortex) (Figure 1.1A)[8,36–38]. Astrogliosis, spongiosis, and microglial activation are also observed surrounding areas of neuronal loss[39–42] and eosinophilic inclusion bodies called Bunina bodies are present in the remaining brainstem and spinal MNs and are pathognomonic to ALS[43–46]. Distinct from Bunina bodies, ubiquitinated cytoplasmic inclusions are also present in all cases of ALS[47,48]. These ubiquitinated inclusions are composed of TAR DNA-Binding Protein 43 (TDP-43) in the majority (~97%) of patients, with the only exceptions occurring in patients with certain genetic forms of disease[49,50]. Specifically, cases of ALS caused by mutations in the superoxide dismutase 1 gene (SOD1) or fused in sarcoma gene (FUS) are pathologically distinct, exhibiting inclusions of these proteins, respectively, instead of TDP-43[51–59]. ALS cases caused by a hexanucleotide repeat expansion in chromosome 9 open reading frame 72 (C9orf72), are further distinct, displaying TDP-43 negative, p62 positive ubiquitinated inclusions[60], intranuclear RNA foci[61], and dipeptide repeat proteins resulting from unconventional translation of the hexanucleotide repeat[62,63].

The composition and distribution of these unique neuropathologic signatures within the central nervous system (CNS) would thus suggest that ALS clinical manifestations are a function of anatomical vulnerability to

focal neuropathologic damages. These neuropathological damages in turn are caused by genetic mutations, age, and/or environmental exposures. Since both genetic and nongenetic forms of ALS share clinical symptoms and core pathologic features, mechanisms in common between genetic forms of ALS may inform what occurs in all forms of ALS, revealing critical disease processes that may be targeted for therapeutic interventions.

1.5 ALS disease mechanisms- lessons learned from genetic studies and mouse models

A minority of ALS cases (~10%) are caused by genetic mutations, most often inherited within families in an autosomal dominant manner[14,64,65]. These cases are referred to as familial ALS (fALS), while the remaining majority of cases (~90%) are considered sporadic (sALS), with no known family history of disease. fALS and sALS are likely more related than this strict dichotomization implies, as de novo fALS mutations have been reported in sALS patients[66], fALS mutations can show incomplete penetrance[67,68] and pleiotropic manifestations[61,69,70], and multiple fALS genes can drive ALS through an oligogenic etiology[71–73]. Nonetheless, familial and sporadic forms of ALS result in similar clinical presentations and retain the core pathological features, supporting the proposition that processes in common between genetic forms of ALS may inform our overall understanding of disease.
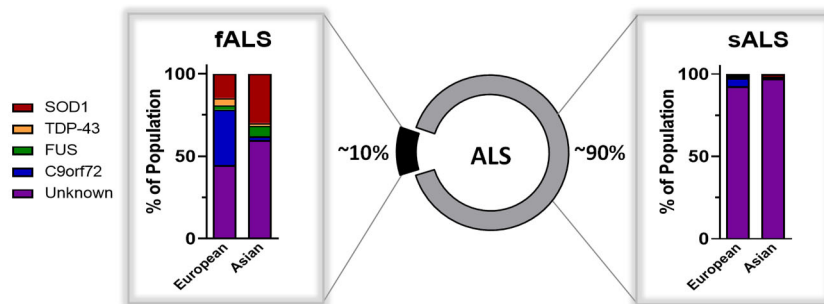
Figure 1.2. Genetic contributions to ALS.
Mutations in superoxide dismutase 1 (SOD1), TDP-43 (Tar-DNA binding protein 43), fused in sarcoma (FUS), and chromosome 9 open reading frame 72 (C9orf72) are the most common known genetic causes of familial ALS (fALS) and sporadic ALS (sALS). Data adapted from Mejzini et al., 2019[64].

Currently, the most frequent mutations in ALS occur in 4 genes- superoxide dismutase 1 (SOD1), TAR DNA binding protein 43 (TDP-43), fused in sarcoma (FUS), and chromosome 9 open reading frame 72 (C9orf72)(Figure 1.2)[14,64,74,75]. The development of several transgenic mouse models harboring ALS mutations in these genes have since been pivotal in identifying disease mechanisms driving MN degeneration in ALS, which we will briefly review below.

1.5.1 Studies of SOD1- the prototypical ALS gene

The first gene to be associated with ALS was the cytosolic superoxide dismutase 1 gene (SOD1) in 1993[76,77]. The SOD1 gene encodes a ubiquitously expressed metalloenzyme that functions as a protective cellular antioxidant, converting toxic superoxide species to molecular oxygen and hydrogen peroxide after binding copper and zinc ions and homodimerizing[78,79]. More than 185 different mutations spanning the full length of the encoded SOD1 protein have been reported to cause fALS, almost all of which are highly penetrant missense mutations inherited in a dominant manner[75,80]. These mutations result in characteristic neuropathological SOD1 aggregates[51,56], and can manifest with dramatically different clinical presentations[81], ranging from extremely aggressive, limb onset[82,83] to rare, respiratory onset with atypical sensory involvement[84]. Today, SOD1 mutations are the second most frequent cause of fALS, and together account for ~15-30% of fALS cases, and ~1-2% of total cases[64,74].

Pivotal studies using nonhuman models of SOD1-associated ALS swiftly followed the initial linkage reports, illuminating key pathogenic mechanisms that underlie the various clinical phenotypes. These included early studies supporting a model where SOD1 mutations initiate ALS through a toxic gain-of-function rather than through a loss of antioxidant function. These reports demonstrated that SOD1 enzymatic activity was retained, even increased, in several ALS associated variants[85], that SOD1 activity was not correlated with disease severity[86] or rate of progression[87], and that mice deficient in SOD1 did not develop MN disease[88]. Loss of SOD1 function was therefore insufficient to cause ALS, yet may nonetheless still contribute to disease, as SOD1 knockout mice demonstrate enhanced susceptibility to stress, including axonal injury and cerebral ischemia[88,89].

The generation of transgenic mouse models overexpressing mutant SOD1 provided strong evidence in support of a toxic gain-of-function mechanism. In general, all mouse models expressing mutant SOD1 displayed some feature of MN disease, including astrogliosis, selective loss of spinal MNs, and/or muscle wasting that progressed to paralysis and death[90–96]. These mice also developed pronounced aggregation of the SOD1 protein, similar to those seen in SOD1 ALS patient post-mortem samples. A common theme that emerged from these studies was that development of disease appeared dose-dependent, requiring threshold levels of mutant SOD1 protein[96,97]. These data supported a causal role for SOD1 in ALS, with proposed toxic-gain-of-function mechanisms related to the abnormal SOD1 protein conformation and aggregation, including obstructive intracellular accumulation[51,53,98–100], disrupted axonal transport[101–103], sequestered cellular components, induced ER stress[104–109], dysregulated

ubiquitin-proteasomal homoeostasis[24,110] as well as oxidative damage caused by aberrant dismutase activity[111–116] and mitochondrial dysfunction[117–119].

The recognition that cell types other than MNs directly contributed to MN damage in ALS was another particularly major discovery made using mutant SOD1 mice[120,121]. Evidence for this non-cell-autonomous mechanism was first demonstrated using chimeric mice, where mutant SOD1 activity in surrounding non-neuronal cells was demonstrated to be required for MN death, while conversely healthy, wild type non-neuronal cells promoted the survival of neighboring mutant SOD1 MNs[122]. Subsequent studies using cell-type-specific depletion of SOD1 then further confirmed the direct contribution of non-MN cell types in MN degeneration. Diminishing SOD1 levels in MNs was demonstrated to influence the time of disease initiation, while decreased levels in astrocytes and microglia- the major non-neuronal cells of the CNS- affected disease progression[123–125]. Moreover, restricted expression of mutant SOD1 to any one cell type was insufficient to reproducibly induce the full spectrum of disease phenotypes, indicating an important interplay between neuronal and non-neuronal cell types in the development and progression of this disease[126–130]. ALS disease mechanisms are thus thought to consist of a dynamic crosstalk between MN-intrinsic damages and non-MN extrinsic damages. Proposed non-cell-autonomous mediated mechanisms in SOD1 associated ALS critically include the upregulation of proinflammatory cytokines (such as interleukins, TNFα and NF-κB[131–135]) from surrounding neuroglial populations, the secretion of neurotoxic factors[136,137], and glutamate-mediated MN excitotoxicity due to reduced activity of the glial EAAT2 transporter[138–142].

1.5.2 Investigations into TDP-43- the shift to RNA binding protein biology in ALS

In 2006, a landmark study discovered that the core pathological inclusions seen in ALS patients were primarily composed of the TAR DNA binding protein (TDP-43)[49,50]. This study, along with the identification in 2008 that mutations in TDP-43 directly cause fALS, subsequently resulted in a paradigm shift from the SOD1 focused ALS studies[143–146]. TDP-43 is a ubiquitously expressed DNA/RNA binding protein that normally shuttles between the cytoplasm and nucleus to regulate multiple aspects of RNA metabolism and gene expression[147–151]. These include roles in pre-mRNA splicing[152–156], mRNA stability[157,158], mRNA translation[159–162], mRNA transport[163,164], pre-miRNA biogenesis and processing[165,166], regulation of noncoding RNAs[167,168], and stress granule formation[169–171]. To date, over 55 mutations in the gene encoding TDP-43 have been associated with ALS[75],

accounting for ~1.5-4.2% fALS cases and ~0.2-0.8% sALS cases[64,74]. The majority of these mutations are dominant missense mutations located in the prion-like, glycine rich C-terminal domain that mediates protein-protein interactions[172–174]. As might be expected given the hundreds to thousands of potential RNA and protein interacting partners, as well as the plethora of known endogenous functions, mutations in TDP-43 likely cause ALS due to both loss- and gain-of-function mechanisms related to RNA metabolism and RNA/protein aggregation.

The generation of multiple transgenic mouse lines modulating TDP-43 levels, with and without ALS-associated mutations, indeed revealed serious effects on cellular and organismal function. Mice with a constitutive and ubiquitous knockout of TDP-43 were the first reported, displaying early embryonic lethality and indicating an essential role for this protein during development[175,176]. Heterozygous mice of the same genetic background containing one functional TDP-43 allele were able to live to adulthood and importantly displayed features of ALS, including late-onset motor impairments[175,176]. The subsequent generation of mice with a conditional, post-natal, homozygous deletion of TDP-43 in the CNS circumvented the problem of embryonic lethality and heterozygosity, and further supported that loss of TDP-43 in mouse spinal MNs or CNS cell types like astrocytes could influence the development of ALS, with phenotypes of MN loss, axonal degeneration, neuromuscular junction denervation, muscular atrophy, and movement dysfunction[177–180].

Similar to TDP-43 deletion, mice with increased mutant TDP-43 expression also demonstrated features of motor neuron degeneration. Mouse lines expressing transgenic TDP-43 alleles using either a ubiquitous prion-promoter[180–186], a neuron specific promoter (Thy1.2 or CaMK2a)[187–192], or a motor neuron specific promoter (Hb9)[177], all generally showed spinal MN loss, neuromuscular denervation and motor deficits. While these studies had notable differences in the amount of TDP-43 expression, the degree of TDP-43 neuropathology observed, and the severity of MN disease, these data suggested that mutation-based modulation of TDP-43 expression significantly impacted motor phenotypes[96].

An important caveat throughout these studies however was the observation that TDP-43 tightly controlled its own expression in a negative autoregulatory feedback loop[193] and that abundant expression of TDP-43, even without an ALS mutation, could drive MN phenotypes. The recent development of mouse models expressing mutant TDP-43 within the endogenous locus[194–196] eliminated these overexpression artifacts to clarify that ALS associated TDP-43 mutations alone are sufficient to drive MN disease. Proposed TDP-43 associated ALS mechanisms thus include both a toxic gain-of-function caused by accumulated TDP-43 cytoplasmic aggregates, as well as a gain- and

loss- of normal TDP-43 function perturbing nucleocytoplasmic shuttling, dysregulating mRNA expression of hundreds to thousands of target genes, and causing aberrant mRNA splicing events[153–155,195,197–199].

1.5.3 Studies of FUS- an RNA binding protein driving aggressive and pathologically distinct ALS

A year after the discovery of TDP-43 mutations in ALS patients, pathogenic variants in another DNA/RNA binding protein, fused in sarcoma (FUS), were reported in ALS patients[200,201]. Genetic variants in FUS are similar in frequency to TDP-43 mutations, ~2.8-6.4% of fALS and ~0.3-0.9% sALS cases[64,74], making mutations in these DNA/RNA binding proteins the third and fourth most frequent cause of ALS. Like TDP-43, FUS normally shuttles between the nucleus and cytoplasm[202] to serve multiple functions regulating gene expression. These include roles in RNA transcription[203–206], pre-mRNA splicing[207,208], RNA transport and translation[209–211], miRNA processing[212,213], as well as functions in stress granule formation[214–216], and DNA damage repair via non-homologous end joining and homologous recombination[217–219]. Over 75 different FUS variants have been identified in ALS patients[75], most clustered within the N-terminal prion-like domain or the C-terminal region important for nuclear localization and DNA damage repair[220]. FUS-associated ALS are some of the most aggressive cases, with early onset, rapid progression[221–224], and are characterized by a unique pathology of large, basophilic, FUS positive cytoplasmic inclusions lacking TDP-43[200,225]. Consistent with these pathological observations and the extensive roles in DNA/RNA metabolism like TDP-43, mutations in FUS are hypothesized to contribute to ALS through a gain- and loss- of function mechanism driven by mis-localization of nuclear FUS into cytoplasmic aggregates.

Vertebrate models of FUS mutations have been useful in testing these mechanistic disease hypotheses. The first generation of FUS knockout mice was reported in 2000 by 2 independent groups, with distinct phenotypic inconsistencies between them. One study showed that homozygous FUS deficient mice in the inbred C57BL/6 J (B6) background died within the first 16 hours of life with substantial chromosomal abnormalities, indicating an essential function of FUS in genomic stability and viability[226]. However, a different outbred mouse background was used in the other report, and this time FUS knockout mice survived to adulthood, albeit with decreased body size, hypersensitivity to radiation, reduced female fertility and complete male sterility[227]. These data demonstrated that FUS was indispensable for cellular processes such as DNA repair and development, yet additional genetic elements were capable of significantly modifying or compensating for FUS function. A subsequent report further showed that the adult-viable FUS knockout mice did not develop ALS-like motor phenotypes until 2 years of age, and instead

showed neuropsychiatric phenotypes[228]. Moreover, conditional depletion of FUS from MNs also did not result in MN loss or neuromuscular junction denervation[229] cumulatively suggesting that loss of FUS function was not sufficient to cause ALS.

Data supporting a toxic gain-of-function in FUS-associated ALS were rather more convincing. The majority of mouse lines expressing ALS-linked mutant FUS developed some feature of MN disease, including pathological cytoplasmic FUS aggregates, neuroinflammation, denervated neuromuscular junctions, loss of spinal MNs, movement deficits and premature death[58,229–237]. Importantly, mutant alleles associated with some of the most aggressive, juvenile-onset forms of ALS were also more pathogenic in these mice, demonstrating a direct correlation between FUS mutations and both mouse and human disease severity. These data supported a toxic gain-of-function mechanism in FUS-associated ALS, with proposed disease mechanisms including the aggregation-mediated impairment in nucleocytoplasmic shuttling[202], aberrant RNA splicing defects[238], altered stress granule dynamics[59], sequestered essential cellular proteins, perturbed axonal trafficking[239,240], impaired NMJ formation[151,241,242], as well as loss-of function DNA damage repair[232].

1.5.4 Discovering C9orf72- the most frequent genetic driver of ALS

Lastly, a groundbreaking discovery in 2011 identified that the most common genetic cause of ALS was a hexanucleotide GGGGCC repeat expansion in the non-coding region of the C9orf72 gene[61,69]. These repeat expansions account for ~34% of fALS cases and ~5% of sALS cases in European and North American populations[64,74]. Pathological C9orf72 expansions display an impressive range in length, spanning hundreds to thousands of repeats in ALS patients, with substantial variability observed, not only between ALS patients and neuropathologically healthy individuals[243], but also between different tissues of the same individual[244]. Despite this somatic mosaicism and heterogeneity in the numbers of pathological GGGGCC expansions, a signature neuropathology exists. This is characterized by predominantly nuclear RNA foci due to sense and antisense transcription of the repetitive RNA, and inclusion bodies of 5 different dipeptide repeat proteins (DPRs) caused by non-canonical translation of the repetitive RNAs[62,63,245–248]. To account for these neuropathological features, three primary mechanisms have been proposed to explain how C9orf72 mutations cause ALS. These include a toxic gain-of-function from the C9orf72 repeat RNA foci, a toxic gain-of-function from the DPR inclusions, and/or a loss-of-function of nuclear C9orf72 protein (haploinsufficiency)[249–251]. Currently, the data for each of these mechanisms are

compelling, and it is likely that various permutations and combinations of these mechanisms are involved in ALS pathogenesis to some extent.

Initial insights into C9orf72 associated ALS disease mechanisms were gained by investigating the endogenous role of the C9orf72 protein product, which remained poorly understood at the time of the ALS-linkage studies. Early bioinformatic analyses predicted a homology with DENN family proteins that regulate membrane trafficking[252,253], and cell culture experiments supported this proposed role, with C9orf72 regulating endosomal transport within the cell[254,255] and autophagic clearance mechanisms[256,257]. These results fueled hypotheses that loss of C9orf72-mediated intracellular trafficking and degradation processes were contributing to MN loss and ALS progression. Mouse models depleted of C9orf72 however failed to recapitulate neurodegeneration and motor phenotypes reminiscent of ALS. These models include loss-of-function mice generated by conditional reduction of C9orf72 in neurons and glia[258], transient reduction in the CNS by antisense oligonucleotides[259], as well as full C9orf72 knockouts[260–265], all of which presented with extreme immunological problems instead of major deficits in neuronal survival or motor function. These data suggested that loss of C9orf72 function was insufficient to precipitate ALS. C9orf72 loss may instead contribute to disease propagation by dysfunctional macrophage and microglial neuroinflammatory processes[261] with recently published mouse models containing dual loss- and gain-of-function C9orf72 mutations supporting a synergistic effect of C9orf72 depletion in the development of MN deficits in ALS[266,267].

Mouse models exclusively overexpressing C9orf72 support a toxic gain-of-function disease mechanism. Strong adeno-associated virus (AAV)-mediated overexpression of C9orf72 GGGGCC repeats in the CNS of mice resulted in signature RNA foci, DPR inclusions, neurodegeneration and motor impairments[268,269]. AAV-induced CNS expression of specific C9orf72 DPRs (poly-GA or -GR) also resulted in age-dependent neurodegeneration and movement deficits through the accumulation of diffuse, cytoplasmic inclusions[270,271], effects that were notably not observed when the DPR sequence was mutated to prevent aggregation[270]. Importantly, non-viral germline expression of C9orf72 DPRs in neurons additionally resulted in neurodegeneration and motor dysfunction reminiscent of ALS[272–274]. Intriguingly, mouse models using bacterial artificial chromosome (BAC) mediated expression of C9orf72 sequences were the only murine models that did not universally result in motor phenotypes[275–277], with the exception of one research group[278]. The reasons behind these phenotypic discrepancies between overexpression techniques remain unclear but confounding genetic factors and epigenetic modifications

such as promoter methylation may be playing a role. These discrepancies withstanding, cumulative data from Drosophila[250,279–286], zebrafish[287–289], and most mouse models generally support the proposition that C9orf72 hexanucleotide repeat expansions are sufficient to cause ALS in a toxic gain-of-mechanism manner. Mechanisms implicated in C9orf72-ALS thus include dysfunctional macrophage and microglial neuroinflammatory processes[261], RNA foci/DPR-mediated disruptions in nucleocytoplasmic shuttling[250,282], perturbed intracellular trafficking, RNA processing[290], protein translation[271,291], stress granule formation[285,292], ER stress induction[293] and compromised autophagic[267], lysosomal[263], and ubiquitin-proteasome[294] degradation systems.

These C9orf72-associated mechanisms are reminiscent of pathways affected in the other major genetic causes of ALS (including SOD1-, TDP-43-, and FUS-associated ALS, among others). The impressive efforts to understand these genetic forms of ALS using nonhuman models have cumulatively allowed the identification of consensus drivers of MN vulnerability in ALS, include early impairments in DNA damage repair, aberrant RNA metabolism, altered intracellular trafficking (particularly nucleocytoplasmic transport, vesicular transport, and axonal transport), mitochondrial dysfunction, excitotoxicity, dysregulated ER/protein homeostasis, and non-cell-autonomous contributions mediating neuroinflammation (astrocyte/microglia) and oligodendrocyte myelination (Figure 1.3). These ALS disease mechanisms are further reviewed and explored in recent publications (Ragagnin et al., 2019[34], Cook et al., 2019[295], Mejzini et al., 2019[64], Hardiman et al., 2017[24], and Taylor et al., 2016[11]). Ultimately understanding how these common genetic mutations and age-related cellular stresses culminate in the core neuropathological phenotypes of MN degeneration and protein aggregation may augment the discovery of new drugs that can attenuate these final disease phenotypes.
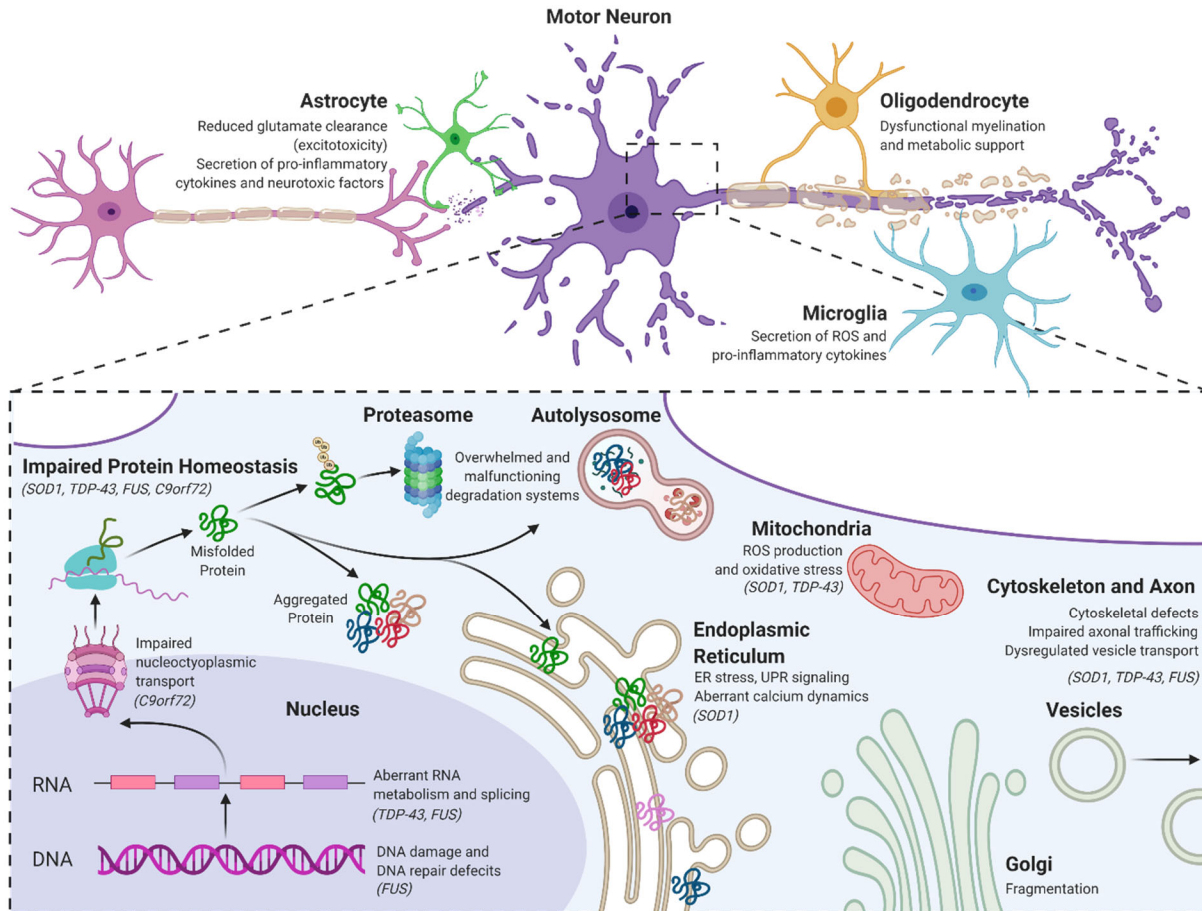
Figure 1.3. ALS disease mechanisms.

      ALS disease mechanisms consist of cell-autonomous dysfunctions in MNs and non-cell-autonomous contributions from non-MN cell types. Non-cell-autonomous mechanisms include dysfunctional myelination and reduced metabolic support from oligodendrocytes, secretion of toxic entities by microglia and astrocytes, as well as reduced synaptic clearance of glutamate by astrocytes. Within MNs, deficits occur in nearly all functional compartments, including deficiencies in DNA damage repair, aberrant RNA metabolism and splicing reactions, impaired nucleocytoplasmic transport, dysregulated protein homeostasis, degradation pathways and endoplasmic reticulum (ER) function, reduced mitochondrial function and oxidative stress management, as well as perturbed vesicular and axonal trafficking. Common mutant proteins that contribute to each of these mechanisms are italicized. Original figure generated by M. Watts, inspired by Hardiman et al., 2017[4].

1.6 Translating disease mechanisms to therapeutics- challenges with nonhuman research models

Our understanding of ALS has been irrefutably improved by using animal model systems. Yet there are limits to what animal models can teach us about human disease. This fact has been made soberingly clear by the failure of ALS drugs shown to be effective in animal models to confer clinical benefits in patients. After 3 decades, and over 70 different compounds tested in ALS clinical trials, only two have been approved- the anti-glutamatergic drug Riluzole and the antioxidant Edaravone[19]. Problems with clinical trial design undoubtably have contributed to these failures, including pharmacodynamic issues of CNS penetration, drug-target engagement, timing and dosing of treatments, and patient selection criteria, to name just a few[296–298]. Yet key discrepancies between animals and humans have also played a role in these past clinical trial failures.

Perhaps the most apparent discrepancy, the anatomy of the human nervous system is distinctly different from that of a mouse, the preclinical model of choice. These differences include obvious divergences in MN size and lengths of axonal projections, which can reach up to meters-long in an adult human. Yet synaptic circuitry and signal propagation within this neuroanatomy also differ. In humans, monosynaptic connections between upper cortical spinal MNs in the brain and lower MNs in the spinal cord can coordinate control of muscles, particularly those of the hands and fingers[299,300]. This direct cortico-motoneuronal (CM) control of muscles is unique to dexterous primates, and different from mice which rely more on interneuron-mediated connections[299,300]. In addition to anatomical and neural circuitry differences, humans are genetically different from mice, with distinct non-conserved intronic and non-coding regions. The fact that the most common genetic mutation to cause ALS, C9orf72, occurs in an intronic region[61,69] makes this a particularly important distinction, as well as recent results from pivotal studies using patient cells[198,199] which indicate a critical role for these human-specific regions in ALS pathogenesis.

Even ignoring potentially unavoidable species-species differences, mouse models expressing ALS transgenes raise additional challenges when recapitulating human disease. Up until recently, the majority of ALS mouse models have involved supraphysiological overexpression of mutant alleles, up to 1700% of endogenous expression in the most widely used preclinical SOD1^{G93A} mouse model[96,296]. Such extreme overexpression may overstate phenotypes and overshadow disease relevant features, thereby failing to accurately reflect disease and predict therapeutic interventions. There is also the distinct possibility that this widely used SOD1 preclinical mouse model may only be predictive for SOD1 patients. Moreover, even recent mouse models using other genetic

mutations and avoiding overexpression artifacts have limitations, as no current model fully recapitulates all features of ALS seen in humans[96,301,302].

The ability to complement the current mouse models and study human ALS MNs, which contain the patient's full genetic background, may begin to bridge this gap between mice and men and improve mechanistic insights and preclinical drug discovery. Previous efforts to obtain human ALS MNs for study however were fraught with challenges, simply because MNs from ALS patients are fundamentally limited. By definition, MN numbers are significantly depleted in ALS patients, and biopsies and collections of brain and spinal cord tissue are risky and therefore only performed if required for clinical diagnosis and management. Even if CNS tissue were easily accessed and biopsies were routinely done, MNs are post-mitotic and incapable of proliferation and expansion, further diminishing their utility for culture and study. CNS tissue from ALS patients can be obtained post-mortem, yet specimens from deceased patients are still limiting as they can only inform end-stage disease manifestations- that of a damaged tissue completely depleted of the cell type of interest. The ability to augment mouse models and study ALS mechanisms in patient cells was thus essentially impossible until the recent advent of reprogramming technologies and directed neural differentiation methods.

1.7 Human cellular models of ALS using patient induced pluripotent stem cells

The discovery that a lineage-specified cell, such as a skin cell, could be reprogrammed back in time to an embryonic-like state was a revolutionary scientific breakthrough achieved by Takahashi and Yamanaka in 2006[303,304]. These reprogrammed cells, referred to as induced pluripotent stem cells (iPSCs), can create almost any cell type of the human body and can expand indefinitely, similar to stem cells from a human embryo but without the corresponding ethical and moral issues. IPSCs transformed the scientific field and have been incredibly useful for studying complex neurological disorders like ALS, where diseased human neural tissue is otherwise inaccessible and the genetic components driving disease are complex, uniquely human, and largely unknown. Using iPSCs from ALS patients, we can now generate mass quantities of diseased human MNs containing the precise known and unknown genetic components causing disease, recapitulating features of ALS MN degeneration in vitro. These patient-matched "disease-in-a-dish" models of ALS may augment existing animal models for improved disease understanding and therapeutic identification.

To be useful as a disease model, MNs generated from ALS patient iPSCs must accurately represent their endogenous counterparts. The best way to do this is to follow developmental paradigms, differentiating iPSCs into MNs by mimicking the molecular signals that induce embryonic stem cells to form neuroectoderm and MN populations[305]. In brief, during early development, the neuroectoderm is initially fated by signals produced by the dorsal lip of the blastopore, which inhibit bone morphogenic proteins (BMPs) and transforming growth factor-β (TFGβ) driving the alternative mesodermal and endodermal lineages[306–312]. These neuroectodermal cells then fold into a neural tube that is further specified along the rostral-caudal and dorsal-ventral axes by gradients of morphogenic signaling molecules[313]. Along the rostral-caudal axis, the neural tube is specified into the forebrain, midbrain, hindbrain, and spinal cord domains by graded concentrations of retinoic acid (RA), fibroblast growth factors (FGFs) and wingless-type MMTV integration site family members (Wnts)[314–320]. Along the dorsal-ventral axis, MN and interneuron subtypes are specified by Sonic Hedgehog (SHH), a morphogen secreted from the notochord and floor plate[321–323]. The precise combination of these signaling molecules provides a matrix of positional identity cues by regulating the expression of transcription factors, which delineate sharp boundaries of neuronal progenitor domains[320,324–329]. All ventral, caudal spinal cord MNs arise from the one pMN progenitor domain, requiring high SHH concentrations[330] to generate terminally differentiated MN populations expressing the transcription factors Hb9 (Mnx1), Lhx3, and Ils1/2[329,331–334]. MN maturation and subtype specification is then further aided by axonal guidance molecules and neurotrophic factors, such as brain-derived neurotrophic factor (BDNF), ciliary neurotrophic factor (CNTF), glial-derived neurotrophic factor (GDNF), and nerve growth factor (NGF), which support MN survival, axonal targeting, and functional maturation into MN pools, which innervate muscle fibers to allow coordination of movement[305,335,336].

Protocols generating MNs from pluripotent stem cells thus aim to recapitulate these key developmental steps (Figure 1.4A). The first protocol differentiating spinal motors neurons from mouse embryonic stem cells was reported in a seminal paper by Wichterle et al. in 2002[337], where the authors emulated the main embryogenic steps of neuralization, caudalization, ventralization, and trophic support. This protocol produced functional spinal MNs that populated the embryonic spinal cord, extended axons, and formed synapses with target muscles[337], and was subsequently adapted to human embryonic stem cells in 2005[338], and finally to iPSCs from ALS patients in 2008 by Dimos and colleagues[339].
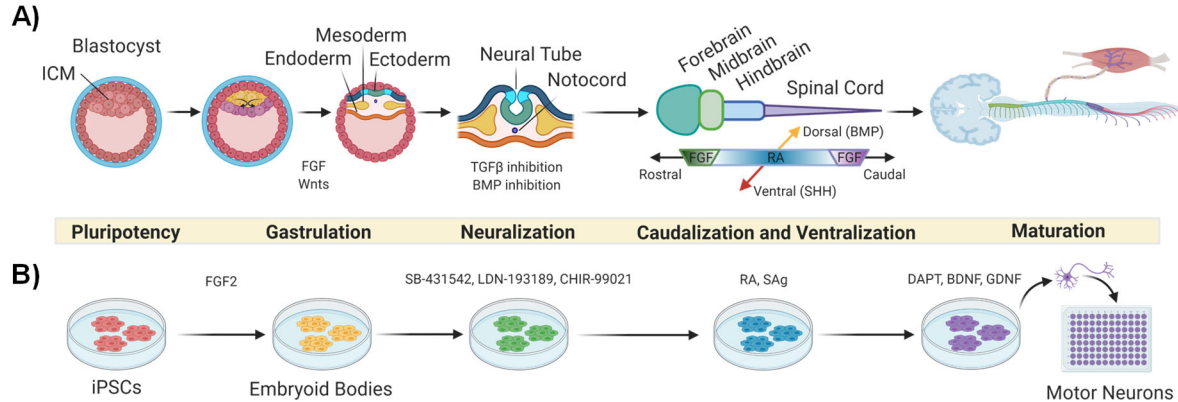
Figure 1.4. Producing MNs from iPSCs by recapitulating developmental signals.
  A) During development, pluripotent cells of the inner cell mass (ICM) produce cells of the 3 germ layers of the
     body- endoderm, mesoderm, and ectoderm- in a process called gastrulation. Ectodermal cells are fated
     during this process by activation of fibroblast growth factors (FGFs) and wingless-type MMTV integration
     site family members (Wnts). Neuroectoderm is then further specified by the dual inhibition of mesodermal
     factors (bone morphogenic proteins, BMPs) and endodermal factors (transforming growth factor β, TGFβ),
     a process referred to as neuralization. Rostral-caudal specification of the neuroectoderm is then directed by
     retinoic acid, produced by presomitic mesodermal cells surrounding the spinal cord, and dorsal-ventral
     identity is determined by Sonic Hedgehog (SHH), produced by the notochord. The developing MNs in the
     central nervous system then extend axonal projections and survive and mature with trophic support from
     innervated target cells.
  B) Induced pluripotent stem cells (iPSCs) are directed to produce MNs by following developmental
     paradigms. IPSC colonies are first dissociated and cultured in suspension in self-organizing cellular
     aggregates termed embryoid bodies (EBs) that are sequentially exposed to recombinant proteins or small
     molecules that mimic gastrulation, neuralization, caudalization, ventralization, and maturation signals.
     (FGF2; SB-431542, a TGFβ inhibitor; LDN-193189, a BMP inhibitor; CHIR-99021, a Wnt activator; RA,
     retinoic acid; Sag, smoothened agonist, a SHH signaling pathway activator; DAPT, a γ-secretase inhibitor;
     BDNF, brain derived neurotrophic factor; GDNF, glial-derived neurotrophic factor). Original figure
     generated by M. Watts, inspired by Sances et al., 2016[305] and Davis-Dusenbery, et al., 2014[329].

Since this time, numerous protocols have been published differentiating patient pluripotent stem cells into

MNs, most generating heterogeneous LMN populations characterized by pan LMN transcription factor markers

(Hb9, Isl1/2, and Lhx3)[305,320]. However, the main developmental steps of neuralization, caudalization, ventralization

and trophic support are largely conserved (Figure 1.4B). Neuralization of iPSCs is first commonly achieved by

reducing BMP and TGFβ signaling with the efficient small-molecule inhibitors SB431542 and LDN193189, termed

dual-SMAD inhibition[340]. Caudalization is then directed by treatment with retinoic acid, frequently supplemented

with CHIR-99021, which activates Wnt signaling via inhibition of glycogen synthase kinase 3 (GSK3β)[341].

Ventralization is then achieved by addition of a small molecule SHH or recombinant SHH signaling agonists like

Smoothened Agonist (Sag). Culture media supplemented with neurotrophic factors subsequently promotes survival

and MN maturation in vitro[305]. These MN differentiation protocols, as well as alternative strategies using

transcription factor mediated neural induction of iPSCs[342] and direct reprogramming of fibroblasts to MNs[343],

ultimately demonstrate the incredible ability we now have to generate these unique, and once inaccessible, human

cell types.

1.7.2 Recapitulating ALS using patient iPSC-derived MNs

Since the first report in 2008, an overwhelming number of studies have derived and utilized MNs from

ALS patient iPSCs. These include studies using fALS patient MNs with defined genetic mutations, as well as studies

using sALS patient MNs without any known genetic causes. Such investigations would be impossible in nonhuman

models. As a resource for future investigators, a compendium of all published ALS-iPSC-derived neuronal works

has been compiled in Appendix A, highlighting the key pathological findings of each paper as well as the

methodology used to interrogate these disease features. This comprehensive literature review has shed light on

several themes relevant to fALS and sALS disease and demonstrated that ALS patient derived MNs generally

corroborate data from animal models and recapitulate ALS phenotypes. These include MN vulnerability, neuritic

degeneration, DNA damage, aberrant RNA metabolism, nucleocytoplasmic transport, mitochondrial dysfunction,

altered excitability, and enhanced ER proteostatic stress. While critical areas for further research have been

identified, some of which this thesis aims to address, several groundbreaking iPSC-derived ALS reports have

discovered novel disease mechanisms and therapeutic interventions that are currently in clinical trials, highlighting

the advantages of complementing mouse models with patient derived cellular systems for improved drug discovery.

We will briefly review these key studies here, with attention towards the ability of iPSC-derived systems to

recapitulate early disease mechanisms and final convergent phenotypes of MN death and insoluble protein

aggregation.

1.7.3 fALS patient derived MN studies

SOD1 iPSC-derived MN studies

Beginning investigations into ALS using iPSC-derived MNs were first published from the Eggan lab using

SOD1 fALS patient lines. This group demonstrated that SOD1 mutant alleles did not affect the ability to produce

functional MNs[339,344], and that the derived SOD1 patient MNs additionally recapitulated cellular features of ALS,

including reduced ALS MN viability with prolonged time in culture, enhanced apoptosis, reduced soma size, fewer and shorter neuritic processes, as well as intracellular abnormalities in mitochondria, ER stress, and hyperexcitability[345,346]. The sufficiency of the SOD1 A4V mutation (SOD1^{A4V}) to specifically drive these phenotypes in patient MNs was also critically confirmed using a gene corrected isogenic control, in one of the first instances to use such an approach. These ALS MN degenerative phenotypes were later corroborated by Bhinge and colleagues using a separate SOD1^{E100G} patient line and gene corrected control, demonstrating similar decreases in SOD1 patient MN viability with time in culture, altered soma morphology, damaged neuritic properties, and elevated ER stress transcripts that activated ERK and JNK-cJUN apoptotic pathways[347]. In fact, while the ability to observe reduced SOD1 MN viability compared to controls has not always been reproducibly demonstrated[348,349], the dysregulation of ER stress related gene expression has been broadly reported in studies using various different SOD1 patient lines (SOD1^{A4V}, SOD1^{E100G}, SOD1^{D90A}, SOD1^{R115G}, and SOD1^{A272C}) even those without apparent viability defects, supporting an association between early ER-stress signaling to precede SOD1-ALS MN degeneration[345,347,348,350].

Moreover, the ability to detect the characteristic SOD1 inclusions in patient derived MNs like those seen in patient postmortem samples and mouse models has also been inconsistent between groups. Some studies report SOD1 aggregates in patient MNs kept in basal conditions[351,352], while others report aggregates only in combination with proteasomal inhibition[345,347]. These phenotypic discrepancies may be due to differences in MN differentiation and culture conditions between groups. Alternatively, the insoluble aggregates themselves may represent an over-reflected phenomenon in end-stage postmortem samples and an exaggerated feature in mice expressing supraphysiological levels of mutant transgenes. The preservation of diminished viability phenotypes in SOD1 patient derived MNs, even without detectable aggregates, supports the proposition that earlier disease drivers may link the initial SOD1 genetic mutation to MN death, and that insoluble protein aggregation is a more late-stage, accumulated disease phenotype. The ability to capture these early disease phenotypes as they temporally progress in time is a great advantage of using ALS patient derived MN cultures. The observed signatures of ER stress and aberrant electrical activity may represent two prominent prodromal features of SOD1-ALS, which may be further leveraged in disease models and targeted for therapeutic interventions[345,346].

TDP-43 iPSC-derived MN studies

Studies using TDP-43 fALS patient lines quickly followed those of SOD1, reporting similar inconsistencies to observe ALS phenotypes of decreased MN viability and pathological protein aggregation. Some reports demonstrate TDP-43 patient MN survival that is comparable with controls[349,353], while others report TDP-43 MN viability deficits in basal conditions[352,354–358] or with exogenous stress[354,359–361]. The ability to recapitulate the characteristic pathological cytoplasmic inclusions has also been met with conflicting results, with some reports demonstrating insoluble TDP-43 inclusions and cytoplasmic mislocalization in basal long-term culture conditions[354,357,359], while others report TDP-43 pathology and stress granule induction only when exposed to cellular stressors[198,361,362]. Looking at the data from all model systems, the accumulation of insoluble cytoplasmic aggregates and stress granules likely reflect downstream features of advanced cellular stress that begin with earlier disease processes. In the case of TDP-43 associated ALS, these early disease manifestations include loss of nuclear TDP-43 and dysregulated TDP-43 cytoplasmic functions, each feature synergistically aggravating the other in a vicious disease cycle to result in MN death and inclusion bodies.

Indeed, recent groundbreaking work has demonstrated that critical upstream disease processes specifically include altered nuclear pore morphology, aberrant nucleocytoplasmic transport, and dysregulated splicing functions. Chou and colleagues demonstrated that TDP-43[G298S] patient derived MNs exhibited abnormal nuclear morphology with mislocalized nuclear pore proteins[363]. Suppressing aberrant nuclear export importantly was able to rescue TDP-43 neurotoxicity in both mouse cortical neuron and Drosophila models[363]. Klim et al. and Melamed et al. then both independently identified that TDP-43 mutations in patient MNs resulted in altered nucleocytoplasmic transport as well as profound splicing defects, particularly in the stathmin 2 gene (STMN) which normally functions as a microtubule regulator promoting neurite outgrowth and axonal regeneration[198,364]. These degenerative phenomena notably occurred without the presence of detectable insoluble aggregates, suggesting a model where altered nuclear pore morphology, perturbed nucleocytoplasmic transport, and splicing defects are upstream to MN death and insoluble protein aggregation, and illustrating the power of patient MN disease models to identify these early disease manifestations. Attenuating these early TDP-43/STMN2 splicing deficits with a JNK inhibitor (notably convergent with the ER-stress JNK signaling occurring in SOD1 patient MNs) provided a proof-of-concept that therapeutic modulation of these upstream drivers may be beneficial[198].

FUS iPSC-derived MN studies

In contrast with both SOD1 and TDP-43 patient MN studies, the ability to detect ALS phenotypes with FUS patient derived MNs has been met with near uniform success, particularly, the observation of FUS mislocalization into cytoplasmic aggregates[244,356,365–377]. This is likely due to the aggressive nature of the FUS mutations lacking nuclear localization signals, which drive severe forms of juvenile onset ALS. Indeed, early studies by Japtok et al. and Lenzi et al. elegantly demonstrated that the severity of the FUS mutation in patients directly correlated with the degree of pathological cytoplasmic FUS mislocalization observed in patient derived MNs[366,367]. This cytoplasmic mislocalization as well as FUS MN viability defects were enhanced with age in culture and with exogenous stress, arguing in favor of a sequential model for FUS-ALS pathogenesis, where upstream disease processes include the mutation-based cytoplasmic mislocalization of FUS, and secondary aggravating disease processes occur with accumulated cellular stress with aging and environmental exposures. The formation of downstream inclusion bodies may be part of these secondary disease processes that further exacerbate nuclear exclusion loss-of-function with cytoplasmic gain-of-function in a self-perpetuating vicious cycle to drive MN death.

Work by Guo et al. and Naumann et al. corroborated these initial reports of FUS associated mislocalization phenotypes in patient derived MNs, and additionally reported that axonal transport defects and DNA damage represented upstream FUS-ALS disease process[239,371]. The authors demonstrated that FUS patient derived MNs had impaired ER vesicle transport and mitochondrial trafficking[239], and that DNA damage occurred even before FUS mislocalization and observable axonal trafficking deficits[371]. Intriguingly, induction of DNA damage even in control MNs phenocopied distal axonal transport deficits, and impairing FUS nucleocytoplasmic shuttling reciprocally caused DNA damage and repair deficits. These data illuminated multiple, self-perpetuating disease processes in FUS-ALS patient MNs, where FUS mutations disturbed nucleocytoplasmic shuttling and DNA damage repair, which then exacerbated each other to drive cytoplasmic aggregation, cellular trafficking deficits, and MN death.

C9orf72 iPSC-derived MN studies

Finally, recapitulating C9ORF72 associated fALS mechanisms has also been met with some success and some inconsistencies. Many independent groups have demonstrated that C9ORF72 patient derived MNs display the characteristic pathological RNA foci transcribed from the hexanucleotide repeat[250,377–384], and dipeptide repeat proteins (DPRs) non-canonically translated from the repeat RNA[380,383–392]. The cumulative body of work using

C9ORF72 patient MNs has additionally demonstrated similar early cellular dysfunctions, including DNA damage like FUS fALS patient derived MNs[379,384,388], RNA binding protein defects and nucleocytoplasmic transport abnormalities like FUS and TDP-43 patient MNs[250,377,378,390–392], as well as ER stress[380,393] and abnormal electrical activity[346,353,378,394]. However, comparable to TDP-43 patient MNs, C9ORF72 MNs also failed to reproducibly display insoluble TDP-43 pathology or viability deficits unless exposed to exogenous stress[377,381,383,386,387,395]. These data demonstrating comparable early cellular deficits yet inconsistent end-stage phenotypes are ultimately in line with the proposition that conserved upstream dysfunctions, namely DNA damage, nucleocytoplasmic RNA perturbation, ER stress, axonal transport defects, and excitability, accumulate with time and/or advanced cellular stress, and critical thresholds must be surpassed to result in the final convergent phenotypes of MN degeneration and insoluble aggregates.

1.7.4 sALS patient derived MN studies and emerging therapeutic candidates

Lastly, the ability to investigate disease processes without a monogenic origin is an unparalleled benefit of using patient cells. The initial studies of fALS patient MNs revealed several critical early disease mechanisms that generally converged at the level of cell death and insoluble protein accumulation with time or added stress. Yet ALS is primarily sporadic and most often without a familial genetic history. Evaluating these disease mechanisms in cells from sporadic ALS (sALS) patients, which contain the complete genetic constellation that drives their disease, allows researchers to identify disease phenotypes that are most relevant to the majority patient population and therapeutic agents that may rescue those disease features. In perhaps one of the most impressive reports to date, Fujimori and colleagues utilized 32 sporadic ALS lines, in combination with SOD1, TDP-43, and FUS fALS patient lines (totaling 58 ALS lines) to demonstrate that ALS patient MNs displayed reduced neurite outgrowth, pathological TDP-43/FUS protein aggregation, and apoptotic MN death with prolonged time in culture (40-70 days in vitro)[357]. The authors additionally went on to show that the derived MN degenerative phenotypes correlated with the corresponding patient's clinical progression, demonstrating the value of using patient cells to accurately represent ALS "in a dish". The authors leveraged these multi-phenotypic ALS cellular readouts for a small molecule screen, ultimately identifying the dopamine receptor agonist Ropinirole as a top therapeutic candidate that rescued these degenerative phenotypes. Ropinirole is now currently in controlled clinical trials for ALS (trial registration number UMIN000034954 and JMA-IIA00397)[396,397].

The transformative power of ALS iPSC-derived MNs to recapitulate human disease and identify novel ALS drug candidates for clinical trials has also been successfully demonstrated by other groups. Wainger and colleagues for example identified the anticonvulsant drug Retigabine as a suppressor of the early hyperexcitability phenotype of ALS patient derived MNs[346]. Retigabine functioned to effectively block aberrant early electrical activity as well as ER stress pathways in ALS MNs by activating Kv7 channels, subsequently promoting the downstream survival of SOD1, FUS, and C9ORF72 patient derived MNs aged in culture. Since this publication, Retigabine has also been effective in phase II clinical trials to lower excitability in ALS patients, measured by transcranial magnetic stimulation and threshold tracking nerve conduction studies (clinicaltrials.gov identifier NCT02450552). These data are encouraging, and it will be exciting to see if modulating excitability ultimately translates to modifying disease progression in ALS patients. Imamura and colleagues additionally identified a candidate ALS therapeutic by performing a small molecule MN survival screen. Bosutinib emerged as a hit neuroprotective drug from this screen, improving the survival of SOD1, TDP-43, C9ORF72, and some sALS patient derived MNs by inhibiting Src/cAbl kinases and enhancing autophagic clearance of aggregated mutant SOD1 protein[352]. Bosutinib is now too being evaluated in a phase I dose escalation clinical trial for ALS patients (trial registration number UMIN000036295)[398].

It is noteworthy that all 3 clinical trial candidates for ALS identified in patient MNs- Retigabine, Bosutinib, and Ropinirole- were effective against the final conserved ALS phenotype, MN death, each by attenuating distinctly different upstream processes. While ALS is vastly heterogeneous in its etiology, these data support the premise that a smaller number of core initiators may drive MN death and attenuating these processes may serve therapeutic benefit. Identifying these core initiators of MN death in patient cells, as well as selective blockers of this death, may ultimately augment the identification of new targets for ALS therapeutics.

1.8 Endoplasmic reticulum stress as a specific initiator of MN degeneration and specific thesis aims

Human stem cell modeling research has vastly improved our understanding of ALS and advanced the identification of novel therapeutic candidates. Yet a current limitation to using iPSC-derived MN cultures to study ALS is the variability in observing the hallmark disease phenotypes of selective MN death preceded by increasing protein aggregation (reviewed in section 1.7.3, Appendix A). While this phenotypic variation can be attributed to the heterogeneous MN production protocols used between groups, another important contributing factor is the immaturity of the derived cells[399]. This cellular immaturity is significant since ALS is commonly an age-related disease, occurring over several decades in patients with a combination of genetic predispositions and accumulated cellular stresses. It is possible that specific cellular conditions or core stresses must be enhanced to recapitulate these age-associated dysfunctions and initiate ALS MN degenerative phenotypes (Figure 1.5). Identifying the specific stressors that initiate MN death and pathological protein aggregation in patient cells will thus improve our understanding of what makes human MNs particularly vulnerable in disease, as well as enable precise conditions to consistently observe hallmark ALS phenotypes for disease studies and neuroprotective drug screening.
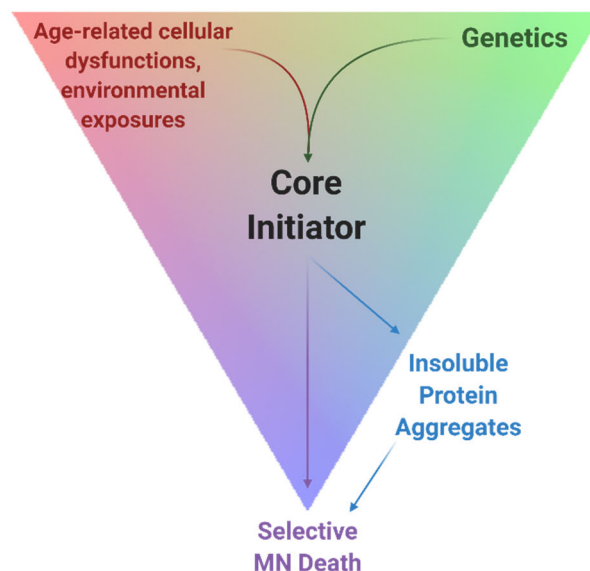
Figure 1.5. Genetic and environmental triggers may converge on one or more core initiators to drive ALS cellular phenotypes.

Currently, our understanding of the stressors that initiate degeneration of patient MNs remain limited in number and in scope. The majority of studies using iPSC-derived MNs have relied on prolonged culture times, variably ranging from several weeks to months[345,357]. Other groups have removed supporting trophic factors[360,400] or

added exogenous stressors, the most common including glutamate to produce excitotoxic stress[377,386,395], sodium arsenite to induce DNA damage and oxidative stress[367,369,401], and MG132 to impair proteasome-mediated degradation[198,345,347,372].

Yet these stressors are not the only ones implicated in ALS progression and therefore not the only processes needing to be uniquely modeled and evaluated for their ability to selectively initiate human MN degeneration. In particular, endoplasmic reticulum (ER) stress is another prominent mechanism implicated in ALS model systems[402], one that is still relatively understudied in iPSC-derived ALS patient MN cultures. So far, a few groups have utilized ER stressors for studies largely related to intracellular calcium stores, calcium flux and excitability properties[380,393,394,403]. Yet these studies leave open the possibility that initiating prolonged ER dysfunction in patient MNs can induce the late-onset degenerative phenotypes of preferential MN degeneration and pathological protein aggregation, and further inform how human MNs respond to this unique type of stress compared to other stressors.

Indeed, ER stress is one of the primary mechanisms hypothesized to influence MN vulnerability in ALS mouse models. The ER functions to ensure the proper folding and quality control of proteins trafficking through the ER-Golgi-secretory pathway, and is distributed extensively throughout the entire somatic, dendritic, and axonal compartments to serve these essential functions[34,404]. MNs, with their meters-long axonal projections, place unusually large demands on this organellar network, and display elevated basal levels of ER stress transcripts compared to other cell types[345]. In MNs with ALS mutations, the burden on the ER is even further enhanced. Misfolded mutant proteins physically interact with and aberrantly modulate ER-resident folding chaperones[402,405], resulting in the chronic upregulation of ER stress signaling and the activation of the unfolded protein response (UPR)[106,109,345] (Figure 1.6). The UPR is initially cytoprotective against misfolded protein stress in the ER lumen, (1) upregulating ER-resident protein chaperones that aid proper protein folding, such as binding immunoglobulin protein (BiP); (2) downregulating new protein translation via phosphorylation of eukaryotic initiation actor 2α (eIF2α); and (3) enhancing ER associated degradation processes[406]. Yet prolonged and chronic activation of the UPR results in apoptotic signaling driving MN death[402].
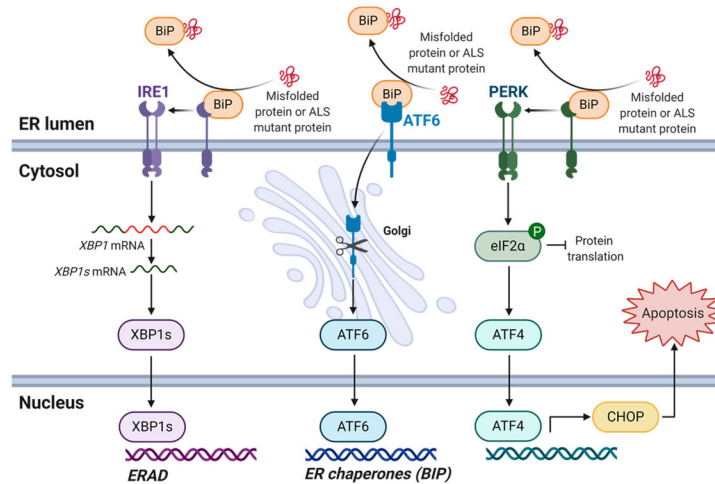
Figure 1.6. ER stress and the unfolded protein response.
     In conditions of ER stress, such as when ALS mutant proteins accumulate in the ER lumen or with pharmacological stressors thapsigargin or tunicamycin, the unfolded protein response (UPR) is activated. This begins when the ER chaperone binding immunoglobulin protein (BiP) binds to misfolded proteins and dissociates from the 3 transmembrane receptors protein kinase R-like endoplasmic reticulum kinase (PERK), activating transcription factor 6 (ATF6), and inositol-requiring enzyme 1 (IRE1). PERK dimerizes and phosphorylates eukaryotic initiation factor 2α (eIF2α) to stop additional protein production and activate the transcription factor ATF4. ATF6 translocates to the Golgi, where it is proteolytically cleaved to become an active transcription factor. IRE1 also dimerizes and splices X-box-binding protein (XBP1) to form another transcription factor. Spliced XBP1 (sXBP1), ATF6, and ATF4 upregulate ER protein folding chaperones and genes responsible for ER-associated-degradation (ERAD). This UPR signaling is initially cytoprotective. However, with prolonged signaling, pro-apoptotic proteins like CHOP are upregulated to drive cell death by apoptosis. Figure adapted from "UPR Signaling (ATF6, PERK, IRE1)", by BioRender.com (2020). Retrieved from https://app.biorender.com/biorender-templates.

     These early, enhanced signatures of ER stress, and the subsequent chronic activation of the UPR may underlie MN susceptibility to mutant proteins that are ubiquitously expressed in ALS[26,402,407]. Particularly, a longitudinal transcriptomic analysis of MNs in a mutant *SOD1* ALS mouse model demonstrated that particularly vulnerable MNs (the fast-fatigable MNs) displayed elevated ER stress transcripts at birth, which initiated an unfolded protein response in these cells weeks before neuromuscular junction denervation[109]. This initiation of the UPR was notably not observed or delayed in the resistant MN populations (the fast-fatigue resistant or slow MNs), indicating that vulnerable MNs were intrinsically more susceptible to ER stress signals. Thus, activation of a chronic UPR causes selective MN subtype degeneration and ALS disease progression[109]. Moreover, ER resident proteins, SIL1 and Calreticulin (CRT), have been proposed to specifically underlie this intrinsic vulnerability in the fast-fatigable MNs. SIL1, the nucleotide exchange factor assisting BiP to catalyze folding reactions and reduce the formation of mutant SOD1 inclusions, was expressed in vulnerable MNs at levels 6-times lower than resistant MNs[408]. SIL1 depletion, like that observed in vulnerable MNs, resulted in increased mutant SOD1 aggregates and

exacerbated ER stress[409], while SIL1 overexpression alternatively preserved the vulnerable MN population and prolonged survival in mice[408], relating the decreased levels of SIL1 to MN subtype vulnerability in ALS. Moreover, vulnerable MNs also displayed a 2 fold lower expression level of CRT, a calcium binding ER chaperone, compared to resistant MN populations[410]. Decreased levels of CRT contributed to ER stress and disturbed calcium homeostasis in vitro[410], and accelerated neuromuscular junction denervation and muscle weakness in SOD1-ALS mice[411], supporting the role of ER proteostasis and ER chaperone proteins in ALS MN vulnerabilities.

Finally, ER stress and ER calcium-binding chaperones are also intimately connected with another prodromal signature of ALS- altered excitability. The ER harbors the vast majority of intracellular calcium stores and neurons require an intricate balance of these calcium concentrations to confer the propagation of synaptic signals and the competence to receive electrical stimuli[412]. Decreased levels of the ER-calcium binding chaperone CRT in vulnerable MNs therefore diminishes the ability of these neurons to buffer Ca^{2+} levels and increases their susceptibility to excitotoxic stimuli[26,34]. In fact, Kiskinis et al. and Wainger et al. thoroughly demonstrated that ALS patient derived MNs had altered ER stress levels and aberrant electrical activity, and pharmacologically manipulating either property reciprocally affected the other[345,346]. Increasing ER stress by treating ALS patient derived MNs with DTT increased MN electrical activity, while reducing ER stress with salubrinal conversely reduced abnormal electrical activity. Similarly, blocking electrical activity with tetrodotoxin reduced ER stress, while activating electrical activity with kainate, a glutamate agonist, or linopiridine, increased ER stress. These data cumulatively demonstrated that protein and calcium homeostasis within the ER coordinates with electrical activity, and each property is physiologically altered in ALS disease conditions.

Since ER stress is altered early in vulnerable MNs of mouse models and is interconnected with other disease phenotypes in patient cells, a comparative study of ER stressors to potentiate the late stage ALS phenotypes of preferential MN degeneration and pathological protein accumulation would improve our understanding of the cellular mechanisms underlying MN vulnerability in iPSC-derived MNs and aid the development of additional age-related disease models. Concurrently, the use of these exogenous stressors could reduce the time needed to observe late-onset ALS phenotypes in patient cells, facilitating screening methodologies and "-omics" technologies for neuroprotective drug identification.

This dissertation thus tested the hypothesis that pharmacological ER stressors could initiate selective MN degenerative phenotypes in ALS patient derived MNs. We used a combination of immunofluorescent microscopy,

live cell imaging, western blotting, and qPCR analyses to demonstrate that compounds dysregulating ER stress were preferentially more toxic to MNs compared to non-MN cell types, in both healthy and ALS patient cultures, without inducing insoluble proteins. In contrast, proteasome inhibition drove the stereotypical insoluble aggregates seen in ALS pathology, yet did not uniformly cause selective MN death in patient lines. These experiments demonstrated, for the first time, an intrinsic vulnerability of iPSC-derived MNs to ER stress with distinctly differential effects to other proteostatic stressors. These studies additionally defined assay conditions necessary to induce convergent ALS MN degenerative phenotypes in a synchronous and scalable manner. We demonstrated that these assays could accurately predict and identify compounds with neuroprotective potential by showing that kenpaullone, a well-established MN protective agent, was able to preserve SOD1 and TDP-43 ALS patient MN viability in proteostatic stress conditions. We further demonstrated, for the first time, that a small molecule inhibitor to one of kenpaullone's targets, MAP4K4, was also able to maintain ALS patient MN viability in all conditions of proteostatic stress. This protection was notably independent of a direct reduction in insoluble protein buildup, separating the role of insoluble protein aggregates in selective MN death- with MN survival occurring without their reduction, and selective MN death occurring without their production. Finally, we utilized global phosphoproteomic remodeling analyses to discover a core proteome that is changed with kenpaullone and MAP4K4 inhibition and identified several novel drugs that preserved MN viability. Cumulatively, the work reported in this dissertation provides an accessible, robust, and therapeutically predictive model of proteotoxicity in human MNs that gives insight into the mechanisms contributing to patient MN degeneration and expands on the molecular targets protecting these unique cells from irrevocably damaging disease processes

Chapter 2

Proteostatic stressors induce ALS associated phenotypes in patient derived MNs

2.1 Attributions

All experiments presented in this chapter were designed, performed, and analyzed by Ms. Michelle Watts, with assistance from Ms. Kris Holton for statistical analyses. All aspects of this research were supervised by Dr. Lee L. Rubin, with funding graciously provided by Biogen and the Harvard Brain Science Initiative.

2.2 Introduction

Amyotrophic lateral sclerosis (ALS) is a fatal neurodegenerative disorder characterized by the preferential death of motor neurons (MNs)[1]. The loss of this unique cell type from the brain and spinal cord manifests in symptoms of muscle weakness and atrophy which progress rapidly to paralysis and respiratory failure approximately 1-5 years after diagnosis[24]. There are only 2 FDA approved treatments for this disease, neither of which extends life expectancy beyond a couple of months or improves muscle function in all patients[297]. Discovering effective treatments for ALS patients has been particularly challenging because affected human tissue is largely inaccessible for study and animal models are limited in reflecting complex human disease processes and predicting therapeutic interventions in patients[298]. Encouragingly, the recent advent of induced pluripotent stem cell (iPSC) technologies and neuronal differentiation methods has begun to address these challenges by allowing, for the first time, the production and study of MNs from ALS patients[304,339]. Researchers around the world can now develop patient-specific cellular models of ALS to investigate disease mechanisms in the correct, affected human cell type and perform drug screens for novel neuroprotective agents.

Taking advantage of this incredible opportunity, several groups have since identified therapeutic agents that can attenuate ALS patient MN degeneration in vitro, 3 of which are now currently in clinical trials[397]. Wainger and colleagues identified the anticonvulsant drug Retigabine (Ezogabine) as a suppressor of an early hyperexcitability phenotype in ALS patient MNs, which has now also demonstrated effectiveness in phase II clinical trials to lower excitability in ALS patients (clinicaltrials.gov identifier NCT02450552)[346]. Imamura and colleagues additionally demonstrated that the Src/cAbl inhibitor bosutinib could enhance the autophagic clearance of mutant SOD1 protein and improve the survival of SOD1, TDP-43, C9ORF72, and sALS patient derived MNs[352], with Bosutinib now too being evaluated in a phase I dose escalation clinical trial for ALS patients (trial registration number UMIN000036295)[398]. Finally, Fujimori and coworkers identified the dopamine receptor agonist Ropinirole as a therapeutic candidate that rescued reduced neurite outgrowth, pathological TDP-43/FUS protein aggregation, and

apoptotic MN death in a multi-phenotypic screen[357], with Ropinirole now the third compound identified in patient MNs to go into clinical trials for ALS (trial registration number UMIN000034954 and JMA-IIA00397)[396,397].

These studies, as well as others, have led the way in utilizing ALS iPSC-derived MNs to advance therapeutic discovery. Yet a remaining challenge encountered in modeling ALS, an age-related disease, with stem cell derivatives is the requirement of even the most successful studies to wait extensive periods of time in culture to observe ALS cellular phenotypes of selective MN death and degeneration[357,413]. Moreover, such long-term culture systems do not reproducibly recapitulate selective ALS MN death between different mutant lines or different groups[347–349,352,353,357,358,378,386,414] and are not easily amenable for high throughput drug screening platforms. The use of exogenous stressors to recapitulate age-related cellular dysfunctions may serve as a useful way to synchronously produce ALS associated phenotypes for neuroprotective drug screening assays, yet these systems remain limited in number and in the scope of stressors used, namely sodium arsenite to induce DNA damage and oxidative stress[367,369,401], MG132 to inhibit proteasomal degradation and induce protein accumulation[198,345], and glutamate to potentiate glutamate-mediated excitotoxicity[377,386,395]. Investigating whether additional age-related exogenous stressors can reproducibly potentiate ALS patient MN degenerative phenotypes in vitro may ultimately enable the development of cellular assays modeling distinct elements of disease in a manner compatible with large scale "-omics" technologies and drug screening platforms.

Furthermore, understanding how different stressors initiate human ALS MN damage may also advance our understanding of what makes MNs so vulnerable in ALS patients and why they display such differential sensitivities to ubiquitously expressed mutations and environmental exposures. Currently the majority of studies of differential MN vulnerability have been performed in ALS mouse models, using laser capture microdissection of vulnerable populations and resistant populations, and transcriptomic analyses to determine differential gene expression patterns. While a number of diverse expression differences have been identified[34], a particularly pivotal study reported by Saxena et al. demonstrated that upregulation of endoplasmic reticulum (ER) stress may underlie MN vulnerability in ALS. The authors demonstrated that MNs vulnerable to disease progression in SOD1-ALS mice displayed elevated ER stress transcripts at birth, which initiated an unfolded protein response (UPR) in these cells weeks prior to neuromuscular junction denervation and motor deficits[109]. This initiation of the UPR was notably not observed or delayed in the resistant neuronal populations, suggesting that vulnerable MNs were intrinsically more susceptible to ER stress signals and the activation of a chronic UPR to cause preferential MN degeneration in ALS disease

progression[26,109,402,407]. Moreover, while ER stressors remain minimally studied in iPSC-derived ALS patient MN cultures, work by Kiskinis et al. has demonstrated that human patient MNs place unusually large demands on the organellar ER network and that MNs, even those without an ALS mutation, display elevated basal levels of ER stress transcripts compared to other neurons[345].

Given the prominent role that ER stress plays in ALS mouse models and human MN homeostasis, we hypothesized that stressors targeting this organelle would initiate the convergent late-onset ALS pathologies of preferential MN degeneration and protein aggregation in patient derived cells. We selected compounds known to induce ER stress by distinct mechanisms- thapsigargin, an inhibitor of the sarcoplasmic/endoplasmic reticulum calcium ATPase pump importing calcium into the ER lumen, and tunicamycin, an inhibitor of a post-translational modification (N-linked glycosylation) causing ER protein accumulation. Alongside the ER stressors, we concurrently tested MG132, the well-studied proteasomal inhibitor known to produce insoluble ALS proteins in derived MN cultures[198,345]. We then comparatively evaluated each stressor for the ability to exacerbate ALS associated phenotypes of preferential MN death, progressive damage of neuritic structures, enhanced susceptibility of fALS MNs, induction of ER stress signaling cascades and the accumulation of intracellular, insoluble TDP-43 and ubiquitinated proteins.

We demonstrate here that compounds dysregulating ER stress were preferentially toxic to MNs compared to non-MN cells, in both healthy and ALS patient derived cultures. In contrast to the effects of ER stress, proteasomal stress drove the stereotypical insoluble aggregates but did not uniformly induce selective MN death. These experiments support an intrinsic vulnerability of MNs to ER stress in human cells with differential effects to other proteostatic stressors. Importantly these experiments also defined precise culture conditions to induce convergent ALS degenerative phenotypes in a manner amenable for therapeutic validation, large scale "omics" technologies, and neuroprotective drug screening (Chapters 3 and 4 of this thesis).

2.3 Results

2.3.1 Mechanistically distinct proteostatic stressors induce death and neuritic degeneration in human MNs.

To investigate the ability of proteostatic stressors to initiate ALS associated degenerative phenotypes in derived MNs, we first established a method to reliably generate this cell type. Starting with a healthy control iPSC line, the differentiation method used here took advantage of a published 15-day embryoid body-based protocol,

which recapitulated the molecular signals known to drive MN specification during embryonic development (Figure 2.1A)[341]. Neural induction was initiated by the dual inhibition of SMAD signaling using the small molecule antagonists SB-431542 and LDN-193189. Caudal ventral MN identity was then directed by supplementation with retinoic acid (RA), Wnt activation via inhibition of GSK3β by CHIR-99021, and activation of the Sonic Hedgehog pathway with smoothened agonist (SAg). Addition of a γ-secretase inhibitor DAPT and the neurotrophic factors BDNF and GDNF subsequently promoted and preserved spinal MN survival. Following these treatments, the embryoid bodies were then dissociated into single-cells, plated, and matured for 6 days resulting in ~95% neuronal-specific βIII-Tubulin (TUJ1)$^+$ cells, ~30% of which expressed the mature MN marker Isl1/2 (Figure 2.1B). We considered these cells as MNs for the duration of this study, while the remaining population of Isl1/2$^-$, βIII-Tubulin (TUJ1)$^+$ neurons, Chx10$^+$ V2a spinal interneurons, and βIII-Tubulin (TUJ1)$^-$ non-neuronal cells were considered non-MNs (Figure 2.1B).

The selective vulnerability of spinal cord MNs relative to other spinal cord neurons and non-neuronal glial cells is a pathological hallmark of ALS[1,34]. To address the question of whether various proteostatic stressors could induce preferential degeneration in human MNs similar to that seen in ALS patients, we challenged control iPSC-derived MN cultures with increasing doses of thapsigargin, tunicamycin, and MG132 and utilized a high content image acquisition and analysis platform to quantify the surviving MN and non-MN populations. After 48 hours of stressor challenge, we found that all stressors were toxic to the MN population in a dose and time dependent manner (Figure 2.1C-E). However, only the ER stressors thapsigargin and tunicamycin displayed cell-type-selectively, with preferential death of MNs compared to the non-MN populations (Figure 2.1C-E).

Figure 2.1. ER stressors induce preferential MN death in iPSC-derived cultures.
  A) Schematic of MN differentiation protocol and proteostatic stressor assay.
  B) Quantification and representative immunofluorescent images of cell types in iPSC-derived MN cultures. MN populations include Isl1/2$^+$, TUJ1$^+$ immunostained cells, non-MN populations include Isl1/2$^-$, TUJ1$^+$ neuronal populations, such as CHX10$^+$, TUJ1$^+$ spinal interneurons, as well as TUJ1$^-$ non-neuronal cells. N_b=3, n_t=3.
  C) Representative immunofluorescent images of iPSC-derived MN cultures in control (DMSO) or proteostatic stress (1μM compound, 48hrs) conditions.
  D) Quantification of MN and non-MN viability 48hrs after treatment with increasing concentrations of proteostatic stressors. Two-way ANOVA for interaction between cell-type and concentration- thapsigargin- N_b>3, n_t>2, p = 0.015; tunicamycin- N_b=4, n_t>5, p = 0.000127; MG132- N_b=3, n_t=12, p = 0.394.
  E) Quantification of MN and non-MN viability after treatment with 1μM proteostatic stressors for various lengths of time. Two-way ANOVA for interaction between cell-type and concentration- thapsigargin- N_b=3, n_t=6, p = 0.000215; tunicamycin- N_b=3, n_t=6, p = 1.64×10^{-33}.

Biological replicates (N_b) represent independent MN differentiations, each with technical replicate wells (n_t). Data are mean value +/- SEM.

A)

Adaptation Day-2 · PSC · EB Day 0 · Dual SMAD + GSK/WNT inhibition · EB Day 2 +RA+SAg · EB Day 5 · EB Day 7 +BDNF · EB Day 9 + γ Secretase Inhibition · EB Day 11 +GDNF · EB Day 15 Dissociate · MN Plating Day 0 · MN ½ Media Change Day 3 · Stressor Addition Day 6 · Fix and Image Day 8 · Analyze MN Population · Analyze Non-MN Population

B) Cellular Composition of MN cultures

Percentage of Cells — TUJ1+,Isl1/2+ (MN) / TUJ1+,Isl1/2- (Non-MN) / TUJ1- (Non-MN)

Hoechst Tuj1 Isl1/2 · Hoechst Isl1/2 CHX10 · Hoechst Tuj1 CHX10

C)

DMSO · Thapsigargin · Tunicamycin · MG132

Hoechst TUJ1 Isl1/2 — 50 µm

D)

MN vs nonMN Thapsigargin Dose Curve — % Viable Cells — µM Thapsigargin — *

MN vs nonMN Tunicamycin Dose Curve — % Viable Cells — µM Tunicamycin — ***

MN vs nonMN MG132 Dose Curve — % Viable Cells — µM MG132 — ns

→ Isl1/2+ MNs → Isl1/2- nonMNs

E)

MN vs nonMN Thapsigargin Time Course — % Viable Cells — Hrs of Thapsigargin — ***

MN vs nonMN Tunicamycin Time Course — % Viable Cells — Hrs of Tunicamycin — ****

MN vs nonMN MG132 Time Course — % Viable Cells — Hrs of MG132

Isl1/2+ MNs ■ Isl1/2- nonMNs

36

Since the stress-response of cells can be influenced by density and maturation, we next ensured that these cell-type-selective phenotypes were maintained in different culture conditions. The original assay parameters used 6-day old MNs, cultured at 50,000 cells per well of a 96-well plate. We found that 2-fold and 4-fold lower density MN cultures (Figure 2.2A), as well as cultures maintained for an additional 2-3 weeks prior to treatment (Figure 2.2B), remained consistently more vulnerable to perturbations in ER function than other cell types in the culture, while MG132 again equally affected both MN and non-MN populations. These data demonstrate a collective and robust inability of MNs to buffer ER stress as well as other cell types, even other neurons. This enhanced susceptibility profile may ultimately explain some of the cell-type-selectivity observed in ALS patients and ALS mouse models, where the most vulnerable MN populations display ER stress signatures before neuromuscular junction denervation and observations of motor deficits[109].
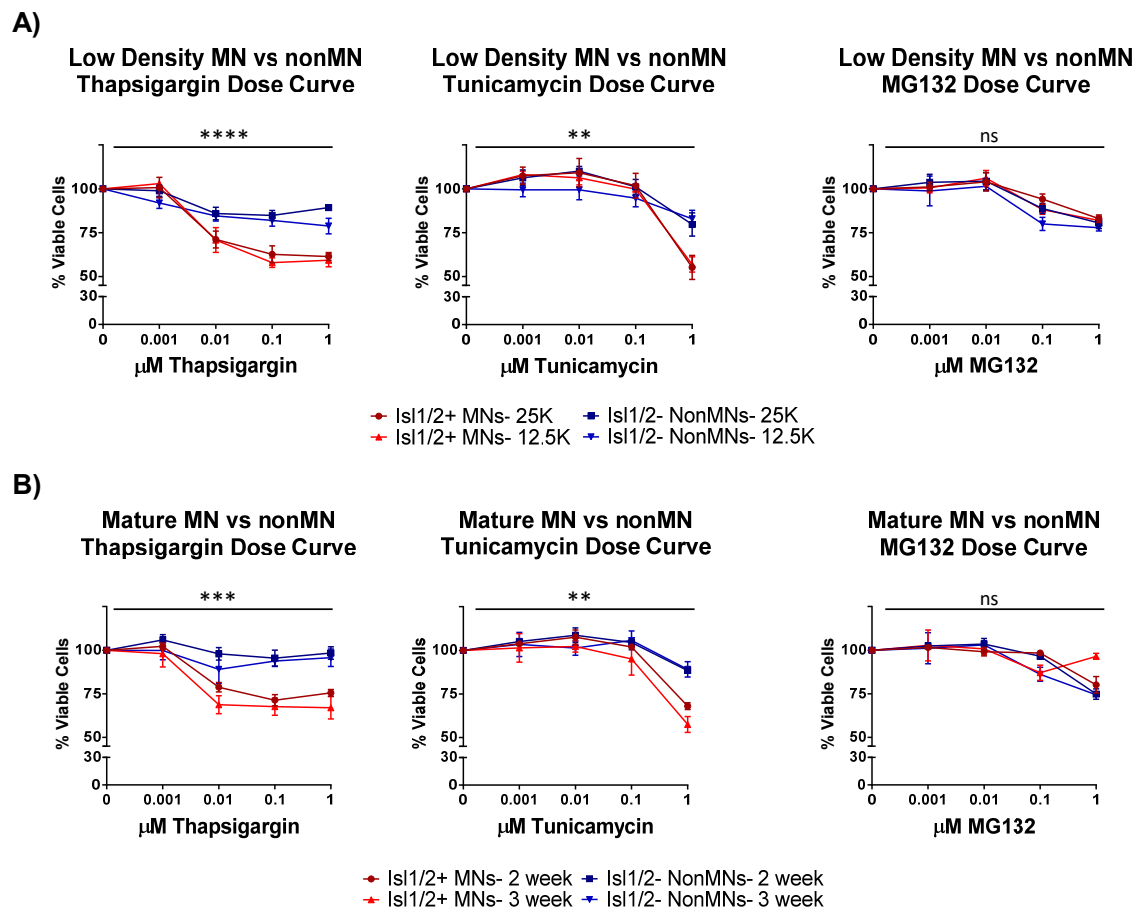
Figure 2.2. Preferential MN death with ER stress is maintained in various culture conditions.

A) MN and non-MN viability from low density cultures (25K per 96 well or 12.5K per 96 well) after 48hrs exposure to increasing doses of proteostatic stressors. N_b=3, n_t=2, two-way ANOVA for interaction between cell-type and concentration- 25K thapsigargin- p = 7.67×10^{-6}, 12.5K thapsigargin- p = 0.000258, 25K tunicamycin- p = 0.008, 12.5K tunicamycin- p = 2.63×10^{-7}, 25K MG132- p = 0.894, 12.5K MG132- p = 0.947. For simplicity, stars indicating statistical significance are shown for 25K conditions only.

B) MN and non-MN viability after 2 or 3 week old cultures were treated for 48hrs with increasing doses of proteostatic stressors. N_b=3, n_t=2, two-way ANOVA for interaction between cell-type and concentration- 2week thapsigargin- p = 0.000691, 3week thapsigargin- p = 0.125, 2week tunicamycin- p = 0.002, 3week tunicamycin- p = 0.008, 2week MG132- p = 0.284, 3week MG132- p = 0.004. For simplicity, stars indicating statistical significance are shown for 2week conditions only.

Biological replicates (N_b) represent independent MN differentiations, each with technical replicate wells (n_t). Data are mean value +/- SEM.

In conjunction with and often preceding outright MN death, damage to neuritic structures is another degenerative ALS feature, with progressive deterioration of neurite length observed in long-term cultures of ALS patient MNs[1,357]. We used live cell imaging to qualitatively show that each stressor results in fragmentation and degeneration of the neuritic processes prior to loss of the cell body (Supplementary Video Files 1-4). We additionally observed a loss of the neuron specific βIII-Tubulin (TUJ1)[+] networking and increases in βIII-Tubulin (TUJ1)[+] punctate debris in end-stage stressor treated cultures, further indicating axonal and dendritic fragmentation (Figure 2.3A). We then measured the extent of these morphometric damages using an unbiased neurite detection software, which quantified a dose and time-dependent decrease in neuritic properties with each proteostatic stressor (Figure 2.3B-C). These included decreases in the maximum neurite length per cell body (Figure 2.3B) and total neurite length (Figure 2.3C), as well as total number of neurites, number of neuritic extensions from the cell body (roots), and number of neuritic branch points (nodes) (data not shown). These data together demonstrate the ability of each of the proteostatic stressors to induce the characteristic ALS associated phenotypes of MN death and neuritic degeneration in patient derived cells, with the ER stressors particularly recapitulating the MN selectivity seen in ALS patients.
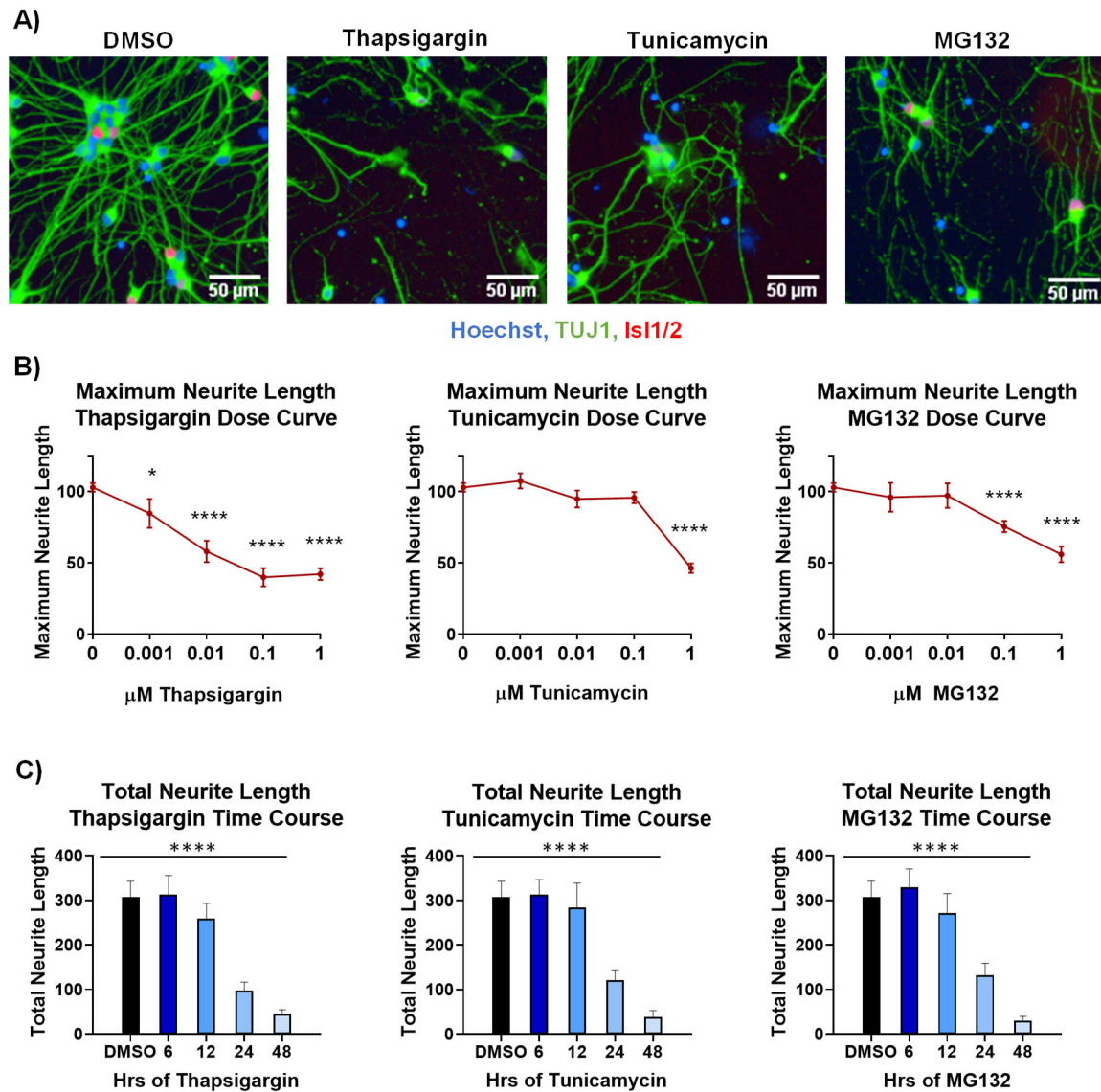
Figure 2.3. Proteostatic stressors induce progressive neuritic damage.
  A) Representative immunofluorescent images of neurite morphologies in control (DMSO) or proteostatic stress (1μM compound, 48hrs) conditions.
  B) Quantification of maximum neurite length (μm) after 48hrs exposure to increasing doses of proteostatic stressors. N_b=4, n_t=2, $p < 0.05*$, $<0.01**$, $<0.001***$, $<0.0001****$ one-way ANOVA with Tukey's hsd post-hoc test.
  C) Quantification of total neurite length (μm) after exposure to 1μM proteostatic stressors for increasing amounts of time. N_b=3, n_t=6, $p < 0.05*$, $<0.01**$, $<0.001***$, $<0.0001****$ one-way ANOVA.

Biological replicates (N_b) represent independent MN differentiations, each with technical replicate wells (n_t). Data are mean value +/- SEM.

2.3.2 Familial ALS backgrounds and intrinsic health properties influence MN susceptibility to proteotoxicity.

Rare mutations cause familial forms of ALS (fALS) in a small percentage of patients (~5-10%)[14]. This suggests that these mutations either drive MN degenerative phenotypes or, at the very least, enhance MN susceptibility to degenerative stress. We therefore next wanted to evaluate how MNs with familial ALS mutations would respond to the proteostatic stressors. We obtained iPSC lines from 2 ALS patients - one harboring a TDP-43$^{G298S/+}$ mutation (47D) and another harboring a SOD1$^{L144F/+}$ mutation (29D) - each with comparable pluripotent stem cell properties and differentiation capacity as the healthy control line (1016A) (Figure 2.4A-D, 2.5B). Using the same conditions as for the healthy iPSC line, we found that both SOD1 and TDP-43 fALS MNs again displayed enhanced vulnerability to the ER stressors thapsigargin and tunicamycin compared to the non-MN populations, similar to what was observed with the healthy MN line (Figure 2.5A). Notably, however, we found that the fALS MNs now also displayed an enhanced vulnerability to the proteasome inhibitor MG132 compared to the non-MNs (Figure 2.5A). These data further support that MNs are intrinsically vulnerable to ER stressors, with preferential MN degeneration in both healthy and fALS patient lines. Yet these data also indicate a differential MN vulnerability to proteasome inhibition, with variable susceptibilities to this type of stress due either to line-to-line variability in iPSC cultures or, potentially, due to the presence of the fALS mutant backgrounds. Furthermore, in addition to the enhanced cell-type vulnerability (MN vs non-MN), we found that both the fALS TDP-43 and SOD1 fALS MNs also demonstrated increased susceptibility to each proteostatic stressor compared to the healthy control MNs (Figure 2.5C-D). This enhanced vulnerability was maintained or enhanced in low density conditions (Figure 2.5D, 2.6A) as well as preserved in more mature MN cultures (Figure 2.6A), cumulatively suggesting that all proteotoxic stressors, ER as well as proteasomal, could exacerbate selective MN vulnerabilities of fALS mutant lines compared to the unmatched healthy line.
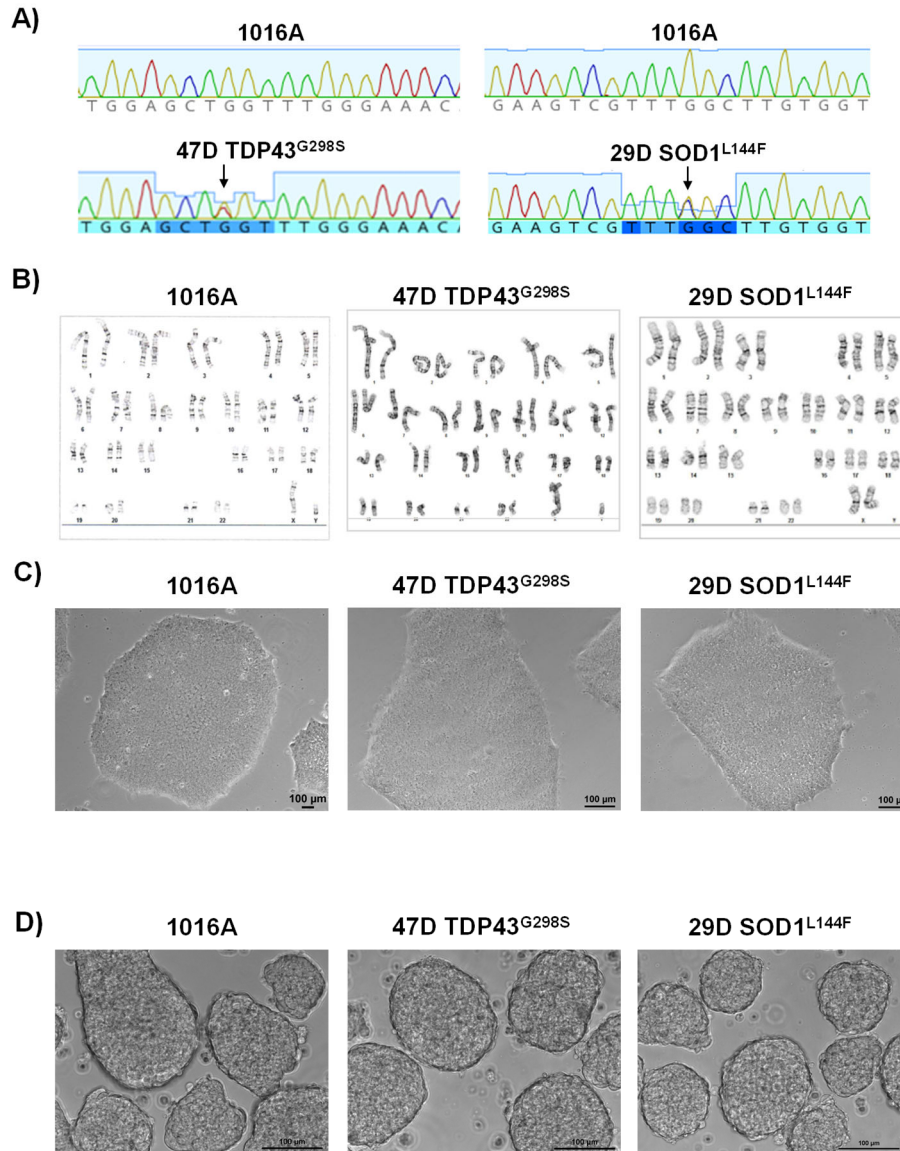
Figure 2.4. Characterization of healthy and ALS patient iPSCs and EBs.
  A) Sequencing chromatograms and (B) G-banded karyotypes of a healthy control patient iPSC line (1016A), a TDP-43^{G298S} ALS patient iPSC line (47D), and a SOD1^{L144F} ALS patient iPSC line (29D).
  C) Phase contrast microscopy images of iPSC colonies and (D) embryoid bodies (EBs) derived from the healthy control patient iPSC line (1016A), the TDP-43^{G298S} ALS patient iPSC line, and the SOD1^{L144F} ALS patient iPSC line.

42

Figure 2.5. ALS patient MNs are more vulnerable to proteostatic stressors than healthy patient MNs.

A) Comparison of viable non-MNs and viable MNs after TDP-43^{G298S} mutant or SOD1^{L144F} mutant ALS patient derived MN cultures were treated with 48hrs 1μM proteostatic stressors. N_b=3, n_t≥2, unpaired t-test; 47D-Thapsigargin- p = 1.526x10^{-5}, 47D-Tunicamycin- p = 1.450x10^{-6}, 47D-MG132- p = 0.000314, 29D-Thapsigargin- p = 0.02698, 29D-Tunicamycin- p = 6.07742x10^{-7}, 29D-MG132- p = 0.00955.

B) Total viable cell counts and MN cell counts in cultures derived from the healthy control patient iPSC line (1016A), the TDP-43^{G298S} ALS patient iPSC line (47D), and the SOD1^{L144F} ALS patient iPSC line (29D). 3 different densities tested. N_b=3, n_t=2.

C) Representative immunofluorescent images of healthy patient derived MN cultures (1016A) or ALS patient MNs cultures (47D-TDP-43^{G298S}, 29D-SOD1^{L144F}) in control (DMSO) and proteostatic stress (1μM compound, 48hrs) conditions.

D) Quantification of viable MNs from a healthy patient line (1016A) compared to ALS patient lines (47D-TDP-43^{G298S} or 29D-SOD1^{L144F}) after 48hrs of proteostatic stressor exposure. 4 different concentrations of each stressor were tested, in 3 different densities of each line. N_b=3, n_t=2, three-way ANOVA for interaction between cell line and concentration- 47D-Thapsigargin- p = 5.81x10^{-11}, 47D-Tunicamycin- p = 1.37x10^{-17}, 47D-MG132- p = 7.23x10^{-20}, 29D-Thapsigargin- p = 0.515, 29D-Tunicamycin- p= 0.016, 29D-MG132- p = 0.00000153.

Biological replicates (N_b) represent independent MN differentiations, each with technical replicate wells (n_t). Data are mean value +/- SEM.

A)

TDP43^G298S ALS MN vs NonMN Vulnerability

SOD1^L144F ALS MN vs NonMN Vulnerability

Isl1/2⁻ NonMNs
Isl1/2⁺ MNs

B)

Viable Cells at DIV6 1016A vs 29D-SOD1^L144F

Viable Isl1/2+ MNs at DIV6 1016A vs 29D-SOD1^L144F

Viable Cells at DIV6 1016A vs 47D-TDP43^G298S

Viable Isl1/2+ MNs at DIV6 1016A vs 47D-TDP43^G298S

C) DMSO   Thapsigargin   Tunicamycin   MG132

1016A Control

29D-SOD1^L144F

47D-TDP43^G298S

TUJ1, Isl1/2

D)

Thapsigargin Dose Response, 1016A vs 47D-TDP43^G298S, DIV6

Tunicamycin Dose Response, 1016A vs 47D-TDP43^G298S, DIV6

MG132 Dose Response, 1016A vs 47D-TDP43^G298S, DIV6

1016A 50K
1016A 25K
1016A 12.5K
47D-TDP43^G298S 50K
47D-TDP43^G298S 25K
47D-TDP43^G298S 12.5K

Thapsigargin Dose Response, 1016A vs 29D-SOD1^L144F, DIV6

Tunicamycin Dose Response, 1016A vs 29D-SOD1^L144F, DIV6

MG132 Dose Response, 1016A vs 29D-SOD1^L144F, DIV6

1016A 50K
1016A 25K
1016A 12.5K
29D-SOD1^L144F 50K
29D-SOD1^L144F 25K
29D-SOD1^L144F 12.5K

44

A)

Figure 2.6. ALS MNs maintain increased vulnerability to proteostatic stress in mature cultures.

A) Quantification of viable MNs from mature patient cultures (control- 1016A versus ALS- 47-TDP-43[G298S] or 29D-SOD1[L144F]) after 48hrs of proteostatic stressor treatment. 4 different concentrations of each stressor were tested, in 3 different densities of each line. $N_b=3$, $n_t=2$, three-way ANOVA for interaction between cell line and concentration- 47D-Thapsigargin- $p = 0.003$, 47D-Tunicamycin- $p = 9.11 \times 10^{-11}$, 47D-MG132- $p = 6.71 \times 10^{-14}$, 29D-Thapsigargin- $p = 0.076$, 29D-Tunicamycin- $p= 0.0000117$, 29D-MG132- $p = 0.033$.

Biological replicates (N_b) represent independent MN differentiations, each with technical replicate wells (n_t). Data are mean value +/- SEM.

45

Since the previous experiments were performed with 3 separate patient lines, we could not determine whether the ALS mutations themselves were causing this increased MN vulnerability, or whether this phenotype was simply due to line-to-line variability. Therefore, to eliminate confounding genetic and epigenetic differences between patient iPSC lines, and determine whether a single fALS mutation was sufficient to cause enhanced MN degeneration with proteostatic stressors, we obtained a published ALS iPSC line harboring a SOD1[A4V] mutation (39B) and its isogenic corrected partner (39B-Corrected) (Figure 2.7)[345]. Interestingly, we immediately observed strong health deficits in the isogenic corrected line, including decreased pluripotent stem cell viability with routine culture and thawing from liquid nitrogen stocks (Figure 2.7C) and decreased survival of embryoid bodies (Figure 2.7D).
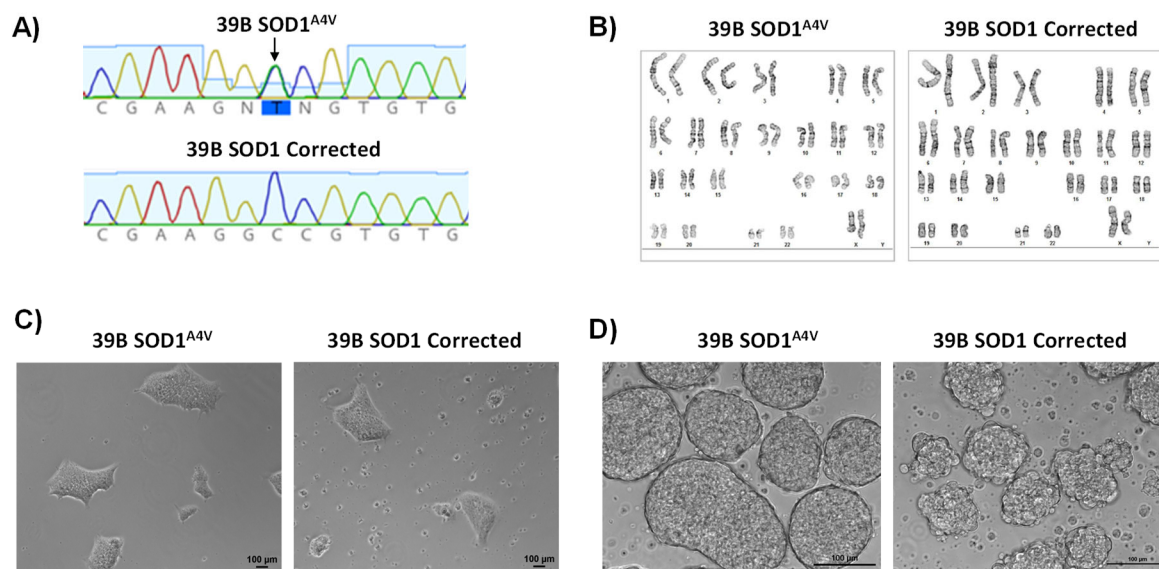
Figure 2.7. Characterization of isogenic corrected and SOD1 ALS patient iPSCs and EBs.
  A) Sequencing chromatograms and (B) G-banded karyotypes of a SOD1[A4V] ALS patient iPSC line (39B) and its isogenic-gene-corrected control (39B-Corrected).
  C) Phase contrast microscopy images of iPSC colonies and (D) embryoid bodies (EBs) derived from the SOD1[A4V] ALS patient iPSC line and its isogenic corrected control.

We additionally observed decreased isogenic MN survival with time in culture (Figure 2.8A) compared to the ALS MNs. These data were surprising, as they were inconsistent with the original published data for these lines[345] and raised strong concerns that the integrity of the isogenic line had been significantly altered since its original generation. These differences in intrinsic health properties additionally made conclusions about the sufficiency of the fALS mutation to drive a vulnerability phenotype challenging.

Figure 2.8. Intrinsic health deficits determine MN vulnerability to proteostatic stressors.

A) Quantification of viable SOD1^{A4V} patient MN numbers and isogenic corrected MN numbers with time in culture. 3 densities tested for each line. N_b=3, n_t=2, p = 0.000595, three-way ANOVA for interaction between cell line and time.

B) Total viable cell counts and MN cell counts from the derived SOD1^{L144F} ALS cultures and the isogenic corrected control. 3 different densities tested. N_b=3, n_t=2.

C) Representative immunofluorescent images of SOD1^{A4V} ALS patient MN cultures or isogenic corrected MN cultures in control (DMSO) and proteostatic stress (1μM compound, 48hrs) conditions.

D) Quantification of viable ALS MNs (39B-SOD1^{A4V}) compared to isogenic corrected MNs after 48hrs of proteostatic stressor exposure. 4 different concentrations of each stressor were tested, with 3 different densities of each line, at 3 different days in vitro (DIV). N_b=3, n_t=2, three-way ANOVA for interaction between cell line and concentration- DIV6-Thapsigargin- p = 0.00000685, DIV6-Tunicamycin- p = 1.64x10^{-13}, DIV6-MG132- p = 3.31x10^{-23}, DIV14-Thapsigargin- p = 0.064, DIV14-Tunicamycin- p = 0.000000113, DIV14-MG132- p = 1.79x10^{-11}, DIV21-Thapsigargin- p = 0.035, DIV21-Tunicamycin- p = 0.000000638, DIV21-MG132- p = 3.09x10^{-8}.

Biological replicates (N_b) represent independent MN differentiations, each with technical replicate wells (n_t). Data are mean value +/- SEM.

A) MN Loss with Time, Corrected vs 39B-SOD1^{A4V}

B) Viable Cells at DIV6 Corrected vs 39B-SOD1^{A4V}; Viable Isl1/2+ MNs at DIV6 Corrected vs 39B-SOD1^{A4V}

C) DMSO, Thapsigargin, Tunicamycin, MG132

39B-SOD1^{A4V} Isogenic Corrected Control

39B-SOD1^{A4V}

TUJ1, Isl1/2

D) Thapsigargin Dose Response, Corrected vs 39B-SOD1^{A4V}, DIV6; Tunicamycin Dose Response, Corrected vs 39B-SOD1^{A4V}, DIV6; MG132 Dose Response, Corrected vs 39B-SOD1^{A4V}, DIV6

Thapsigargin Dose Response, Corrected vs 39B-SOD1^{A4V}, DIV14; Tunicamycin Dose Response, Corrected vs 39B-SOD1^{A4V}, DIV14; MG132 Dose Response, Corrected vs 39B-SOD1^{A4V}, DIV14

Thapsigargin Dose Response, Corrected vs 39B-SOD1^{A4V}, DIV21; Tunicamycin Dose Response, Corrected vs 39B-SOD1^{A4V}, DIV21; MG132 Dose Response, Corrected vs 39B-SOD1^{A4V}, DIV21

48

Since these paired lines, as well as all lines used in this thesis, passed quality control genotyping, karyotyping and mycoplasma infection measurements, we decided to still investigate the effect of each proteostatic stressor to drive MN degeneration in the ALS and corrected lines. In line with the growth defects at the pluripotent stages, the isogenic corrected MN line was more susceptible to all 3 proteostatic stressors compared to the ALS mutant, in every condition tested (Figure 2.8C-D).

Cumulatively, two possibilities explain all the data from the 5 patient MN lines. Either the degree of MN toxicity with proteostatic stress is random and due to line-to-line variability between each patient iPSC, or the degree of MN toxicity with proteostatic stress is a function of intrinsic viability, with each stressor enhancing existing health disparities between "healthy" and "diseased" lines. With this latter possibility, the unmatched familial TDP-43 and SOD1 mutant backgrounds caused enhanced MN susceptibility to proteostatic stress conditions compared to the healthy line when pluripotent stem cell properties were equivalent. However, with extremely damaged stem cell properties, the strong pre-existing intrinsic health deficits influenced MN response to proteostatic stressors beyond that of the ALS mutation. While we cannot conclude between these two possibilities with the current small number of lines and confounding genetic and health properties, the ability of ER stressors to uniformly induce a cell-type-specific MN vulnerability, in both healthy and ALS MNs, indicates this type of stress as a unique initiator of selective MN degeneration. The ability to induce this MN degeneration may also be leveraged to identify compounds that protect and preserve MN viability in these stress conditions (Chapters 3 and 4 of this thesis).

2.3.3 ER stressors specifically drive apoptotic death in patient derived MNs.

The MN selective toxicants thapsigargin and tunicamycin are known inducers of ER stress and the unfolded protein response (URP). These signaling pathways are linked to ALS pathogenesis, occurring weeks, sometimes months, before symptom onset as well as at disease end stage[109,406,415]. While initial signaling is cytoprotective, preventing ER burden and protein buildup, prolonged signaling eventually drives apoptotic death (Figure 1.6). Understanding the molecular time course of each ER stressor to induce the UPR and apoptosis in patient derived MNs would further our understanding of the mechanisms driving induced MN death. These data would also provide precise windows where protective compounds can be evaluated for their ability to mitigate each signaling component. To thus temporally track the induction of the UPR with each stressor, we utilized a combination of western blotting techniques, PCR splicing assays, and qRT-PCR measurements.

We found that thapsigargin first induced PERK-mediated phosphorylation of eIF2α to block protein translation as soon as 15 minutes after treatment, with a maximum response after 1 hour (Figure 2.9A). Tunicamycin also increased phosphorylated eIF2α, but more slowly, becoming observable after 4 hours (Figure 2.9A). IRE1-mediated splicing of XBP1 was evident next, as soon as 30 minutes after thapsigargin treatment, with consistent and robust splicing activity observed for both thapsigargin and tunicamycin between 2 and 4 hours after treatment (Figure 2.9A). The upregulation of the resident ER chaperone BiP was also quickly initiated, with increases at the mRNA level between 1-4 hours after each stressor treatment, and significant increases in protein levels by 8 and 24 hours (Figure 2.9A-B). The induction of the pro-apoptotic transcription factor CHOP displayed a similar expression profile to BiP, with mRNA increases between 1-4 hours after each stressor treatment, and significant increases in protein levels by 8 and 24 hours (Figure 2.9A-B).

Prolonged ER stress signaling (8-24 hours) eventually resulted in the cleavage of caspase 3. This led to an active form of apoptotic MN death indicated by the increase in terminal deoxynucleotidyl transferase dUTP nick end labeling (TUNEL) of apoptotic DNA fragments in MNs and the protection of MNs by a pan-caspase apoptosis inhibitor Z-VAD-FMK (Figure 2.9C-D). These data illuminate a molecular clock of death signaling cascades with each ER stressor, providing indications that an active apoptotic death underlies the selective MN degeneration with sustained ER stress. These data also provide time frames where protective compounds can be evaluated for their ability to attenuate this degenerative signaling (Chapters 3 and 4 of this thesis).

Figure 2.9. ER stressors induce the unfolded protein response to drive apoptotic MN death.
   A) Western blot and splicing-PCR analyses of patient derived MN cultures treated with either DMSO, 1μM thapsigargin or 1μM tunicamycin for various times points. N_b=3.
   B) qRT-PCR analyses of patient derived MN cultures treated with DMSO, 1μM thapsigargin or 1μM tunicamycin for various times points. ΔΔCt values are graphed, normalizing target gene qPCR Ct values (BiP or CHOP) to housekeeping gene Ct values (GAPDH) and then calculating the fold change of this normalized Ct value to control conditions such that DMSO =1 at all time points. N_b=3, n_t=3, $p < 0.05^*$, $<0.01^{**}$, $<0.001^{***}$, $<0.0001^{****}$ one-way ANOVA.
   C) The percentage of apoptotic MNs in control (DMSO), 1μM thapsigargin, or 1μM tunicamycin stress conditions, quantified by the number of TUNEL$^+$ MNs (Isl1/2$^+$) per total MN numbers (Isl1/2$^+$). N_b=3, n_t >4, unpaired t-test, Thapsigargin- $p = 0.02853$, Tunicamycin- $p = 0.0011$.
   D) Quantification of MN viability in patient cultures treated with either control vehicle (DMSO), stressors alone (1μM thapsigargin or tunicamycin), or stressors with a pan-caspase inhibitor (100μM Z-VAD-FMK). N_b=3, n_t >2, unpaired t-test, Thapsigargin- $p = 0.011583$, Tunicamycin- $p = 0.018997$.

Biological replicates (N_b) represent independent MN differentiations, each with technical replicate wells (n_t). Data are mean value +/- SEM.

A) UPR Induction

- DMSO +Thapsigargin +Tunicamycin

30mins | 1hr

Phospho-eIF2α
eIF2α

2hrs | 4hrs

Phospho-eIF2α
eIF2α
sXBP1
uXBP1 PstI digested

8hrs | 24hrs

BiP
β-Actin
CHOP
β-Tubulin
β-Actin
Cleaved Caspase 3
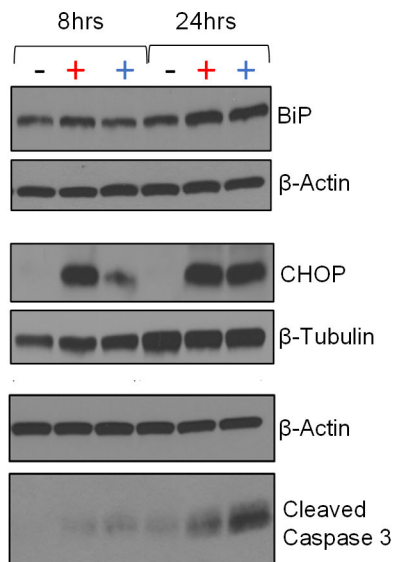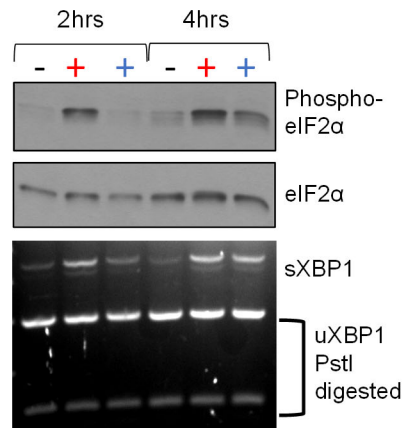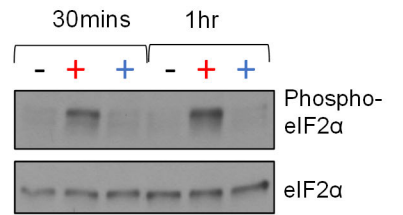
B)

Time Course of BiP Upregulation (RNA)
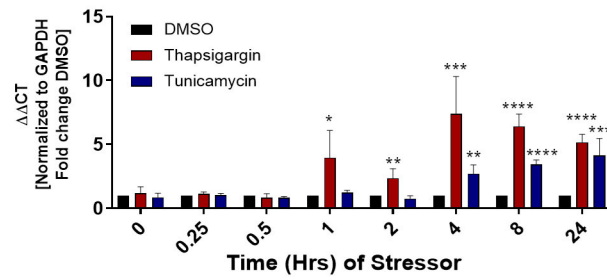
Time Course of CHOP Upregulation (RNA)
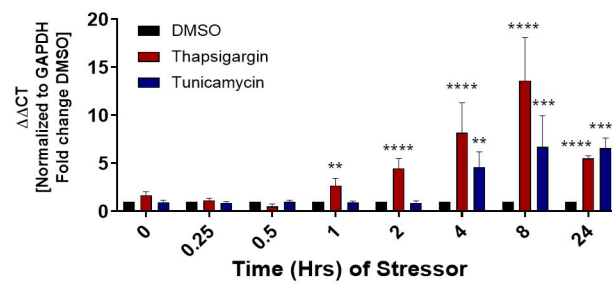
C) Apoptotic MNs
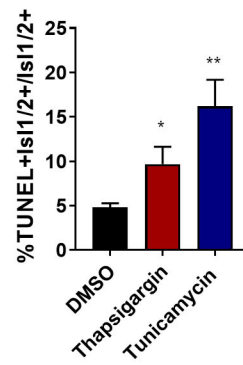
D) MN Protection with Caspase Inhibition
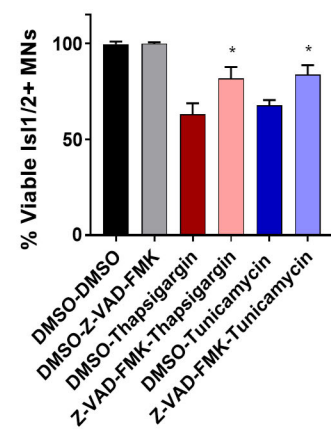
2.3.4 Proteasomal inhibition stimulates formation of ALS characteristic insoluble TDP-43 and ubiquitin.

In addition to neuritic damage, selective MN death, and early signatures of ER stress, the accumulation of intracellular, insoluble TDP-43^{+}, ubiquitin[+] aggregates are pathological hallmarks of ALS, with these aggregates occurring in >97% of ALS patients[49,50]. The proteasomal inhibitor MG132 has been reported to force the formation of accumulated protein aggregates in various cell types by preventing the cell's ability to break down ubiquitinated proteins targeted for degradation[416]. To test whether MG132 could recapitulate these hallmark inclusions, we optimized a sequential protein extraction protocol, where detergent-soluble proteins were first extracted from cell pellets using RIPA buffer supplemented with 1% Triton X-100, leaving behind detergent-insoluble proteins that were then extracted with the powerful protein denaturant urea. Following 2D electrophoresis and immunoblotting, we found that patient derived MN cultures treated with MG132 had increased insoluble TDP-43 and ubiquitin, compared to DMSO, thapsigargin, or tunicamycin treated MNs, in which the majority of TDP-43 and ubiquitin proteins remained in the soluble fraction (Figure 2.10A-B). Thapsigargin and tunicamycin might not have driven a strong aggregation state due to the compensatory upregulation of protein folding chaperones, the fast induction of apoptotic death, or both.
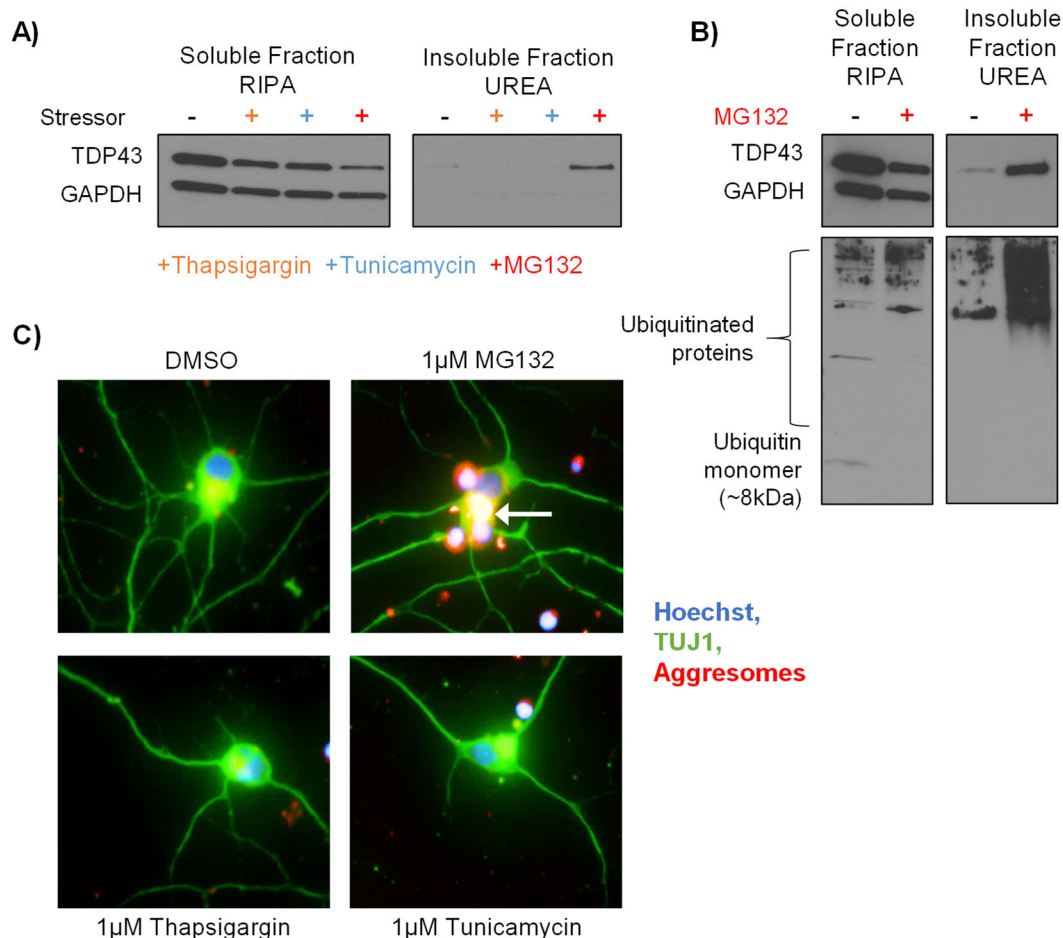
Figure 2.10. Proteasome inhibition increases the levels of insoluble TDP-43, ubiquitin, and aggresomal inclusion bodies.

A/B) Western blot analyses of soluble proteins and insoluble proteins extracted from patient derived MN cultures treated for 48hrs with control vehicle (DMSO) or 1μM proteostatic stressors (thapsigargin, tunicamycin, MG132).

C) Representative immunofluorescent staining of aggresomes in patient derived MNs treated for 48hrs with control vehicle (DMSO) or 1μM proteostatic stressors (thapsigargin, tunicamycin, MG132). Arrow indicates an intracellular aggresome.

To confirm the ability of MG132 to trigger protein aggregation, we next utilized an orthogonal assay, which measured the increase in fluorescence-based immunostaining of aggresomes. Aggresomes are inclusion bodies of aggregated and misfolded proteins that form in cells when the protein degradation pathways are overwhelmed or malfunctioning. Comparable to the results of the insoluble western blot assays, we found that again only MG132 treatment resulted in an increase in aggresomes, while the ER stressors thapsigargin or tunicamycin did not trigger formation of these inclusion bodies (Figure 2.10C).

Each proteostatic stressor thus differentially affected patient derived MNs and exacerbated distinct cellular features of ALS. The ER stressors were preferentially damaging to MNs, driving a cell-type selective MN degeneration in both healthy and diseased cultures. In contrast, the proteasomal inhibitor induced the characteristic TDP-43$^+$, ubiquitin$^+$ insoluble aggregates seen in ALS patients, but did not universally enhance selective MN vulnerabilities. These data ultimately shed light on the in vitro stressors influencing cell-type-specific vulnerabilities and suggest a combined and collective utility for each proteotoxic stressor to accelerate convergent ALS disease phenotypes in patient derived cells.

2.4 Conclusions and Discussion

In this study, we provided data supporting the hypothesis that proteostatic stress influences differential MN vulnerability in human cells and that proteostatic stressors can accelerate convergent cellular features of ALS in patient derived MN cultures. We demonstrated that pharmacological stressors targeting the ER were preferentially toxic to MNs compared to non-MN cell types, an observation that was observed using 2 separate, mechanistically distinct ER stressors, quantified in both healthy and ALS cells, maintained in multiple different culture conditions. In contrast with the effects of ER stress, we demonstrated that proteasomal stress increased the levels of ALS-associated insoluble TDP-43 and ubiquitin yet did not universally initiate selective MN toxicity. These experiments support ER stress as a common initiator of preferential MN degeneration in patient cells and additionally defined precise assay parameters needed to potentiate convergent ALS phenotypes of MN degeneration and protein aggregation in a robust, scalable, and temporally synchronous manner. While such defined conditions are important features of any experimental set-up, they are particularly critical for those intended for screening and large scale "-omics" technologies, where synchronicity of effects is essential. The diverse pharmacological models of proteostatic stress described here thus add to the growing number of in vitro assays used to interrogate disease pathologies in ALS patient derived MNs, with the expectation that these may complement the current systems used for ALS drug discovery.

2.4.1 The role of ER and proteasomal stress in ALS patient derived MN vulnerabilities

In ALS, MNs are preferentially affected and disproportionately damaged. A key question in the field is why MNs display such vulnerability to ubiquitously expressed ALS mutations and seemingly uniform age-related

insults, and indeed, why some MN subtypes are even more vulnerable to ALS disease progression than other MN subtypes. To date, most work aimed to understand these differential MN vulnerabilities have relied on laser-capture microdissection and transcriptomic profiling of mouse tissues expressing mutant proteins. These studies have been critical in identifying a number of key genes and pathways that differ between resistant MN populations and sensitive MN populations, including ER stress, calcium buffering, electrical activity, and trophic support[34]. The advent of iPSC technologies and neuronal differentiation methods has offered the continued investigation of these MN vulnerabilities in the correct human cell type by allowing the unprecedented opportunity to culture MNs from ALS patients. Current studies addressing these MN vulnerabilities in ALS patient cultures generally employ extensive maturation times to observe and study these cell-specific susceptibilities, and several key publications have also tested proteotoxic perturbagens on ALS patient MNs. However, to the best of our knowledge, our study is the first report to comparatively investigate the effects of different proteostatic stressors on iPSC-derived ALS MN vulnerabilities.

Our study has demonstrated that not all proteostatic stress is created equal, and MN and non-MN populations respond to these stressors in distinctly different manners. For example, we demonstrated that the inhibition of the proteasome with MG132 induces a phase-shift of soluble TDP-43 and ubiquitin into an insoluble fraction in patient derived MN cultures. This is comparable to work by Kiskinis et al. and Klim et al., who demonstrated that MG132 increases insoluble SOD1[345] and forces TDP-43 nuclear exclusion and cytoplasmic aggregation in ALS patient MNs[198]. However, we further expanded upon these critical observations and showed that MG132 does not uniformly induce a MN-specific degeneration, like the ER stressors thapsigargin or tunicamycin do. Rather MN and non-MN populations displayed comparable levels of death with proteasomal stress in a healthy patient MN line, yet demonstrated enhanced MN death in fALS iPSC backgrounds.

These data have important implications for the way that MN pathologies may progress in ALS. Particularly, these data suggest that proteasomal overload and malfunction by itself is not inherently more toxic to MNs compare to other cell types, but rather that proteasomal stress becomes preferentially more toxic to MNs as a "second-hit", in conjunction with different patient backgrounds and health properties. This 2 hit hypothesis, put forth by Japtok et al. postulates that initial cellular dysfunctions directly affected by ALS mutations or initial triggers drive the onset of MN-specific disease processes, and that cumulative or exacerbated stress, such as the eventual overwhelming of proteasomal mediated degradation, acts as a second hit that furthers disease and advances MN

pathologies[366]. Our data support the idea that proteasomal impairment may act as this "second hit" in concert with ALS mutations and particular cellular backgrounds to further aggravate MN-specific ALS degeneration.

Moreover, ER stressors have been largely understudied in iPSC-derived ALS patient MN cultures, with only a few groups utilizing ER stressors for studies largely related to intracellular calcium stores, calcium flux and excitability properties[380,393,394,403]. Our work presented here using two distinct ER stressors- thapsigargin, a sarcoplasmic/endoplasmic reticulum calcium ATPase (SERCA) inhibitor, and tunicamycin- an N-linked glycosylation inhibitor, is the first to demonstrate that iPSC-derived MNs are preferentially more vulnerable to modulations in ER function compared to non-MN cell types in the culture. This MN-specific degeneration occurred in both healthy and ALS cultures, in contrast with proteasomal inhibition, suggesting that age or mutation-based modulation of ER function could be a more primary pathological manifestation driving MN-specific degeneration in the early ALS disease cascade.

While our study is limited by the small number of iPSC-derived lines used, the agreement and reproducibility of our findings with multiple groups using primary or ESC- derived MN cultures add robust support to our conclusion that ER stress causes selective MN vulnerability in ALS. In particular, Thams and colleagues recently developed an elegant dual-reporter system in embryonic stem cell (ESC)-derived ALS MNs to demonstrate that cyclopiazonic acid (CPA), a SERCA inhibitor analogous to the ER stressor thapsigargin used in this study, also caused preferential ALS-MN degeneration. The authors demonstrated that ALS MNs were more susceptible to CPA compared to non-ALS MNs, and that MNs were also more susceptible to CPA than non-MNs, in a cell-autonomous manner[417]. Furthermore, An et al. used both primary mouse MN cultures and mouse ESC-derived MNs to corroborate that ALS sensitive spinal cord MNs were also more vulnerable to the ER stressors CPA, thapsigargin, and tunicamycin compared to ALS resistant cranial MNs[418]. Together these data robustly implicate ER stress as a strong driver of MN-specific vulnerabilities in ALS. Critically, while MG132 was not evaluated for a survival phenotype, An et al. also demonstrated that sensitive spinal cord MNs had a reduced dependence on proteasome-degradation and a decreased degradation efficiency compared to ALS resistant cranial MNs[418], suggesting that the hypothesized proteasomal overload 2nd-hit may be achieved more quickly in sensitive MN populations in response to accumulated ALS mutant proteins. These published data, as well as the data presented in this chapter, thus cumulatively implicate a role for both ER and proteasomal stress in differential MN susceptibility to ALS pathological insults and inform how these distinct vulnerability profiles govern MN degeneration in ALS.

2.4.2 The therapeutic implications of an accelerated, scalable, robust model of ALS MN degeneration

In addition to enabling the study of ALS MN vulnerability profiles, the opportunity to derive and culture ALS human MNs also enables the ability to screen for new therapeutic agents that protect against these vulnerabilities. To date, the majority of screening projects using iPSC-derived ALS MNs have waited extensive periods of time in culture to mimic the aging process and observe the convergent ALS cellular phenotypes of selective MN death and degeneration needed to screen for neuroprotective compound modulators[357,413]. However, these long-term culture systems do not reproducibly recapitulate selective ALS MN death between different mutant lines or different groups and are not easily amenable for high throughput drug screening. The use of exogenous stressors to recapitulate other age-related cellular dysfunctions in ALS neuroprotective drug screening assays have been leveraged, yet they remain remarkably limited in number and in the scope of stressors used, namely sodium arsenite, glutamate, or trophic factor withdrawal.

The development and characterization here of accelerated, scalable, and robust models of ER and proteasomal proteotoxicity in ALS MNs add to the current culture systems used to study ALS MN degeneration and screen for neuroprotective agents. These assays recapitulate the characteristic selective and differential MN vulnerabilities observed in ALS patients, in a quick, cost-effective, and reproducible timeline that is more compatible than extensive culture systems for high throughput and automated drug screening platforms. These capabilities offer a complementary and biologically relevant method to identifying novel treatment options for ALS patients.

In the following thesis chapters, we provide a proof-of-principle that these assays not only implicate the role that ER and proteasomal stress play in ALS MN vulnerabilities but that they can, in fact, complement the current neuroprotective screening assays. We demonstrate that these systems predict known neuroprotective agents (Chapter 3) and that they can be employed to identify novel neuroprotective drugs (Chapters 3 and 4). While caution must always be taken to balance disease-relevant observations with the powerful stressor related phenotypes, we believe that these systems aid our understanding of what makes patient derived MNs vulnerable or healthy, and what may ultimately benefit an ALS patient who suffers from this fatal MN disease.

Chapter 3

Pharmacological protection against proteotoxic ALS MN degeneration

3.1 Attributions

Portions of this chapter have been published as Wu, C., **Watts, M. E.,** & Rubin, L. L. MAP4K4 Activation Mediates Motor Neuron Degeneration in Amyotrophic Lateral Sclerosis. *Cell Rep.* **26**, 1143–1156 (2019). All experiments presented in this chapter were designed, performed, and analyzed by Ms. Michelle Watts, with assistance from Ms. Kris Holton for statistical analyses. All aspects of this research were supervised by Dr. Lee L. Rubin, with funding graciously provided by Biogen and the Harvard Brain Science Initiative.

3.2 Introduction

Amyotrophic lateral sclerosis (ALS) is a debilitating neurodegenerative disorder characterized by the preferential death of motor neurons (MNs)[1]. The progressive loss of MNs from the brain and spinal cord of ALS patients is paralyzing, universally fatal, and treatment options remain seriously limited. Only 2 interventional therapies are currently approved by the US Food and Drug Administration (FDA) for the treatment of ALS- the anti-glutamatergic agent Riluzole (Rilutek) and the antioxidant Edaravone (Radicava), neither of which improve patient survival beyond a couple of months[19]. Effective drug discovery for ALS has been particularly challenging because of the heterogeneous etiology of this disease, the inability to obtain diseased human tissue for study, and the limitation of animal models to accurately reflect human disease and predict therapeutic interventions. The recent discovery and subsequent development of stem cell technologies and neuronal differentiation methods, however, has since improved ALS drug discovery by enabling the mass production of mouse and human MNs for neuroprotective screening projects.

In 2013, our lab leveraged this unique opportunity and performed one of the first ever stem-cell based MN survival screens for new ALS therapeutics[360]. Approximately 5,000 compounds were screened for their ability to preserve the survival of both wild type and ALS mouse embryonic stem cell (ESC)-derived MNs, resulting in the identification of kenpaullone as the compound with the strongest survival-promoting activity. Kenpaullone importantly showed protection of MNs treated with various different exogenous stressors, including 2 PI3K inhibitors, as well as trophic factor withdrawal, and additionally showed remarkable ability to preserve the viability of MNs derived from SOD1 or TDP-43 ALS patient induced pluripotent stem cells (iPSCs) and MNs from unaffected patients. These data demonstrated the broadly protective function of kenpaullone to maintain MN viability in exogenous or endogenous stress conditions associated with ALS pathogenesis. Importantly, kenpaullone

also significantly outperformed 2 ALS compounds, olesoxime and dexpramipexole, both of which had recently failed in clinical trials, indicating the potential value of using human ALS patient MNs to inform the clinical efficacy of neuroprotective agents[360,419].

Since our publication, several groups have confirmed the protective effect of kenpaullone[417,420] and a handful of impactful papers have reported the successful use of ALS patient derived MNs to identify new and novel therapeutic compounds- ranging from digoxin[421] and autophagy enhancers[352,372] to potassium channel openers[346] and dopamine agonists[357]. These screening assays have significantly improved and expanded the quest for new ALS treatments, with several exciting on-going clinical trials[396–398]. However, there is still room for improved drug discovery assays in ALS patient MNs, with the current studies employing only a limited range of methods to recapitulate the convergent ALS phenotypes of selective MN degeneration and insoluble protein accumulation. In Chapter 2 of this thesis, we described the development of several new accelerated human stem cell-based models of ALS MN degeneration using 3 mechanistically distinct proteostatic stressors. These studies shed light on the mechanisms underlying differential MN vulnerability to proteostatic stress and importantly, were designed with compatibility to small molecule screening and imaging platforms. As a first step in ensuring that these ALS proteostatic assays would be effective additions to the existing patient derived models used for drug discovery, we next evaluated whether these assays could predict known therapeutic compounds.

In this study, we tested whether the current FDA approved drugs for ALS, Riluzole or Edaravone, as well as kenpaullone, the well-established MN survival agent, could attenuate proteotoxic induced ALS MN damage. We report here that Riluzole and Edaravone failed to preserve neuritic morphology and MN survival in response to proteostatic stress. However, kenpaullone was able to significantly protect MN degeneration caused by all proteostatic stressors, in multiple fALS patient lines. We further demonstrate, for the first time, that a selective small molecule inhibitor to one of kenpaullone's cellular targets, MAP4K4, was also able to prevent ALS MN degeneration. This protection consisted of maintained neuritic morphology and preserved MN viability, which were independent of a direct reduction in UPR induction or insoluble protein buildup. These experiments highlight the utility of the proteostatic stressor models to validate therapeutic compounds identified from other model systems and raise the possibility that common protective targets shared between kenpaullone and the MAP4K4 inhibitor may have greater disease modifying benefits than the current FDA approved therapeutics.

3.3 Results

3.3.1 Current FDA approved drugs for ALS fail to preserve MN viability.

To determine the therapeutic predictive power of our established ALS MN proteotoxicity models, we first tested the protective effects of Riluzole and Edaravone. These compounds are the only FDA approved drugs for the treatment of ALS, demonstrating modest improvements in patient motor function and slight delays in disease progression[296]. Using automated fluorescent microscopy and an unbiased quantification platform, we found that none of the concentrations of Riluzole and Edaravone tested (10nM-10μM) preserved MN viability in response to thapsigargin stress (Figure 3.1A). This inability to maintain MN numbers was also concomitant with a failure to preserve the βIII-Tubulin (TUJ1)$^+$ neuronal connections within the culture (Figure 3.1B).
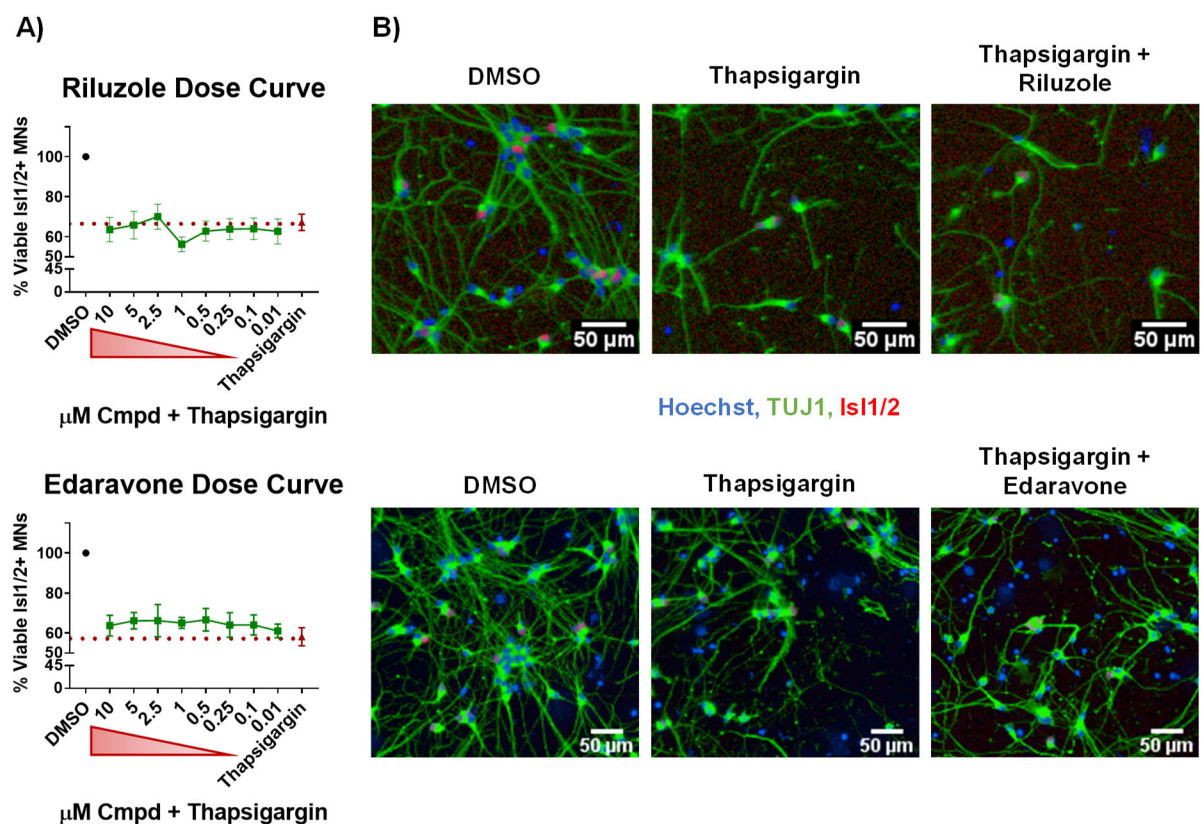
Figure 3.1. Current FDA approved drugs for ALS fail to preserve MN viability in proteostatic stress conditions.

    A) Quantification of MN viability in patient derived cultures treated for 48hrs with various doses of Riluzole or Edaravone in 1μM thapsigargin. N_b=3, n_t=3.

    B) Representative immunofluorescent staining of patient derived MNs in control (DMSO), thapsigargin, or Riluzole/Edaravone and thapsigargin treated conditions.

Biological replicates (N_b) represent independent MN differentiations, each with technical replicate wells (n_t). Data are mean value +/- SEM.

Two possible conclusions explained these negative data- either the proteostatic stressors were too strong an insult, and hench, incapable of predicting therapeutic activity of compounds, or Riluzole and Edaravone were truly inefficient MN protective compounds, given that they had never been tested for their effects on human neurons prior to FDA approval. To distinguish between these two possibilities, we next tested kenpaullone, a kinase inhibitor known to protect in a variety of neuronal damage models.

3.3.2 Kenpaullone and MAP4K4 inhibitor 29 strongly protect against proteotoxic induced degeneration of ALS patient MNs.

Kenpaullone is a kinase inhibitor that was first identified as having significant neuroprotective activity from a mouse MN survival screen performed in our lab[360]. Since this publication, multiple independent groups have confirmed kenpaullone's robust ability to preserve neuronal health[417,420]. Consistent with these studies, we found that treatment with kenpaullone was also able to dramatically improve MN survival in response to all proteostatic stressors, in control, as well as TDP-43 and SOD1 fALS patient lines (Figure 3.2A-B). This preservation of MN viability consisted of a complex βIII-Tubulin (TUJ1)$^+$ neural network, and well-preserved individual neurites (Figure 3.2B), cumulatively demonstrating the substantial ability of kenpaullone to maintain neuronal viability in diverse pathological conditions. Furthermore, since the MNs subjected to proteostatic stress were, in fact, rescuable by compounds such as kenpaullone, Riluzole and Edaravone were therefore simply ineffective neuroprotective agents, an observation consistent with recent publications using alternative ALS patient models[357]. These data also raised the exciting possibility that compounds more effective than Riluzole and Edaravone in human cellular models of ALS might have greater disease modifying benefits than the current approved therapies.
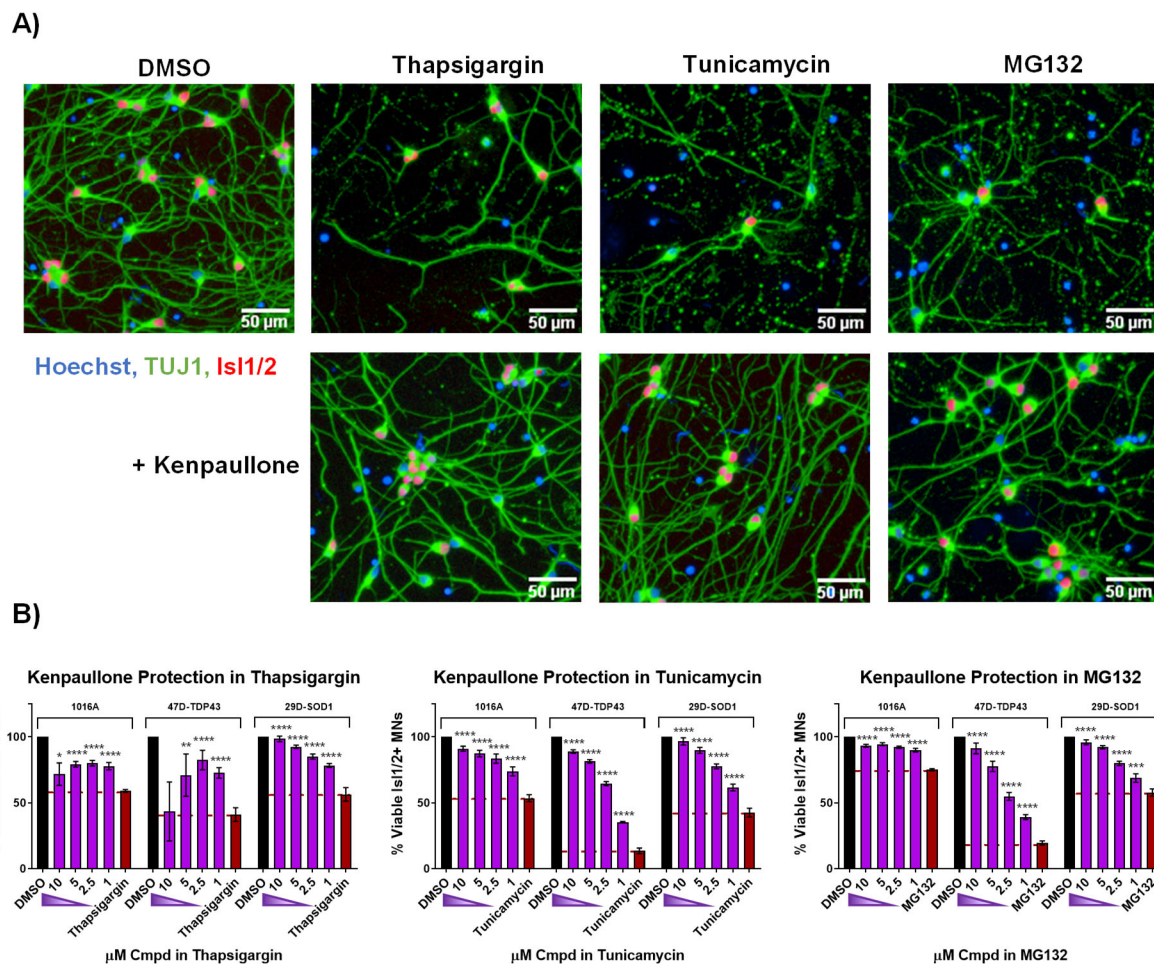
Figure 3.2. Kenpaullone protects ALS patient MNs from all proteostatic stressors.
A) Representative immunofluorescent images of ALS TDP-43^{G298S} patient derived MN cultures in control (DMSO), proteostatic stress, or proteostatic stress and kenpaullone rescued conditions.
B) Quantification of healthy patient MN viability (1016A) or ALS patient MN viability (47-TDP-43^{G298S} or 29D-SOD1^{L144F}) after 48hrs treatment with various doses of kenpaullone in proteostatic stress conditions (1µM thapsigargin, tunicamycin, or MG132). N_b=3, n_t=3, $p < 0.05$*, <0.01**, <0.001***, <0.0001**** one-way ANOVA with Tukey's hsd post-hoc test.

Biological replicates (N_b) represent independent MN differentiations, each with technical replicate wells (n_t). Data are mean value +/- SEM.

Despite the ability of kenpaullone to confer MN protection, in nearly all endogenous and exogenous stress conditions, kenpaullone itself, however, may not be a viable drug candidate. First, there is reason to suggest that kenpaullone may have limited ability to access the central nervous system (CNS). While kenpaullone has structural properties that would appear advantageous to pass the blood-brain-barrier, such as low molecular weight (327.18g/mol), lipophilic affinities conferred by its benzene rings, and insolubility in aqueous solutions, recent data using mice treated with intraperitoneal injection of kenpaullone actually demonstrated a failure of kenpaullone to confer target inhibition in the brain[422]. Second, kenpaullone has multiple cellular targets[360,423]. Increased specificity, as well as CNS penetrance, are required for effective drug development. Despite these limitations, the incredible ability of kenpaullone to protect ALS MNs is far too interesting to disregard. Rather, identifying the specific cellular targets of kenpaullone that are conferring its protective function may instead lead to the identification and generation of new ALS drugs with improved pharmacodynamic properties and specificity.

To gain insight into these potential protective targets of kenpaullone, members of our lab performed a phosphokinase antibody array on MN cultures treated with kenpaullone as well as in vitro phosphorylation assays to demonstrate that kenpaullone specifically inhibited the activation of an upstream kinase- MAP4K4[360]. It was therefore possible that the inhibition of MAP4K4 by kenpaullone was conferring protective activity. Previous work from Larhammar et al. indeed supported this hypothesis, demonstrating that treatment with a chemical inhibitor of MAP4K4 (MAP4K4 inhibitor 29), was also capable of promoting survival of dorsal root ganglion neurons deprived of nerve growth factor[400,424]. We therefore next tested whether treatment with MAP4K4 inhibitor 29 would also protect ALS patient derived MNs from proteostatic stressors. Similar to kenpaullone treatment, we found that MAP4K4 inhibitor 29 indeed protected and preserved patient derived MN viability in response to all proteostatic stressors, in both control, TDP-43, and SOD1 ALS patient lines (Figure 3.3A-B). While MN protection with MAP4K4 inhibitor 29 did not always reach levels achieved by kenpaullone, this protection also included the maintenance of healthy neurites (Figure 3.3B), cumulatively suggesting that the attenuation of MAP4K4 signaling was itself sufficient to confer MN protective activity.

Figure 3.3. MAP4K4 inhibitor 29 protects ALS patient MNs from all proteostatic stressors.
A) Representative immunofluorescent images of ALS TDP-43^{G298S} patient derived MN cultures in control (DMSO), proteostatic stress, or proteostatic stress and MAP4K4 inhibitor 29 rescued conditions.
B) Quantification of healthy patient MN viability (1016A) or ALS patient MN viability (47-TDP-43^{G298S} or 29D-SOD1^{L144F}) after 48hrs treatment with various doses of MAP4K4 inhibitor 29 in proteostatic stress conditions (1µM thapsigargin, tunicamycin, or MG132). N_b=3, n_t=3, $p < 0.05^*$, $<0.01^{**}$, $<0.001^{***}$, $<0.0001^{****}$ one-way ANOVA with Tukey's hsd post-hoc test.

Biological replicates (N_b) represent independent MN differentiations, each with technical replicate wells (n_t). Data are mean value +/- SEM.

3.3.3 Kenpaullone and MAP4K4 inhibitor 29 promote MN protection without reducing UPR induction or the amount of insoluble protein.

Since the stressors thapsigargin and tunicamycin rapidly upregulate ER stress signaling cascades and the unfolded protein response, and the proteasomal inhibitor MG132 robustly induces insoluble protein aggregates, there was a possibility that kenpaullone and MAP4K4 inhibitor 29 were conferring protection by directly blocking this stress induction or aggregate production. To test this hypothesis, we next used semiquantitative western blotting and found instead the maintained upregulation of the ER chaperone BiP and the ER stress-induced transcription factor CHOP following MN treatment with kenpaullone or MAP4K4 inhibitor 29 in thapsigargin stress (Figure 3.4A). We found that only the cleavage of caspase 3 was significantly reduced, indicating that the dominant protective mechanism of these compounds was through the reduction in cytosolic apoptotic signaling cascades, rather than through a mechanism dependent on directly inhibiting ER stress induction. Furthermore, utilizing the sequential solubilization western blotting assay developed in Chapter 2, we also found that both kenpaullone and MAP4K4 inhibitor 29 failed to prevent the accumulation of insoluble TDP-43 or ubiquitin (Figure 3.4B). These data indicate that MN protection conferred by the small molecules kenpaullone and MAP4K4 inhibitor 29 were also independent of a reduction in insoluble protein build up, or alternatively that this level of insoluble aggregation was not the main driver of death in these cells.
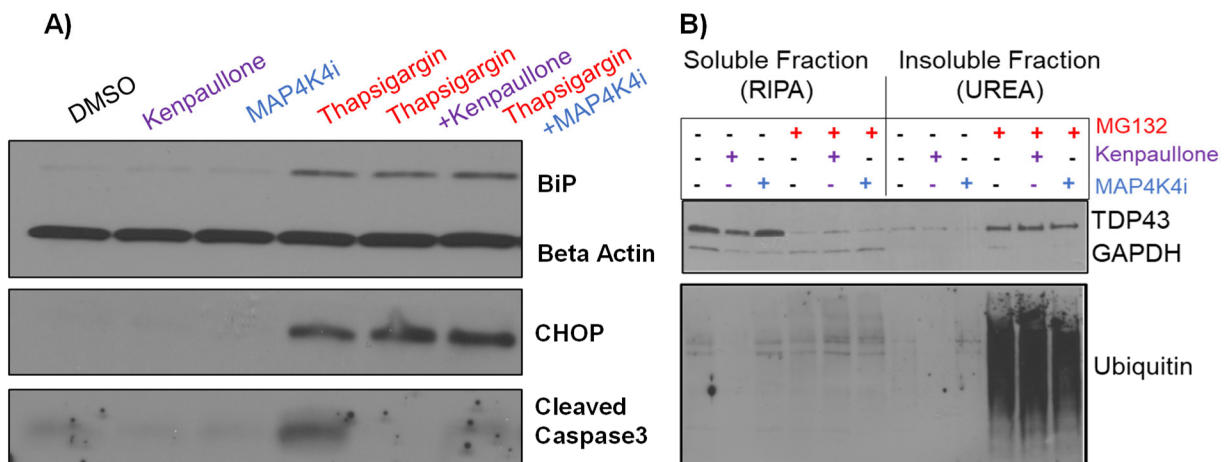
Figure 3.4. Kenpaullone and MAP4K4 inhibitor 29 do not directly reduce UPR induction or insoluble protein accumulation.
  A) Western blot analyses of patient derived MN cultures treated for 48hrs with either DMSO vehicle, 3μM kenpaullone, 5μM MAP4K4i, 1μM thapsigargin, or kenpaullone/MAP4K4i in thapsigargin.
  B) Western blot analyses of patient derived MN cultures treated for 48hrs with either DMSO vehicle, 3μM kenpaullone, 5μM MAP4K4i, 1μM MG132, or kenpaullone/MAP4K4i in MG132 stress.

The mechanism through which kenpaullone and MAP4K4 inhibitor 29 were conferring MN protection was thus likely due, in part, to the direct attenuation of the MAP4K4 signaling pathway, rather than the direct prevention of ER stress induction or protein aggregation. Subsequent investigations into MAP4K4 specifically as a neuronal protective target, however, have been met with conflicting results. RNA interference-based reduction in MAP4K4 alone was sufficient to cause MN survival in trophic factor withdrawal conditions performed by members of our lab[400]. Yet, results from Larhammar et al. showed instead a functional redundancy between the highly homologous MAP kinases MAP4K4, TNIK, and MINK1, with RNA interference-based reduction in all 3 upstream signaling molecules being required for protection of mouse dorsal root ganglion neurons[424]. While these discrepancies may be due to differences in cell types and stressors, the observation that kenpaullone also generally provided MN protection beyond that of the more specific MAP4K4 inhibitor 29 suggested that multiple kinases and molecular targets, in addition to the MAP4 kinases, were conferring MN protection. To identify those additional protective targets, we chose to continue pursuing kenpaullone and MAP4K4 inhibitor 29 in Chapter 4 instead of diving deeper into MAP4K4 specifically with RNA interference assays. While this decision is not without its drawbacks, it nevertheless allowed us to capture a more complete landscape of the mechanisms underlying pharmacological MN protection, particularly those mechanisms and molecular players not already identified.

3.4 Conclusions and Discussion

In this study, we provided evidence that our assays of proteostatic stress in ALS patient MNs were capable of identifying compounds with neuroprotective potential. We demonstrated that kenpaullone, a previously identified MN protective agent, was able to significantly preserve both SOD1 and TDP-43 ALS MN viability in all proteostatic stressor conditions. This rescue effect was substantially greater than the effect of Riluzole or Edaravone which failed to protect MN survival or maintain healthy neurites. We further demonstrated, for the first time, that a small molecule inhibitor to one of kenpaullone targets, MAP4K4, was also able to preserve ALS patient MN viability in all conditions of proteostatic stress[400]. This protection consisted of maintained neuritic morphology as well as preserved MN viability, and was independent of a direct reduction in UPR induction or insoluble protein buildup. These experiments ultimately highlight the utility of the proteostatic stressor models to validate therapeutic compounds identified from other model systems and raise the exciting possibility that common protective targets

shared between kenpaullone and the MAP4K4 inhibitor may have greater disease modifying benefits than the current FDA approved therapeutics.

3.4.1 The implications of a therapeutically predictive model of proteostatic stress in ALS patient MNs

The development of a cellular assay that robustly models the late-onset degenerative features of ALS, in the correct human cell type, in a reasonable time frame, while still retaining a rescuable-window for neuroprotective compound identification is not trivial. Yet, these assays are fundamental to the identification of new neuroprotective treatments for ALS. To date, the majority of human ALS MN assays used for small-scale therapeutic candidate evaluations or even high throughput, multiparametric drug screening have employed extensive culture times or a limited number of small molecule stressors to reveal the age-related degenerative phenotypes of selective ALS MN death and insoluble protein accumulation. While these studies have been irrefutably impactful, there remained an unaddressed need for the additional evaluation of proteostatic stressors for their ability to reveal differential ALS MN vulnerabilities for disease modeling and accelerated neuroprotective drug screening projects.

Our work in Chapter 2 described the development of 3 proteostatic stressor assays in ALS patient MNs which revealed differential and selective ALS MN vulnerabilities, degenerative morphologies, and the upregulation of stress response pathways and ALS-associated insoluble proteins. These assays were reproducible, synchronous, and scalable, and most importantly, as shown here in Chapter 3, capable of validating and identifying neuroprotective compounds. This was demonstrated using kenpaullone, a well-validated MN protective agent, which we showed rescued both SOD1 and TDP-43 ALS MNs from undergoing all 3 forms of proteostatic induced degeneration. This was a particularly critical observation as this demonstrated that the proteostatic stressor assays were, in fact, rescuable and consistent with established long-term culture systems of ALS demonstrating kenpaullone's protection[360]. Since these assays are accelerated, phenotypically robust, and compatible with high throughput automated imaging, these data confirm that the use of proteostatic stressors in ALS patient derived MNs can effectively complement the current model systems for novel therapeutic identification and drug screening efforts.

3.4.2 Limitations of the current FDA approved drugs for ALS

It is worthwhile mentioning that the current FDA approved drugs for ALS, Riluzole and Edaravone, notably failed to show robust effects in our proteostatic stressor ALS models. While this was initially concerning, these data were actually consistent with previous data from our lab[360] as well as data from the Okano group, who used several different metrics of ALS MN degeneration[357]. In the studies done by Fujimori and colleagues using 58 patient derived lines, extended culture maturation times revealed ALS MN neurite regression, cytotoxicity, and FUS$^+$ or phosphorylated-TDP-43$^+$ protein aggregates. Riluzole and Edaravone failed to protect against these maturation-induced degenerative phenotypes. The comparable inefficacy of Riluzole and Edaravone to protect ALS MNs in both our assay as well as in the Fujimori and colleagues system adds support to the claim that these agents are ineffective neuroprotective agents, and not simply inactive due to a synergistic or adverse effect with the type of stress used - proteostatic stress or age in culture. Moreover, this lack of efficacy was also not likely due to a limitation of either assay to detect protective compounds with mechanistically distinct actions. For example, Ropinirole- a dopamine agonist, cortisone acetate- an adrenocortical hormone, as well as ketorolac tromethamine- a nonsteroidal anti-inflammatory drug (NSAID), among others were all effective in rescuing neurite length, cytotoxicity and protein aggregates in the Fujimori study[357]. Moreover, foretinib, a VEGFR inhibitor, was also able to preserve MN viability in the proteostatic stressor models developed here, in addition to the kinase inhibitor kenpaullone (data not shown). These cumulatively support the conclusion that Riluzole and Edaravone are ineffective MN protective agents. Importantly, since Riluzole and Edaravone are both only modestly helpful in prolonging patient survival and improving motor function, these data leave open the possibility that drugs with more robust in vitro MN protective activity may benefit patients more than the existing ALS treatments. While this promising notion remains to be confirmed in the clinic, it appears well accepted, with 3 compounds identified in ALS patient MN assays currently in clinical trials for new ALS treatments[396–398].

3.4.3 The role of kenpaullone's targets (GSK3β, CDKs, and MAP4K4) and insoluble proteins in MN death and protection

The ability of kenpaullone to protect MNs from an array of cellular insults, including ALS mutations as well as various exogenous stressors, indicates an important role for the cellular targets of kenpaullone in MN protection. Kenpaullone is an annotated inhibitor of GSK3β and CDKs[423], with additional inhibitory activity against

MAP4K4 identified from phosphokinase arrays, in vitro phosphorylation assays[360], and kinase catalytic activity assays[425,426]. It was therefore possible that the inhibition of any or all of these cellular targets was contributing to kenpaullone's observed MN protection (Figure 3.5).
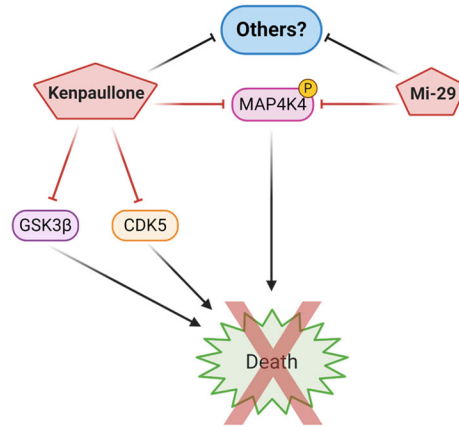
Figure 3.5. Kenpaullone targets in MN protection.
Kenpaullone confers MN protection against various forms of degenerative stress through the inhibition of GSK3β, CDKs, and MAP4K4, among others. More selective inhibition of MAP4K4 with MAP4K4 inhibitor 29 (Mi-29) also promotes MN protection. However, due to the high homology of upstream kinases and the potential for off-target effects from kinase inhibitors, additional targets may also play a role in MN survival and remain to be identified.

Glycogen Synthase Kinase 3 beta (GSK3β) has known roles in neuronal apoptosis[427,428] and modulation of GSK3β activity has been implicated as a protective factor in ALS mouse models[429,430]. It was therefore surprising that multiple methods of selectively reducing GSK3 activity, including small molecule mediated reduction, lentiviral mediated knockdown, as well as genetic deletion, all failed to show patient MN protection levels comparable to kenpaullone in trophic factor withdrawal conditions[360]. Moreover, CHIR-99021, thought to be one of the most specific inhibitors of GSK3β, notably did not promote any survival at all, either in trophic factor withdrawal conditions[360] or in our proteostatic stressor assays (Figure 4.7C). These data indicated to us that many of the beneficial effects of kenpaullone were likely being mediated by another target.

Cyclin dependent kinases (CDKs) are well-annotated targets of kenpaullone, normally functioning to regulate cell cycle progression in mitotic cells. Intriguingly, CDK inhibition in neurons, which are post-mitotic, has been demonstrated to protect against toxic stimuli[431–434]. It was therefore possible that kenpaullone's ability to inhibit CDKs in addition to GSK3β was conferring MN survival. Indeed, a study by Reinhardt et al. recently demonstrated that CDK5, the primary neuronal CDK, was involved in, but notably was not sufficient for,

neuroprotection of patient MN degeneration induced by neuroinflammatory stimuli[420]. Instead, they demonstrated that RNAi-mediated knockdown of both GSK3β and CDK5 inhibition was required to synergistically enhance a protective phenotype. These data indicated that the dual inhibition of both kinases by kenpaullone may be mediating ALS MN protection.

Yet, GSK3β and CDK5 are not the only targets of kenpaullone. MAP4K4 is another cellular target of kenpaullone that could be driving MN survival. Work by Larhammar et al. supported this proposition, demonstrating that the pharmacological inhibition of MAP4K4 could indeed improve the survival of mouse dorsal root ganglion neurons after nerve growth factor (NGF) withdrawal[424]. Prior to our published data and the work presented here[400], however, no work had been done to investigate the role of this kinase in MN viability, or in a specific neurodegenerative disease context.

Here and in our recent publication, we demonstrated for the first time that the pharmacological suppression of MAP4K4 attenuates ALS MN degeneration potentiated by trophic factor withdrawal[400] and the proteostatic stressors thapsigargin, tunicamycin, and MG132. We additionally demonstrated that this preservation of MN cell numbers was coincident with a conservation of healthy neurites and that this protection was not mediated by a direct reduction in UPR induction or the production of insoluble aggregates. This latter result was notably different from the findings after trophic factor withdrawal, where MAP4K4 reduction induced autophagy to reduce the accumulation of SOD1 protein aggregates[400]. These data indicated that while our assays of proteostatic stress are predictive of changes in MN survival and morphologic features, they are limited in their ability to detect potentially small changes in protein build-up that accumulate over time.

Nonetheless, these data begin to shed light on the potential role of insoluble protein aggregates in MN death. The fact that MN survival with MAP4K4 inhibition could occur with insoluble aggregates, and that selective MN death induced by the ER stressors could occur without insoluble proteins or aggresomes, separates protein aggregation from MN death. This is important, because insoluble proteins are largely viewed as causal drivers in neurodegenerative disorders like ALS. However insoluble aggregates might not be necessary for disease. In fact, it has already been demonstrated that ALS-linked mutations in TDP-43 can give rise to adult-onset motor neuron disease in mice, without the apparent cytosolic aggregation of TDP-43[185]. Moreover, inclusion body formation, rather than being necessary and causal of disease, may even be protective. In perhaps one of the first demonstrations of this, Arrasate et al. used longitudinal live cell imaging to show that inclusion body formation of aggregated

huntingtin actually improved neuronal survival, functioning as a cellular protective mechanism to sequester the more toxic diffuse mutant entity[435]. These data, plus our work here in human MNs, cumulatively point to the conclusion that insoluble protein accumulation, at least to a certain degree, is not a necessary component for selective neuronal death in neurodegenerative disease, and that reduction of the insoluble forms of these proteins may not be a requirement for effective therapeutic candidates.

Moreover, following our publication demonstrating the ability of MAP4K4 inhibition to protect MN survival, the protective effect of reduced MAP4K4 signaling has been demonstrated in additional models of ALS. Bos and colleagues demonstrated that MAP4K4 inhibitors can rescue ALS MN death induced by the ER stressor cyclopiazonic acid, and they further developed and optimized a series of potent, stable, and brain penetrant inhibitors[425]. This is particularly important as the current pharmacological MAP4K4 inhibitors were developed for alternative peripheral indications and are unlikely to penetrate the CNS[436]. It will therefore be exciting to see if these novel CNS-penetrant MAP4K4 inhibitors will be efficacious in animal models and in clinical trials.

Cumulatively, the work in this thesis, our lab's recent publication, as well as the work from Bos and colleagues, make it abundantly clear that the continued pursuit of MAP4K4 as a target for ALS treatments holds great promise. However, rather than pursuing specific RNA interference (RNAi) mediated approaches to MAP4K, we chose instead to continue using the small molecule inhibitors kenpaullone and MAP4K4 inhibitor 29. While this decision is not without its drawbacks, there were discrepancies between groups to observe comparable neuroprotection using specific MAP4K4 RNAi versus combined inhibition of the highly homologous MAP4K4, TNIK, and MINK1[400,424]. This fact, as well as the fact that kenpaullone generally outperformed the more selective MAP4K4 inhibitor, suggested to us that there may be multiple upstream kinases conferring MN protection (Figure 3.5). To identify these additional cellular players, both kenpaullone and MAP4K4 inhibitor 29 were used in the following chapter in conjunction with global proteomic analyses to delineate the complete cellular landscape involved in stress and protected conditions, leading to the identification of several MN survival pathways and novel neuroprotective compounds.

Chapter 4

Identifying novel MN protective compounds and convergent survival pathways

using phosphoproteomic analyses

4.1 Attributions

All experiments presented in this chapter were designed, performed, and analyzed by Ms. Michelle Watts, with collaboration from Dr. Alban Ordureau for SPS-MS3-based quantification and analysis of TMT-labeled proteins and phosphopeptides, and assistance from Ms. Kris Holton for statistical analyses. All aspects of this research were supervised by Dr. Lee L. Rubin, with funding graciously provided by Biogen and the Harvard Brain Science Initiative.

4.2 Introduction

Amyotrophic Lateral Sclerosis (ALS) is an incapacitating and uniformly fatal motor neuron (MN) disease that has few therapeutic options. Discovering effective therapeutics for ALS patients has been particularly challenging due to the complex etiology of the disease, the fundamental inability to access and culture human MNs, and the failure of animal models to predict clinical efficacy in patients. The recent discovery of induced pluripotent stem cell (iPSC) technologies and the development of neuronal differentiation protocols have since improved ALS therapeutic identification by allowing, for the first time, the production and culture of ALS patient MNs. ALS patient MNs recapitulate key features of ALS in vitro, offering an "ALS in a dish" model system that now expands the possibilities to explore mechanisms of ALS MN degeneration and discover protective pathways that can be modulated for potential new therapeutics.

In Chapters 2 and 3 of this thesis, we used several ALS patient derived cultures to demonstrate that MNs are particularly sensitive to proteostatic stress and that pharmacological stressors can accelerate the late-onset convergent ALS phenotypes of MN death, neuritic damage, and insoluble protein accumulation. These assays of proteostatic stress in ALS patient derived MNs were compatible with the types of automated imaging platforms used in drug screening and importantly capable of identifying compounds with neuroprotective potential. We demonstrated this using a previously well characterized MN protective agent, kenpaullone, which we showed was able to robustly preserve MN viability and neuritic morphology of various ALS patient lines exposed to multiple proteostatic stressors. We further demonstrated, for the first time, that a more selective inhibitor to one of kenpaullone's cellular targets, MAP4K4, was also protective against proteostatic stress induced ALS patient MN degeneration, highlighting the ability of these culture systems to not only validate, but also identify new potential ALS targets. Critically, while MAP4K4 is a promising new drug target, the fact that kenpaullone generally

outperformed the more selective MAP4K4 inhibitor, as well as the observation that specific RNAi-based reduction of MAP4K4[400,424] did not reproducibly achieve neuroprotection comparable to the compound inhibitors led us to reason that supplementary protective targets were also at play.

To capture these additional potential protective mechanisms, in this study, we took advantage of the scalability of the proteostasis stress assays and performed global phosphoproteomic and proteomic analyses on MN cultures treated with thapsigargin, with or without the protective compounds kenpaullone and MAP4K4 inhibitor 29. These data identified a core proteome that was changed with the 2 MN protective agents and implicated several molecular perturbations mediating MN survival in response to proteotoxic stress. These included expected molecular changes, such as decreases in the annotated targets of kenpaullone, GSK3β and CDKs, as well as decreases in the pro-apoptotic downstream effectors of MAP4K4- JNK and cJUN. Yet these studies also identified several novel molecular targets that were commonly dysregulated with each protective compound, including the downregulation of protein kinase family members and RAFs, among others. To determine whether these proteomics-implicated molecular perturbations were functionally mediating MN survival, we then performed a small, proof-of-concept screen of a collection of small molecule inhibitors. These experiments resulted in the identification of several novel MN protective drugs, including a PKC inhibitor enzastaurin, and a B-RAF inhibitor GDC-0879. Importantly, enzastaurin and GDC-0879 are compounds that are already in clinical development or have been demonstrated in clinical trials to be well tolerated in patients[437–440], suggesting these drugs may be more readily repurposed for potential new ALS treatments. These studies cumulatively underscore the power of proteomics to uncover functional cellular players driving MN protection and ultimately highlight the potential of the proteostatic stress assays for successful neuroprotective drug discovery.

4.3 Results

4.3.1 Global proteomic and phosphoproteomic analyses of degenerating and protected MNs implicate convergent survival pathways.

To capture a complete picture of all potential protective pathways occurring in human MNs treated with kenpaullone or MAP4K inhibitor 29, global proteomic and phosphoproteomic analyses were performed, in collaboration with Dr. Ordureau from the Harper lab at Harvard Medical School. MN cultures were first treated with a moderate dose of thapsigargin (0.1μM), alone or in combination with kenpaullone or MAP4K4 inhibitor 29, and

total protein lysates were then collected at early (24 hours) and late (48 hours) time points (Figure 4.1A). These

conditions allowed a dynamic view of cellular perturbations occurring with time while ensuring that relevant

molecular changes were captured in populations of surviving cells.

A)

B)

Data Set	# Peptides (Set 1)	# Peptides (Set 2)	# Unique Proteins	# Unique Phosphorylation Sites
Stress+Protection (Protein)	67,357	59,708	6,697	
Stress+Protection (Phospho-protein)	28,399	28,973	2,764	7,999
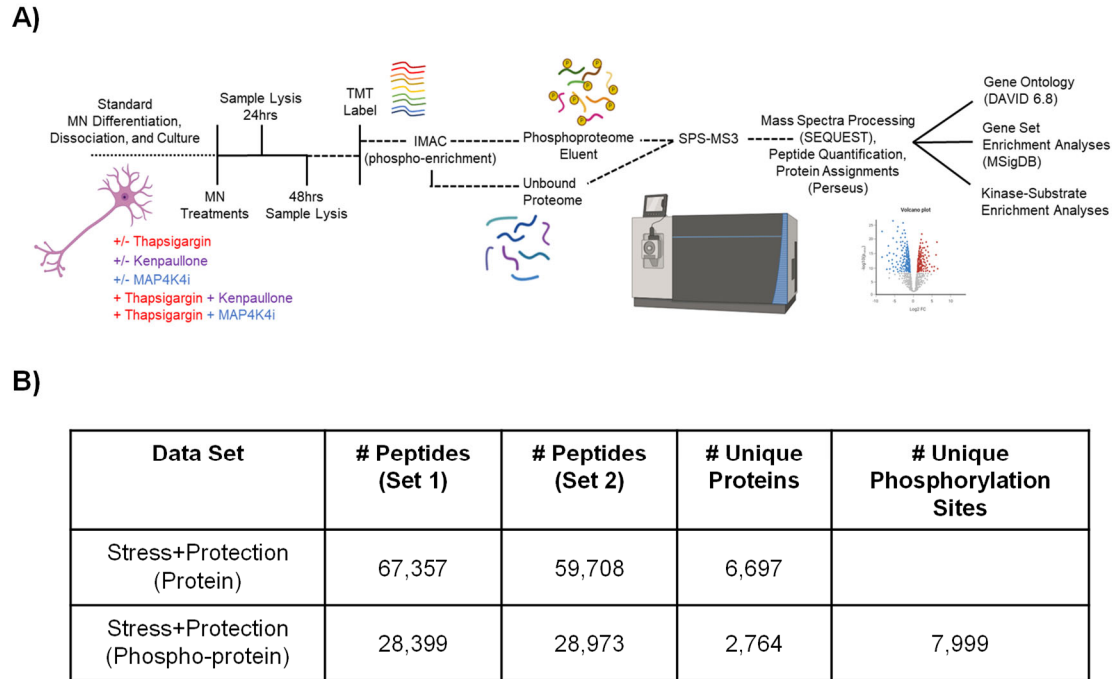
Figure 4.1. Overview of global proteomics experiment and dataset characteristics.
A) Schematic of the proteostatic stress and protection assay and quantitative proteomics analysis pipeline.
B) Table depicting the number of quantified peptides, proteins, and phosphorylation sites obtained from 2 biological replicate proteomics experiments.

From 2 biological replicate experiments, a total of 67,357 and 59,708 peptides were quantified to make up

the proteomics data set, corresponding to 6,697 unique proteins (Figure 4.1B). A total of 28,399 and 28,973 peptides

were additionally quantified in the phosphoproteomic dataset, corresponding to 2,764 unique phosphoproteins and

7,999 nonredundant phosphorylation sites (Figure 4.1B). These datasets are deposited in Supplementary Data Set 1,

and include 9 total sample comparisons- 24 hours and 48 hours of thapsigargin treatment compared to untreated

control cultures, 24 hours and 48 hours of kenpaullone or MAP4K4 inhibitor 29 protection in thapsigargin compared

to thapsigargin treatment, and 48 hours of kenpaullone or MAP4K4 inhibitor 29 treatment compared to untreated

cultures.

A combination of bioinformatic tools was then used to analyze these datasets to identify individual proteins

or groups of proteins that were involved in thapsigargin induced degeneration and in pharmacological protection

with kenpaullone or MAP4K4 inhibitor 29. These included gene ontology (GO) analyses using DAVID 6.8 software, which identifies enriched biological processes, cellular components, or molecular functions from the set of significantly changed proteins and phosphoproteins with each compound treatment (False Discovery Rate Q<0.05). For sample comparisons that did not have individually dysregulated proteins that reached our statistical significance cutoff, gene set enrichment analyses (GSEA) were performed, which instead ranked and tracked incremental changes in groups of proteins that could be conferring significant biological activity with each treatment. Lastly, kinase-substrate enrichment analyses (KSEA), were utilized to make sense of the phosphoproteomic datasets, correlating specific substrate protein phosphorylation sites to the activity of kinases known to target those substrate phospho-sites.

Several noteworthy results arose from these cumulative analyses. First, investigating the proteomics dataset, we found that only thapsigargin treatment resulted in statistically significant dysregulated proteins. This is visualized in Figure 4.2A as a volcano plot of quantified individual proteins (represented as dots) that are plotted as a function of $\log_2$fold change and statistical significance. Significantly upregulated proteins included the ER chaperone BiP (HSPA5) and the proapoptotic protein Bcl-2 binding protein 3 (BBC3), consistent with our data in Chapter 2 showing thapsigargin induces ER stress and drives apoptosis (Figure 4.2A). Gene ontology analyses of all significantly upregulated proteins in thapsigargin stress additionally revealed enriched terms "response to endoplasmic reticulum stress" and "positive regulation of cytosolic calcium ion concentration" (Figure 4.2B). These data were further internally validating, given the known effects of thapsigargin on ER stress via the inhibition of the ER calcium ATPase pump, which actively transports calcium from the cytosol into the ER lumen.
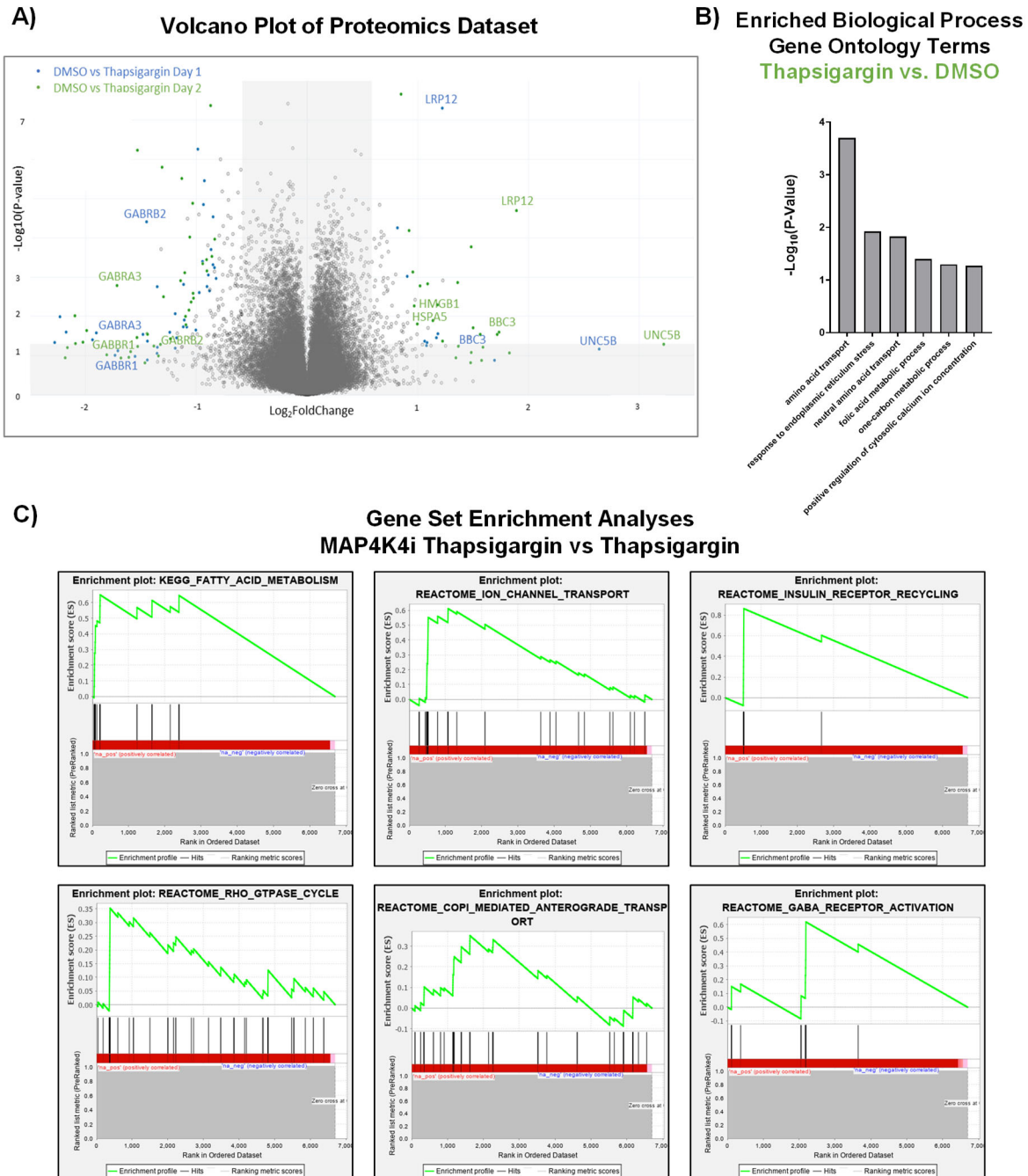
Figure 4.2. Proteomic analyses implicate fatty acid metabolism, Rho-GTPase cycles, anterograde transport, and extracellular receptors in pharmacological MN protection.

A) Volcano plot of all proteins quantified in the proteomics dataset. Individual proteins represented as single dots.

B) Gene ontology analyses of the significantly upregulated proteins in response to thapsigargin treatment.

C) Gene set enrichment analyses of all significantly dysregulated proteins in MAP4K4i and thapsigargin treated conditions, compared to thapsigargin stress conditions.

79

A number of new and intriguing observations, however, were also noted within the thapsigargin-changed proteins. These included the downregulation of GABA receptor subunits (GABRA3, GABBR1, GABRB2), as well as the upregulation of ligand activated cell surface receptors (the netrin receptor UNC5B and the low-density lipoprotein receptor-related protein 12 LRP12), and the exported death associated molecule HMGB1 (Figure 4.2A). While these data need to be further explored and mechanistically investigated, these data suggest that an extracellular receptor-mediated pathway may be modulated by a secreted toxic ligand in response to ER stress to confer cellular death.

Since neither kenpaullone nor MAP4K4 inhibitor 29 treatment resulted in significant changes at the individual protein level, at least with the N=2 biological replicates collected, gene set enrichment analyses were then performed, in collaboration with Kris Holton, to interrogate changes in groups of proteins. With both kenpaullone and MAP4K4 inhibitor 29 treatment, we found significant enrichments in "fatty acid metabolism", modulations in receptor dynamics such as "insulin receptor recycling" and "GABA receptor activation" as well as enrichments in "Rho-GTPASE cycle", and transport mechanisms such as "ion transport" and "COP1 mediated anterograde transport" (Figure 4.2C). These data began to provide an indication of how each protective compound was working, which we stratified into multiple potential protective processes in Table 4.1.

Table 4.1. Protective processes implicated by proteomic analyses.

Protective Compound	Implicated Protective Processes	Targets
Kenpaullone	Microtubule Dynamics	Phospho-CLASP2, Phospho-DPYSL2, MAP1B, MAPT, TPP, Kif11
Kenpaullone + MAP4K4i	Signaling	GSK3β, PKC, JNK, c-JUN, mTOR/S6K, RAF, PIM
Kenpaullone + MAP4K4i	Metabolism (Fatty Acid, Lipid, Cholesterol)	ACSL4, HMG-CoA Reductase, SCD, ODC, CHDH
Kenpaullone + MAP4K4i	Receptors	Insulin, GABA
Kenpaullone + MAP4K4i	Cell Cycle Proteins	Cdc42, CDK3/5
Kenpaullone + MAP4K4i	Calcium Dynamics	Cam2K, CSNK2
Kenpaullone + MAP4K4i	ER-Golgi Anterograde Transport	GBF1, Phospho-EXOC1
MAP4K4i	HDACs	HDAC1, 2, 5

Investigating the phosphoproteomics datasets allowed further identification and stratification of potential protective mechanisms. In this dataset, kenpaullone, as well as thapsigargin treatment, resulted in significantly dysregulated phosphoproteins, visualized as a volcano plot in (Figure 4.3A). We found that annotated targets of kenpaullone, phosphorylated MAP4K4 and GSK3β/α, were decreased with kenpaullone treatment, validating the ability of this technique to capture relevant biological changes (Figure 4.3A). Gene ontology terms of the significantly dysregulated proteins from kenpaullone treatment largely indicated changes in neuron extension processes, such as "positive regulation of axon extension", "neuron projection development", "dendrite morphogenesis', and "microtubule cytoskeleton organization" (Figure 4.3B). The main drivers of these changes included the microtubule plus-end tracking protein CLASP2, the neuronal guidance microtubule assembly protein DPYSL2, and the microtubule associated proteins MAP1B and MAPT (Figure 4.3A). Since cultures treated with the more selective MAP4K4 inhibitor 29 did not exhibit these changes in phosphorylated microtubule proteins, it is likely that these changes were due to kenpaullone's dual inhibition of GSK3β and CDK5, rather than MAP4K4 inhibition, consistent with a recent publication demonstrating the combined suppression of GSK3β and CDK5 protected the cytoskeleton of neurons exposed to inflammatory stress[420]. Moreover, these microtubule associated proteins have also previously been implicated in neuronal extension processes and neuronal survival[441–444], suggesting that changes in neuritic processes were either strong functional consequences of improved survival or potentially even driving kenpaullone's survival effect. Downregulation of "apoptotic signaling pathways" was also observed in the gene ontology terms (Figure 4.3B), further supporting the pro-survival effect observed with kenpaullone treatment.

Last, and perhaps most important, kinase-substrate enrichment analyses of the phosphoproteomics dataset revealed several common kinase pathways downregulated by kenpaullone and MAP4K4 inhibitor 29 treatment (Figure 4.3C). Some of these changes in kinase activity were expected, including decreases in the JNK pathway (annotated as MAPK8/9/10), a known downstream apoptotic target of MAP4K4 signaling, as well as GSK3β and CDKs, both annotated targets of kenpaullone. However, a number of unanticipated targets were additionally commonly downregulated between kenpaullone and MAP4K4 inhibitor 29 treatment, including protein kinase family members as well as RAFs. These data were added to and collated into the table of potential protective hit groups implicated by all bioinformatic analyses (Table 4.1).
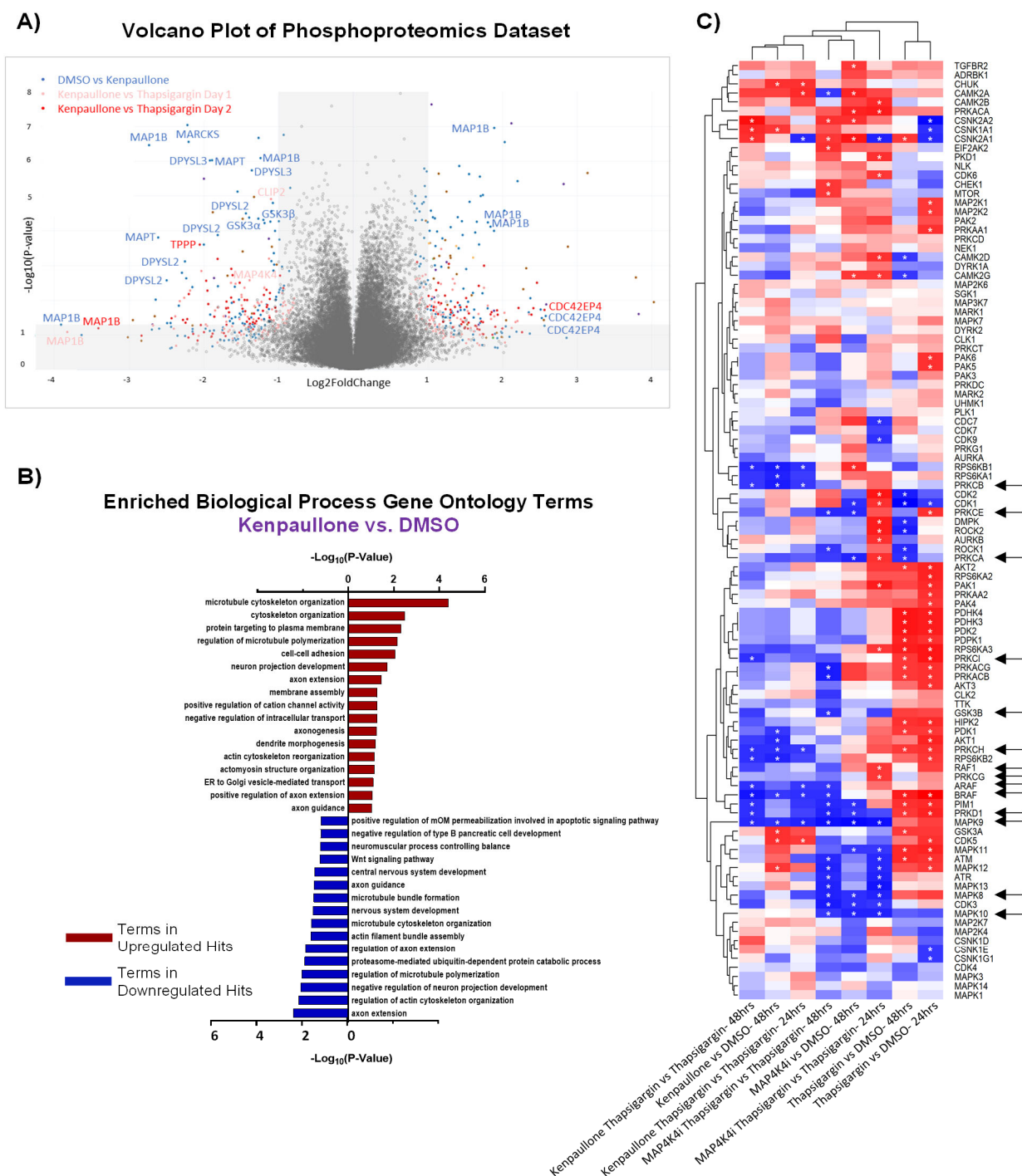
Figure 4.3. Phosphoproteomic analyses implicate neuritic processes, GSK3β, JNK, PKC, and RAF in pharmacological MN protection.

A) Volcano plot of all phosphoproteins quantified in the phosphoproteomics dataset. Individual phosphoproteins represented as single dots.

B) Gene ontology analyses of the significantly upregulated phosphoproteins or downregulated phosphoproteins in response to kenpaullone treatment.

C) Unbiased hierarchical clustering of kinases whose phospho-substrates were perturbed with compound treatments (identified by kinase-substrate enrichment analyses (KSEA)). Red boxes indicate upregulated kinase activity; blue boxes indicate downregulated kinase activity. Stars indicate FDR q values < 0.05.

4.3.2 A series of small molecule inhibitor tests targeting proteomics-implicated convergent survival pathways identifies novel MN protective compounds.

As a first pass at interrogating whether these potential protective hit groups were functionally relevant, 25 small molecule inhibitors to the proteomics-implicated targets were selected and tested for protective activity in the thapsigargin MN stress assay. Compounds were selected from SelleckChem's bioactive compounds collection with three main considerations in mind- 1) maximum target specificity, 2) minimum off-target activities, and 3) status of FDA approval, if applicable (Table 4.2). 3 concentrations (10nM, 100nM, and 1μM) of each compound were initially tested for protection in 2 biological replicate MN cultures challenged with thapsigargin, then compounds were further tested in a full 8-point dose curve (10nM-10μM) with 3 subsequent MN differentiations. The compound reconstitution vehicle DMSO was used as a negative control and both kenpaullone and MAP4K4 inhibitor 29 in thapsigargin stress were used as positive controls.

Table 4.2. Small molecule inhibitors tested.

Implicated Protective Processes	Small Molecule Inhibitors Tested
Microtubule Dynamics	Nocodazole, Docetaxel, Monastrol, ML-141
Signaling	1-Azakenpaullone, CHIR-99021, SP600125, Enzastaurin, GDC-0879, Torin 1, Torin 2, LY2584702 Tosylate, SMI-4a, AZD-1390
Metabolism (Fatty Acid, Lipid, Cholesterol)	ACSS2i, Simvastatin, Eflornithine, MK-8245
Receptors	Gabapentin, (+)-Bicuculline, R-7050
Cell Cycle Proteins	Roscovitine
ER-Golgi Anterograde Transport	Golgicide A
HDACs	Tubastatin A, Valproic Acid

From these cumulative tests, we identified 5 compounds that robustly protected against thapsigargin induced MN degeneration (4.4A-B). These included a JNK inhibitor SP600125, a PKC inhibitor enzastaurin, a B-RAF inhibitor GDC-0879, a HDAC inhibitor tubastatin A, and a GSK3β/CDK inhibitor 1-azakenpaullone, an analogue of kenpaullone (Figure 4.4A-B). Some of these protective hit compounds were expected, such as the JNK inhibitor SP600125, the HDAC/microtubule acetylation inhibitor tubastatin A, and the GSK3β/CDK inhibitor 1-

azakenpaullone, as these targets have known roles in neuronal viability and inhibitors to them have reported efficacy against various models of neuronal stress[239,400,420,428–430,445,446]. Importantly, however, 2 of these hit compounds, the PKC inhibitor enzastaurin and the B-RAF inhibitor GDC-0879 had not previously been tested in MN survival. While the targets of these inhibitors, PKC as well as B-RAF, have been associated with neuronal viability, with context and cell-type dependent effects[447–452], the results shown here in Figure 4.4A-B add additional data supporting that pharmacological inhibition of PKC and B-RAF can promote MN viability and that the proteomics-based analyses were accurately identifying and predicting functional protective cellular perturbations.
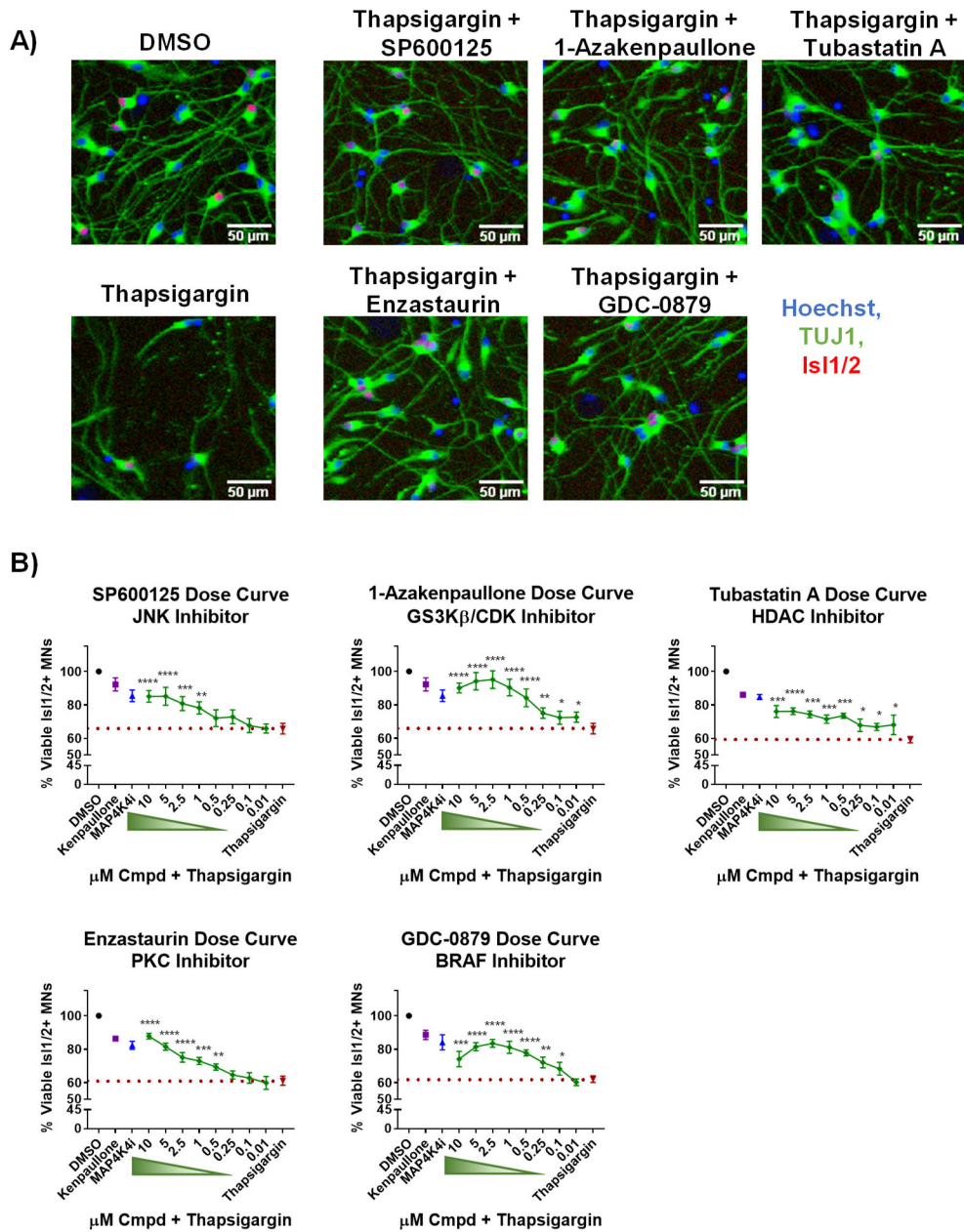
Figure 4.4. Small molecule inhibitors to GSK3β, JNK, PKC, and B-RAF are MN protective compounds.

A) Representative immunofluorescent images of patient derived MN cultures in control (DMSO), thapsigargin stress, or small-molecule-inhibitor-rescued conditions.

B) Quantification of MN viability in patient derived cultures after 48hrs treatment with various doses of small molecule inhibitors in 1μM thapsigargin. 3μM kenpaullone or 5μM MAP4K4i in thapsigargin stress were used as positive controls, DMSO vehicle as a negative control. $N_b \geq 3$, $n_t = 3$, $p < 0.05^*$, $<0.01^{**}$, $<0.001^{***}$, $<0.0001^{****}$ one-way ANOVA with Tukey's hsd post-hoc test.

Biological replicates (N_b) represent independent MN differentiations, each with technical replicate wells (n_t). Data are mean value +/- SEM.

Importantly, the 5 protective hit compounds identified additionally preserved healthy βIII-tubulin (TUJ1)[+] neurites (Figure 4.4A), similar to what was observed with kenpaullone and MAP4K4 inhibitor 29. This preservation of both cellular compartments, neuronal soma and neuritic extensions, in effective survival-promoting compounds was a critical observation throughout the proteomics-informed inhibitor tests, particularly in light of the perplexing result observed with golgicide A treatment. Golgicide A is a stressor that blocks anterograde transport from the ER to the Golgi and this mode of intracellular trafficking was implicated in the proteomics dataset as being dysregulated by the protective compounds kenpaullone and MAP4K4 inhibitor 29 (Figure 4.2C). Intriguingly, we found that blocking anterograde transport with golgicide A was in fact able to transiently preserve MN numbers (Figure 4.5A-B), while failing to protect the extensive damage to neurites (Figure 4.5B) or MN loss at longer time points (Figure 4.5C). We speculate that the inhibition of anterograde transport with golgicide A might have transiently protected neuronal cell bodies by preventing export of a potential death signal carried through the ER-to-Golgi secretory pathway. This speculation is consistent with the proteomics dataset showing that thapsigargin stress upregulated exported death associated molecules and ligand-associated receptors, and the proteomics data showing both protective compounds kenpaullone and MAP4K4 inhibitor 29 protection modulated anterograde transport. However, further experiments interrogating this potential extracellular death cascade with ER stress need to be performed.
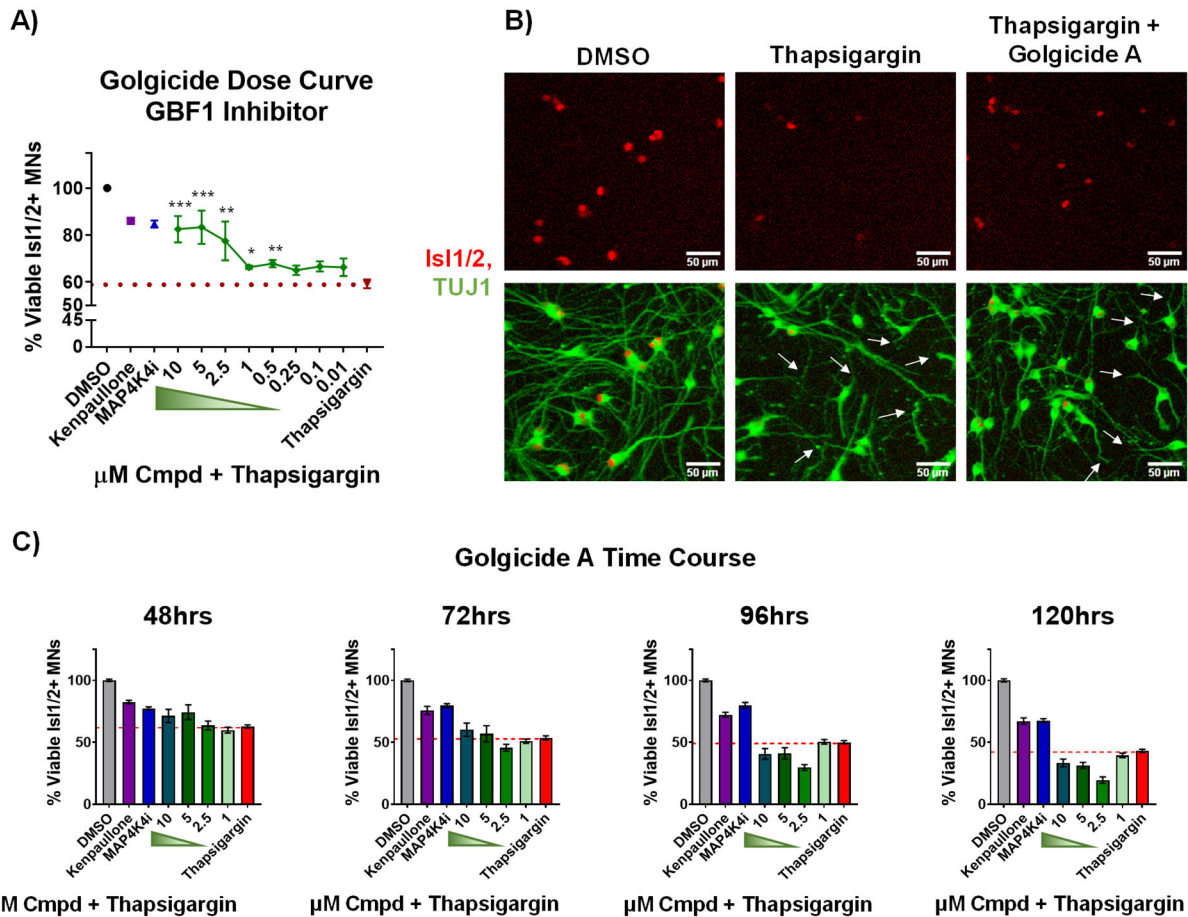
Figure 4.5. Blocking anterograde transport transiently preserves MN numbers but fails to preserve neurite morphology or long-term survival.

A) Quantification of MN viability in patient derived cultures after 48hrs treatment with various doses of golgicide A in 1μM thapsigargin. 3μM kenpaullone or 5μM MAP4K4i in thapsigargin stress were used as positive controls, DMSO vehicle as a negative control. $N_b \geq 3$, $n_t = 3$, $p < 0.05^*$, $<0.01^{**}$, $<0.001^{***}$, $<0.0001^{****}$ one-way ANOVA with Tukey's hsd post-hoc test.

B) Representative immunofluorescent images of patient derived MN cultures in control (DMSO), thapsigargin, or golgicide A and thapsigargin treated conditions. Arrows indicate damaged neurites.

C) Quantification of MN viability in patient derived cultures at various time points of treatment with golgicide A in 1μM thapsigargin stress. 3μM kenpaullone or 5μM MAP4K4i in thapsigargin stress were used as positive controls, DMSO vehicle as a negative control.

Biological replicates (N_b) represent independent MN differentiations, each with technical replicate wells (n_t). Data are mean value +/- SEM.

Additional results observed from the inhibitor tests further supported the importance of neuritic health in therapeutic candidate identification. We found that treatment with agents that primarily affected neurites, the microtubule depolymerizing agent nocodazole and the stabilizing agent docetaxel, were toxic, causing a dose-dependent decrease in MN numbers (Figure 4.6A) and that this toxicity was observed even in the presence of kenpaullone (Figure 4.6B). Moreover, 2 additional compounds modulating cytoskeletal dynamics, the Kif11 inhibitor monastrol, as well as the Cdc42/Rac1 inhibitor ML-141 were not toxic but did fail to demonstrate substantial MN survival effects (Figure 4.6C). These data cumulatively suggest that the modulations of neuritic dynamics observed in the phosphoproteomic dataset of kenpaullone treated cultures was thus a consequence, and not a cause, of MN survival with kenpaullone.
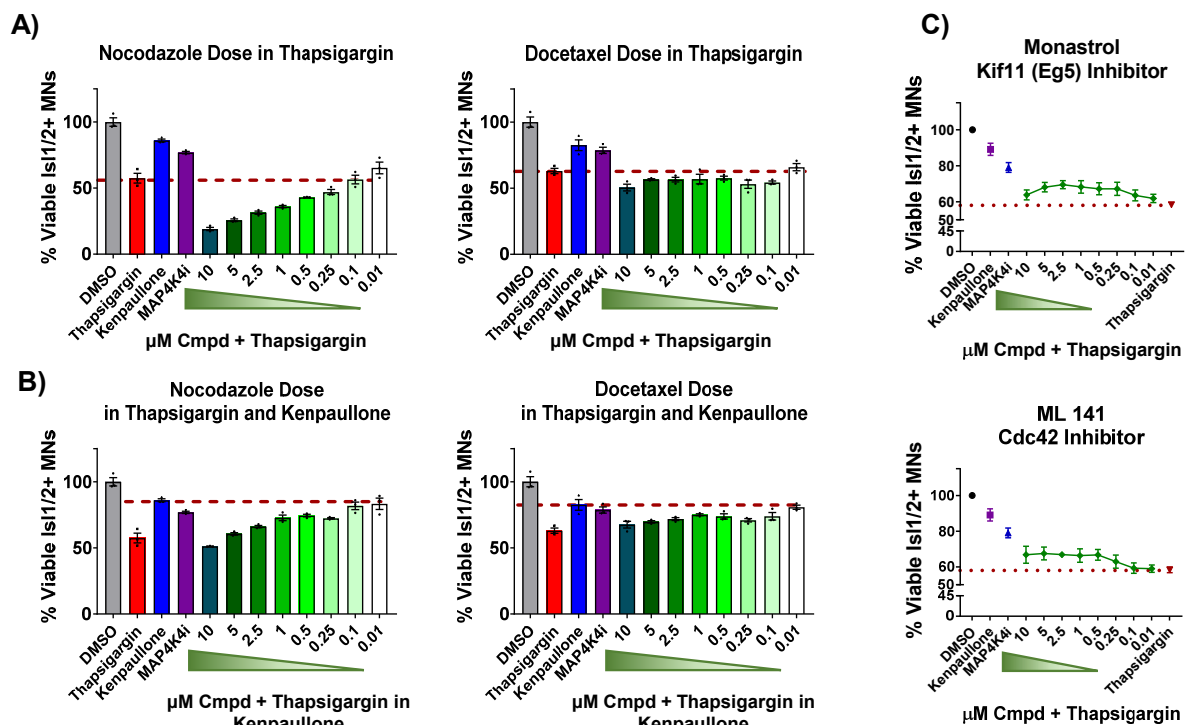
Figure 4.6. Modulating microtubule dynamics is not sufficient to promote MN survival.
  A) Quantification of MN viability in patient derived cultures after 48hrs treatment with various doses of nocodazole or docetaxel in 1μM thapsigargin. 3μM kenpaullone or 5μM MAP4K4i in thapsigargin stress were used as positive controls, DMSO vehicle as a negative control. N_b=1, n_t=3. Data are mean value +/- STDEV.
  B) Quantification of MN viability in patient derived cultures after 48hrs treatment with various doses of nocodazole or docetaxel in 1μM thapsigargin/3μM kenpaullone rescued conditions. N_b=1, n_t=3. Data are mean value +/- STDEV.
  C) Quantification of MN viability in patient derived cultures after 48hrs treatment with various doses of monastrol or ML 141 in 1μM thapsigargin. 3μM kenpaullone or 5μM MAP4K4i in thapsigargin stress were used as positive controls, DMSO vehicle as a negative control. N_b=3, n_t=3. Data are mean value +/- SEM.
Biological replicates (N_b) represent independent MN differentiations, each with technical replicate wells (n_t).

Looking at the remaining results from the inhibitor tests, we observed that specific inhibitors to either GSK3β (CHIR-99021) or CDKs (roscovitine) failed to demonstrate a survival phenotype comparable to the dual inhibition of GSK3β and CDKs by 1-azakenpuallone (Figure 4.7C), corroborating the conclusions made by Reinhardt et al. that both kinases must be inactivated to confer MN protection[420]. Moreover, modulators of metabolic processes, particularly lipid and cholesterol metabolism (such as with the HGM-CoA reductase inhibitor simvastatin, the acetyl coA synthetase inhibitor ACSS2i, the ornithine decarboxylase inhibitor eflornithine, or the stearoyl coA desaturase inhibitor MK-8245) were also inefficient at maintaining MN viability (Figure 4.7A). Similarly, treatment with receptor agonists or antagonists (such as the GABA agonist gabapentin, the GABA antagonist +-Bicuculline, or the TNFα receptor antagonist R-7050) additionally showed minimal MN survival effects (Figure 4.7B) as did treatment with mTOR signaling pathway inhibitors (torin 1, torin 2, or LY2584702 tosylate), the Pim1 inhibitor and the ATM inhibitor. These data cumulatively suggest that either sub-optimal concentrations of these compounds were used in these tests to visualize a protective effect or that the dysregulation of these processes identified in the proteomics data sets were consequences, rather than causal drivers, of MN protection.

Figure 4.7. Targeting lipid and cholesterol metabolism or extracellular receptors do not robustly protect MN viability in proteostatic stress.

    A/B) Quantification of MN viability in patient derived cultures after 48hrs treatment with various doses of small molecule inhibitors in 1μM thapsigargin. 3μM kenpaullone or 5μM MAP4K4i in thapsigargin stress were used as positive controls, DMSO vehicle as a negative control. N_b=3, n_t=3. Data are mean value +/- SEM.

    C) Quantification of MN viability in patient derived cultures after 48hrs treatment with indicated doses of small molecule inhibitors in 1μM thapsigargin. 3μM kenpaullone or 5μM MAP4K4i in thapsigargin stress were used as positive controls, DMSO vehicle as a negative control. N_b=2, n_t=2. Data are mean value +/- STDEV.

Biological replicates (N_b) represent independent MN differentiations, each with technical replicate wells (n_t).

A)

Simvastatin
HGM-CoA Reductase
Inhibitor

ACSS2i
Acetyl-CoA Synthetase 2
Inhibitor

Eflornithine
Ornithine Decarboxylase
Inhibitor

MK-8245
Stearoyl-CoA Desaturase
Inhibitor

B)

Gabapentin
GABA agonist

(+)-Bicuculline
GABA Antagonist

R-7050
TNFα Receptor
Antagonist

C)

Additional Compounds Tested
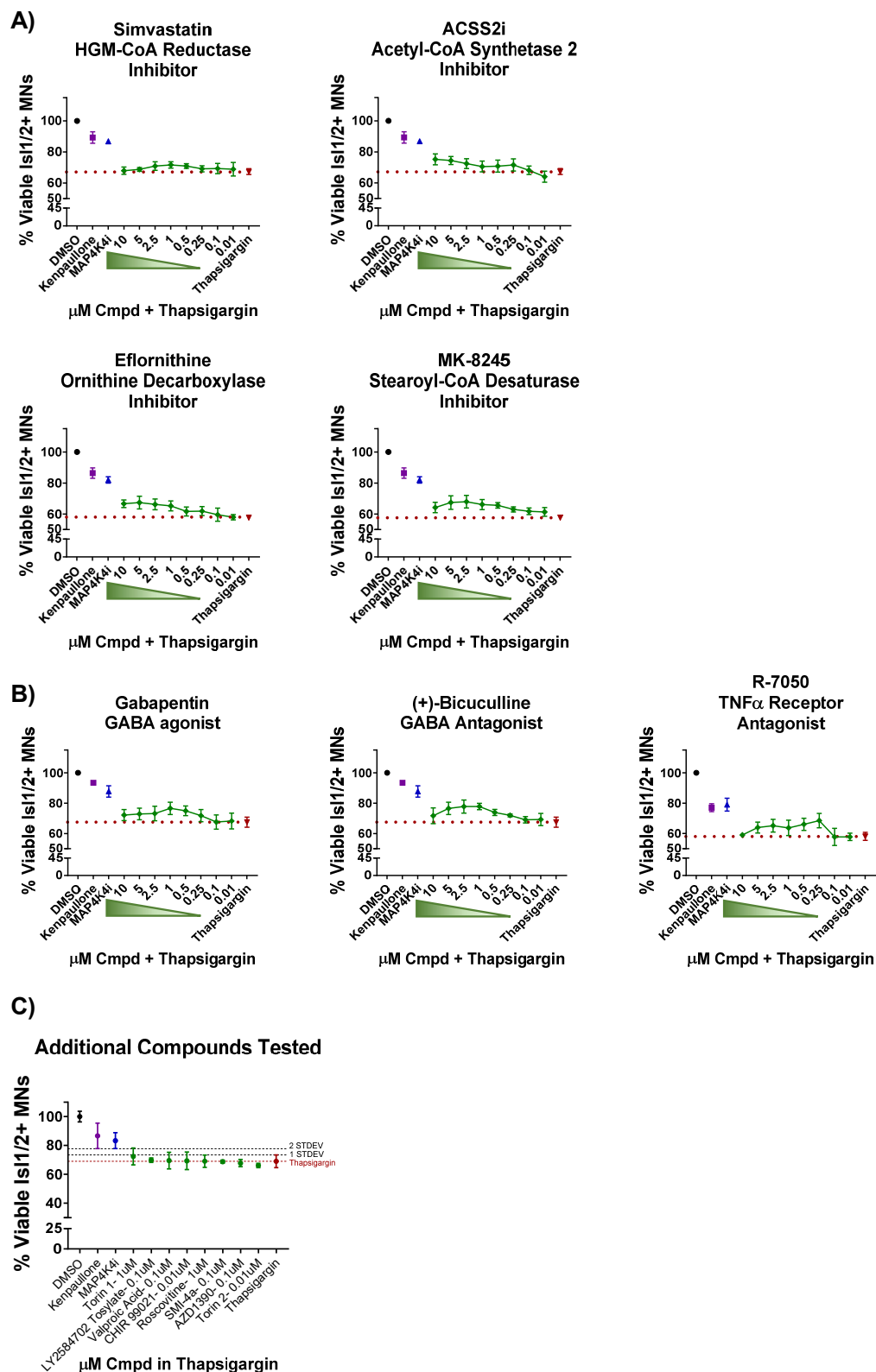
4.3.3 Hit compounds are active against multiple proteotoxic stressors.

Our ultimate goal from these studies was to identify common cellular pathways underlying kenpaullone and MAP4K4 inhibitor 29 protection, and to discover new neuroprotective drugs targeting these convergent points. To be truly effective neuroprotective agents, it was important to confirm all 5 protective hit compounds identified from the proteomics-informed inhibitor tests were also effective against other stressor models. To do this, we tested the 5 neuroprotective compounds- the JNK inhibitor SP600125, the GSK3β/CDK inhibitor 1-azakenpaullone, the HDAC inhibitor tubastatin A, the PKC inhibitor enzastaurin, and the B-RAF inhibitor GDC-0879 for their ability to protect against tunicamycin stress. 3 concentrations were tested for each compound based on the efficacy range determined from the proteomics-inhibitor tests (1μM-5μM), each in the presence of 1μM of tunicamycin. Similar to the protective effect observed with these compounds in thapsigargin stress, we found that the JNK inhibitor SP600125, the GSK3β/CDK inhibitor 1-azakenpaullone, the PKC inhibitor enzastaurin, and the B-RAF inhibitor GDC-0879 all significantly protected MN numbers and neuritic morphologic parameters in the presence of tunicamycin stress (Figure 4.8A-B). The HDAC/microtubule acetylation inhibitor tubastatin A was significant at one concentration, but overall not as effective in these tests, favoring instead JNK, GSK3β/CDK, PKC, and B-RAF in MN protection. These data ultimately demonstrate the power of proteomics to inform effective drug selection for neuroprotective screening assays and the utility of the proteostatic-stressor assays to identify novel MN protective drugs. We propose that future experiments using specific RNA interference-based assays validating these protective targets, as well as experiments ensuring these compounds protect against additional models of ALS will yield important further information into the mechanisms underlying proteotoxic induced degeneration and ALS MN protection.
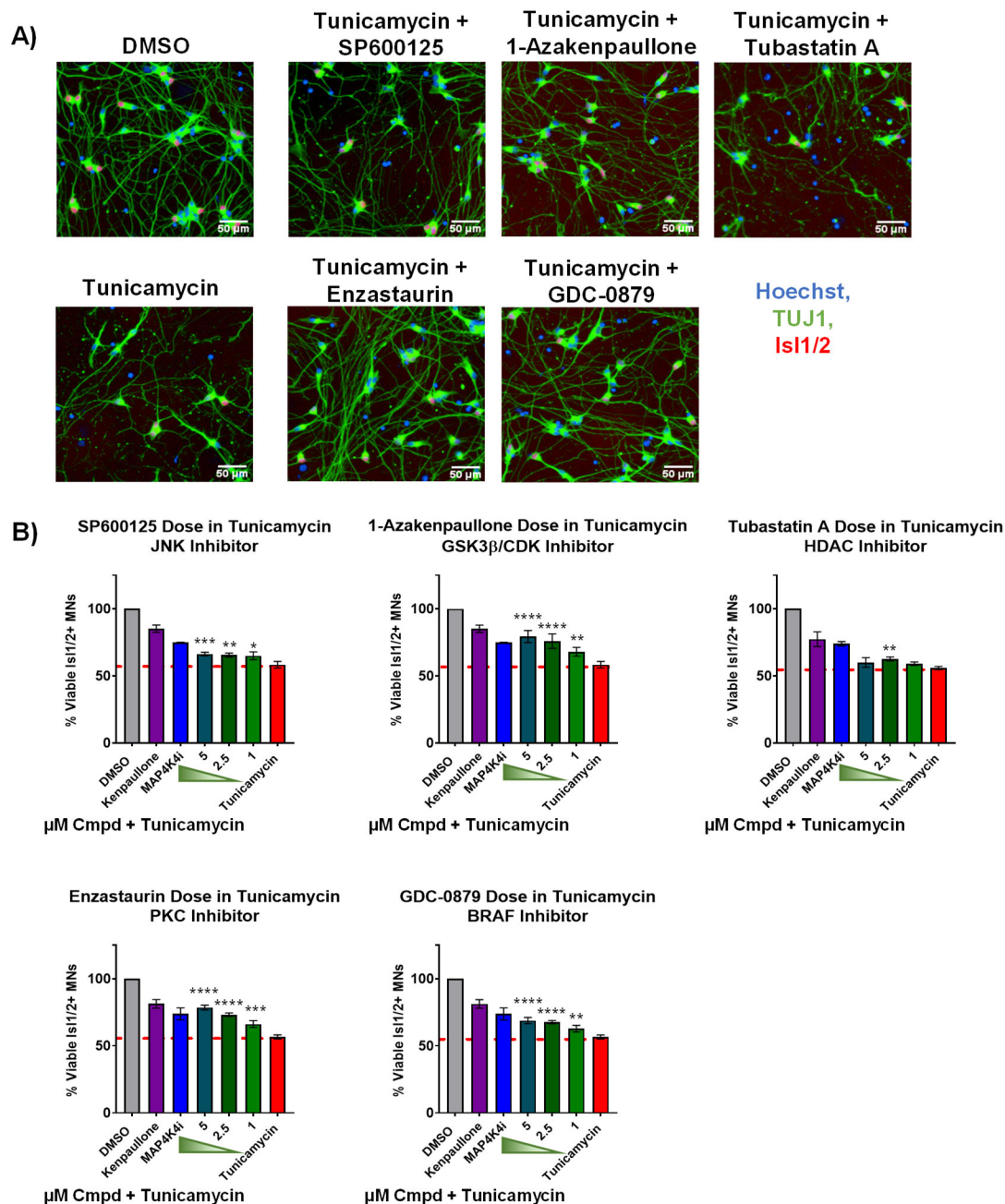
Figure 4.8. Small molecule inhibitors to GSK3β, JNK, PKC, and B-RAF are protective against multiple proteotoxic stressors.

A) Representative immunofluorescent images of patient derived MN cultures treated with control vehicle (DMSO), 1μM tunicamycin, or 1μM tunicamycin with 5μM small molecule-inhibitors.

B) Quantification of MN viability in patient derived cultures after 48hrs treatment with various doses of small molecule inhibitors in 1μM tunicamycin. 3μM kenpaullone or 5μM MAP4K4i in tunicamycin stress were used as positive controls, DMSO vehicle as a negative control. N_b=3, n_t=3, $p < 0.05*$, $<0.01**$, $<0.001***$, $<0.0001****$ one-way ANOVA with Tukey's hsd post-hoc test.

Biological replicates (N_b) represent independent MN differentiations, each with technical replicate wells (n_t). Data are mean value +/- SEM.

4.4 Conclusions and Discussion

In this study, we used global phosphoproteomic remodeling analyses to identify the molecular pathways in common between MN protective agents and performed a series of small molecule inhibitor tests to discover novel MN protective compounds targeting these pathways. We confirmed that GSK3β, CDKs, and the downstream effectors of MAP4K4, JNK and cJUN, were decreased with the MN protective agents kenpaullone and MAP4K4 inhibitor 29, and that pharmacological reduction of these signaling pathways was protective. Importantly, we discovered that protein kinase family members and RAFs were also significantly dysregulated with kenpaullone and MAP4K4 inhibitor 29, and identified enzastaurin, a PKC inhibitor, and GDC-0879, a B-RAF inhibitor, as novel MN protective agents. These results ultimately demonstrate the power of proteomics to uncover functional cellular players driving MN protection and the value of the proteostatic stress assays for neuroprotective drug discovery.

4.4.1 Molecular pathways of MN protection

The development of new neuroprotective drugs depends on the successful identification of cellular pathways conferring MN protection. In this study, several molecular players were implicated in pharmacological MN protection. These include GSK3β as well as CDKs, whose inhibition have previously been reported to be protective in various neurodegenerative models[360,420,428–432,434]. Our data showing that the GSK3β and CDK inhibitors kenpaullone and 1-azakenpaullone preserve MN viability in the presence of exogenously added proteostatic stressors add support to this neuroprotective phenomenon. Moreover, corroborative results from our group, as well as from Reinhardt et al., using specific RNAi-mediated depletion of GSK3β and CDK5 have further demonstrated that the protective activity conferred by the dual inhibition of these proteins exceeds those conferred by the singular suppression of either GSK3β or CDKs alone[360,420]. Together, these data suggest that the specific inactivation of both kinases is critical for the highest degree of MN protection. The mechanism through which GSK3β and CDK inhibition confers MN protection is likely multifaceted and complex, but may include the reduction in aberrant hyperphosphorylation of microtubule proteins (such as microtubule associated proteins MAP1B and MAPT (Tau), the microtubule plus-end tracking protein CLASP2, and the microtubule assembly protein DPYSL2 identified in the kenpaullone phosphoproteomic dataset and absent from MAP4K4 inhibitor samples), as well as the reduction of various pro-apoptotic signals (including activated caspase 3) to name just a few mechanisms (Figure 4.9)[420,430,432,453].
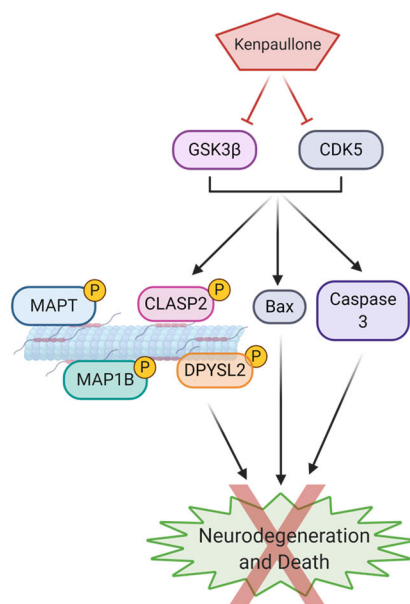
Figure 4.9. GSK3β and CDK inhibition in MN survival.
    Treatment with kenpaullone, a multi-kinase inhibitor, protects human MNs from degeneration. Our phosphoproteomic data suggest that part of this protection may be mediated by the dual inhibition of GSK3β and CDKs, which prevents the aberrant hyperphosphorylation of microtubule associated proteins and/or reduces pro-apoptotic signals.

In addition to GSK3β or CDKs, the Jun N-terminal kinase (JNK)/c-Jun pathway was another signaling

cascade implicated in patient MN survival. In conditions of cellular stress, including aberrant disease states, trophic

factor withdrawal, and ER stress, JNK is activated, resulting in the phosphorylation of the transcription factor c-JUN

to drive neuronal apoptosis[445,454]. The attenuation of this pro-apoptotic signaling, either by the specific reduction of

JNK or c-JUN is sufficient to preserve neuronal viability[400,445,454,455]. Our results utilizing a specific JNK inhibitor

SP600125 corroborate this protective activity in patient MNs (Figure 4.10). Moreover, MAP4K4 is an upstream

signaling molecule to JNK. In a series of kinase activations, MAP4K4 activates TAK1, which subsequently

activates MKK4/MKK7, which then activates JNK/cJUN[456]. The inhibition of MAP4K4 thus decreases the levels of

activated JNK and c-JUN to promote ALS patient MN survival, as shown for the first time in this thesis using small

molecule inhibitors to MAP4K4 and JNK, as well as demonstrated in our most recent publication using specific

RNA interference to MAP4K4, JNK, and c-JUN (Figure 4.10)[400]. The robust MN protective capabilities achieved by

MAP4K4 inhibition were also notably better than the current FDA approved drugs for ALS, raising the possibility

that targeting MAP4K4 may be a viable therapeutic option to pursue for new ALS treatments. In line with this

promising notion, multiple groups are now developing and optimizing additional small molecule inhibitors to

MAP4K4 for improved CNS penetration and pharmacodynamic parameters[425]. It will be exciting to see how these novel inhibitors fare in additional ALS models and ultimately, in ALS patients.
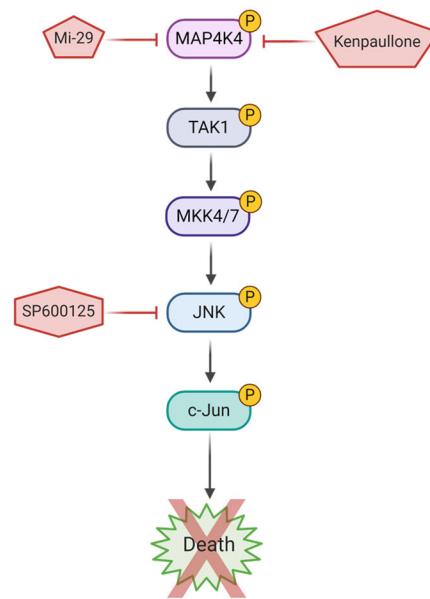
Figure 4.10. MAP4K4 and JNK inhibition in MN survival.
Attenuation of the upstream MAP kinase MAP4K4 or the downstream Jun-N-Terminal Kinase (JNK) confer MN protection, shown in this thesis using pharmacological inhibitors MAP4K4 inhibitor 29 (Mi-29) and SP600125, and demonstrated in our recent publication using siRNA and shRNA mediated reduction of MAP4K4, JNK, and c-JUN[400].

The reduction of MAP4K4 signaling is significantly protective- yet how MAP4K4 is being activated in the first place under stress conditions remains unclear. Inferences from model systems and homologous MAPKs provide some clues, suggesting that TNFα receptor activation and/or interaction with GTPases may be potential ways in which MAP4K4 is activated[457,458]. While a dysregulation in TNFα signaling was not specifically observed in our proteomics dataset, our initial analyses did corroborate the possibility that a secreted, ligand-activated extracellular receptor may be an upstream effector initiating the intracellular MAP4K4/JNK/cJUN cascade. Specifically, the netrin receptor UNC5B was one of the most significantly upregulated proteins in stress conditions, as well as the exported death associated molecule HMGB1. Both of these proteins have already been well linked with cell-death pathways, with UNC5B stimulating neuronal apoptosis in the absence of its ligand netrin 1[459,460], and HMGB1 acting as a danger associated molecular pattern molecule to trigger neuroinflammatory responses[461]. It may thus be worthwhile further investigating how these proteins are involved in ER stress-induced MN death and the protection by MAP4K4 inhibition. Ultimately, delineating the upstream effectors of MAP4K4 will not only expand our basic understanding of how MNs respond to stress but may also have therapeutic implications if they can be targeted to

decrease MAP4K4 signaling. Moreover, both JNK and c-JUN are activated quickly in response to ER stress and trophic factor withdrawal (~2-4hours, data not shown). Going forward, it will also be important to understand the time course of both MAP4K4 and JNK/cJUN activation after stress induction to better delineate a working model of how the MAP4/JNK signaling cascades are cooperating.

Protein kinase C (PKC) was another target implicated in MN protection conferred by kenpaullone and the MAP4K4 inhibitor 29. PKC is a complex enzyme with several different isoforms serving multiple, context-dependent cellular functions[447]. PKC activation[449] as well as inhibition[417,448] have both previously been reported to be protective in neuronal cultures. Our work here demonstrates for the first time that enzastaurin, a small molecule inhibitor of PKCβ, can robustly protect against thapsigargin and tunicamycin induced MN degeneration, with protection levels comparable to those of the MAP4K4 inhibitor. These data are particularly exciting since enzastaurin has already been determined in multiple phase I/II clinical trials to be well tolerated in cancer patients[437,439]. It may therefore be worthwhile determining if enzastaurin works well to preserve MN function in animal models of ALS and in ALS patients, in addition to the efforts focused on MAP4K4 inhibitors. Moreover, it will be important to better define the mechanism of how enzastaurin is conferring MN protection. The specificity of PKC as a singular target of enzastaurin mediating patient MN survival should be evaluated first and confirmed using specific RNAi-based reduction of PKC isoforms. Interrogations of how PKC inhibition then confers MN survival will also be important. Previous data from rat cerebellar granule cell neurons in low potassium conditions have demonstrated that the activation of the AKT pro-survival pathway by PKC inhibition can mediate neuronal survival[448]. This mechanism may additionally be occurring in ALS MNs protected with enzastaurin and will be interesting to further pursue with specific PKC depletion and immunoblotting assays (Figure 4.11).
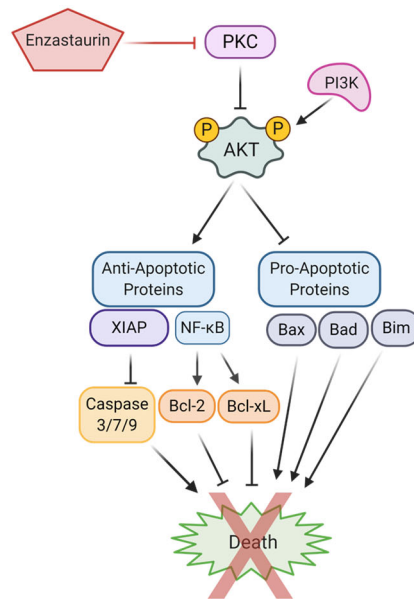
Figure 4.11. PKC inhibition in MN survival.
Enzastaurin, a PKC inhibitor, promotes MN survival in conditions of proteostatic stress. The mechanism through which enzastaurin confers MN survival may be through the restoration of AKT signaling, which suppresses pro-apoptotic proteins and increases anti-apoptotic proteins. Specific reduction of PKC isoforms with RNAi and immunoblotting of pathway reactivation will be needed to further evaluate this target and mechanism.

Finally, B-RAF was also significantly implicated in MN protection from our experiments. B-RAF is a proto-oncogene in the RAS-RAF-MEK-ERK pathway that is aberrantly activated in a broad range of cancers[462]. Previous data using embryonic MNs and sensory neurons have also reported an essential role for B-RAF in cellular survival in response to neurotrophic factors, with the deletion of B-RAF resulting in the failure of explanted neurons to survive in culture[450]. It was thus intriguing to us that a specific inhibitor to B-RAF would promote MN survival as it did here. As it turns out, compound inhibitors to B-RAF, like GDC-087 target the mutated form of B-RAF$^{V600E/K}$ present in cancers. Yet, these inhibitors actually display paradoxical activation of the MEK/ERK pro-survival pathway in cells with B-RAF^{WT} due to RAF transactivation and priming[463]. Recent work using B-RAF inhibitors in non-mutated kidney podocytes or SH-SY5Y neuronal-like cells have confirmed this pro-survival effect and attributed this to the reactivation of ERK to inhibit JNK activation and cell death[464,465]. Our data here, showing for the first time that the B-RAF inhibitor GDC-0879 is protective in patient MNs challenged with proteostatic stressors, supports this pro-survival role (Figure 4.12).
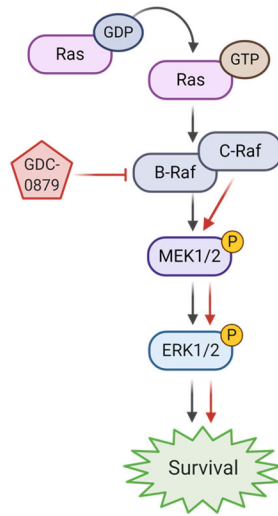
Figure 4.12. B-RAF inhibition in MN survival.
        The B-RAF inhibitor GDC-0879 preserves MN viability in conditions of proteostatic stress. We hypothesize GDC-0879 may promote MN protection by the paradoxical activation of MEK1/2 and ERK1/2. This remains to be experimentally tested with immunoblotting of pathway activation and specific RNAi mediated kinase inhibition.

Going forward, it will be critical to confirm the restored activation of the MAPK/ERK pro-survival signaling pathway in MNs treated with GDC-0879, as well as demonstrate the specificity of B-RAF as a neuroprotective target, using specific si/shRNA approaches and other, more specific RAF inhibitors. These experiments will ultimately further delineate the molecular players involved in MN protection. Notably, since GDC-0879 is already in clinical development for oncologic indications[440], following target specificity and mechanistic experiments, we propose that the repurposing of this drug might also be another viable avenue to pursue in ALS animal models and, potentially, clinical trials.

Chapter 5

Discussion

5.1 Summary of Dissertation

Throughout this dissertation, we aimed to understand how exogenous proteostatic stressors influence differential ALS patient derived MN vulnerabilities and to identify novel compounds that protect against these vulnerabilities. In Chapter 2, we demonstrated that proteostatic stressors targeting the endoplasmic reticulum (ER) were preferentially toxic to MNs compared to non-MNs, in both healthy and ALS patient MN cultures, without inducing insoluble proteins. In contrast, proteasomal stress induced insoluble TDP-43 and ubiquitin, yet did not uniformly initiate selective MN toxicities. These studies indicated, for the first time, a fundamental vulnerability of iPSC-derived MNs to ER stress, with a distinctly different susceptibility to proteasome inhibition. These experiments additionally defined precise assay parameters to potentiate ALS MN degeneration in a robust, scalable, and temporally synchronous manner.

In Chapter 3, we extended this work and demonstrated that our assays of proteostatic stress in ALS patient MNs could accurately predict and identify compounds with neuroprotective potential. We demonstrated that kenpaullone, a well-established MN protective agent, was able to significantly preserve both SOD1 and TDP-43 ALS patient MN viability in all proteostatic stressor conditions. This rescue effect was substantially greater than the effect of the 2 current FDA approved drugs for ALS, Riluzole or Edaravone, which both failed to protect MN numbers or healthy neurites. We further demonstrated, for the first time, that a small molecule inhibitor to one of kenpaullone's targets, MAP4K4, was also able to preserve ALS patient MN viability in all conditions of proteostatic stress. As with kenpaullone, this protection consisted of maintained neuritic morphology and was independent of a direct reduction in the unfolded protein response (UPR) induction or insoluble protein buildup. These experiments conclusively separated the role of insoluble protein aggregates in selective MN death, with MN survival occurring without their reduction, and selective MN death occurring without their production. These studies also substantiated the ability of the proteostatic stressor assays to identify neuroprotective agents.

Finally, in Chapter 4, in collaboration with both Dr. Alban Ordureau and Kris Holton, we used global phosphoproteomic remodeling analyses to identify the molecular targets in common between the MN protective agents kenpaullone and MAP4K4 inhibitor 29, and performed a series of small molecule inhibitor tests to discover novel MN protective compounds. We confirmed that GSK3β, CDKs, and the downstream effectors of MAP4K4, JNK and cJUN, had decreased activity with the MN protective agents kenpaullone and MAP4K4 inhibitor 29, and that pharmacological reduction of these signaling pathways was protective. Importantly, we discovered that protein

kinase family members and RAFs also had significantly decreased activity with kenpaullone and MAP4K4 inhibitor 29, and identified enzastaurin, a PKC inhibitor, and GDC-0879, a B-RAF inhibitor, as novel MN protective agents. These results demonstrate the power of proteomics to uncover functional cellular players driving MN protection and the value of modulating proteostatic stress in patient cells for novel neuroprotective drug discovery.

5.2 Working model of proteostatic stress induced MN degeneration and mechanisms of pharmacological protection

Overall, the data presented in this thesis support the following models of MN degeneration in proteostatic stress conditions and mechanisms of pharmacological protection:

(1)   Proteotoxic stressors differentially affect ALS patient MNs. ER stress (such as with thapsigargin or tunicamycin) quickly induces an unfolded protein response (UPR) that drives an active form of apoptotic death preferentially in MNs. Insoluble proteins are not detected in these stress conditions, yet MNs from healthy patients, as well as ALS patients, are uniformly more vulnerable to ER stress compared to non-MN cell types in the culture (Figure 5.1A). In contrast, proteasome inhibition with MG132 increases the levels of ALS characteristic insoluble TDP-43 and ubiquitin yet does not uniformly induce selective MN toxicity (Figure 5.1A). MNs are, therefore, not inherently more vulnerable to proteasomal inhibition than are non-MN cell types, but rather fALS mutant backgrounds, intrinsic health defects, or confounding genetic factors contribute to selective MN degeneration.

(2)   ALS patient MNs undergoing proteostatic stress-induced degeneration can be protected by small molecule inhibitors to several key signaling proteins (Figure 5.1). Kenpaullone, an inhibitor of MAP4K4, GSK3β, and CDKs, prevents MN degeneration without directly blocking UPR induction or the production of insoluble TDP-43 and ubiquitinated proteins (Figure 5.1A-B). These data, along with the data that the ER stressors do not drive detectable aggregates, separates insoluble proteins from MN death. Kenpaullone's protection can be attributed in part to the dual inhibition of GSK3β and CDKs, which reduces the aberrant hyperphosphorylation of microtubule proteins (including Tau, the microtubule plus-end tracking protein CLASP2, the neuronal guidance microtubule assembly protein DPYSL2, and the microtubule associated proteins MAP1B and MAPT), and reduces various pro-apoptotic signals and effectors (including activated caspase 3)(Figure 5.1B). However, the inhibition of MAP4K4-JNK/cJUN signaling is likely the strongest pro-survival target underling kenpaullone's activities. Pharmacological inhibition of MAP4K4 (MAP4K4 inhibitor 29, Mi-29) or JNK (SP600125) protects ALS patient MNs undergoing

proteotoxic degeneration, and more specific reduction of MAP4K4, JNK, or cJUN with RNA interference methods additionally protects ALS patient MNs from trophic factor withdrawal induced degeneration (Figure 5.1B)[456]. What remains unclear is how MAP4K4 is being activated in stress conditions in the first place such that its inhibition is protective. Indications from our proteomics analyses suggest that an exported ligand may be activating an extracellular receptor, but these upstream effectors remain to be identified and experimentally validated.

Furthermore, phosphoproteomic analyses indicated that PKC and RAF were additional signaling points shared between kenpaullone and MAP4K4 inhibitor 29. Small molecule inhibitors targeting these points, namely enzastaurin (PKC) and GDC-0879 (RAF), also preserved MN viability (Figure 5.1B). While the specificity of PKC and RAF as neuroprotective targets remains to be confirmed with specific RNAi experiments, along with the mechanisms through which each compound is working, we hypothesize that PKC inhibition with enzastaurin may mediate neuronal survival through the activation of the AKT pro-survival pathway[448] and that the B-RAF inhibitor GDC-0879 preserves MN viability through the paradoxical activation of the MEK/ERK pro-survival pathway[463]. Both mechanistic experiments, as well as target validation experiments, are ongoing.

Figure 5.1. Model of proteostatic stress induced MN degeneration and pharmacological protection.

A) Endoplasmic reticulum stress (ER stress) uniformly causes preferential MN degeneration compared to non-MNs in patient derived cultures, driving an UPR and apoptotic death, without the production of insoluble aggregates. In contrast, proteasomal inhibition induces insoluble proteins, but does not universally drive MN-selective degeneration. Different genetic backgrounds or pre-existing cellular deficits drive MN-selective degeneration with proteasomal inhibition. Neuroprotective compounds kenpaullone and MAP4K4 inhibitor 29 preserve MN survival without blocking UPR induction or reducing insoluble aggregates.

B) Various small molecule inhibitors protect against MN degeneration induced by proteostatic stress. (1) Kenpaullone mediates MN protection through the inhibition of GSK3β and CDKs to reduce the aberrant hyperphosphorylation of microtubule associated proteins, as well as the inhibition of MAP4K4. (2) MAP4K4 inhibition by kenpaullone or MAP4K4 inhibitor 29 promotes MN protection by attenuating the pro-apoptotic JNK/cJUN pathway. How MAP4K4 is activated in degenerative conditions is still unclear, but we hypothesize an exported ligand and/or an extracellular receptor mediated pathway is involved. PKC and B-RAF are additional proteins dysregulated by the protective agents kenpaullone and MAP4K4 inhibitor 29 that were identified by phosphoproteomic analyses. (3) A PKC inhibitor enzastaurin also promotes MN protection, potentially through the activation of AKT, and (4) a B-RAF inhibitor GDC-0879 promotes MN protection, potentially through the activation of ERK1/2 signaling.

A)

Age-related cellular dysfunctions, environmental exposures

Genetics

ER STRESS

UPR

Proteasome Inhibition

Insoluble Protein Aggregates

Selective MN Death

Neuroprotective Compounds (Kenpaullone and MAP4K4 Inhibitor 29)

B)

Motor Neuron Protected with Neuroprotective Compounds

HMGB1   **?**   UNC5B

NT/Trk

Kenpaullone

MAP4K4

Mi-29

(3) Reduction of PKC signaling by Enzastaurin blocks MN degeneration, potentially through the activation of AKT to reduce levels of pro-apoptotic proteins.

Ras GDP

Ras GTP

(4) Targeting BRAF with GDC-0879 protects MN viability, potentially via the paradoxical activation of ERK1/2, which reduces pro-apoptotic proteins and enhances pro-survival proteins.

GSK3β   CDK5

TAK1

MKK4/7

Enzastaurin   PKC

GDC-0879   B-Raf   C-Raf

MEK1/2

Neuritic Damage MN Degeneration

SP600125   JNK

AKT

ERK1/2

MAPT   CLASP2

MAP1B   DPYSL2

(2) Inhibition of the MAP4K4-JNK pathway by kenpaullone, MAP4K4 inhibitor 29, or SP600125 suppresses cJUN-mediated apoptosis.

c-Jun

Pro-Apoptotic Proteins

Bad

Caspases   Bax   Bim

(1) Kenpaullone blocks GSK3β and CDK5 mediated hyperphosphorylation of microtubule proteins, reducing neuritic damage and MN degeneration.

5.3 Overcoming limitations in iPSC-based ALS MN models of proteostatic stress

This thesis described the development of 3 iPSC-based models of ALS MN degeneration using mechanistically distinct proteostatic stressors. This work shed light on the mechanisms underlying differential MN vulnerability in patient cells and importantly allowed for the identification of several novel neuroprotective compounds. However, several challenges remain from these studies, which, if addressed, may improve our understanding of ALS disease mechanisms, and may facilitate the development of novel ALS treatments.

5.3.1 Improving differential vulnerability studies with expanded cell-type classifications and measurements

MNs in the spinal cord and brain are preferentially damaged in ALS, while other neurons and cell types in the central nervous system are less affected. Work in this thesis has demonstrated, using an established MN differentiation protocol, that $Isl1/2^+TUJ1^+$ MN populations are universally more vulnerable to ER stressors compared to the heterogeneous non-MN populations remaining in the culture, comprised of "ALS-resistant" $Chx10^+$ spinal interneurons and astroglia. These findings were reproduced with various different patient lines and culture conditions, and were consistent with findings in hESC-based MNs[417] and ALS animal models[109] suggesting that an enhanced response to ER stress underlies differential MN vulnerability in ALS. However, the incorporation of additional MN and non-MN markers in our heterogeneous MN cultures would further improve our understanding of the mechanisms underlying these differential vulnerabilities in disease. As an example, the transcription factor Hb9 (MNX1) is another predominately MN specific marker, in addition to Isl1/2 used in this study[334]. While issues of antibody non-specificity precluded our ability to interrogate a $Hb9^+$ neuronal population in this study, patient MN cultures retaining an fluorescent reporter of Hb9 expression could be used to allow for an improved quantification of how different MN subtypes ($Hb9^+$, $Hb9^+/Isl1/2^+$) are affected by each stressor. We could also further separate the bulk "non-MN" populations in our study and individually measure the effect of each stressor on singular non-MN populations such as the $Chx10^+$ spinal interneurons. Single cell analysis of immunostained cultures could again be used for these experiments, or alternatively, single-cell RNA sequencing of MN cultures treated with or without each stressor could be used to massively inform the cell-type-specific effects of these toxicants.

5.3.2 Deconvoluting non-cell-autonomous effects and creating a "motor unit"

MNs are preferentially damaged in ALS through both cell-autonomous mechanisms and non-cell-autonomous mechanisms mediated by additional cell types residing in the brain and spinal cord, such as microglia, interneurons, and astrocytes. In our study, we assumed the heterogeneous MN cultures to be broadly reflective of the spinal cord niche with the inclusion of the relevant cell types, MNs, spinal interneurons and astroglia, and we reasoned a single cell quantification of individual cell type responses would best reflect the pathological events contributing to ALS disease progression. However, it is possible that the non-MN cell types in our MN culture, for example the Chx10$^+$ spinal interneurons and astroglia, may not accurately represent these spinal cord cell types and we further cannot distinguish between cell-autonomous effects and non-cell-autonomous effects of each stressor. Various groups have addressed these potential confounding issues by using purified, single neuronal populations, most often isolated by magnetic-activated cell sorting (MACs) based on neuronal surface markers (p75NTR or NCAM for example) or fluorescence-activated cell sorting (FACs) based on a fluorescent reporter marking the expression of a lineage-specific transcription factor (such as Hb9)[345,360,400,417]. We propose that in addition to adding further immunological staining profiles in our heterogeneous cultures, that we also compare the proteostatic degeneration of a pure patient MN culture to the effects on a pure cortical neuronal culture, or a dopaminergic neuronal culture. Both experiments would further our understanding of the differential cell type sensitivities in ALS and their cell-autonomous behaviors to proteostatic stressors.

Moreover, each purified neuronal population could also be co-cultured together or treated with conditioned media from these other isolated cell types to further deconvolute the non-cell-autonomous effects. These techniques have perhaps been most widely used with MN and astrocyte cultures, demonstrating that astrocytes with ALS mutations can drive MN degeneration, even degeneration of MNs without an ALS mutation, and that this cell non-autonomous degenerative effect is mediated by soluble secreted factors[403,466–468]. It may be worthwhile to pursue such investigations here with various combinations of pure single cultures, co-cultures, and conditioned media experiments to demonstrate both the cell-autonomous effects of proteostatic stressors on purified cell types and the non-cell-autonomous effects of different cell types. We expect that our results demonstrating that MNs are preferentially vulnerable to ER stress would stand, consistent with the recent publication by Thams and colleagues demonstrating that cyclopiazonic acid, an ER stressor with a homologous mechanism of action to thapsigargin used here, was preferentially toxic to hESC-derived MNs compared to the heterogeneous non-MN cells in the culture

(comparable to our technique used here) as well as to separately differentiated dorsal spinal inhibitory interneurons[417].

Perhaps most exciting, advances in biomedical engineering have recently enabled the development of physiologically representative microfluidic based devices, where each purified cell type is localized to a unique chamber to constitute a "motor circuit in a dish". Osaki and colleagues reported a 3D model of ALS by culturing skeletal muscle fibers in one microfluidic chamber and iPSC-derived, optogenetic MN spheroids in another[469]. The MNs appropriately extended axons and formed functional neuromuscular junctions on the muscle fiber bundles such that the muscle could contract when the MNs were optogenetically stimulated with light. ALS MNs notably had increased degeneration, fewer muscle contractions, and muscle apoptosis. It may be interesting to see how ALS MNs are affected if only the skeletal muscle fibers are treated with proteostatic stressors or vice versa. Furthermore, work by Birey and colleagues have demonstrated the functional integration of dorsal and ventral forebrain spheroids to form a microphysiological circuit[470]. It may then be conceivable to assemble a forebrain-MN-muscle fiber unit, to serve as the most accurate physiological model of the human motor unit for neurodevelopmental or degenerative disease studies.

5.3.3 Enhancing genetic representation and preserving epigenetic signatures

This study took advantage of several healthy and ALS patient iPSC lines to address the effects of proteostatic stressors on MN cultures and the protective potential of small molecule inhibitors. While these studies retained the ability to capture genetic components from two SOD1 ALS patients and one TDP-43 patient, these experiments were limited in their detection of the vast genetic diversity that occurs in ALS, as well as the unknown heterogeneity that sporadic forms of ALS encompass. The development of consortia, such as AnswerALS (https://www.answerals.org/), which generates and phenotypically characterizes thousands of ALS patient iPSC lines, will likely lead the way in capturing and recapitulating the genetic diversity represented in the human population. Moreover, in addition to enhancing genetic representation, it will also be important to expand this work with cultures that preserve epigenetic landscapes. While iPSC-derived MN technologies were groundbreaking and opened the door for the first human cellular models of ALS[339], reprogramming to the pluripotent state resets age-related epigenetic hallmarks[471]. Using direct lineage-reprogrammed ALS MN cultures alternatively preserves these signatures, which may be incredibly important for a disease like ALS that retains a high degree of age-related,

environmental, and unknown causes. We believe research into these more age-conserved models as well as the continued efforts of large-scale consortia will improve ALS disease modeling and therapeutic identification.

5.4 Future directions and big picture implications

5.4.1 Testing the protective mechanism of enzastaurin and GDC-0879

In Chapter 4 of this thesis, we demonstrated that PKC and RAF family members were commonly dysregulated with neuroprotective agents, and showed, for the first time, that the PKC inhibitor enzastaurin and the B-RAF inhibitor GDC-0879 could preserve human MN viability in conditions of proteostatic stress. Going forward it will be important to confirm the sufficiency of PKC and B-RAF as neuroprotective targets using specific genetic or RNA interference approaches, as well as define the mechanisms through which these compounds are acting.

Regarding the PKC inhibitor enzastaurin, previous data from rat cerebellar granule cell neurons in low potassium conditions have indicated that pharmacological PKC inhibition can mediate neuronal survival through the restoration of the AKT pro-survival pathway[448]. We hypothesize that this mechanism may also be occurring in human MNs subjected to proteostatic stress protection with enzastaurin. Western blotting for active AKT in protein lysates from MN cultures treated with stressors and enzastaurin will begin to address this mechanism. Additionally, experiments using genetic or selective RNAi mediated reduction of specific PKC isoforms will also be necessary to determine the specificity of this kinase as a neuroprotective target of enzastaurin. If target specificity and mechanism can be ascertained, it may then be worthwhile to determine if enzastaurin works well in animal models of ALS to confer rescue of MN number, muscle function, and survival. Since enzastaurin has already been determined to be well tolerated in cancer patients[437,439], if enzastaurin proves effective in vivo, the repurposing of enzastaurin may be a more readily available treatment option for patients, who have a limited life expectancy and cannot wait the extensive time needed to develop new drugs.

Additionally, the B-RAF inhibitor GDC-0879 was also effective in conferring MN survival. GDC-087 was designed to target the mutated form of B-RAF$^{V600E/K}$ present in certain cancers, yet demonstrates paradoxical activation of the MEK/ERK pro-survival pathway in cells with B-RAF^{WT} due to RAF transactivation and priming[463]. Recent work using B-RAF inhibitors in non-mutated kidney podocytes and SH-SY5Y neuronal-like cells have also confirmed this reactivation of ERK to inhibit JNK-mediated cell death[464,465]. We propose that, in addition to determining the restoration of the AKT pathway with enzastaurin, western blotting confirming the reactivation of

ERK in MNs treated with GDC-0879 will also help delineate the neuroprotective mechanism of this compound. Experiments evaluating other selective RAF inhibitors, as well as genetic and RNAi mediated RAF reduction, will also be important to further understand the sufficiency of this protein in neuroprotection and its potential as a drug target. Notably, since GDC-0879 is already in clinical development for oncologic indications[440], if target specificity and mechanism can be better defined, we propose that the repurposing of this drug might be yet another viable avenue to pursue in ALS animal models and, potentially, clinical trials.

5.4.2 MAP4K4- broad reaching neuroprotective activities and the search for the upstream activator

In Chapter 3 of this thesis, and in our recent publication, we demonstrated for the first time that MAP4K4 inhibition could robustly preserve ALS patient MN viability[400]. These results were truly exciting and raised the possibility that targeting MAP4K4 might be a worthful avenue for new ALS therapeutics. Notably however, MAP4K4 inhibition was protective to MNs broadly, not just to ALS MNs. We demonstrated that MAP4K4 suppression also conferred protection to healthy MNs in proteostatic stress conditions, as well as healthy MNs undergoing even basal levels of death with time in culture[400]. Moreover, Larhammar and coworkers also showed that dorsal root ganglion neurons were protected from nerve growth withdrawal induced degeneration with pharmacological MAP4K4 reduction[424]. These cumulative data suggest that there may be broad reaching implications for MAP4K4 reduction in various pathological contexts, and that MAP4K4 may provide therapeutic benefit for other MN diseases, such as Spinal Muscular Atrophy (SMA). It will therefore be worthwhile pursuing MAP4K4 inhibitors as potential protective agents in other patient derived MN disease models, in addition to ALS. It will also be critical to demonstrate that inhibiting MAP4K4 in vivo confers a similar protective benefit as that seen in vitro. While pharmacodynamic parameters, including CNS penetration, are still being established and optimized for this compound class[425], the robust neuroprotective activity observed in various MN assays leads us to predict that targeting MAP4K4 may confer a delay in neuromuscular function deficits in ALS as well as other MN diseases.

Furthermore, in Chapter 4 of this thesis, we described a comprehensive phosphoproteomic and proteomic dataset that details the singular molecular changes and pathway perturbations that occur, over time, in patient MNs undergoing ER stress-induced degeneration and protection by pharmacological MAP4K4 inhibitors. Extensive interrogations of these datasets using gene ontology analyses, gene set enrichment analyses, and kinase-substrate enrichment analyses have already led to the identification of several neuroprotective targets, in addition to

110

MAP4K4, as well as the discovery of novel neuroprotective compounds. Yet, these data can continue to be explored. A clear next question that remains unaddressed is how MAP4K4 is activated in the first place in response to cellular stressors like thapsigargin. Data from model systems and homologous MAPKs suggest that TNFα receptor activation and/or interaction with GTPases may be potential ways in which MAP4K4 is activated[457,458]. While a dysregulation in TNFα signaling was not specifically observed in our proteomics dataset, our initial analyses did corroborate the possibility that a secreted, ligand-activated extracellular receptor may be initiating the intracellular MAP4K4/JNK/cJUN cascade. Specifically, the netrin receptor UNC5B was one of the most significantly upregulated proteins in stress conditions, as well as the exported death associated molecule HMGB1. Both of these proteins have already been well linked with cell-death pathways, with UNC5B stimulating neuronal apoptosis in the absence of its ligand netrin 1[459,460], and HMGB1 acting as a danger associated molecular pattern molecule to trigger neuroinflammatory responses[461]. It may thus be worthwhile further investigating how these proteins are involved in ER stress-induced MN death and the protection by MAP4K4 inhibition. Specifically, we propose testing whether supplementation with netrin 1 reduces activated MAP4K4 in stress conditions and whether this protects MNs, as well as whether depletion of extracellular HMGB1 with a targeting antibody reduces MAP4K4 activation and MN death. Ultimately, delineating the upstream effector of MAP4K4 will not only expand our basic understanding of how MNs respond to stress but may also have therapeutic implications if it can be targeted to decrease MAP4K4 signaling.

5.4.3 The role of insoluble proteins in MN death and implications for therapeutics

In Chapter 3 of this thesis, we demonstrated that pharmacological inhibition of MAP4K4 protected MNs from death, without reducing the levels of insoluble TDP-43 and ubiquitin. In Chapter 2 of this thesis, we additionally demonstrated that the ER stressors thapsigargin and tunicamycin caused selective MN death, without inducing insoluble proteins or aggresomes. These data are the first, to our knowledge, to conclusively separate insoluble protein aggregation from preferential MN death in iPSC-derived cells, with selective MN death without insoluble aggregates, and MN survival possible even with insoluble aggregates (Figure 5.1A). While the accelerated nature of these assays may lack the resolution to detect small, but potentially meaningful, changes in protein aggregation, these data nonetheless highlight that other cellular initiators, such as early misfolding and ER stress, are

critical drivers of selective neuronal degeneration, and importantly demonstrate that attenuating the insoluble proteins themselves may not be necessary for potential therapeutic compounds.

Indeed, there is precedent for this premise. ALS-linked mutations in TDP-43 can give rise to adult-onset motor neuron disease in mice, without the apparent cytosolic aggregation of TDP-43[185], demonstrating that insoluble TDP-43 is not a requirement for disease. Moreover, inclusion body formation, rather than being necessary and causal of disease, may in fact be protective. In perhaps one of the first demonstrations of this, Arrasate et al. used longitudinal live cell imaging to show that inclusion body formation of aggregated huntingtin actually improved neuronal survival, functioning as a cellular protective mechanism to sequester the more toxic diffuse mutant entity[435]. Recent work by Bolognesi et al. has further corroborated this notion as it relates to ALS, investigating >50,000 mutations in the prion-like domain of TDP-43 to demonstrate that mutations increasing hydrophobicity and aggregation actually decrease toxicity in yeast[472]. These data thus point to the conclusion that insoluble protein accumulation is not a necessary component for selective neuronal death in neurodegenerative disease, and that these aggregates rather are serving a protective role, titrating out a more toxic, soluble form.

This has important implications for therapeutics. Particularly, approaches to exclusively eliminate insoluble aggregates may not have the desired effect to delay disease progression. Effectively neutralizing soluble forms of aggregation-prone proteins may be necessary for effective clinical trial outcomes in ALS and other neurodegenerative disorders displaying uniquely aggregated proteins. We propose this be done either with antibody-based methods that target both soluble monomeric and oligomeric forms, or with antisense oligonucleotide (ASO) mediated approaches that are upstream to protein production.

5.4.4 The utility of modulating stressor points- cell-type vulnerability studies and drug screening for other neurodegenerative disorders

Cumulatively, this thesis has demonstrated that modulating proteostatic stress in human MNs can give insights into cell-type-specific vulnerabilities and enable observations of disease-relevant phenotypes that can be scaled for drug screening projects. This approach is not exclusive to ALS and MN vulnerabilities; these types of studies can be expanded to other neurodegenerative disease conditions that also display unique cell-type-specific degeneration. For example, in Parkinson's disease, dopaminergic neurons within the substantia nigra are preferentially damaged and depleted[473]. Certain pesticides, metals, and contaminants in synthetic heroin have also

already been linked to the development of parkinsonism and damage to dopaminergic neurons[474]. It may therefore be worthwhile to investigate how these various toxicants affect patient dopaminergic neurons, particularly those with different genetic mutations. This would further inform why this cell type is preferentially vulnerable in patients and how certain genes interact with environmental exposures to drive this vulnerability. Moreover, this stressor-system approach can also be leveraged for drug screening projects. Current dopaminergic neuron differentiations are already quite time-consuming (between 15 and 80 days), with observations of selective degeneration also inconsistent between patient lines[475]. If accelerated stress conditions for preferential dopaminergic degeneration can be optimized to complement the traditional long-term culture approaches, this system may ultimately be able to more rapidly identify compounds that preserve dopaminergic viability for novel therapeutic agents.

5.5 Concluding Remarks

ALS is devastating, with few therapeutic options. This thesis has aimed to add to the current patient derived systems used for ALS drug discovery by developing robust conditions for an accelerated pharmacological model of ALS patient MN proteotoxicity. We have shown that 3 proteostatic stressors induce differential MN vulnerabilities, recapitulate convergent ALS cellular phenotypes in vitro, and predict therapeutic protective compounds discovered in other ALS model systems. We further demonstrated that these assays are scalable for large scale proteomics technologies and drug screening projects and identified several novel neuroprotective compounds. These studies ultimately add to our understanding of what keeps patient MNs healthy in stress and disease conditions and hopefully provide even the smallest step forward towards finding new and effective treatments for ALS patients.

"Let us keep looking, in spite of everything. Let us keep searching.

It is indeed the best method of finding, and perhaps thanks to our efforts,

the verdict we will give such a patient tomorrow will not be the same we must give this man today"

Charcot (1889)

Chapter 6

Materials and Methods

6.1. hiPSC culture

All human induced pluripotent stem cell (hiPSC) culture was performed with approval by the institutional review board and the Harvard Committee on the Use of Human Subjects. Table 6.1 lists all hiPSC lines used in this dissertation.

Table 6.1. Human induced pluripotent stem cell lines used.

Line ID	Diagnosis	Mutation	Age of Onset	Age of Biopsy	Gender	Lab	Publication
1016A	Healthy Control	/		20s	M	Melton	Pagliuca et al., 2014[476]
47d	ALS	TDP-43^{G298S}	43	43	M	Eggan	Alami et al., 2014[164]
29d	ALS	SOD1^{L144F}		82	F	Eggan	Boulting et al., 2011[344]
39b	ALS	SOD1^{A4V}	43	43	F	Eggan	Kiskinis et al., 2014[345]
39b-Corrected	Isogenic Control	/	43	43	F	Eggan	Kiskinis et al., 2014[345]

Cell cultures were maintained at 37°C with 5% CO_2 in a ThermoFisher Scientific biological incubator. hiPSCs were cultured with supplemented StemFlex medium (ThermoFisher Scientific) on Matrigel-coated (BD Biosciences) tissue culture plates. Cells were fed every other day and passaged at ~80% confluency using 5 minutes of room temperature 0.5mM EDTA (Life Technologies) and mechanical disruption with a cell lifter. All cultures were tested monthly for mycoplasma contamination and confirmed genotypically correct and karyotypically normal.

6.2 Motor neuron differentiation and dissociation

hiPSCs were differentiated into MNs as described in Maury, et al., 2014[341]. Briefly, confluent (60-90%) hiPSC cultures were detached from Matrigel (BD Biosciences) coated plates and dissociated into single cells using Accutase (Stem Cell Technologies) at 37°C for ~5 minutes. Accutase was quenched and single cells were seeded for differentiation in suspension at a density of 1x10^6 cells/mL in complete mTeSR media (Stem Cell Technologies) supplemented with 10ng/mL FGF2 (Peprotech) and 10μM ROCK-inhibitor Y-27632 (Stemgent). 24 hours after seeding, cells were filtered through a 100μm cell strainer (VWR) and additional, equal volume complete mTeSR media (Stem Cell Technologies) was added. 48 hours after seeding (differentiation day 0), mTeSR media was replaced with N2B27 MN differentiation media. This media was composed of a v:v mixture of DMEM/F12 and Neurobasal media (Life Technologies), supplemented with 1% N2 (Life Technologies), 2% B27 (Life

Technologies), 1% Pen-Strep (Life Technologies), 1% Glutamax (Life Technologies), 0.1% beta-mercaptoethanol (βME, Life Technologies), and 20μM ascorbic acid (Sigma Aldrich). Day 0 and day 1 of differentiation, N2B27 MN differentiation media was supplemented with 10μM SB-431542 (R&D Systems), 100nM LDN-193189 (ReproCELL), and 3μM CHIR-99021 (ReproCELL). Day 2 and Day 4, differentiation media was supplemented with 10μM SB-431542, 100nM LDN-193189, 3μM CHIR-99021, 1μM retinoic acid (Sigma Aldrich), and 1μM smoothened agonist (DNSK International, LLC). Day 5, differentiation media was supplemented with 1μM retinoic acid, and 1μM smoothened agonist, Day 7 with 1μM retinoic acid, 1μM smoothened agonist, and 20ng/mL brain derived neurotrophic factor (BDNF, R&D Systems). Day 9, differentiation media was supplemented with 1μM retinoic acid, 1μM smoothened agonist, 20ng/mL BDNF, and 10μM DAPT (R&D Systems). Day 11 and 13, differentiation media was supplemented with 1μM retinoic acid, 1μM smoothened agonist, 20ng/mL BDNF, 10μM DAPT, and 20ng/mL glial derived neurotrophic factor (GDNF, R&D Systems).

Day 15 of differentiation, embryoid bodies (EBs) were collected, washed once with 1x phosphate buffer solution (PBS) without calcium and magnesium (VWR), and dissociated with 0.25% Trypsin-EDTA (Life Technologies) and 50μg/mL DNase1 (Worthington Biochemical) for 5 minutes at 37°C with movement. Trypsin was quenched with fetal bovine serum (FBS, Sigma Aldrich), and centrifuged at 400g for 5 minutes. The cell pellet was then resuspended in dissociation buffer, consisting of 5% fetal bovine serum (FBS, Sigma Aldrich), 25mM glucose, 1% Glutamax, in 1x PBS without calcium and magnesium, and mechanically triturated using a p1000 pipet. Dissociated single cells were pelleted by centrifugation (400g, 5 minutes) and resuspended in complete MN media, consisting of Neurobasal media supplemented with 1% N2, 2% B27, 1% Pen-Strep, 1% Glutamax, 1% Non-essential amino acids (Life Technologies), 0.1% βME, 20μM ascorbic acid, 20ng/mL BDNF, GDNF, and CNTF (ciliary neurotrophic factor, R&D Systems), and 10μM UFDU (v:v Uridine (Sigma Aldrich):Fluorodeoxyuridine (Sigma Aldrich)). Resuspended dissociated single cells were filtered through a 40μm cell strainer, counted with a 1:1 trypan blue dilution using an automated cell counter, and plated at the desired density on tissue culture treated plates coated with 1X borate buffer (Life Technologies), 25μg/mL poly-ornithine (Sigma Aldrich), 5μg/mL mouse laminin (Life Technologies), and 10μg/mL fibronectin (VWR).

6.3 Proteostatic stressor assays

For survival analyses, dissociated MNs were plated in complete MN media at a density of 50,000 cells/well (unless otherwise indicated) in the inner 60 wells of borate/poly-ornithine/laminin/fibronectin coated 96-well plates (Perkin Elmer). Outer wells were filled with water to avoid evaporation effects. 3 days after plating, ¾ of the media was removed and replaced with fresh complete MN media. 6 days after plating, all media was removed, and MN cultures were treated with stressor media or stressors with protective compounds. Unless otherwise indicated in dose response curves, 1μM of thapsigargin (Sigma Aldrich), tunicamycin (Sigma Aldrich) or MG132 (Sigma Aldrich) were used for standard stressor conditions, and 3μM of kenpaullone (Tocris) and 5μM of MAP4K4 inhibitor 29 (Genentech) in stressor media were used as protective positive controls. 0.1% DMSO (Sigma Aldrich) complete MN media was used as a negative control, and total concentration of DMSO was equal to 0.1% in all wells. MNs were incubated with stressors, protective compounds, and test compounds, for 48hours and fixed with 4% paraformaldehyde (PFA, VWR) prior to quantitative analysis of Isl1/2 (Abcam), TUJ1 (Biolegend) staining with fluorophore-conjugated secondary antibodies (Life Technologies) and Hoechst (Life Technologies), as described in Section 6.4 Immunofluorescent staining and image analysis. All cell counts were expressed as a percentage of surviving DMSO-control cells.

For gene expression analyses, dissociated MNs were plated in complete MN media at a density of $2x10^6$ cells/well of 6-well plates coated with borate/poly-ornithine/laminin/fibronectin. 3 or 6 days after plating, media was removed and MN cultures were treated with 1μM thapsigargin, tunicamycin, MG132 stressor media, alone or with 3μM of kenpaullone (Tocris) or 5μM of MAP4K4 inhibitor 29 (Genentech). Equal concentration DMSO was used as a negative control. Samples were collected at the appropriate timepoints for RNA and protein expression analyses as indicated in Section 6.7 RNA isolation, reverse transcription, and quantitative PCR and Section 6.6 Protein extraction and western blotting.

6.4 Immunofluorescent staining and image analysis

Cells were fixed for 15 minutes at room temperature with 4% paraformaldehyde (PFA, Sigma Aldrich) in PBS, achieved by adding equal volume 8% PFA to equal volume culture media. Fixed cells were gently washed once with PBS, then blocked with 10% normal goat serum, 0.1% Triton X-100 in 1x PBS for 30 minutes at room temperature. Blocked cells were then incubated for 1 hour at room temperature with primary antibodies anti-Isl1/2

(Abcam ab109517, 1:2000), anti-Chx10 (Santa Cruz Biotechnology sc-365519, 1:50), and anti-TUJ1 (Biolegend 801202, 1:2000, or Novus Biologicals NB100-1612, 1:2000). Following primary antibody incubation, cells were gently washed with PBS once, and incubated for 1 hour at room temperature with 2µg/mL Hoechst (Life Technologies H3569) and species-matched, fluorophore-conjugated secondary antibodies (Life Technologies Alexa-488, -546, -555, or -647, 1:1000) diluted in 10% normal goat serum, 0.1% Triton X-100, in PBS. Immunofluorescent labeled cells were gently washed twice with PBS before image acquisition.

High content screening systems (Operetta (PerkinElmer) or ImageXpress (Molecular Devices)) were used for all image acquisition. Images were acquired automatically using a 10x or 20x objective, a solid-state laser light source, and a sCMOS (scientific complementary metal-oxide-semiconductor) camera, corresponding to 9-12 evenly distributed fields per well of each 96-well plate. Using these parameters, at least 2,000 cells were imaged per well of each 96-well plate, with typically >5,000 cells/well with normal assay conditions. Quantitative analyses of these images were then performed using the Columbus/Harmony image analysis software (PerkinElmer). Manually designed scripts were written to define a viable cell population, which consisted of intact, Hoechst-stained nuclei larger than ~45µm^2 (range 37-55) in surface area and with intensities lower than the threshold brightness of pyknotic nuclei (Figure 6.1A). From this viable cell population, the neuron-specific βIII-Tubulin marker was used to define the neuronal population (~95% of all cells, Figure 2.1B) and neurite morphologies (as described below, Figure 6.2). From the viable population, nuclear Isl1/2 antibody staining was used to define the MN population, using intensity thresholds that accurately reflect positive nuclear staining (Figure 6.1B). With these set parameters, total numbers of nuclei, viable neurons, and viable MNs were then quantified automatically across the plate, ensuring unbiased measurements for all test conditions. Images were visually inspected during analysis and script generation, and after analysis to ensure data validity. All cell counts were then expressed as a percentage of surviving DMSO-control cells.
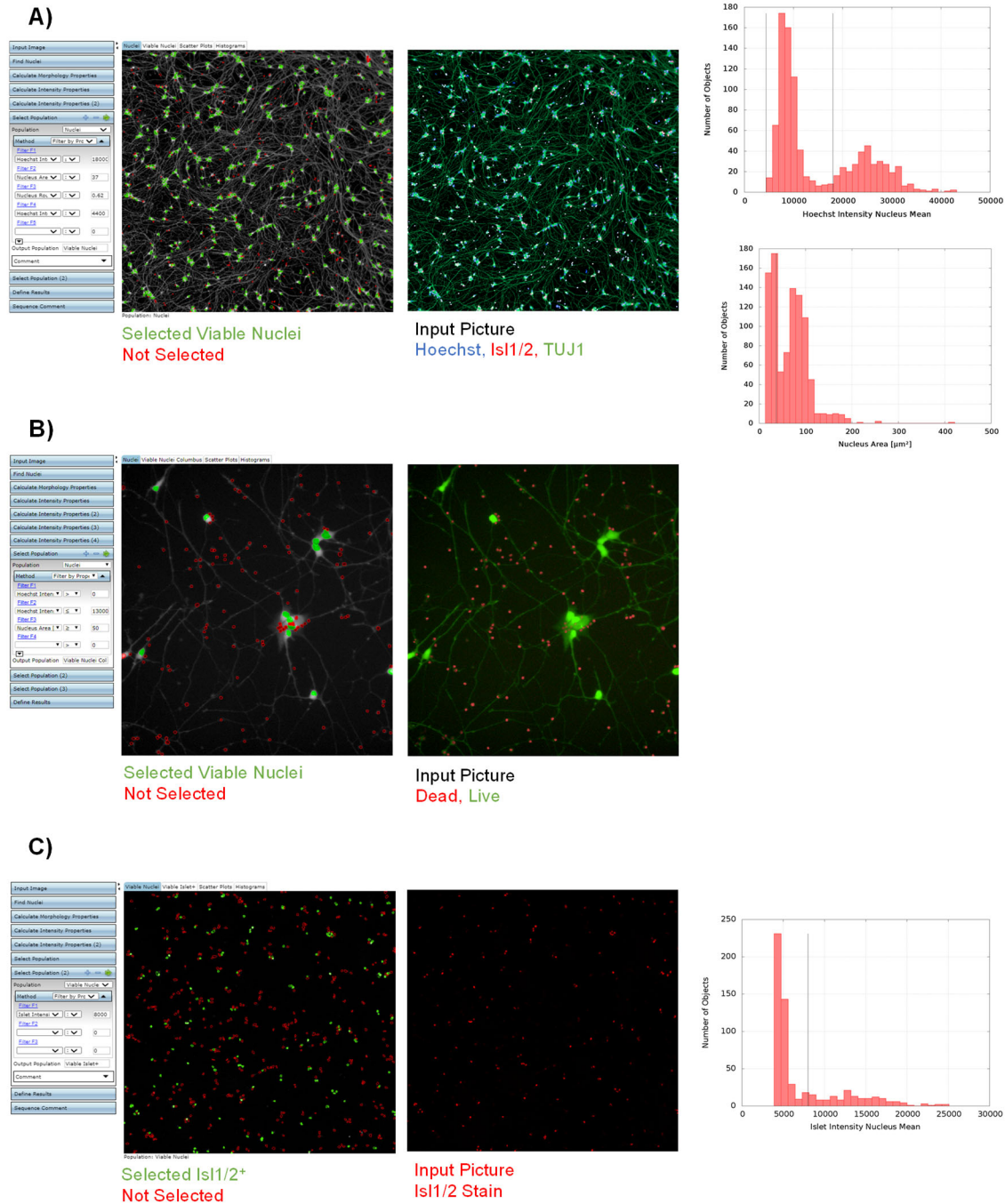
Figure 6.1. Approach to identifying viable MNs.

A) Example nuclear size exclusion parameters and Hoechst intensity thresholding used to identify the viable cell population. Histograms to the right of the selection script and input image demonstrate 2 distinct cell populations, live or dead, with live cells demonstrating a nuclear area $>\sim$37-55μm^2 and Hoechst intensities lower than the threshold brightness of pyknotic nuclei (18,000 in this example).

B) Viable cell script accuracy confirmed with LIVE/DEAD Viability/Cytotoxicity Kit, for mammalian cells (Life Technologies L3224).

C) Example Isl1/2 intensity thresholding used to identify the viable motor neuron population. Histogram to the right of the selection script and input image demonstrate that selected Isl1/2$^+$ cell populations must have an Isl1/2 intensity greater than the basal intensity (>8000 in this example).

119

For neurite detection, the CSIRO neurite analysis 2 method (Harmony/Columbus, PerkinElmer) was used on βIII-Tubulin (TUJ1) staining of total Hoechst$^+$ nuclei populations. This generated a mask that traced and segmented neuritic processes extending from individual neurons (Figure 6.2). Scripts were optimized per plate to achieve accurate neurite tracking, with the following parameters typically used- smoothing width at ~2-3px was used to suppress noise and obtain a single maximum intensity across the neurites with gaussian filtering; linear windows at ~11px specified the dimension in pixels used to find local βIII-Tubulin intensity maxima and contrast parameters between 1-2.5 were used to decrease background noise. Small, spurious objects were eliminated by removal of small diameter objects <3px, and extraneous lateral projections were cleaned using a debarb length of <9-15px. Gap closure distance and tree length were optimized to ensure gaps between detected neurites were closed, without making false connections, and that neurite bodies were linked to their corresponding mother cell. All outputs counts were the values per neuron (i.e. number of segments, maximum length), averaged per well.
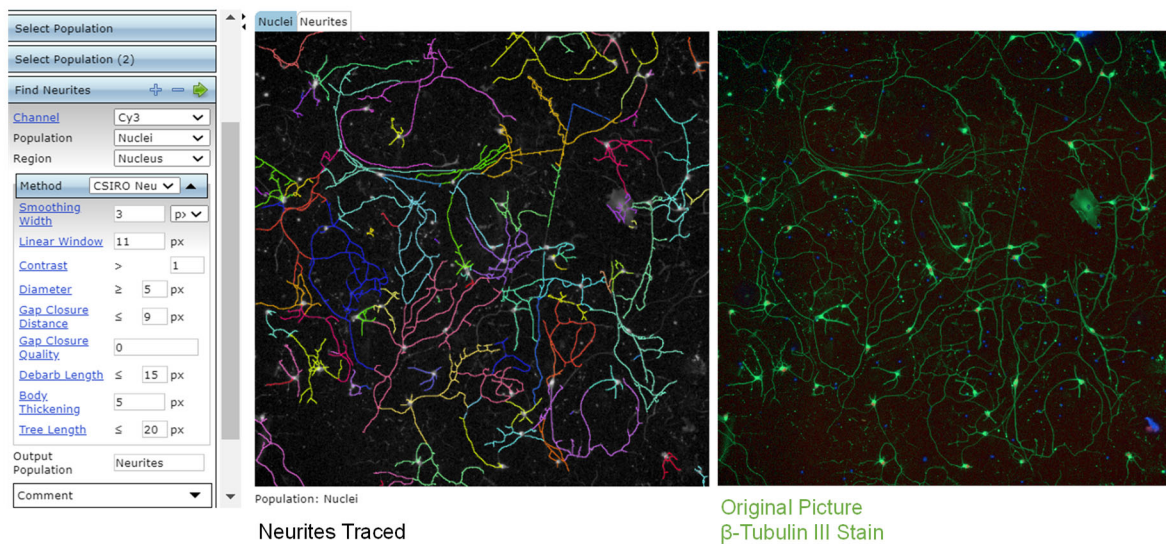
Figure 6.2. Neurite tracing of β-Tubulin III (TUJ1) staining.

Representative images displayed in figures were cropped using FIJI/ImageJ. All automatic contrast settings in Harmony/Columbus were first disabled. Images were then selected for each condition, saved from the database, and imported into FIJI/ImageJ. A region of interest (ROI) was generated and used for each image per condition, allowing the preservation of equal image scale. Cropped images were then saved as final high-resolution TIFs.

6.5 Automated live cell imaging

Dissociated MNs were plated in complete MN media at a density of 50K, 25K, and 12.5K cells/well in the inner 60 wells of borate/poly-ornithine/laminin/fibronectin coated 96-well plates (Greiner). Outer wells were filled with water to avoid evaporation effects. 3 days after plating, ¾ of the media was removed and replaced with fresh complete MN media. 6 days after plating, and before treatment, the MN culture plate was entered into the Nikon BioStation CT for an initial image acquisition. A 10x objective was used to acquire phase images across the plate with a 4 x 4 stitched tiling capture area equivalent to 3.08 x 3.08mm per well. After an initial image acquisition, the plate was removed, and MN culture media was replaced with stressor media as indicated in Section 6.3 Proteostatic stressor assays. The plate was then returned to the Nikon BioStation CT for image acquisition every 6 hours for 48 hours. Final images were then saved as time-lapse video files using CL-Quant software (Nikon) and FIJI/ImageJ was used to select and crop a region of interest for representative video files.

6.6 Protein extraction and western blotting

Protein from $2x10^6$ cells was harvested on ice after 1 PBS wash using the Pierce RIPA lysis and extraction buffer (25 mM Tris-HCl, pH 7.6, 150 mM NaCl, 1% NP-40, 1% sodium deoxycholate, 0.1% SDS, Life Technologies) containing fresh protease and phosphatase inhibitors (Life Technologies). Collected samples sat on ice for an additional 30 minutes and were pulled through a 28G insulin syringe for complete lysis. Protein concentrations were then determined using the Pierce BCA Protein Assay Kit (ThermoFisher Scientific). Equal amounts of protein samples (5-20µg) were diluted in RIPA buffer and βME-Laemmli buffer (Bio-Rad Laboratories) to equal volumes and boiled for 7 minutes at 95°C. Denatured samples were then loaded and run on Criterion TGX (Tris-Glycine eXtended) precast gels (Bio-Rad) for ~15 minutes at 80V, and then ~45 minutes at 150V. Migrated proteins were transferred from the gels to PVDF membranes using the Trans-Blot Turbo Transfer System (Bio-Rad) and run settings of 2.5A, 25V, for 7 minutes. Equal loading and complete transfer were checked with Ponceau S (Sigma Aldrich) staining for 30 minutes, shaking. After removing Ponceau, membranes were blocked with 5% nonfat milk diluted in 1x TBS-T for 45 minutes, shaking (or SuperBlock T20 (Life Technologies) for phosphoproteins). Blocked membranes were incubated with primary antibodies overnight at 4°C, with shaking, with the following primary antibodies: Phospho-eIF2α (Cell Signaling Technology 9721S, 1:1000), eIF2α (Cell Signaling Technology 9722S, 1:1000), GRP78 BiP (Abcam ab21685, 1:1000), CHOP (Cell Signaling Technology 2895T,

1:1000), Cleaved Caspase-3 (Cell Signaling Technology 9664S, 1:1000), TDP-43 (Abcam ab109535, 1:1000), Ubiquitin (Abcam ab7780, 1:1000), β-Actin (Cell Signaling Technology 3700S, 1:5000), β-Tubulin (Abcam ab6046, 1:10,000), GAPDH (Life Technologies AM4300, 1:5000).

Primary antibody solutions were removed after overnight incubation, and membranes washed 3 times with 1x TBS-T for 5 minutes. Membranes were then incubated for 1 hour, shaking, with species-matched secondary antibodies conjugated to horseradish peroxidase (Goat anti-Rabbit IgG (H+L) HRP, Life Technologies 31460, 1:5,000; Goat anti-Mouse IgG (H+L) HRP, Life Technologies 31430, 1:5000), diluted in block (either 5% milk or SuperBlock). Following 3 TBS-T washes, chemiluminescent signal was produced using the SuperSignal West Dura Extended Duration Substrate (ThermoFisher Scientific) and membrane signal was detected on film. All films were scanned using an EPSON scanner without automatic intensity contrast adjustments. Scanned images were cropped and measured for pixel intensity using FIJI/ImageJ. Figure quantifications display fold changes normalized for background film intensity and loading control protein.

For sequential extraction of detergent-soluble proteins and insoluble-aggregated proteins, cells were lysed on ice after 1 PBS wash using the RIPA buffer described above, supplemented with an additional 1% Triton X-100 (Sigma Aldrich). Samples were pulled through a 28G insulin syringe 2 times, sonicated 4 times (10 seconds on, 20 seconds off), and incubated on ice for 30 minutes. The RIPA-cell solution was then centrifuged at 17,000g for 30 minutes at 4°C. The supernatant (detergent-soluble fraction) was collected and transferred to a clean Eppendorf tube. The detergent-insoluble pellet was resuspended and centrifuged again, as above, discarding the supernatant wash. The final detergent-insoluble fraction was extracted using Urea buffer (8M Urea, 4% CHAPS, 40mM Tris). Protein concentrations of the detergent-soluble fraction were determined using the Pierce BCA Protein Assay Kit. 5-10μg of detergent-soluble fractions and equivalent volumes of detergent-insoluble fractions were then diluted to equal volumes with the appropriate buffer and βME-Laemmli buffer. Detergent-soluble fractions were boiled (95°C, 7 minutes). All samples were then separated by SDS-PAGE and immunoblotted as described above.

6.7 RNA isolation, reverse transcription, and quantitative PCR

Total RNA was isolated from $2x10^6$ cells with Trizol (Life Technologies) according to manufacturer's instructions. Briefly, cells were washed once with 1x PBS, on ice, and lysed with 250μL Trizol Reagent and mechanical disruption using a cell lifter. 50μL of chloroform was added to the Trizol-cell extract, and samples were

centrifuged at 12,000g at 4°C for 15 minutes. The aqueous phase was collected into a clean Eppendorf tube and 125µL isopropanol, 15µg GlycoBlue Coprecipitant (Life Technologies) were added. Samples were then incubated for 10 minutes at room temperature, and centrifuged at 12,000g at 4°C for 10 minutes. The RNA pellet was washed twice with 250µL 75% ethanol, air-dried, and resuspended in 30µL of 1x DNase1 buffer (Life Technologies). 1µL of amplification grade DNase 1 was then added and incubated for 15 minutes at room temperature to degrade contaminating genomic DNA. 1µL of 25mM EDTA was added to each sample and incubated at 65°C for 10 minutes to quench the reaction.

Total RNA concentrations were analyzed using a nanodrop, and equal amounts of sample RNA were used to synthesize cDNA using the iScript Reverse Transcription Supermix for RT-qPCR (Bio-Rad). Per reaction, 4µL of 5X iScript RT supermix was combined with 0.5-1µg of total RNA, in water to a final volume of 20µL. Sample reactions were then run through the following thermocycler conditions- 5 minutes at 25°C, 20 minutes at 46°C, and 1 minute at 95°C.

Quantitative PCR (qPCR) was then performed on cDNA samples using Fast SYBR Green (Life Technologies). Per reaction, 5µL of 2X Fast SYBR Green Master Mix was combined with 1µL (50ng) of cDNA sample, 1µL of 10µM forward and reverse primer solution, and 3µL water. The following primer pairs were designed for target transcripts using Primer3Plus and validated using NCBI Blast and Geneious software (GAPDH forward 5'-TGACTTCAACAGCGACACCCA-3', GAPDH reverse 5'-CACCCTGTTGCTGTAGCCAAA-3'; BiP forward 5'-TCTTCAGGAGCAAATGTCTTTGT-3'; BiP reverse 5'-CATCAAGTTCTTGCCGTTCA-3'; CHOP forward 5'-AGGGCTAACATTCTTACCTCTTCA-3', CHOP reverse 5'-GATGAAAATGGGGGTACCTATG-3'). Technical triplicate reactions were set up for each sample and target primer in MicroAmp Optical 384-well Reaction Plates (Life Technologies), and reactions were run and analyzed on a Quant Studio 12K Flex Real-Time PCR system (ThermoFisher Scientific) following the standard Fast SYBER Green protocol. Melt curves of each target primer pair were analyzed to ensure amplification and quantification of a single PCR product. Differential gene expression was then determined using the ΔΔCT method and visualized as fold change values.

6.8 XBP1 splicing analysis

For XBP1 splicing analysis, 2µl (100ng) of cDNA samples were combined with 12.5µl Phusion Hot Start Flex 2X Master Mix (New England Biolabs), 2.5µL of 10µM forward and reverse primer solution (forward: 5'-

GGGGCTTGGTATATATGTGG-3', reverse: 5'- CCTTGTAGTTGAGAACCAGG-3') and water to a final reaction volume of 25μl. Reactions were run with the following thermocycler conditions: 1 cycle of 98°C for 30 seconds; 40 cycles of 98°C for 10 seconds, 60°C for 30 seconds, and 72°C for 30 seconds; and 1 cycle of 72°C for 5 minutes. 2μg of resulting PCR products were then digested with Pst1-HF restriction enzyme (New England Biolabs) to cleave the unspliced XBP1 template. Digested PCR reactions were then run on a 2% agarose gel containing ethidium bromide at 135V. Bands were observed using a ChemiDoc XRS+ (Bio-Rad).

6.9 TUNEL assay

The Click-iT Plus TUNEL Assay for In Situ Apoptosis Detection using an Alexa Fluor 647 dye (Life Technologies) was performed according to manufacturer's instructions. Cells were first fixed for 15 minutes at room temperature using 4% PFA diluted in 1x PBS. Samples were then permeabilized with 0.25% Triton X-100 in 1x PBS for 20 minutes at room temperature and washed twice with deionized water. Terminal deoxynucleotidyl transferase (TdT) reaction buffer was added to cells for 10 minutes at 37°C. TdT reaction buffer supplemented with TdT enzyme and EdUTP were then added for 60 minutes at 37°C for labeling of double-stranded DNA breaks. Following this incubation, cells were washed twice with 3% BSA in 1x PBS for 5 minutes each, and the Click-iT plus TUNEL reaction cocktail was added to cells at 37°C protected from light. Following 30 minutes of fluorescent labeling of EdUTP with click chemistry, the reaction mixture was removed, and cells were washed twice for 5 minutes with 3% BSA in 1x PBS. Cells were then stained with Hoechst, and immunofluorescent Isl1/2, and TUJ1 antibodies as normal for image acquisition and analysis of TUNEL$^+$ MNs.

6.10 PROTEOSTAT aggresome assay

The presence of intracellular insoluble inclusion bodies was visualized using the PROTEOSTAT Aggresome detection kit (ENZO Life Sciences) following manufacturer's instructions. Briefly, cells were fixed with 4% PFA for 30 minutes at room temperature. Following fixation, cells were washed once with PBS, and permeabilized for 30 minutes with 0.5% Triton X-100, 3mM EDTA, pH 8.0 diluted in 1X assay buffer. Cells were then washed with PBS and incubated for 30 minutes with the PROTEOSTAT Aggresome Detection Reagent and primary TUJ1 antibody, protected from light. Cells were then washed with PBS and stained with Hoechst and

species-specific secondary fluorescent antibodies as normal for image acquisition and analysis of Aggresome^{+} neurons.

6.11 ER stress protection assay and sample collection for global proteomic and phosphoproteomic analyses

$3x10^6$ patient derived MNs were plated in complete motor neuron media on borate/poly-ornithine/laminin/fibronectin coated 6-well tissue culture plates. 3-day old cultures were treated with 0.1µM thapsigargin, 3µM kenpaullone, 5µM MAP4K4 inhibitor 29 or 0.1µM thapsigargin with 3µM kenpaullone or 5µM MAP4K4 inhibitor 29. 24 hours and 48 hours after compound treatment, MN cultures were washed 3 times with chilled PBS, on ice, and total protein was collected using 200µL/well of freshly prepared lysis buffer containing 6M urea (Life Technologies), 50mM EPPS (Sigma Aldrich), 1% triton X-100 (Sigma Aldrich), 5mM tris(2-carboxyethyl)phosphine (ThermoFisher Scientific), 20mM chloroacetamide (Sigma Aldrich), with 1x protease and phosphatase inhibitors (Life Technologies). Mechanical disruption with a cell lifter was used to collect the protein lysates into Eppendorf tubes which were then flash frozen in liquid nitrogen and stored at -80°C until mass spectrometry analysis.

6.12 Global proteomic and phosphoproteomic analyses
Proteomics - Sample preparation and digestion

Protein concentrations from sample lysates were determined using the Bradford assay (ThermoFisher Scientific). Proteins denatured in 1% SDS were subjected to disulfide bond reduction with 5mM tris (2-carboxyethyl) phosphine (room temperature, 15 minutes) and alkylation with 20mM chloroacetamide (room temperature, 20 minutes). Methanol-chloroform precipitation was then performed, adding 400µL of 100% methanol to the 100µg/100µL protein sample, vortexing 5 seconds, and then adding 100µL of 100% chloroform and vortexing 5 seconds. 300µL of water was added to the sample, vortexed 5 seconds, and centrifuged for 1 minute at 14,000g to generate distinct phase separations. The aqueous phase and organic phases were removed, leaving behind the protein disk that was washed twice with 400µL 100% methanol, and centrifuged at 21,000g for 2 minutes at room temperature. containing 0.1% RapiGest and digested at 37°C for 2 h with LysC protease at a 200:1 protein-to-

protease ratio. Trypsin was then added at a 100:1 protein-to-protease ratio and the reaction was incubated for 6 h at 37°C.

Tandem mass tag labeling of each sample was performed by adding 10µl of the 20 ng/µL stock of TMT reagent along with acetonitrile to achieve a final acetonitrile concentration of approximately 30% (v/v). Following incubation at room temperature for 1 h, labeling efficiency of a small aliquot was tested, and the reaction was then quenched with hydroxylamine to a final concentration of 0.5% (v/v) for 15 min. The TMT-labeled samples were pooled together at a 1:1 ratio. The sample was vacuum centrifuged to near dryness, resuspended in 5% formic acid for 15 min, centrifuged at 10000×g for 5 minutes at room temperature and subjected to C18 solid-phase extraction (SPE) (Sep-Pak, Waters).

Proteomics – TMT-labeled phosphopeptide enrichment

Phosphopeptides were enriched using Pierce Fe-NTA phosphopeptide enrichment kit (Thermo Fisher Scientific, A32992) following the provided protocol. In brief, combined TMT-labeled dried peptides were enriched for phosphopeptides, while the unbound peptides (flow through) and washes were combined and saved for total proteome analysis. The enriched phosphopeptides were dried down and fractionated according to manufacturer's instructions using High pH reversed-phase peptide fractionation kit (Thermo Fisher Scientific, 84868) for a final 6 fractions and subjected to C18 StageTip desalting prior to MS analysis.

Proteomics - Off-line basic pH reversed-phase (BPRP) fractionation

Unbound TMT-labeled peptides (flow through from phospho-peptide enrichment step) and washes were dried down and resuspended in 100µl of 10 mM NH_4HCO_3 pH 8.0 and fractionated using BPRP HPLC[477]. Briefly, samples were offline fractionated over a 90 min run, into 96 fractions by high pH reverse-phase HPLC (Agilent LC1260) through an aeris peptide xb-c18 column (Phenomenex; 250 mm x 3.6 mm) with mobile phase A containing 5% acetonitrile and 10 mM NH_4HCO_3 in LC-MS grade H_2O, and mobile phase B containing 90% acetonitrile and 10 mM NH_4HCO_3 in LC-MS grade H_2O (both pH 8.0). The 96 resulting fractions were then pooled in a non-continuous manner into 24 fractions (as outlined in Supplemental Fig. 5 of Paulo et al., 2016[477]) and 12 fractions (even numbers) were used for subsequent mass spectrometry analysis. Fractions were vacuum centrifuged to near

dryness. Each consolidated fraction was desalted via StageTip, dried again via vacuum centrifugation, and reconstituted in 5% acetonitrile, 1% formic acid for LC-MS/MS processing.

Proteomics - Liquid chromatography and tandem mass spectrometry

Phosphopeptide mass spectrometry data were collected using an Orbitrap Fusion Lumos mass spectrometer (Thermo Fisher Scientific) coupled to a Proxeon EASY-nLC1200 liquid chromatography (LC) pump (Thermo Fisher Scientific). Peptides were separated on a 100 μm inner diameter microcapillary column packed in house with ~35 cm of Accucore150 resin (2.6 μm, 150 Å, ThermoFisher Scientific) with a gradient consisting of 5%–16% (0-78 min), 16-22% (78-98min), 22-28% (98-110 min) (ACN, 0.1% FA) over a total 120 min at ~500 nL/min. For analysis, we loaded 1/2 of each fraction onto the column. Each analysis used the Multi-Notch MS^3-based TMT method[478]. The scan sequence began with an MS^1 spectrum (Orbitrap analysis; resolution 120,000 at 200 Th; mass range 400−1400 m/z; automatic gain control (AGC) target 1×10^6; maximum injection time 50 ms). Precursors for MS^2 analysis were selected using a Top10 method. MS^2 analysis consisted of collision-induced dissociation (quadrupole ion trap analysis; Turbo scan rate; AGC 2.0×10^4; isolation window 0.7 Th; normalized collision energy (NCE) 35; maximum injection time 150 ms) with MultiStage Activation (MSA) for neutral loss of 97.9763. Monoisotopic peak assignment was used, and previously interrogated precursors were excluded using a dynamic window (150 s ±7 ppm). Following acquisition of each MS^2 spectrum, a synchronous-precursor-selection (SPS) MS^3 scan was collected on the top 10 most intense ions in the MS^2 spectrum[478]. MS^3 precursors were fragmented by high energy collision-induced dissociation (HCD) and analyzed using the Orbitrap (NCE 65; AGC 1.5×10^5; maximum injection time 250 ms, resolution was 50,000 at 200 Th).

Proteomic mass spectrometry data were collected using an Orbitrap Fusion Lumos mass spectrometer (Thermo Fisher Scientific) coupled to a Proxeon EASY-nLC1200 liquid chromatography (LC) pump (Thermo Fisher Scientific). Peptides were separated on a 100 μm inner diameter microcapillary column packed in house with ~35 cm of Accucore150 resin (2.6 μm, 150 Å, Thermo Fisher Scientific) with a gradient consisting of 5%–22% (0-125 min), 22-28% (125-140min) (ACN, 0.1% FA) over a total 150 min run at ~500 nL/min. For analysis, we loaded 1/10 of each fraction onto the column. Each analysis used the Multi-Notch MS^3-based TMT method[478], to reduce ion interference compared to MS^2 quantification. The scan sequence began with an MS^1 spectrum (Orbitrap analysis; resolution 120,000 at 200 Th; mass range 350−1400 m/z; automatic gain control (AGC) target 5×10^5; maximum

injection time 50 ms). Precursors for MS^2 analysis were selected using a Top10 method. MS^2 analysis consisted of collision-induced dissociation (quadrupole ion trap analysis; Turbo scan rate; AGC 2.0×10^4; isolation window 0.7 Th; normalized collision energy (NCE) 35; maximum injection time 35 ms). Monoisotopic peak assignment was used, and previously interrogated precursors were excluded using a dynamic window (150 s ±7 ppm), and dependent scan was performed on a single charge state per precursor. Following acquisition of each MS^2 spectrum, a synchronous-precursor-selection (SPS) MS^3 scan was collected on the top 10 most intense ions in the MS^2 spectrum[478]. MS^3 precursors were fragmented by high energy collision-induced dissociation (HCD) and analyzed using the Orbitrap (NCE 65; AGC 3×10^5; maximum injection time 150 ms, resolution was 50,000 at 200 Th).

Proteomics - Data analysis

Mass spectra were processed using a Sequest-based (v.28, rev. 12) in-house software pipeline[479]. Spectra were converted to mzXML using a modified version of ReAdW.exe. Database searching included all entries from the UniProt Human Reference Proteome database (2017 - SwissProt and TrEMBL). Sequences of common contaminant proteins (for example, trypsin, keratins and so on) were appended and the database was concatenated with one composed of all size-sorted protein sequences in reverse order. Searches were performed using a mass tolerance of 20 p.p.m. for precursors and a fragment-ion tolerance of 0.9 Da, and a maximum of two missed cleavages per peptide was allowed. TMT tags on lysine residues and peptide N termini (+229.163 Da) and carbamidomethylation of cysteine residues (+57.021 Da) were set as static modifications (except when testing for labeling efficiency, in which case the TMT modifications are set to variable), while oxidation of methionine residues (+15.995 Da) was set as a variable modification. Peptide-spectrum matches (PSMs) were adjusted to a 1% false discovery rate (FDR) and PSM filtering was performed using a linear discriminant analysis, as described previously[479], while considering the following parameters: Xcorr and Diff Seq. Delta Score, missed cleavages, peptide length, charge state, and precursor mass accuracy. Using the Picked FDR method[480], proteins were filtered to the target 1% FDR level. Moreover, protein assembly was guided by principles of parsimony to produce the smallest set of proteins necessary to account for all observed peptides. For TMT-based reporter ion quantitation, we extracted the summed signal-to-noise (S:N) ratio for each TMT channel and found the closest matching centroid to the expected mass of the TMT reporter ion (integration tolerance of 0.003 Da). Proteins were quantified by summing reporter ion counts across all matching PSMs using in-house software, as described previously[479]. PSMs with poor

quality, MS$_3$ spectra with more than 8 TMT reporter ion channels missing, or isolation specificity less than 0.7 (or

0.6 for phosphorylation dataset), or with TMT reporter summed signal-to-noise ratio that were less than 150 (100 for

phosphorylation dataset), or had no MS$_3$ spectra were excluded from quantification.

For phosphorylation dataset search, phosphorylation (+79.966 Da) on Serine, Threonine or Tyrosine and

deamidation (+0.984 Da) on Asparagine or Glutamine were set as additional variable modifications.

Phosphorylation site localization was determined using the AScore algorithm[481]. AScore is a probability-based

approach for high-throughput protein phosphorylation site localization. Specifically, a threshold of 13 corresponded

to 95% confidence in site localization.

Protein quantification values were exported for further analysis in Microsoft Excel and Perseus[482] and

statistical test and parameters used are indicated in the corresponding Supplementary Data Set 1. Briefly, Welch's t-

test analysis was performed to compare two datasets, using s0 parameter (in essence a minimal fold change cut-off)

and correction for multiple comparison was achieved by the permutation-based FDR method, both functions that are

built-in in Perseus software. For whole cell proteome analysis, each reporter ion channel was summed across all

quantified proteins and normalized assuming equal protein loading of all samples. For phospho-peptide dataset,

peptide abundance was normalized to the protein abundance when available.

6.13 Gene ontology analyses

Gene ontology enrichment analyses were performed using the Database for Annotation, Visualization, and

Integrated Discovery (DAVID) v6.8. Differentially expressed genes that reached a false discovery rate q-value

significance threshold <0.05 were analyzed for enrichment compared to the total protein list quantified using default

stringency parameters.

6.14 Gene set enrichment analyses

Gene set enrichment analyses were performed on Supplementary Data Set 1 using the Gene Set Enrichment

Analyses software (GSEA, v.3.0, Broad Institute)[483]. Differentially expressed proteins in each treatment group were

first ranked from smallest to largest false discovery rate q-values. All pre-ranked protein lists were then input into

the GSEA software and the Molecular Signatures Database (MsigDB) collections REACTOME, HALLMARK, and

KEGG pathway were used to interrogate the ranked lists for enriched biological terms. P-values for each pathway

were calculated by performing 1,000 random permutations, and only gene sets with a false discovery rate q-value <0.05 were considered significantly enriched.

6.15 Kinase-substrate enrichment analyses

Kinase-substrate enrichment analyses were performed on Supplementary Data Set 1 using the KSEA software, available as the R package 'KSEAapp' on CRAN: CRAN.R-project.org/package=KSEAapp/ and online at https://casecpb.shinyapps.io/ksea/[484]. The $\log_2$(fold change) of phosphoproteins in each treatment-comparison group were used as input, and kinase-substrate annotations were derived from both PhosphoSitePlus and NetworKIN datasets. The resulting output displayed a z-score for each kinase, which described the collective phosphorylation status of its substrates, such that a kinase with a negative score had substrates that were generally dephosphorylated with the test group, and vice versa for a kinase with a positive score. P values for kinase z-scores were then determined by assessing the one-tailed probability of having a more extreme score than the one measured, followed by a Benjamini-Hochberg false discovery rate correction for multiple hypothesis testing. Kinase z-scores with $p < 0.05$ were determined significant, and unbiased hierarchical clustering was performed to determine the relative similarity of kinase scores between each treatment group.

6.16 Proteomics-informed compound small molecule inhibitor tests

Patient derived MNs were plated in complete MN media at a density of 50,000 cells/well in the inner 60 wells of borate/poly-ornithine/laminin/fibronectin coated 96-well plates (Perkin Elmer). Outside wells were filled with water to avoid evaporation effects. 3 days after plating, ¾ of the media was removed and replaced with fresh complete MN media. 6 days after plating, all media was removed, and MN cultures were treated simultaneously with 1µM of thapsigargin (Sigma Aldrich) and increasing doses (10nM-10µM) of test compounds (Table 4.2). 3µM of kenpaullone (Tocris) and 5µM of MAP4K4 inhibitor 29 (Genentech) in 1µM thapsigargin were positive controls. 0.2% DMSO (Sigma Aldrich) complete MN media was used as a negative control, and total concentration of DMSO was equal to 0.2% in all wells. MNs were incubated with stressors, protective compounds, and test compounds, for 48hours and fixed with 4% paraformaldehyde (PFA, VWR) prior to staining with Hoechst, and Isl1/2 (Abcam), TUJ1 (Biolegend) fluorescent antibodies, as described in Section 6.4 Immunofluorescent staining and image analysis. All cell counts were expressed as a percentage of surviving DMSO-control cells per plate.

6.17 DNA extraction and PCR

Genomic DNA was extracted using the Wizard Genomic DNA Purification Kit (Promega). Approximately $2x10^6$ cells were lysed using 600µL of nuclei lysis solution and mechanical trituration by pipetting. 3µL of RNase solution was added to the nuclear lysate and incubated for 15 minutes at 37°C. 200µl Protein Precipitation Solution was then added, vortexed briefly, and centrifuged for 4 minutes at 16,000g. DNA containing supernatant was then transferred to a fresh Eppendorf tube containing 600µl isopropanol. Sample solutions were mixed gently by inversion until white thread-like strands of DNA were visible. Samples were centrifuged for 1 minute at 16,000g, and the DNA pellet was washed with 70% ethanol before centrifuging again (1 minute, 16,000). The DNA pellet was air dried for 15 minutes and resuspended with 100µl DNA rehydration solution for 1 hour at 65°C or overnight at 4°C. Total DNA concentrations were analyzed using a nanodrop.

Polymerase chain reaction (PCR) was performed using the Phusion Hot Start Flex 2X Master Mix (New England Biolabs). Reactions were set up according to manufacturer's instructions- 50-100ng of genomic DNA sample was added to 12.5µL Phusion Hot Start Flex 2x Master Mix and 2.5µL 10µM forward and reverse primer solution. (TDP-43^{G298S} forward 5'- CGACTGAAATATCACTGCTGCTG-3', TDP-43^{G298S} reverse 5'- GGATGCTGATCCCCAACCAA-3'; SOD1^{L144F} forward 5'- GTTATTTTTCTAATATTATGAGG-3', SOD1^{L144F} reverse 5'- GTTTTATAAAACTATACAAATCTTCC-3'; SOD1^{A4V} forward 5'- GTTTGGGGCCAGAGTGGG-3', SOD1^{A4V} reverse 5'- CCGGGCGCTGGACCAGGGCGGCCCC-3'). Water was added to a final reaction volume of 25µL. Thermocycler conditions were the following- 1 cycle of 98°C for 30 seconds; 30 cycles of 98°C for 10 seconds, 45-72°C for 30 seconds (depending on melting temperature of primer pairs determined by NEB Tm calculator), 72°C for 30 seconds/kb; and 1 cycle of 72°C for 10 minutes. PCR products were run at 135V on a 1% agarose gel containing ethidium bromide and bands were observed using a ChemiDoc XRS+ (Bio-Rad).

6.18 Sequencing

Sequencing of PCR products was outsourced to and performed by Psomagen. We provided 25-50ng/µL of PCR products, along with 5pmol/µL forward and reverse primers, to allow for 10µL per sequencing reaction. Resulting sequencing files were analyzed with Geneious software using NCBI gene data.

6.19 Karyotyping

G-banded karyotyping was outsourced to and performed by Cell Line Genetics or WiCell Cytogenetics. Live cell cultures between 40-60% confluency were prepared in T25 flasks filled with media and shipped overnight to either company for analysis. 20 metaphase spreads were analyzed for each line.

6.20 Mycoplasma Testing

Routine testing for mycoplasma contamination in cell cultures was performed monthly using either the LookOut Mycoplasma PCR Detection Kit (Sigma Aldrich) or the MycoAlert PLUS Mycoplasma Detection Kit (Lonza). For the LookOut Mycoplasma PCR Detection Kit, 1mL of media supernatant was collected from 90% confluent cell cultures, boiled for 5 minutes at 95°C, and centrifuged briefly to pellet cellular debris. 2µL of boiled samples were added to 23µL of Rehydration Buffer containing JumpStart Taq DNA polymerase (Sigma Aldrich). Negative controls included 2µL of DNA-free water, and positive controls included non-infectious DNA fragments of *Mycoplasma orale* provided in reaction tubes. Reactions were then run using the following thermocycler conditions: 1 cycle of 94°C for 2 minutes; 40 cycles of 94°C for 30 seconds, 55°C for 30 seconds, and 72° C for 40 seconds. Cooled samples (4-12°C) were loaded on a 1.2% agarose gel containing ethidium bromide and migrated bands were visualized using a ChemiDoc XRS+ (Bio-Rad). Negative controls and samples showed a single distinct band at 481bp. Positive controls and samples had an additional band at 259bp.

For the LookOut Mycoplasma PCR Detection Kit, 1mL of media supernatant was collected from 90% confluent cell cultures, centrifuged for 5 minutes at 200g, and 100µL transferred to an optically clear luminescent-compatible 96-well plate. 100µL of MycoAlert PLUS Reagent was added to each sample and incubated for 5 minutes prior to collecting an initial luminescence reading. 100µL of MycoAlert PLUS Substrate was then added to each sample, incubated for 10 minutes, and then read again for a final luminescence reading. A ratio of final luminescence reading/initial luminescence > 1.2 was interpreted as positive for mycoplasma contamination.

6.21 Statistical Analyses

All statistical analyses were performed using rstatix: Pipe-Friendly Framework for Basic Statistical Tests. R package version 0.6.0. https://CRAN.R-project.org/package=rstatix (Alboukadel Kassambara, 2020). Data were determined to be normally distributed using the Shapiro Wilk test and variance was determined equal between

groups using Levene's test. For comparisons of 2 groups, a 2 tailed, unpaired student's t-test was used. For comparisons of 3 or more groups, an analysis of variance (ANOVA) was used followed by Tukey's HSD post hoc tests. $p < 0.05$ was considered statistically significant and denoted in graphs with a *, $p < 0.01$ **, $p < 0.001$ ***, and $P < 0.0001$ ****.

Chapter 7

References

1. Brown, R. H. & Al-Chalabi, A. Amyotrophic lateral sclerosis. *N. Engl. J. Med.* **377**, 162–172 (2017).

2. Aran, F. A. Recherches sur une maladie non encore décrite du système musculaire (atrophie musculaire progressive). *Arch Gen Med* **24**, 172 (1850).

3. Thouvenet, A. De la paralysie musculaire atrophique. *Thèse pour le Dr. en Médecine.* (1851).

4. Cruveilhier, J. Sur la paralysie musculaire progressive atrophique. *Arch. Générales Médecine* **91**, 561–603 (1853).

5. Duchenne (de Boulogne) G. Etude comparée des lésions anatomiques dans l'atrophie musculaire progressive et dans la paralysie générale. *Rep. Société Médico-chirurgicale Paris* (1853).

6. Charcot, J. & Joffroy, A. Deux cas d'atrophie musculaire progressive avec lésions de la substance grise et des faisceaux antérolatéraux de la moelle épinière. *Arch. Physiol. Norm. Pathol.* (1869).

7. Charcot, J. De la sclérose latérale amyotrophique. *Prog Med* **2**, 341–453 (1874).

8. Saberi, S., Stauffer, J. E., Schulte, D. J. & Ravits, J. Neuropathology of Amyotrophic Lateral Sclerosis and Its Variants. *Neurol. Clin.* **33**, 855–876 (2015).

9. Logroscino, G. & Piccininni, M. Amyotrophic lateral sclerosis descriptive epidemiology: The origin of geographic difference. *Neuroepidemiology* **52**, 93–103 (2019).

10. Chiò, A. *et al.* Global epidemiology of amyotrophic lateral sclerosis: A systematic review of the published literature. *Neuroepidemiology* **41**, 118–130 (2013).

11. Taylor, J. P., Brown, R. H. & Cleveland, D. W. Decoding ALS: From genes to mechanism. *Nature* **539**, 197–206 (2016).

12. Grad, L. I., Rouleau, G. A., Ravits, J. & Cashman, N. R. Clinical Spectrum of Amyotrophic Lateral Sclerosis (ALS). *Cold Spring Harb. Perspect. Med.* **7**, a024117 (2017).

13. Talbott, E. O., Malek, A. M. & Lacomis, D. The epidemiology of amyotrophic lateral sclerosis. *Handb. Clin. Neurol.* **138**, 225–238 (2016).

14. Mathis, S., Goizet, C., Soulages, A., Vallat, J. M. & Masson, G. Le. Genetics of amyotrophic lateral sclerosis: A review. *J. Neurol. Sci.* **399**, 217–226 (2019).

15. Gladman, M. & Zinman, L. The economic impact of amyotrophic lateral sclerosis: a systematic review. *Expert Rev. Pharmacoecon. Outcomes Res.* **15**, 439–450 (2015).

16. Obermann, M. & Lyon, M. Financial cost of amyotrophic lateral sclerosis: A case study. *Amyotroph. Lateral Scler. Front. Degener.* **16**, 54–57 (2015).

17. Feigin, V. L. *et al.* Global, regional, and national burden of neurological disorders, 1990–2016: a systematic analysis for the Global Burden of Disease Study 2016. *Lancet Neurol.* **18**, 459–480 (2019).

18. Arthur, K. C. *et al.* Projected increase in amyotrophic lateral sclerosis from 2015 to 2040. *Nat. Commun.* **7**, 12408 (2016).

19. Wobst, H. J., Mack, K. L., Brown, D. G., Brandon, N. J. & Shorter, J. The clinical trial landscape in amyotrophic lateral sclerosis—Past, present, and future. *Med. Res. Rev.* **Epub**, (2020).

20.	Bensimon, G., Lacomblez, L. & Meininger, V. A controlled trial of riluzole in amyotrophic lateral sclerosis. *N. Engl. J. Med.* **330**, 585–591 (1994).

21.	Lacomblez, L., Bensimon, G., Leigh, P. N., Guillet, P. & Meininger, V. Dose-ranging study of riluzole in amyotrophic lateral sclerosis. *Lancet* **347**, 1425–1431 (1996).

22.	Bellingham, M. C. A Review of the Neural Mechanisms of Action and Clinical Efficiency of Riluzole in Treating Amyotrophic Lateral Sclerosis: What have we Learned in the Last Decade? *CNS Neurosci. Ther.* **17**, 4–31 (2011).

23.	Abe, K. *et al.* Safety and efficacy of edaravone in well defined patients with amyotrophic lateral sclerosis: a randomised, double-blind, placebo-controlled trial. *Lancet Neurol.* **16**, 505–512 (2017).

24.	Hardiman, O. *et al.* Amyotrophic lateral sclerosis. *Nat. Rev. Dis. Prim.* **3**, 17071 (2017).

25.	Ravits, J., Paul, P. & Jorg, C. Focality of upper and lower motor neuron degeneration at the clinical onset of ALS. *Neurology* **68**, 1571–1575 (2007).

26.	Rochat, C., Bernard-Marissal, N. & Schneider, B. L. Selective Vulnerability of Neuronal Subtypes in ALS: A Fertile Ground for the Identification of Therapeutic Targets. *Updat. Amyotroph. Lateral Scler.* **Ch. 9**, 165–194 (2016).

27.	Fang, T., Jozsa, F. & Al-Chalabi, A. Nonmotor Symptoms in Amyotrophic Lateral Sclerosis: A Systematic Review. *Int. Rev. Neurobiol.* **134**, 1409–1441 (2017).

28.	Piccione, E. A., Sletten, D. M., Staff, N. P. & Low, P. A. Autonomic system and amyotrophic lateral sclerosis. *Muscle Nerve* **51**, 676–679 (2015).

29.	Baltadzhieva, R., Gurevich, T. & Korczyn, A. D. Autonomic impairment in amyotrophic lateral sclerosis. *Curr. Opin. Neurol.* **18**, 487–493 (2005).

30.	Tao, Q.-Q., Wei, Q. & Wu, Z.-Y. Sensory nerve disturbance in amyotrophic lateral sclerosis. *Life Sci.* **203**, 242–245 (2018).

31.	Dupuis, L., Pradat, P.-F., Ludolph, A. C. & Loeffler, J.-P. Energy metabolism in amyotrophic lateral sclerosis. *Lancet Neurol.* **10**, 75–82 (2011).

32.	Strong, M. J. & Yang, W. The Frontotemporal Syndromes of ALS. Clinicopathological Correlates. *J. Mol. Neurosci.* **45**, 648–655 (2011).

33.	Tsermentseli, S., Leigh, P. N. & Goldstein, L. H. The anatomy of cognitive impairment in amyotrophic lateral sclerosis: More than frontal lobe dysfunction. *Cortex* **48**, 166–182 (2012).

34.	Ragagnin, A. M. G., Shadfar, S., Vidal, M., Jamali, M. S. & Atkin, J. D. Motor Neuron Susceptibility in ALS/FTD. *Front. Neurosci.* **13**, 532 (2019).

35.	Gibbs, R. M. *et al.* Toward Precision Medicine for Neurological and Neuropsychiatric Disorders. *Cell Stem Cell* **23**, 21–24 (2018).

36.	Hughes, J. T. Pathology of amyotrophic lateral sclerosis. *Adv. Neurol.* **36**, 61–74 (1982).

37.	Hammer, R. P., Tomiyasu, U. & Scheibel, A. B. Degeneration of the human Betz cell due to amyotrophic lateral sclerosis. *Exp. Neurol.* **63**, 336–346 (1979).

38.	Nihei, K., McKee, A. C. & Kowall, N. W. Patterns of neuronal degeneration in the motor cortex of amyotrophic lateral sclerosis patients. *Acta Neuropathol.* **86**, 55–64 (1993).

39.	Schiffer, D., Cordera, S., Cavalla, P. & Migheli, A. Reactive astrogliosis of the spinal cord in amyotrophic

lateral sclerosis. *J. Neurol. Sci.* **139**, 27–33 (1996).

40.   Kawamata, T., Akiyama, H., Yamada, T. & McGeer, P. L. Immunologic reactions in amyotrophic lateral sclerosis brain and spinal cord tissue. *Am. J. Pathol.* **140**, 691–707 (1992).

41.   Murayama, S., Inoue, K., Kawakami, H., Bouldin, T. W. & Suzuki, K. A unique pattern of astrocytosis in the primary motor area in amyotrophic lateral sclerosis. *Acta Neuropathol.* **82**, 456–461 (1991).

42.   Nagy, D., Kato, T. & Kushner, P. D. Reactive astrocytes are widespread in the cortical gray matter of amyotrophic lateral sclerosis. *J. Neurosci. Res.* **38**, 336–347 (1994).

43.   Bunina, T. On intracellular inclusions in familial amyotrophic lateral sclerosis. *Zh. Nevropatol. Psikhiatr. Im. S. S. Korsakova* 1293–1299 (1962).

44.   Tomonaga, M., Saito, M., Yoshimura, M., Shimada, H. & Tohgi, H. Ultrastructure of the Bunina bodies in anterior horn cells of amyotrophic lateral sclerosis. *Acta Neuropathol.* **42**, 81–86 (1978).

45.   Okamoto, K., Mizuno, Y. & Fujita, Y. Bunina bodies in amyotrophic lateral sclerosis. *Neuropathology* **28**, 109–115 (2008).

46.   Takeda, T., Kitagawa, K. & Arai, K. Phenotypic variability and its pathological basis in amyotrophic lateral sclerosis. *Neuropathology* **40**, 40–56 (2020).

47.   Leigh, P. N. *et al.* Ubiquitin deposits in anterior horn cells in motor neurone disease. *Neurosci. Lett.* **93**, 197–203 (1988).

48.   Lowe, J. *et al.* A filamentous inclusion body within anterior horn neurones in motor neurone disease defined by immunocytochemical localisation of ubiquitin. *Neurosci. Lett.* **94**, 203–210 (1988).

49.   Neumann, M. *et al.* Ubiquitinated TDP-43 in frontotemporal lobar degeneration and amyotrophic lateral sclerosis. *Science* **314**, 130–133 (2006).

50.   Arai, T. *et al.* TDP-43 is a component of ubiquitin-positive tau-negative inclusions in frontotemporal lobar degeneration and amyotrophic lateral sclerosis. *Biochem. Biophys. Res. Commun.* **351**, 602–611 (2006).

51.   Watanabe, M. *et al.* Histological evidence of protein aggregation in mutant SOD1 transgenic mice and in amyotrophic lateral sclerosis neural tissues. *Neurobiol Dis* **8**, 933–941 (2001).

52.   Bosco, D. A. *et al.* Wild-type and mutant SOD1 share an aberrant conformation and a common pathogenic pathway in ALS. *Nat. Neurosci.* **13**, 1396–1403 (2010).

53.   Forsberg, K. *et al.* Novel Antibodies Reveal Inclusions Containing Non-Native SOD1 in Sporadic ALS Patients. *PLoS One* **5**, e11552 (2010).

54.   Forsberg, K., Andersen, P. M., Marklund, S. L. & Brännström, T. Glial nuclear aggregates of superoxide dismutase-1 are regularly present in patients with amyotrophic lateral sclerosis. *Acta Neuropathol.* **121**, 623–634 (2011).

55.   Liu, H.-N. *et al.* Lack of evidence of monomer/misfolded superoxide dismutase-1 in sporadic amyotrophic lateral sclerosis. *Ann. Neurol.* **66**, 75–80 (2009).

56.   Kerman, A. *et al.* Amyotrophic lateral sclerosis is a non-amyloid disease in which extensive misfolding of SOD1 is unique to the familial form. *Acta Neuropathol.* **119**, 335–344 (2010).

57.   Huang, E. J. *et al.* Extensive FUS-immunoreactive pathology in juvenile amyotrophic lateral sclerosis with basophilic inclusions. *Brain Pathol.* **20**, 1069–1076 (2010).

58.   Verbeeck, C. *et al.* Expression of Fused in sarcoma mutations in mice recapitulates the neuropathology of

FUS proteinopathies and provides insight into disease pathogenesis. *Mol. Neurodegener.* **7**, 53 (2012).

59.   Vance, C. *et al.* ALS mutant FUS disrupts nuclear localization and sequesters wild-type FUS within cytoplasmic stress granules. *Hum. Mol. Genet.* **22**, 2676–2688 (2013).

60.   Al-Sarraj, S. *et al.* p62 positive, TDP-43 negative, neuronal cytoplasmic and intranuclear inclusions in the cerebellum and hippocampus define the pathology of C9orf72-linked FTLD and MND/ALS. *Acta Neuropathol.* **122**, 691–702 (2011).

61.   DeJesus-Hernandez, M. *et al.* Expanded GGGGCC Hexanucleotide Repeat in Noncoding Region of C9ORF72 Causes Chromosome 9p-Linked FTD and ALS. *Neuron* **72**, 245–256 (2011).

62.   Ash, P. E. A. *et al.* Unconventional Translation of C9ORF72 GGGGCC Expansion Generates Insoluble Polypeptides Specific to c9FTD/ALS. *Neuron* **77**, 639–646 (2013).

63.   Gendron, T. F. *et al.* Antisense transcripts of the expanded C9ORF72 hexanucleotide repeat form nuclear RNA foci and undergo repeat-associated non-ATG translation in c9FTD/ALS. *Acta Neuropathol.* **126**, 829–844 (2013).

64.   Mejzini, R. *et al.* ALS Genetics, Mechanisms, and Therapeutics: Where Are We Now? *Front. Neurosci.* **13**, 1310 (2019).

65.   Boylan, K. Familial Amyotrophic Lateral Sclerosis. *Neurol. Clin.* **33**, 807–830 (2015).

66.   Al-Chalabi, A., van den Berg, L. H. & Veldink, J. Gene discovery in amyotrophic lateral sclerosis: implications for clinical management. *Nat. Rev. Neurol.* **13**, 96–104 (2017).

67.   Murphy, N. A. *et al.* Age-related penetrance of the C9orf72 repeat expansion. *Sci. Rep.* **7**, 2116 (2017).

68.   Elden, A. C. *et al.* Ataxin-2 intermediate-length polyglutamine expansions are associated with increased risk for ALS. *Nature* **466**, 1069–1075 (2010).

69.   Renton, A. E. *et al.* A hexanucleotide repeat expansion in C9ORF72 is the cause of chromosome 9p21-linked ALS-FTD. *Neuron* **72**, 257–268 (2011).

70.   Renton, A. E., Chiò, A. & Traynor, B. J. State of play in amyotrophic lateral sclerosis genetics. *Nat. Neurosci.* **17**, 17–23 (2014).

71.   van Blitterswijk, M. *et al.* Evidence for an oligogenic basis of amyotrophic lateral sclerosis. *Hum. Mol. Genet.* **21**, 3776–3784 (2012).

72.   Kenna, K. P. *et al.* Delineating the genetic heterogeneity of ALS using targeted high-throughput sequencing. *J. Med. Genet.* **50**, 776–783 (2013).

73.   Cady, J. *et al.* Amyotrophic lateral sclerosis onset is influenced by the burden of rare variants in known amyotrophic lateral sclerosis genes. *Ann. Neurol.* **77**, 100–113 (2015).

74.   Zou, Z.-Y. *et al.* Genetic epidemiology of amyotrophic lateral sclerosis: a systematic review and meta-analysis. *J. Neurol. Neurosurg. Psychiatry* **88**, 540–549 (2017).

75.   Abel, O., Powell, J. F., Andersen, P. M. & Al-Chalabi, A. Amyotrophic Lateral Sclerosis Online Database. https://alsod.ac.uk/ (2012).

76.   Rosen, D. R. *et al.* Mutations in Cu/Zn superoxide dismutase gene are associated with familial amyotrophic lateral sclerosis. *Nature* **362**, 59–62 (1993).

77.   Deng, H. *et al.* Amyotrophic lateral sclerosis and structural defects in Cu,Zn superoxide dismutase. *Science* **261**, 1047–1051 (1993).

78.   Fridovich, I. Superoxide Radical and Superoxide Dismutases. *Annu. Rev. Biochem.* **64**, 97–112 (1995).

79.   Perry, J. J. P., Shin, D. S., Getzoff, E. D. & Tainer, J. A. The structural biochemistry of the superoxide dismutases. *Biochim. Biophys. Acta* **1804**, 245–262 (2010).

80.   Abel, O., Powell, J. F., Andersen, P. M. & Al-Chalabi, A. ALSoD: A user-friendly online bioinformatics tool for amyotrophic lateral sclerosis genetics. *Hum. Mutat.* **33**, 1345–1351 (2012).

81.   Yamashita, S. & Ando, Y. Genotype-phenotype relationship in hereditary amyotrophic lateral sclerosis. *Transl. Neurodegener.* **4**, 13 (2015).

82.   Juneja, T., Pericak-Vance, M. A., Laing, N. G., Dave, S. & Siddique, T. Prognosis in familial amyotrophic lateral sclerosis: progression and survival in patients with glu100gly and ala4val mutations in Cu,Zn superoxide dismutase. *Neurology* **48**, 55–57 (1997).

83.   Cudkowicz, M. E., McKenna-Yasek, D., Chen, C., Hedley-Whyte, E. T. & Brown, R. H. Limited corticospinal tract involvement in amyotrophic lateral sclerosis subjects with the A4V mutation in the copper/zinc superoxide dismutase gene. *Ann. Neurol.* **43**, 703–710 (1998).

84.   Corcia, P. *et al.* Respiratory onset in an ALS family with L144F SOD1 mutation. *J. Neurol. Neurosurg. Psychiatry* **82**, 747–749 (2011).

85.   Borchelt, D. R. *et al.* Superoxide dismutase 1 with mutations linked to familial amyotrophic lateral sclerosis possesses significant activity. *Proc. Natl. Acad. Sci.* **91**, 8292–8296 (1994).

86.   Cleveland, D. W., Laing, N., Hurse, P. V & Brown, R. H. Toxic mutants in Charcot's sclerosis. *Nature* **378**, 342–343 (1995).

87.   Ratovitski, T. *et al.* Variation in the Biochemical/Biophysical Properties of Mutant Superoxide Dismutase 1 Enzymes and the Rate of Disease Progression in Familial Amyotrophic Lateral Sclerosis Kindreds. *Hum. Mol. Genet.* **8**, 1451–1460 (1999).

88.   Reaume, A. G. *et al.* Motor neurons in Cu/Zn superoxide dismutase-deficient mice develop normally but exhibit enhanced cell death after axonal injury. *Nat. Genet.* **13**, 43–47 (1996).

89.   Kondo, T. *et al.* Reduction of CuZn-superoxide dismutase activity exacerbates neuronal cell injury and edema formation after transient focal cerebral ischemia. *J. Neurosci.* **17**, 4180–4189 (1997).

90.   Gurney, M. *et al.* Motor neuron degeneration in mice that express a human Cu,Zn superoxide dismutase mutation. *Science* **264**, 1772–1775 (1994).

91.   Dal Canto, M. C. & Gurney, M. E. A low expressor line of transgenic mice carrying a mutant human Cu,Zn superoxide dismutase (SOD1) gene develops pathological changes that most closely resemble those in human amyotrophic lateral sclerosis. *Acta Neuropathol.* **93**, 537–550 (1997).

92.   Jaarsma, D. *et al.* Human Cu/Zn Superoxide Dismutase (SOD1) Overexpression in Mice Causes Mitochondrial Vacuolization, Axonal Degeneration, and Premature Motoneuron Death and Accelerates Motoneuron Disease in Mice Expressing a Familial Amyotrophic Lateral Sclerosis Mutant SO. *Neurobiol. Dis.* **7**, 623–643 (2000).

93.   Jonsson, P. A. *et al.* Motor Neuron Disease in Mice Expressing the Wild Type-Like D90A Mutant Superoxide Dismutase-1. *J. Neuropathol. Exp. Neurol.* **65**, 1126–1136 (2006).

94.   Graffmo, K. S. *et al.* Expression of wild-type human superoxide dismutase-1 in mice causes amyotrophic lateral sclerosis. *Hum. Mol. Genet.* **22**, 51–60 (2013).

95.   Ripps, M. E., Huntley, G. W., Hof, P. R., Morrison, J. H. & Gordon, J. W. Transgenic mice expressing an altered murine superoxide dismutase gene provide an animal model of amyotrophic lateral sclerosis. *Proc.*

Natl. Acad. Sci. **92**, 689–693 (1995).

96.   Philips, T. & Rothstein, J. D. Rodent Models of Amyotrophic Lateral Sclerosis. *Curr. Protoc. Pharmacol.* **69**, 5.67.1-5.67.21 (2015).

97.   Wang, J. *et al.* Coincident thresholds of mutant protein for paralytic disease and protein aggregation caused by restrictively expressed superoxide dismutase cDNA. *Neurobiol. Dis.* **20**, 943–952 (2005).

98.   Münch, C. & Bertolotti, A. Exposure of Hydrophobic Surfaces Initiates Aggregation of Diverse ALS-Causing Superoxide Dismutase-1 Mutants. *J. Mol. Biol.* **399**, 512–525 (2010).

99.   Wang, Q., Johnson, J. L., Agar, N. Y. R. & Agar, J. N. Protein aggregation and protein instability govern familial amyotrophic lateral sclerosis patient survival. *PLoS Biol.* **6**, e170 (2008).

100.   Bruijn, L. I. *et al.* Aggregation and Motor Neuron Toxicity of an ALS-Linked SOD1 Mutant Independent from Wild-Type SOD1. *Science* **281**, 1851–1854 (1998).

101.   Williamson, T. L. & Cleveland, D. W. Slowing of axonal transport is a very early event in the toxicity of ALS-linked SOD1 mutants to motor neurons. *Nat. Neurosci.* **2**, 50–56 (1999).

102.   Warita, H., Itoyama, Y. & Abe, K. Selective impairment of fast anterograde axonal transport in the peripheral nerves of asymptomatic transgenic mice with a G93A mutant SOD1 gene. *Brain Res.* **819**, 120–131 (1999).

103.   Bilsland, L. G. *et al.* Deficits in axonal transport precede ALS symptoms in vivo. *Proc. Natl. Acad. Sci.* **107**, 20523–20528 (2010).

104.   Kikuchi, H. *et al.* Spinal cord endoplasmic reticulum stress associated with a microsomal accumulation of mutant superoxide dismutase-1 in an ALS model. *Proc. Natl. Acad. Sci. U. S. A.* **103**, 6025–6030 (2006).

105.   Nagata, T. *et al.* Increased ER stress during motor neuron degeneration in a transgenic mouse model of amyotrophic lateral sclerosis. *Neurol. Res.* **29**, 767–771 (2007).

106.   Atkin, J. D. *et al.* Endoplasmic reticulum stress and induction of the unfolded protein response in human sporadic amyotrophic lateral sclerosis. *Neurobiol. Dis.* **30**, 400–407 (2008).

107.   Atkin, J. D. *et al.* Mutant SOD1 inhibits ER-Golgi transport in amyotrophic lateral sclerosis. *J. Neurochem.* **129**, 190–204 (2014).

108.   Nishitoh, H. *et al.* ALS-linked mutant SOD1 induces ER stress- and ASK1-dependent motor neuron death by targeting Derlin-1. *Genes Dev.* **22**, 1451–1464 (2008).

109.   Saxena, S., Cabuy, E. & Caroni, P. A role for motoneuron subtype-selective ER stress in disease manifestations of FALS mice. *Nat. Neurosci.* **12**, 627–636 (2009).

110.   Urushitani, M., Kurisu, J., Tsukita, K. & Takahashi, R. Proteasomal inhibition by misfolded mutant superoxide dismutase 1 induces selective motor neuron death in familial amyotrophic lateral sclerosis. *J. Neurochem.* **83**, 1030–1042 (2002).

111.   Beckman, J. S., Carson, M., Smith, C. D. & Koppenol, W. H. ALS, SOD and peroxynitrite. *Nature* **364**, 584–584 (1993).

112.   Wiedau-Pazos, M. *et al.* Altered Reactivity of Superoxide Dismutase in Familial Amyotrophic Lateral Sclerosis. *Science* **271**, 515–518 (1996).

113.   Bruijn, L. I. *et al.* Elevated free nitrotyrosine levels, but not protein-bound nitrotyrosine or hydroxyl radicals, throughout amyotrophic lateral sclerosis (ALS)-like disease implicate tyrosine nitration as an aberrant in vivo property of one familial ALS-linked superoxide di. *Proc. Natl. Acad. Sci. U. S. A.* **94**, 7606–

7611 (1997).

114.   Beal, M. F. *et al.* Increased 3-nitrotyrosine in both sporadic and familial amyotrophic lateral sclerosis. *Ann. Neurol.* **42**, 644–654 (1997).

115.   Andrus, P. K., Fleck, T. J., Gurney, M. E. & Hall, E. D. Protein Oxidative Damage in a Transgenic Mouse Model of Familial Amyotrophic Lateral Sclerosis. *J. Neurochem.* **71**, 2041–2048 (2002).

116.   Harraz, M. M. *et al.* SOD1 mutations disrupt redox-sensitive Rac regulation of NADPH oxidase in a familial ALS model. *J. Clin. Invest.* **118**, 659–670 (2008).

117.   Wong, P. C. *et al.* An adverse property of a familial ALS-linked SOD1 mutation causes motor neuron disease characterized by vacuolar degeneration of mitochondria. *Neuron* **14**, 1105–1116 (1995).

118.   Liu, J. *et al.* Toxicity of Familial ALS-Linked SOD1 Mutants from Selective Recruitment to Spinal Mitochondria. *Neuron* **43**, 5–17 (2004).

119.   Pickles, S. *et al.* ALS-linked misfolded SOD1 species have divergent impacts on mitochondria. *Acta Neuropathol. Commun.* **4**, 43 (2016).

120.   Rothstein, J. D. Current hypotheses for the underlying biology of amyotrophic lateral sclerosis. *Ann. Neurol.* **65**, S3–S9 (2009).

121.   Hayashi, Y., Homma, K. & Ichijo, H. SOD1 in neurotoxicity and its controversial roles in SOD1 mutation-negative ALS. *Adv. Biol. Regul.* **60**, 95–104 (2016).

122.   Clement, A. M. *et al.* Wild-Type Nonneuronal Cells Extend Survival of SOD1 Mutant Motor Neurons in ALS Mice. *Science* **302**, 113–117 (2003).

123.   Boillee, S. *et al.* Onset and Progression in Inherited ALS Determined by Motor Neurons and Microglia. *Science* **312**, 1389–1392 (2006).

124.   Yamanaka, K. *et al.* Astrocytes as determinants of disease progression in inherited amyotrophic lateral sclerosis. *Nat. Neurosci.* **11**, 251–253 (2008).

125.   Beers, D. R. *et al.* Wild-type microglia extend survival in PU.1 knockout mice with familial amyotrophic lateral sclerosis. *Proc. Natl. Acad. Sci. U. S. A.* **103**, 16021–16026 (2006).

126.   Lino, M. M., Schneider, C. & Caroni, P. Accumulation of SOD1 mutants in postnatal motoneurons does not cause motoneuron pathology or motoneuron disease. *J. Neurosci.* **22**, 4825–4832 (2002).

127.   Pramatarova, A., Laganière, J., Roussel, J., Brisebois, K. & Rouleau, G. A. Neuron-specific expression of mutant superoxide dismutase 1 in transgenic mice does not lead to motor impairment. *J. Neurosci.* **21**, 3369–3374 (2001).

128.   Jaarsma, D., Teuling, E., Haasdijk, E. D., De Zeeuw, C. I. & Hoogenraad, C. C. Neuron-Specific Expression of Mutant Superoxide Dismutase Is Sufficient to Induce Amyotrophic Lateral Sclerosis in Transgenic Mice. *J. Neurosci.* **28**, 2075–2088 (2008).

129.   Gong, Y. H., Parsadanian, A. S., Andreeva, A., Snider, W. D. & Elliott, J. L. Restricted expression of G86R Cu/Zn superoxide dismutase in astrocytes results in astrocytosis but does not cause motoneuron degeneration. *J. Neurosci.* **20**, 660–665 (2000).

130.   Turner, B. J., Ackerley, S., Davies, K. E. & Talbot, K. Dismutase-competent SOD1 mutant accumulation in myelinating Schwann cells is not detrimental to normal or transgenic ALS model mice. *Hum. Mol. Genet.* **19**, 815–24 (2010).

131.   Elliott, J. L. Cytokine upregulation in a murine model of familial amyotrophic lateral sclerosis. *Brain Res.*

Mol. Brain Res. **95**, 172–178 (2001).

132.   Ghezzi, P. & Mennini, T. Tumor Necrosis Factor and Motoneuronal Degeneration: An Open Problem. *Neuroimmunomodulation* **9**, 178–182 (2001).

133.   He, B. P., Wen, W. & Strong, M. J. Activated microglia (BV-2) facilitation of TNF-alpha-mediated motor neuron death in vitro. *J. Neuroimmunol.* **128**, 31–38 (2002).

134.   Hensley, K. *et al.* Message and protein-level elevation of tumor necrosis factor alpha (TNF alpha) and TNF alpha-modulating cytokines in spinal cords of the G93A-SOD1 mouse model for amyotrophic lateral sclerosis. *Neurobiol. Dis.* **14**, 74–80 (2003).

135.   Frakes, A. E. *et al.* Microglia Induce Motor Neuron Death via the Classical NF-κB Pathway in Amyotrophic Lateral Sclerosis. *Neuron* **81**, 1009–1023 (2014).

136.   Nagai, M. *et al.* Astrocytes expressing ALS-linked mutated SOD1 release factors selectively toxic to motor neurons. *Nat. Neurosci.* **10**, 615–622 (2007).

137.   Haidet-Phillips, A. M. *et al.* Astrocytes from familial and sporadic ALS patients are toxic to motor neurons. *Nat. Biotechnol.* **29**, 824–828 (2011).

138.   Rothstein, J. D. *et al.* Abnormal excitatory amino acid metabolism in amyotrophic lateral sclerosis. *Ann. Neurol.* **28**, 18–25 (1990).

139.   Rothstein, J. D., Van Kammen, M., Levey, A. I., Martin, L. J. & Kuncl, R. W. Selective loss of glial glutamate transporter GLT-1 in amyotrophic lateral sclerosis. *Ann. Neurol.* **38**, 73–84 (1995).

140.   Rothstein, J. D. *et al.* Knockout of Glutamate Transporters Reveals a Major Role for Astroglial Transport in Excitotoxicity and Clearance of Glutamate. *Neuron* **16**, 675–686 (1996).

141.   Bruijn, L. I. *et al.* ALS-Linked SOD1 Mutant G85R Mediates Damage to Astrocytes and Promotes Rapidly Progressive Disease with SOD1-Containing Inclusions. *Neuron* **18**, 327–338 (1997).

142.   Spreux-Varoquaux, O. *et al.* Glutamate levels in cerebrospinal fluid in amyotrophic lateral sclerosis: a reappraisal using a new HPLC method with coulometric detection in a large cohort of patients. *J. Neurol. Sci.* **193**, 73–78 (2002).

143.   Sreedharan, J. *et al.* TDP-43 mutations in familial and sporadic amyotrophic lateral sclerosis. *Science* **319**, 1668–1672 (2008).

144.   Kabashi, E. *et al.* TARDBP mutations in individuals with sporadic and familial amyotrophic lateral sclerosis. *Nat. Genet.* **40**, 572–574 (2008).

145.   Van Deerlin, V. M. *et al.* TARDBP mutations in amyotrophic lateral sclerosis with TDP-43 neuropathology: a genetic and histopathological analysis. *Lancet Neurol.* **7**, 409–416 (2008).

146.   Yokoseki, A. *et al.* TDP-43 mutation in familial amyotrophic lateral sclerosis. *Ann. Neurol.* **63**, 538–542 (2008).

147.   Ayala, Y. M. *et al.* Structural determinants of the cellular localization and shuttling of TDP-43. *J. Cell Sci.* **121**, 3778–3785 (2008).

148.   Buratti, E. & Baralle, F. E. Multiple roles of TDP-43 in gene expression, splicing regulation, and human disease. *Front. Biosci.* **13**, 867–878 (2008).

149.   Buratti, E. & Baralle, F. E. The multiple roles of TDP-43 in pre-mRNA processing and gene expression regulation. *RNA Biol.* **7**, 420–429 (2010).

150. Cohen, T. J., Lee, V. M. Y. & Trojanowski, J. Q. TDP-43 functions and pathogenic mechanisms implicated in TDP-43 proteinopathies. *Trends Mol. Med.* **17**, 659–667 (2011).

151. Ratti, A. & Buratti, E. Physiological functions and pathobiology of TDP-43 and FUS/TLS proteins. *J. Neurochem.* **138 Suppl**, 95–111 (2016).

152. Buratti, E. & Baralle, F. E. Characterization and Functional Implications of the RNA Binding Properties of Nuclear Factor TDP-43, a Novel Splicing Regulator of CFTR Exon 9. *J. Biol. Chem.* **276**, 36337–36343 (2001).

153. Polymenidou, M. *et al.* Long pre-mRNA depletion and RNA missplicing contribute to neuronal vulnerability from loss of TDP-43. *Nat. Neurosci.* **14**, 459–468 (2011).

154. Tollervey, J. R. *et al.* Characterizing the RNA targets and position-dependent splicing regulation by TDP-43. *Nat. Neurosci.* **14**, 452–458 (2011).

155. Sephton, C. F. *et al.* Identification of neuronal RNA targets of TDP-43-containing ribonucleoprotein complexes. *J. Biol. Chem.* **286**, 1204–1215 (2011).

156. De Conti, L. *et al.* TDP-43 affects splicing profiles and isoform production of genes involved in the apoptotic and mitotic cellular pathways. *Nucleic Acids Res.* **43**, 8990–9005 (2015).

157. Strong, M. J. *et al.* TDP43 is a human low molecular weight neurofilament (hNFL) mRNA-binding protein. *Mol. Cell. Neurosci.* **35**, 320–327 (2007).

158. Kim, S. H., Shanware, N. P., Bowler, M. J. & Tibbetts, R. S. Amyotrophic lateral sclerosis-associated proteins TDP-43 and FUS/TLS function in a common biochemical complex to co-regulate HDAC6 mRNA. *J. Biol. Chem.* **285**, 34097–34105 (2010).

159. Freibaum, B. D., Chitta, R. K., High, A. A. & Taylor, J. P. Global analysis of TDP-43 interacting proteins reveals strong association with RNA splicing and translation machinery. *J. Proteome Res.* **9**, 1104–1120 (2010).

160. Godena, V. K. *et al.* TDP-43 regulates Drosophila neuromuscular junctions growth by modulating Futsch/MAP1B levels and synaptic microtubules organization. *PLoS One* **6**, e17808 (2011).

161. Majumder, P. *et al.* TDP-43 regulates the mammalian spinogenesis through translational repression of Rac1. *Acta Neuropathol.* **124**, 231–245 (2012).

162. Coyne, A. N. *et al.* Futsch/MAP1B mRNA is a translational target of TDP-43 and is neuroprotective in a Drosophila model of amyotrophic lateral sclerosis. *J. Neurosci.* **34**, 15962–15974 (2014).

163. Fallini, C., Bassell, G. J. & Rossoll, W. The ALS disease protein TDP-43 is actively transported in motor neuron axons and regulates axon outgrowth. *Hum. Mol. Genet.* **21**, 3703–3718 (2012).

164. Alami, N. H. H. *et al.* Axonal transport of TDP-43 mRNA granules is impaired by ALS-causing mutations. *Neuron* **81**, 536–543 (2014).

165. Buratti, E. *et al.* Nuclear factor TDP-43 can affect selected microRNA levels. *FEBS J.* **277**, 2268–2281 (2010).

166. Kawahara, Y. & Mieda-Sato, A. TDP-43 promotes microRNA biogenesis as a component of the Drosha and Dicer complexes. *Proc. Natl. Acad. Sci. U. S. A.* **109**, 3347–3352 (2012).

167. Li, W., Jin, Y., Prazak, L., Hammell, M. & Dubnau, J. Transposable Elements in TDP-43-Mediated Neurodegenerative Disorders. *PLoS One* **7**, e44099 (2012).

168. Cirillo, D. *et al.* Neurodegenerative diseases: quantitative predictions of protein-RNA interactions. *RNA* **19**,

129–140 (2013).

169.   Colombrita, C. *et al.* TDP-43 is recruited to stress granules in conditions of oxidative insult. *J. Neurochem.*
       111, 1051–1061 (2009).

170.   Liu-Yesucevitz, L. *et al.* Tar DNA Binding Protein-43 (TDP-43) Associates with Stress Granules: Analysis
       of Cultured Cells and Pathological Brain Tissue. *PLoS One* **5**, e13250 (2010).

171.   McDonald, K. K. *et al.* TAR DNA-binding protein 43 (TDP-43) regulates stress granule dynamics via
       differential regulation of G3BP and TIA-1. *Hum. Mol. Genet.* **20**, 1400–1410 (2011).

172.   Buratti, E. *et al.* TDP-43 Binds Heterogeneous Nuclear Ribonucleoprotein A/B through Its C-terminal Tail.
       J. Biol. Chem. **280**, 37572–37584 (2005).

173.   Pesiridis, G. S., Lee, V. M.-Y. & Trojanowski, J. Q. Mutations in TDP-43 link glycine-rich domain
       functions to amyotrophic lateral sclerosis. *Hum. Mol. Genet.* **18**, R156–R162 (2009).

174.   Lattante, S., Rouleau, G. A. & Kabashi, E. TARDBP and FUS Mutations Associated with Amyotrophic
       Lateral Sclerosis: Summary and Update. *Hum. Mutat.* **34**, 812–826 (2013).

175.   Kraemer, B. C. *et al.* Loss of murine TDP-43 disrupts motor function and plays an essential role in
       embryogenesis. *Acta Neuropathol.* **119**, 409–419 (2010).

176.   Sephton, C. F. *et al.* TDP-43 is a developmentally regulated protein essential for early embryonic
       development. *J. Biol. Chem.* **285**, 6826–6834 (2010).

177.   Wu, L.-S., Cheng, W.-C. & Shen, C.-K. J. Targeted Depletion of TDP-43 Expression in the Spinal Cord
       Motor Neurons Leads to the Development of Amyotrophic Lateral Sclerosis-like Phenotypes in Mice. *J.
       Biol. Chem.* **287**, 27335–27344 (2012).

178.   Iguchi, Y. *et al.* Loss of TDP-43 causes age-dependent progressive motor neuron degeneration. *Brain* **136**,
       1371–1382 (2013).

179.   Yang, C. *et al.* Partial loss of TDP-43 function causes phenotypes of amyotrophic lateral sclerosis. *Proc.
       Natl. Acad. Sci.* **111**, E1121–E1129 (2014).

180.   Ditsworth, D. *et al.* Mutant TDP-43 within motor neurons drives disease onset but not progression in
       amyotrophic lateral sclerosis. *Acta Neuropathol.* **133**, 907–922 (2017).

181.   Wegorzewska, I., Bell, S., Cairns, N. J., Miller, T. M. & Baloh, R. H. TDP-43 mutant transgenic mice
       develop features of ALS and frontotemporal lobar degeneration. *Proc. Natl. Acad. Sci. U. S. A.* **106**, 18809–
       18814 (2009).

182.   Stallings, N. R., Puttaparthi, K., Luther, C. M., Burns, D. K. & Elliott, J. L. Progressive motor weakness in
       transgenic mice expressing human TDP-43. *Neurobiol. Dis.* **40**, 404–414 (2010).

183.   Xu, Y.-F. *et al.* Wild-Type Human TDP-43 Expression Causes TDP-43 Phosphorylation, Mitochondrial
       Aggregation, Motor Deficits, and Early Mortality in Transgenic Mice. *J. Neurosci.* **30**, 10851–10859 (2010).

184.   Xu, Y.-F. *et al.* Expression of mutant TDP-43 induces neuronal dysfunction in transgenic mice. *Mol.
       Neurodegener.* **6**, 73 (2011).

185.   Arnold, E. S. *et al.* ALS-linked TDP-43 mutations produce aberrant RNA splicing and adult-onset motor
       neuron disease without aggregation or loss of nuclear TDP-43. *Proc. Natl. Acad. Sci. U. S. A.* **110**, E736–
       E745 (2013).

186.   Mitchell, J. C. *et al.* Wild type human TDP-43 potentiates ALS-linked mutant TDP-43 driven progressive
       motor and cortical neuron degeneration with pathological features of ALS. *Acta Neuropathol. Commun.* **3**,

36 (2015).

187. Wils, H. *et al.* TDP-43 transgenic mice develop spastic paralysis and neuronal inclusions characteristic of ALS and frontotemporal lobar degeneration. *Proc. Natl. Acad. Sci.* **107**, 3858–3863 (2010).

188. Janssens, J. *et al.* Overexpression of ALS-Associated p.M337V Human TDP-43 in Mice Worsens Disease Features Compared to Wild-type Human TDP-43 Mice. *Mol. Neurobiol.* **48**, 22–35 (2013).

189. Shan, X., Chiang, P.-M., Price, D. L. & Wong, P. C. Altered distributions of Gemini of coiled bodies and mitochondria in motor neurons of TDP-43 transgenic mice. *Proc. Natl. Acad. Sci.* **107**, 16325–16330 (2010).

190. Igaz, L. M. *et al.* Dysregulation of the ALS-associated gene TDP-43 leads to neuronal death and degeneration in mice. *J. Clin. Invest.* **121**, 726–738 (2011).

191. Alfieri, J. A., Pino, N. S. & Igaz, L. M. Reversible Behavioral Phenotypes in a Conditional Mouse Model of TDP-43 Proteinopathies. *J. Neurosci.* **34**, 15244–15259 (2014).

192. Alfieri, J. A., Silva, P. R. & Igaz, L. M. Early Cognitive/Social Deficits and Late Motor Phenotype in Conditional Wild-Type TDP-43 Transgenic Mice. *Front. Aging Neurosci.* **8**, 310 (2016).

193. Ayala, Y. M. *et al.* TDP-43 regulates its mRNA levels through a negative feedback loop. *EMBO J.* **30**, 277–288 (2011).

194. White, M. A. *et al.* TDP-43 gains function due to perturbed autoregulation in a Tardbp knock-in mouse model of ALS-FTD. *Nat. Neurosci.* **21**, 552–563 (2018).

195. Fratta, P. *et al.* Mice with endogenous TDP-43 mutations exhibit gain of splicing function and characteristics of amyotrophic lateral sclerosis. *EMBO J.* **37**, pii: e98684 (2018).

196. Ebstein, S. Y., Yagudayeva, I. & Shneider, N. A. Mutant TDP-43 Causes Early-Stage Dose-Dependent Motor Neuron Degeneration in a TARDBP Knockin Mouse Model of ALS. *Cell Rep.* **26**, 364-373.e4 (2019).

197. Highley, J. R. *et al.* Loss of nuclear TDP-43 in amyotrophic lateral sclerosis (ALS) causes altered expression of splicing machinery and widespread dysregulation of RNA splicing in motor neurones. *Neuropathol. Appl. Neurobiol.* **40**, 670–685 (2014).

198. Klim, J. R. *et al.* ALS-implicated protein TDP-43 sustains levels of STMN2, a mediator of motor neuron growth and repair. *Nat. Neurosci.* **22**, 167–179 (2019).

199. Ling, J. P., Pletnikova, O., Troncoso, J. C. & Wong, P. C. TDP-43 repression of nonconserved cryptic exons is compromised in ALS-FTD. *Science* **349**, 650–655 (2015).

200. Vance, C. *et al.* Mutations in FUS, an RNA processing protein, cause familial amyotrophic lateral sclerosis type 6. *Science* **323**, 1208–1211 (2009).

201. Kwiatkowski, T. J. *et al.* Mutations in the FUS/TLS gene on chromosome 16 cause familial amyotrophic lateral sclerosis. *Science* **323**, 1205–1208 (2009).

202. Zinszner, H., Sok, J., Immanuel, D., Yin, Y. & Ron, D. TLS (FUS) binds RNA in vivo and engages in nucleo-cytoplasmic shuttling. *J. Cell Sci.* **110**, 1741–1750 (1997).

203. Tan, A. Y. & Manley, J. L. TLS Inhibits RNA Polymerase III Transcription. *Mol. Cell. Biol.* **30**, 186–196 (2010).

204. Schwartz, J. C. *et al.* FUS binds the CTD of RNA polymerase II and regulates its phosphorylation at Ser2. *Genes Dev.* **26**, 2690–2695 (2012).

205. Yang, L., Gal, J., Chen, J. & Zhu, H. Self-assembled FUS binds active chromatin and regulates gene transcription. *Proc. Natl. Acad. Sci.* **111**, 17809–17814 (2014).

206. Masuda, A. *et al.* Position-specific binding of FUS to nascent RNA regulates mRNA length. *Genes Dev.* **29**, 1045–1057 (2015).

207. Yang, L., Embree, L. J., Tsai, S. & Hickstein, D. D. Oncoprotein TLS Interacts with Serine-Arginine Proteins Involved in RNA Splicing. *J. Biol. Chem.* **273**, 27761–27764 (1998).

208. Hoell, J. I. *et al.* RNA targets of wild-type and mutant FET family proteins. *Nat. Struct. Mol. Biol.* **18**, 1428–1431 (2011).

209. Fujii, R. *et al.* The RNA Binding Protein TLS Is Translocated to Dendritic Spines by mGluR5 Activation and Regulates Spine Morphology. *Curr. Biol.* **15**, 587–593 (2005).

210. Fujii, R. & Takumi, T. TLS facilitates transport of mRNA encoding an actin-stabilizing protein to dendritic spines. *J. Cell Sci.* **118**, 5755–5765 (2005).

211. Muresan, V. & Ladescu Muresan, Z. Shared Molecular Mechanisms in Alzheimer's Disease and Amyotrophic Lateral Sclerosis: Neurofilament-Dependent Transport of sAPP, FUS, TDP-43 and SOD1, with Endoplasmic Reticulum-Like Tubules. *Neurodegener. Dis.* **16**, 55–61 (2016).

212. Morlando, M. *et al.* FUS stimulates microRNA biogenesis by facilitating co-transcriptional Drosha recruitment. *EMBO J.* **31**, 4502–4510 (2012).

213. Dini Modigliani, S., Morlando, M., Errichelli, L., Sabatelli, M. & Bozzoni, I. An ALS-associated mutation in the FUS 3'-UTR disrupts a microRNA-FUS regulatory circuitry. *Nat. Commun.* **5**, 4335 (2014).

214. Bosco, D. A. *et al.* Mutant FUS proteins that cause amyotrophic lateral sclerosis incorporate into stress granules. *Hum. Mol. Genet.* **19**, 4160–4175 (2010).

215. Gal, J. *et al.* Nuclear localization sequence of FUS and induction of stress granules by ALS mutants. *Neurobiol. Aging* **32**, 2323.e27–40 (2011).

216. Hennig, S. *et al.* Prion-like domains in RNA binding proteins are essential for building subnuclear paraspeckles. *J. Cell Biol.* **210**, 529–539 (2015).

217. Wang, W.-Y. *et al.* Interaction of FUS and HDAC1 regulates DNA damage response and repair in neurons. *Nat. Neurosci.* **16**, 1383–1391 (2013).

218. Mastrocola, A. S., Kim, S. H., Trinh, A. T., Rodenkirch, L. A. & Tibbetts, R. S. The RNA-binding protein fused in sarcoma (FUS) functions downstream of poly(ADP-ribose) polymerase (PARP) in response to DNA damage. *J. Biol. Chem.* **288**, 24731–24741 (2013).

219. Baechtold, H. *et al.* Human 75-kDa DNA-pairing protein is identical to the pro-oncoprotein TLS/FUS and is able to promote D-loop formation. *J. Biol. Chem.* **274**, 34337–34342 (1999).

220. Shang, Y. & Huang, E. J. Mechanisms of FUS mutations in familial amyotrophic lateral sclerosis. *Brain Res.* **1647**, 65–78 (2016).

221. Zou, Z.-Y. *et al.* De novo FUS gene mutations are associated with juvenile-onset sporadic amyotrophic lateral sclerosis in China. *Neurobiol. Aging* **34**, 1312.e1-1312.e8 (2013).

222. Hübers, A. *et al.* De novo FUS mutations are the most frequent genetic cause in early-onset German ALS patients. *Neurobiol. Aging* **36**, 3117.e1-3117.e6 (2015).

223. Hübers, A. *et al.* V42. De novo mutations in the FUS gene are a frequent cause of sporadic ALS in very young patients. *Clin. Neurophysiol.* **126**, e87 (2015).

224. Gromicho, M., Oliveira Santos, M., Pinto, A., Pronto-Laborinho, A. & De Carvalho, M. Young-onset rapidly progressive ALS associated with heterozygous FUS mutation. *Amyotroph. Lateral Scler. Frontotemporal Degener.* **18**, 451–453 (2017).

225. Bäumer, D. *et al.* Juvenile ALS with basophilic inclusions is a FUS proteinopathy with FUS mutations. *Neurology* **75**, 611–618 (2010).

226. Hicks, G. G. *et al.* Fus deficiency in mice results in defective B-lymphocyte development and activation, high levels of chromosomal instability and perinatal death. *Nat. Genet.* **24**, 175–179 (2000).

227. Kuroda, M. *et al.* Male sterility and enhanced radiation sensitivity in TLS-/- mice. *EMBO J.* **19**, 453–462 (2000).

228. Kino, Y. *et al.* FUS/TLS deficiency causes behavioral and pathological abnormalities distinct from amyotrophic lateral sclerosis. *Acta Neuropathol. Commun.* **3**, 24 (2015).

229. Sharma, A. *et al.* ALS-associated mutant FUS induces selective motor neuron degeneration through toxic gain of function. *Nat. Commun.* **7**, 10465 (2016).

230. Mitchell, J. C. *et al.* Overexpression of human wild-type FUS causes progressive motor neuron degeneration in an age- and dose-dependent fashion. *Acta Neuropathol.* **125**, 273–288 (2013).

231. Shelkovnikova, T. A. *et al.* Fused in Sarcoma (FUS) Protein Lacking Nuclear Localization Signal (NLS) and Major RNA Binding Motifs Triggers Proteinopathy and Severe Motor Phenotype in Transgenic Mice. *J. Biol. Chem.* **288**, 25266–25274 (2013).

232. Qiu, H. *et al.* ALS-associated mutation FUS-R521C causes DNA damage and RNA splicing defects. *J. Clin. Invest.* **124**, 981–999 (2014).

233. Sephton, C. F. *et al.* Activity-dependent FUS dysregulation disrupts synaptic homeostasis. *Proc. Natl. Acad. Sci. U. S. A.* **111**, E4769–E4778 (2014).

234. Scekic-Zahirovic, J. *et al.* Toxic gain of function from mutant FUS protein is crucial to trigger cell autonomous motor neuron loss. *EMBO J.* **35**, 1077–1097 (2016).

235. Devoy, A. *et al.* Humanized mutant FUS drives progressive motor neuron degeneration without aggregation in 'FUSDelta14' knockin mice. *Brain* **140**, 2797–2805 (2017).

236. Ling, S.-C. *et al.* Overriding FUS autoregulation in mice triggers gain-of-toxic dysfunctions in RNA metabolism and autophagy-lysosome axis. *Elife* **8**, pii: e40811 (2019).

237. Ho, W. Y. & Ling, S.-C. Elevated FUS levels by overriding its autoregulation produce gain-of-toxicity properties that disrupt protein and RNA homeostasis. *Autophagy* **15**, 1665–1667 (2019).

238. Zhou, Y., Liu, S., Liu, G., Oztürk, A. & Hicks, G. G. ALS-associated FUS mutations result in compromised FUS alternative splicing and autoregulation. *PLoS Genet.* **9**, e1003895 (2013).

239. Guo, W. *et al.* HDAC6 inhibition reverses axonal transport defects in motor neurons derived from FUS-ALS patients. *Nat. Commun.* **8**, 861 (2017).

240. Pal, A. *et al.* High content organelle trafficking enables disease state profiling as powerful tool for disease modelling. *Sci. data* **5**, 180241 (2018).

241. Deng, H., Gao, K. & Jankovic, J. The role of FUS gene variants in neurodegenerative diseases. *Nat. Rev. Neurol.* **10**, 337–348 (2014).

242. Picchiarelli, G. *et al.* FUS-mediated regulation of acetylcholine receptor transcription at neuromuscular junctions is compromised in amyotrophic lateral sclerosis. *Nat. Neurosci.* **22**, 1793–1805 (2019).

243. Beck, J. *et al.* Large C9orf72 Hexanucleotide Repeat Expansions Are Seen in Multiple Neurodegenerative Syndromes and Are More Frequent Than Expected in the UK Population. *Am. J. Hum. Genet.* **92**, 345–353 (2013).

244. Nordin, A. *et al.* Extensive size variability of the GGGGCC expansion in C9orf72 in both neuronal and non-neuronal tissues in 18 patients with ALS or FTD. *Hum. Mol. Genet.* **24**, 3133–3142 (2015).

245. Mizielinska, S. *et al.* C9orf72 frontotemporal lobar degeneration is characterised by frequent neuronal sense and antisense RNA foci. *Acta Neuropathol.* **126**, 845–857 (2013).

246. Zu, T. *et al.* RAN proteins and RNA foci from antisense transcripts in C9ORF72 ALS and frontotemporal dementia. *Proc. Natl. Acad. Sci. U. S. A.* **110**, E4968–E4977 (2013).

247. Mori, K. *et al.* The C9orf72 GGGGCC repeat is translated into aggregating dipeptide-repeat proteins in FTLD/ALS. *Science* **339**, 1335–1338 (2013).

248. Mori, K. *et al.* Bidirectional transcripts of the expanded C9orf72 hexanucleotide repeat are translated into aggregating dipeptide repeat proteins. *Acta Neuropathol.* **126**, 881–893 (2013).

249. Balendra, R. & Isaacs, A. M. C9orf72-mediated ALS and FTD: multiple pathways to disease. *Nat. Rev. Neurol.* **14**, 544–558 (2018).

250. Zhang, K. *et al.* The C9orf72 repeat expansion disrupts nucleocytoplasmic transport. *Nature* **525**, 56–61 (2015).

251. Abramzon, Y. A., Fratta, P., Traynor, B. J. & Chia, R. The Overlapping Genetics of Amyotrophic Lateral Sclerosis and Frontotemporal Dementia. *Front. Neurosci.* **14**, 42 (2020).

252. Zhang, D., Iyer, L. M., He, F. & Aravind, L. Discovery of Novel DENN Proteins: Implications for the Evolution of Eukaryotic Intracellular Membrane Structures and Human Disease. *Front. Genet.* **3**, 283 (2012).

253. Levine, T. P., Daniels, R. D., Gatta, A. T., Wong, L. H. & Hayes, M. J. The product of C9orf72, a gene strongly implicated in neurodegeneration, is structurally related to DENN Rab-GEFs. *Bioinformatics* **29**, 499–503 (2013).

254. Farg, M. A. *et al.* C9ORF72, implicated in amytrophic lateral sclerosis and frontotemporal dementia, regulates endosomal trafficking. *Hum. Mol. Genet.* **23**, 3579–3595 (2014).

255. Aoki, Y. *et al.* C9orf72 and RAB7L1 regulate vesicle trafficking in amyotrophic lateral sclerosis and frontotemporal dementia. *Brain* **140**, 887–897 (2017).

256. Webster, C. P. *et al.* The C9orf72 protein interacts with Rab1a and the ULK 1 complex to regulate initiation of autophagy. *EMBO J.* **35**, 1656–1676 (2016).

257. Sellier, C. *et al.* Loss of C9ORF72 impairs autophagy and synergizes with polyQ Ataxin-2 to induce motor neuron dysfunction and cell death. *EMBO J.* **35**, 1276–1297 (2016).

258. Koppers, M. *et al.* C9orf72 ablation in mice does not cause motor neuron degeneration or motor deficits. *Ann. Neurol.* **78**, 426–438 (2015).

259. Lagier-Tourenne, C. *et al.* Targeted degradation of sense and antisense C9orf72 RNA foci as therapy for ALS and frontotemporal degeneration. *Proc. Natl. Acad. Sci.* **110**, E4530–E4539 (2013).

260. Atanasio, A. *et al.* C9orf72 ablation causes immune dysregulation characterized by leukocyte expansion, autoantibody production, and glomerulonephropathy in mice. *Sci. Rep.* **6**, 23204 (2016).

261. O'Rourke, J. G. *et al.* C9orf72 is required for proper macrophage and microglial function in mice. *Science*

351, 1324–1329 (2016).

262.   Sudria-Lopez, E. *et al.* Full ablation of C9orf72 in mice causes immune system-related pathology and neoplastic events but no motor neuron defects. *Acta Neuropathol.* **132**, 145–147 (2016).

263.   Sullivan, P. M. *et al.* The ALS/FTLD associated protein C9orf72 associates with SMCR8 and WDR41 to regulate the autophagy-lysosome pathway. *Acta Neuropathol. Commun.* **4**, 51 (2016).

264.   Burberry, A. *et al.* Loss-of-function mutations in the C9ORF72 mouse ortholog cause fatal autoimmune disease. *Sci. Transl. Med.* **8**, 347ra93 (2016).

265.   Ugolino, J. *et al.* Loss of C9orf72 Enhances Autophagic Activity via Deregulated mTOR and TFEB Signaling. *PLOS Genet.* **12**, e1006443 (2016).

266.   Shao, Q. *et al.* C9orf72 deficiency promotes motor deficits of a C9ALS/FTD mouse model in a dose-dependent manner. *Acta Neuropathol. Commun.* **7**, 32 (2019).

267.   Zhu, Q. *et al.* Reduced C9ORF72 function exacerbates gain of toxicity from ALS/FTD-causing repeat expansion in C9orf72. *Nat. Neurosci.* **23**, 615–624 (2020).

268.   Chew, J. *et al.* C9ORF72 repeat expansions in mice cause TDP-43 pathology, neuronal loss, and behavioral deficits. *Science* **348**, 1151–1154 (2015).

269.   Herranz-Martin, S. *et al.* Viral delivery of C9orf72 hexanucleotide repeat expansions in mice leads to repeat-length-dependent neuropathology and behavioural deficits. *Dis. Model. Mech.* **10**, 859–868 (2017).

270.   Zhang, Y.-J. *et al.* C9ORF72 poly(GA) aggregates sequester and impair HR23 and nucleocytoplasmic transport proteins. *Nat. Neurosci.* **19**, 668–677 (2016).

271.   Zhang, Y.-J. *et al.* Poly(GR) impairs protein translation and stress granule dynamics in C9orf72-associated frontotemporal dementia and amyotrophic lateral sclerosis. *Nat. Med.* **24**, 1136–1142 (2018).

272.   Schludi, M. H. *et al.* Spinal poly-GA inclusions in a C9orf72 mouse model trigger motor deficits and inflammation without neuron loss. *Acta Neuropathol.* **134**, 241–254 (2017).

273.   Hao, Z. *et al.* Motor dysfunction and neurodegeneration in a C9orf72 mouse line expressing poly-PR. *Nat. Commun.* **10**, 2906 (2019).

274.   Choi, S. Y. *et al.* C9ORF72-ALS/FTD-associated poly(GR) binds Atp5a1 and compromises mitochondrial function in vivo. *Nat. Neurosci.* **22**, 851–862 (2019).

275.   Peters, O. M. *et al.* Human C9ORF72 Hexanucleotide Expansion Reproduces RNA Foci and Dipeptide Repeat Proteins but Not Neurodegeneration in BAC Transgenic Mice. *Neuron* **88**, 902–909 (2015).

276.   O'Rourke, J. G. *et al.* C9orf72 BAC Transgenic Mice Display Typical Pathologic Features of ALS/FTD. *Neuron* **88**, 892–901 (2015).

277.   Jiang, J. *et al.* Gain of Toxicity from ALS/FTD-Linked Repeat Expansions in C9ORF72 Is Alleviated by Antisense Oligonucleotides Targeting GGGGCC-Containing RNAs. *Neuron* **90**, 535–550 (2016).

278.   Liu, Y. *et al.* C9orf72 BAC Mouse Model with Motor Deficits and Neurodegenerative Features of ALS/FTD. *Neuron* **90**, 521–34 (2016).

279.   Xu, Z. *et al.* Expanded GGGGCC repeat RNA associated with amyotrophic lateral sclerosis and frontotemporal dementia causes neurodegeneration. in *Proceedings of the …* vol. 110 7778–7783 (2013).

280.   Mizielinska, S. *et al.* C9orf72 repeat expansions cause neurodegeneration in Drosophila through arginine-rich proteins. *Science* **345**, 1192–1194 (2014).

281. Wen, X. *et al.* Antisense proline-arginine RAN dipeptides linked to C9ORF72-ALS/FTD form toxic nuclear aggregates that initiate in vitro and in vivo neuronal death. *Neuron* **84**, 1213–1225 (2014).

282. Freibaum, B. D. *et al.* GGGGCC repeat expansion in C9orf72 compromises nucleocytoplasmic transport. *Nature* **525**, 129–133 (2015).

283. Tran, H. *et al.* Differential Toxicity of Nuclear RNA Foci versus Dipeptide Repeat Proteins in a Drosophila Model of C9ORF72 FTD/ALS. *Neuron* **87**, 1207–1214 (2015).

284. Yang, D. *et al.* FTD/ALS-associated poly(GR) protein impairs the Notch pathway and is recruited by poly(GA) into cytoplasmic inclusions. *Acta Neuropathol.* **130**, 525–535 (2015).

285. Lee, K.-H. *et al.* C9orf72 Dipeptide Repeats Impair the Assembly, Dynamics, and Function of Membrane-Less Organelles. *Cell* **167**, 774-788.e17 (2016).

286. Boeynaems, S. *et al.* Drosophila screen connects nuclear transport genes to DPR pathology in c9ALS/FTD. *Sci. Rep.* **6**, 20877 (2016).

287. Ohki, Y. *et al.* Glycine-alanine dipeptide repeat protein contributes to toxicity in a zebrafish model of C9orf72 associated neurodegeneration. *Mol. Neurodegener.* **12**, 6 (2017).

288. Swinnen, B. *et al.* A zebrafish model for C9orf72 ALS reveals RNA toxicity as a pathogenic mechanism. *Acta Neuropathol.* **135**, 427–443 (2018).

289. Swaminathan, A. *et al.* Expression of C9orf72-related dipeptides impairs motor function in a vertebrate model. *Hum. Mol. Genet.* **27**, 1754–1762 (2018).

290. Kwon, I. *et al.* Poly-dipeptides encoded by the C9orf72 repeats bind nucleoli, impede RNA biogenesis, and kill cells. *Science* **345**, 1139–1145 (2014).

291. Kanekura, K. *et al.* Poly-dipeptides encoded by the C9ORF72 repeats block global protein translation. *Hum. Mol. Genet.* **25**, 1803–1813 (2016).

292. Boeynaems, S. *et al.* Phase Separation of C9orf72 Dipeptide Repeats Perturbs Stress Granule Dynamics. *Mol. Cell* **65**, 1044-1055.e5 (2017).

293. Zhang, Y.-J. *et al.* Aggregation-prone c9FTD/ALS poly(GA) RAN-translated proteins cause neurotoxicity by inducing ER stress. *Acta Neuropathol.* **128**, 505–524 (2014).

294. Guo, Q. *et al.* In Situ Structure of Neuronal C9orf72 Poly-GA Aggregates Reveals Proteasome Recruitment. *Cell* **172**, 696-705.e12 (2018).

295. Cook, C. & Petrucelli, L. Genetic Convergence Brings Clarity to the Enigmatic Red Line in ALS. *Neuron* **101**, 1057–1069 (2019).

296. Chiò, A., Mazzini, L. & Mora, G. Disease-modifying therapies in amyotrophic lateral sclerosis. *Neuropharmacology* **167**, 107986 (2020).

297. Jaiswal, M. K. & M.K., J. Riluzole and edaravone: A tale of two amyotrophic lateral sclerosis drugs. *Med. Res. Rev.* **39**, 733–748 (2019).

298. Petrov, D., Mansfield, C., Moussy, A. & Hermine, O. ALS clinical trials review: 20 years of failure. Are we any closer to registering a new treatment? *Front. Aging Neurosci.* **9**, 68 (2017).

299. Lemon, R. Recent advances in our understanding of the primate corticospinal system. *F1000Research* **8**, pii: F1000 Faculty Rev-274 (2019).

300. Genc, B., Gozutok, O. & Ozdinler, P. H. Complexity of Generating Mouse Models to Study the Upper

Motor Neurons: Let Us Shift Focus from Mice to Neurons. *Int. J. Mol. Sci.* **20**, 3848 (2019).

301. Alrafiah, A. R. From Mouse Models to Human Disease: An Approach for Amyotrophic Lateral Sclerosis. *In Vivo.* **32**, 983–998 (2018).

302. Picher-Martel, V., Valdmanis, P. N., Gould, P. V., Julien, J.-P. & Dupré, N. From animal models to human disease: a genetic approach for personalized medicine in ALS. *Acta Neuropathol. Commun.* **4**, 70 (2016).

303. Takahashi, K. & Yamanaka, S. Induction of Pluripotent Stem Cells from Mouse Embryonic and Adult Fibroblast Cultures by Defined Factors. *Cell* **126**, 663–676 (2006).

304. Takahashi, K. *et al.* Induction of Pluripotent Stem Cells from Adult Human Fibroblasts by Defined Factors. *Cell* **131**, 861–872 (2007).

305. Sances, S. *et al.* Modeling ALS with motor neurons derived from human induced pluripotent stem cells. *Nat. Neurosci.* **19**, 542–553 (2016).

306. Hamburger, V. *The heritage of experimental embryology: Hans Spemann and the organizer*. (Oxford University Press, 1988).

307. Witkowski, J. A. The work of spemann: the heritage of experimental embryology. *Science* **241**, 365–366 (1988).

308. Piccolo, S., Sasai, Y., Lu, B. & De Robertis, E. M. Dorsoventral Patterning in Xenopus: Inhibition of Ventral Signals by Direct Binding of Chordin to BMP-4. *Cell* **86**, 589–598 (1996).

309. Hemmati-Brivanlou, A., Kelly, O. G. & Melton, D. A. Follistatin, an antagonist of activin, is expressed in the Spemann organizer and displays direct neuralizing activity. *Cell* **77**, 283–295 (1994).

310. Lamb, T. *et al.* Neural induction by the secreted polypeptide noggin. *Science* **262**, 713–718 (1993).

311. Smith, W. C., Knecht, A. K., Wu, M. & Harland, R. M. Secreted noggin protein mimics the Spemann organizer in dorsalizing Xenopus mesoderm. *Nature* **361**, 547–549 (1993).

312. Zimmerman, L. B., De Jesús-Escobar, J. M. & Harland, R. M. The Spemann Organizer Signal noggin Binds and Inactivates Bone Morphogenetic Protein 4. *Cell* **86**, 599–606 (1996).

313. Jessell, T. M. Neuronal specification in the spinal cord: inductive signals and transcriptional codes. *Nat. Rev. Genet.* **1**, 20–29 (2000).

314. Muhr, J., Graziano, E., Wilson, S., Jessell, T. M. & Edlund, T. Convergent Inductive Signals Specify Midbrain, Hindbrain, and Spinal Cord Identity in Gastrula Stage Chick Embryos. *Neuron* **23**, 689–702 (1999).

315. Gavalas, A. & Krumlauf, R. Retinoid signalling and hindbrain patterning. *Curr. Opin. Genet. Dev.* **10**, 380–386 (2000).

316. Liu, J.-P., Laufer, E. & Jessell, T. M. Assigning the Positional Identity of Spinal Motor Neurons. *Neuron* **32**, 997–1012 (2001).

317. Nordström, U., Jessell, T. M. & Edlund, T. Progressive induction of caudal neural character by graded Wnt signaling. *Nat. Neurosci.* **5**, 525–532 (2002).

318. Bel-Vialar, S., Itasaki, N. & Krumlauf, R. Initiating Hox gene expression: In the early chick neural tube differential sensitivity to FGF and RA signaling subdivides the HoxB genes in two distinct groups. *Development* **129**, 5103–5115 (2002).

319. Dasen, J. S., Liu, J.-P. & Jessell, T. M. Motor neuron columnar fate imposed by sequential phases of Hox-c

activity. *Nature* **425**, 926–933 (2003).

320. Patani, R. Generating Diverse Spinal Motor Neuron Subtypes from Human Pluripotent Stem Cells. *Stem Cells Int.* **2016**, 1036974 (2016).

321. Roelink, H. *et al.* Floor plate and motor neuron induction by different concentrations of the amino-terminal cleavage product of sonic hedgehog autoproteolysis. *Cell* **81**, 445–455 (1995).

322. Ericson, J., Briscoe, J., Rashbass, P., van Heyningen, V. & Jessell, T. M. Graded sonic hedgehog signaling and the specification of cell fate in the ventral neural tube. *Cold Spring Harb. Symp. Quant. Biol.* **62**, 451–466 (1997).

323. Patten, I. & Placzek, M. The role of Sonic hedgehog in neural tube patterning. *Cell. Mol. Life Sci.* **57**, 1695–1708 (2000).

324. Ericson, J. *et al.* Pax6 Controls Progenitor Cell Identity and Neuronal Fate in Response to Graded Shh Signaling. *Cell* **90**, 169–180 (1997).

325. Briscoe, J. *et al.* Homeobox gene Nkx2.2 and specification of neuronal identity by graded Sonic hedgehog signalling. *Nature* **398**, 622–627 (1999).

326. Briscoe, J., Pierani, A., Jessell, T. M. & Ericson, J. A Homeodomain Protein Code Specifies Progenitor Cell Identity and Neuronal Fate in the Ventral Neural Tube. *Cell* **101**, 435–445 (2000).

327. Vallstedt, A. *et al.* Different Levels of Repressor Activity Assign Redundant and Specific Roles to Nkx6 Genes in Motor Neuron and Interneuron Specification. *Neuron* **31**, 743–755 (2001).

328. Novitch, B. G., Chen, A. I. & Jessell, T. M. Coordinate regulation of motor neuron subtype identity and pan-neuronal properties by the bHLH repressor Olig2. *Neuron* **31**, 773–789 (2001).

329. Davis-Dusenbery, B. N., Williams, L. A., Klim, J. R. & Eggan, K. How to make spinal motor neurons. *Development* **141**, 491–501 (2014).

330. Ericson, J., Morton, S., Kawakami, A., Roelink, H. & Jessell, T. M. Two Critical Periods of Sonic Hedgehog Signaling Required for the Specification of Motor Neuron Identity. *Cell* **87**, 661–673 (1996).

331. Appel, B. *et al.* Motoneuron fate specification revealed by patterned LIM homeobox gene expression in embryonic zebrafish. *Development* **121**, 4117–4125 (1995).

332. Pfaff, S. L., Mendelsohn, M., Stewart, C. L., Edlund, T. & Jessell, T. M. Requirement for LIM Homeobox Gene Isl1 in Motor Neuron Generation Reveals a Motor Neuron– Dependent Step in Interneuron Differentiation. *Cell* **84**, 309–320 (1996).

333. Sharma, K. *et al.* LIM Homeodomain Factors Lhx3 and Lhx4 Assign Subtype Identities for Motor Neurons. *Cell* **95**, 817–828 (1998).

334. Arber, S. *et al.* Requirement for the Homeobox Gene Hb9 in the Consolidation of Motor Neuron Identity. *Neuron* **23**, 659–674 (1999).

335. Tovar-y-Romo, L. B., Ramírez-Jarquín, U. N., Lazo-Gómez, R. & Tapia, R. Trophic factors as modulators of motor neuron physiology and survival: implications for ALS therapy. *Front. Cell. Neurosci.* **8**, 61 (2014).

336. Stifani, N. Motor neurons and the generation of spinal motor neuron diversity. *Front. Cell. Neurosci.* **8**, 293 (2014).

337. Wichterle, H., Lieberam, I., Porter, J. A. & Jessell, T. M. Directed differentiation of embryonic stem cells into motor neurons. *Cell* **110**, 385–397 (2002).

338.   Li, X. J. *et al.* Specification of motoneurons from human embryonic stem cells. *Nat. Biotechnol.* **23**, 215–221 (2005).

339.   Dimos, J. T. *et al.* Induced pluripotent stem cells generated from patients with ALS can be differentiated into motor neurons. *Science* **321**, 1218–1221 (2008).

340.   Chambers, S. M. *et al.* Highly efficient neural conversion of human ES and iPS cells by dual inhibition of SMAD signaling. *Nat. Biotechnol.* **27**, 275–280 (2009).

341.   Maury, Y. *et al.* Combinatorial analysis of developmental cues efficiently converts human pluripotent stem cells into multiple neuronal subtypes. *Nat Biotechnol* **33**, 89–96 (2014).

342.   Mazzoni, E. O. *et al.* Synergistic binding of transcription factors to cell-specific enhancers programs motor neuron identity. *Nat. Neurosci.* **16**, 1219–1227 (2013).

343.   Son, E. Y. *et al.* Conversion of mouse and human fibroblasts into functional spinal motor neurons. *Cell Stem Cell* **9**, 205–218 (2011).

344.   Boulting, G. L. *et al.* A functionally characterized test set of human induced pluripotent stem cells. *Nat Biotechnol* **29**, 279–286 (2011).

345.   Kiskinis, E. *et al.* Pathways disrupted in human ALS motor neurons identified through genetic correction of mutant SOD1. *Cell Stem Cell* **14**, 781–795 (2014).

346.   Wainger, B. J. *et al.* Intrinsic membrane hyperexcitability of amyotrophic lateral sclerosis patient-derived motor neurons. *Cell Rep.* **7**, 1–11 (2014).

347.   Bhinge, A., Namboori, S. C., Zhang, X., VanDongen, A. M. J. & Stanton, L. W. Genetic Correction of SOD1 Mutant iPSCs Reveals ERK and JNK Activated AP1 as a Driver of Neurodegeneration in Amyotrophic Lateral Sclerosis. *Stem Cell Reports* **8**, 856–869 (2017).

348.   Naujock, M. *et al.* 4-Aminopyridine Induced Activity Rescues Hypoexcitable Motor Neurons from Amyotrophic Lateral Sclerosis Patient-Derived Induced Pluripotent Stem Cells. *Stem Cells* **34**, 1563–1575 (2016).

349.   Seminary, E. R., Sison, S. L. & Ebert, A. D. Modeling Protein Aggregation and the Heat Shock Response in ALS iPSC-Derived Motor Neurons. *Front. Neurosci.* **12**, 86 (2018).

350.   Wang, L. *et al.* CRISPR/Cas9-mediated targeted gene correction in amyotrophic lateral sclerosis patient iPSCs. *Protein Cell* **8**, 365–378 (2017).

351.   Chen, H. *et al.* Modeling ALS with iPSCs Reveals that Mutant SOD1 Misregulates Neurofilament Balance in Motor Neurons. *Cell Stem Cell* **14**, 796–809 (2014).

352.   Imamura, K. *et al.* The Src/c-Abl pathway is a potential therapeutic target in amyotrophic lateral sclerosis. *Sci. Transl. Med.* **9**, eaaf3962 (2017).

353.   Devlin, A.-C. *et al.* Human iPSC-derived motoneurons harbouring TARDBP or C9ORF72 ALS mutations are dysfunctional despite maintaining viability. *Nat. Commun.* **6**, 5999 (2015).

354.   Bilican, B. *et al.* Mutant induced pluripotent stem cell lines recapitulate aspects of TDP-43 proteinopathies and reveal cell-specific vulnerability. *Proc. Natl. Acad. Sci.* **109**, 5803–5808 (2012).

355.   Serio, A. *et al.* Astrocyte pathology and the absence of non-cell autonomy in an induced pluripotent stem cell model of TDP-43 proteinopathy. *Proc. Natl. Acad. Sci. U. S. A.* **110**, 4697–702 (2013).

356.   Barmada, S. J. *et al.* Autophagy induction enhances TDP43 turnover and survival in neuronal ALS models. *Nat. Chem. Biol.* **10**, 677–685 (2014).

357.   Fujimori, K. *et al.* Modeling sporadic ALS in iPSC-derived motor neurons identifies a potential therapeutic agent. *Nat. Med.* **24**, 1579–1589 (2018).

358.   Kreiter, N. *et al.* Age-dependent neurodegeneration and organelle transport deficiencies in mutant TDP43 patient-derived neurons are independent of TDP43 aggregation. *Neurobiol. Dis.* **115**, 167–181 (2018).

359.   Egawa, N. *et al.* Drug screening for ALS using patient-specific induced pluripotent stem cells. *Sci. Transl. Med.* **4**, 145ra104 (2012).

360.   Yang, Y. M. *et al.* A small molecule screen in stem-cell-derived motor neurons identifies a kinase inhibitor as a candidate therapeutic for ALS. *Cell Stem Cell* **12**, 713–726 (2013).

361.   Zhang, Z. *et al.* Downregulation of MicroRNA-9 in iPSC-Derived Neurons of FTD/ALS Patients with TDP-43 Mutations. *PLoS One* **8**, e76055 (2013).

362.   Fang, M. Y. *et al.* Small-Molecule Modulation of TDP-43 Recruitment to Stress Granules Prevents Persistent TDP-43 Accumulation in ALS/FTD. *Neuron* **103**, 802-819.e11 (2019).

363.   Chou, C.-C. *et al.* TDP-43 pathology disrupts nuclear pore complexes and nucleocytoplasmic transport in ALS/FTD. *Nat. Neurosci.* **21**, 228–239 (2018).

364.   Melamed, Z. *et al.* Premature polyadenylation-mediated loss of stathmin-2 is a hallmark of TDP-43-dependent neurodegeneration. *Nat. Neurosci.* **22**, 180–190 (2019).

365.   Liu, X. *et al.* The fused in sarcoma protein forms cytoplasmic aggregates in motor neurons derived from integration-free induced pluripotent stem cells generated from a patient with familial amyotrophic lateral sclerosis carrying the FUS-P525L mutation. *Neurogenetics* **16**, 223–231 (2015).

366.   Japtok, J. *et al.* Stepwise acquirement of hallmark neuropathology in FUS-ALS iPSC models depends on mutation type and neuronal aging. *Neurobiol. Dis.* **82**, 420–429 (2015).

367.   Lenzi, J. *et al.* ALS mutant FUS proteins are recruited into stress granules in induced pluripotent stem cell-derived motoneurons. *Dis. Model. Mech.* **8**, 755–766 (2015).

368.   Higelin, J. *et al.* FUS Mislocalization and Vulnerability to DNA Damage in ALS Patients Derived hiPSCs and Aging Motoneurons. *Front. Cell. Neurosci.* **10**, 290 (2016).

369.   Ichiyanagi, N. *et al.* Establishment of In Vitro FUS-Associated Familial Amyotrophic Lateral Sclerosis Model Using Human Induced Pluripotent Stem Cells. *Stem Cell Reports* **6**, 496–510 (2016).

370.   Wang, H. *et al.* Mutant FUS causes DNA ligation defects to inhibit oxidative damage repair in Amyotrophic Lateral Sclerosis. *Nat. Commun.* **9**, 3683 (2018).

371.   Naumann, M. *et al.* Impaired DNA damage response signaling by FUS-NLS mutations leads to neurodegeneration and FUS aggregate formation. *Nat. Commun.* **9**, 335 (2018).

372.   Marrone, L. *et al.* Isogenic FUS-eGFP iPSC Reporter Lines Enable Quantification of FUS Stress Granule Pathology that Is Rescued by Drugs Inducing Autophagy. *Stem Cell Reports* **10**, 375–389 (2018).

373.   Casci, I. *et al.* Muscleblind acts as a modifier of FUS toxicity by modulating stress granule dynamics and SMN localization. *Nat. Commun.* **10**, 5583 (2019).

374.   Wang, H. *et al.* RT2 PCR array screening reveals distinct perturbations in DNA damage response signaling in FUS-associated motor neuron disease. *Mol. Brain* **12**, 103 (2019).

375.   Marrone, L. *et al.* FUS pathology in ALS is linked to alterations in multiple ALS-associated proteins and rescued by drugs stimulating autophagy. *Acta Neuropathol.* **138**, 67–84 (2019).

153

376. Deshpande, D. *et al.* Synaptic FUS Localization During Motoneuron Development and Its Accumulation in Human ALS Synapses. *Front. Cell. Neurosci.* **13**, 256 (2019).

377. Donnelly, C. J. *et al.* RNA Toxicity from the ALS/FTD C9ORF72 Expansion Is Mitigated by Antisense Intervention. *Neuron* **80**, 415–428 (2013).

378. Sareen, D. *et al.* Targeting RNA Foci in iPSC-Derived Motor Neurons from ALS Patients with a C9ORF72 Repeat Expansion. *Sci. Transl. Med.* **5**, 208ra149 (2013).

379. Lopez-Gonzalez, R. *et al.* Poly(GR) in C9ORF72 -Related ALS/FTD Compromises Mitochondrial Function and Increases Oxidative Stress and DNA Damage in iPSC-Derived Motor Neurons. *Neuron* **92**, 383–391 (2016).

380. Dafinca, R. *et al.* C9orf72 Hexanucleotide Expansions Are Associated with Altered Endoplasmic Reticulum Calcium Homeostasis and Stress Granule Formation in Induced Pluripotent Stem Cell-Derived Neurons from Patients with Amyotrophic Lateral Sclerosis and Frontotemporal Demen. *Stem Cells* **34**, 2063–2078 (2016).

381. Selvaraj, B. T. *et al.* C9ORF72 repeat expansion causes vulnerability of motor neurons to Ca2+-permeable AMPA receptor-mediated excitotoxicity. *Nat. Commun.* **9**, 347 (2018).

382. Simone, R. *et al.* G-quadruplex-binding small molecules ameliorate *C9orf72* FTD / ALS pathology *in vitro* and *in vivo*. *EMBO Mol. Med.* **10**, 22–31 (2018).

383. Yuva-Aydemir, Y., Almeida, S., Krishnan, G., Gendron, T. F. & Gao, F.-B. Transcription elongation factor AFF2/FMR2 regulates expression of expanded GGGGCC repeat-containing C9ORF72 allele in ALS/FTD. *Nat. Commun.* **10**, 5466 (2019).

384. Lopez-Gonzalez, R. *et al.* Partial inhibition of the overactivated Ku80-dependent DNA repair pathway rescues neurodegeneration in *C9ORF72* -ALS/FTD. *Proc. Natl. Acad. Sci.* **116**, 9628–9633 (2019).

385. Westergard, T. *et al.* Cell-to-Cell Transmission of Dipeptide Repeat Proteins Linked to C9orf72 -ALS/FTD. *Cell Rep.* **17**, 645–652 (2016).

386. Shi, Y. *et al.* Haploinsufficiency leads to neurodegeneration in C9ORF72 ALS/FTD human induced motor neurons. *Nat. Med.* **24**, 313–325 (2018).

387. Cheng, W. *et al.* CRISPR-Cas9 Screens Identify the RNA Helicase DDX3X as a Repressor of C9ORF72 (GGGGCC)n Repeat-Associated Non-AUG Translation. *Neuron* **104**, 885-898.e8 (2019).

388. Andrade, N. S. *et al.* Dipeptide repeat proteins inhibit homology-directed DNA double strand break repair in C9ORF72 ALS/FTD. *Mol. Neurodegener.* **15**, 13 (2020).

389. Abo-Rady, M. *et al.* Knocking out C9ORF72 Exacerbates Axonal Trafficking Defects Associated with Hexanucleotide Repeat Expansion and Reduces Levels of Heat Shock Proteins. *Stem Cell Reports* **14**, 390–405 (2020).

390. Moore, S. *et al.* ADAR2 mislocalization and widespread RNA editing aberrations in C9orf72-mediated ALS/FTD. *Acta Neuropathol.* **138**, 49–65 (2019).

391. Yin, S. *et al.* Evidence that C9ORF72 Dipeptide Repeat Proteins Associate with U2 snRNP to Cause Mis-splicing in ALS/FTD Patients. *Cell Rep.* **19**, 2244–2256 (2017).

392. Ortega, J. A. *et al.* Nucleocytoplasmic Proteomic Analysis Uncovers eRF1 and Nonsense-Mediated Decay as Modifiers of ALS/FTD C9orf72 Toxicity. *Neuron* **106**, 90-107.e13 (2020).

393. Dafinca, R. *et al.* Impairment of Mitochondrial Calcium Buffering Links Mutations in C9ORF72 and TARDBP in iPS-Derived Motor Neurons from Patients with ALS/FTD. *Stem Cell Reports* **14**, S2213-

6711(20)30113–2 (2020).

394.   Bursch, F. *et al.* Altered calcium dynamics and glutamate receptor properties in iPSC-derived motor neurons from ALS patients with C9orf72, FUS, SOD1 or TDP43 mutations. *Hum. Mol. Genet.* **28**, 2835–2850 (2019).

395.   Kramer, N. J. *et al.* CRISPR-Cas9 screens in human cells and primary neurons identify modifiers of C9ORF72 dipeptide-repeat-protein toxicity. *Nat. Genet.* **50**, 603–612 (2018).

396.   Morimoto, S. *et al.* Ropinirole hydrochloride remedy for amyotrophic lateral sclerosis – Protocol for a randomized, double-blind, placebo-controlled, single-center, and open-label continuation phase I/IIa clinical trial (ROPALS trial). *Regen. Ther.* **11**, 143–166 (2019).

397.   Okano, H., Yasuda, D., Fujimori, K., Morimoto, S. & Takahashi, S. Ropinirole, a New ALS Drug Candidate Developed Using iPSCs. *Trends Pharmacol. Sci.* **41**, 99–109 (2020).

398.   Imamura, K. *et al.* Induced pluripotent stem cell–based Drug Repurposing for Amyotrophic lateral sclerosis Medicine (iDReAM) study: protocol for a phase I dose escalation study of bosutinib for amyotrophic lateral sclerosis patients. *BMJ Open* **9**, e033131 (2019).

399.   Ho, R. *et al.* ALS disrupts spinal motor neuron maturation and aging pathways within gene co-expression networks. *Nat. Neurosci.* **19**, 1256–1267 (2016).

400.   Wu, C., Watts, M. E. & Rubin, L. L. MAP4K4 Activation Mediates Motor Neuron Degeneration in Amyotrophic Lateral Sclerosis. *Cell Rep.* **26**, 1143–1156 (2019).

401.   Salvio, M. Di *et al.* Pur-alpha functionally interacts with FUS carrying ALS-associated mutations. *Cell Death Dis.* **6**, e1943 (2015).

402.   Webster, C. P., Smith, E. F., Shaw, P. J. & De Vos, K. J. Protein homeostasis in amyotrophic lateral sclerosis: Therapeutic opportunities? *Front. Mol. Neurosci.* **10**, 123 (2017).

403.   Hall, C. E. *et al.* Progressive Motor Neuron Pathology and the Role of Astrocytes in a Human Stem Cell Model of VCP-Related ALS. *Cell Rep.* **19**, 1739–1749 (2017).

404.   Ramirez, O. A. & Couve, A. The endoplasmic reticulum and protein trafficking in dendrites and axons. *Trends Cell Biol.* **21**, 219–227 (2011).

405.   Walker, A. K. & Atkin, J. D. Stress signaling from the endoplasmic reticulum: A central player in the pathogenesis of amyotrophic lateral sclerosis. *IUBMB Life* **63**, 754–763 (2011).

406.   Kanekura, K., Suzuki, H., Aiso, S. & Matsuoka, M. ER stress and unfolded protein response in amyotrophic lateral sclerosis. *Mol. Neurobiol.* **39**, 81–89 (2009).

407.   Saxena, S. & Caroni, P. Selective Neuronal Vulnerability in Neurodegenerative Diseases: From Stressor Thresholds to Degeneration. *Neuron* **71**, 35–48 (2011).

408.   Filézac De L'Etang, A. *et al.* Marinesco-Sjögren syndrome protein SIL1 regulates motor neuron subtype-selective ER stress in ALS. *Nat. Neurosci.* **18**, 227–238 (2015).

409.   Roos, A. *et al.* Cellular Signature of SIL1 Depletion: Disease Pathogenesis due to Alterations in Protein Composition Beyond the ER Machinery. *Mol. Neurobiol.* **53**, 5527–5541 (2016).

410.   Bernard-Marissal, N. *et al.* Reduced calreticulin levels link endoplasmic reticulum stress and fas-triggered cell death in motoneurons vulnerable to ALS. *J. Neurosci.* **32**, 4901–4912 (2012).

411.   Bernard-Marissal, N., Sunyach, C., Marissal, T., Raoul, C. & Pettmann, B. Calreticulin levels determine onset of early muscle denervation by fast motoneurons of ALS model mice. *Neurobiol. Dis.* **73**, 130–136

(2015).

412. Brini, M., Calì, T., Ottolini, D. & Carafoli, E. Neuronal calcium signaling: function and dysfunction. *Cell. Mol. Life Sci.* **71**, 2787–2814 (2014).

413. Hawrot, J., Imhof, S. & Wainger, B. J. Modeling cell-autonomous motor neuron phenotypes in ALS using iPSCs. *Neurobiol. Dis.* **134**, 104680 (2020).

414. Kiskinis, E. *et al.* All-Optical Electrophysiology for High-Throughput Functional Characterization of a Human iPSC-Derived Motor Neuron Model of ALS. *Stem Cell Reports* **10**, 1991–2004 (2018).

415. Matus, S., Valenzuela, V., Medinas, D. B. & Hetz, C. ER dysfunction and protein folding stress in ALS. *Int. J. Cell Biol.* **2013**, 674751 (2013).

416. Kisselev, A. F. & Goldberg, A. L. Proteasome inhibitors: From research tools to drug candidates. *Chem. Biol.* **8**, 739–758 (2001).

417. Thams, S. *et al.* A Stem Cell-Based Screening Platform Identifies Compounds that Desensitize Motor Neurons to Endoplasmic Reticulum Stress. *Mol. Ther.* **27**, 87–101 (2019).

418. An, D. *et al.* Stem cell-derived cranial and spinal motor neurons reveal proteostatic differences between ALS resistant and sensitive motor neurons. *Elife* **8**, pii: e44423 (2019).

419. Kim, Y. J. & Lee, G. Candidate ALS therapeutics motor toward 'in vitro clinical trials'. *Cell Stem Cell* **12**, 633–634 (2013).

420. Reinhardt, L. *et al.* Dual Inhibition of GSK3β and CDK5 Protects the Cytoskeleton of Neurons from Neuroinflammatory-Mediated Degeneration In Vitro and In Vivo. *Stem Cell Reports* **12**, 502–517 (2019).

421. Burkhardt, M. F. *et al.* A cellular model for sporadic ALS using patient-derived induced pluripotent stem cells. *Mol. Cell. Neurosci.* **56**, 355–364 (2013).

422. Kitabayashi, T. *et al.* Identification of GSK3β inhibitor kenpaullone as a temozolomide enhancer against glioblastoma. *Sci. Rep.* **9**, 1–12 (2019).

423. Leost, M. *et al.* Paullones are potent inhibitors of glycogen synthase kinase-3β and cyclin-dependent kinase 5/p25. *Eur. J. Biochem.* **267**, 5983–5994 (2000).

424. Larhammar, M., Huntwork-Rodriguez, S., Rudhard, Y., Sengupta-Ghosh, A. & Lewcock, J. The Ste20 Family Kinases MAP4K4, MINK1, and TNIK Converge to Regulate Stress-Induced JNK Signaling in Neurons. *J. Neurosci.* **37**, 11074–11084 (2017).

425. Bos, P. H. *et al.* Development of MAP4 Kinase Inhibitors as Motor Neuron-Protecting Agents. *Cell Chem. Biol.* **26**, 1–13 (2019).

426. Anastassiadis, T., Deacon, S. W., Devarajan, K., Ma, H. & Peterson, J. R. Comprehensive assay of kinase catalytic activity reveals features of kinase inhibitor selectivity. *Nat. Biotechnol.* **29**, 1039 (2011).

427. Linseman, D. A. *et al.* Glycogen synthase kinase-3β phosphorylates bax and promotes its mitochondrial localization during neuronal apoptosis. *J. Neurosci.* **24**, 9993–10002 (2004).

428. Koh, S. H. *et al.* Role of GSK-3β activity in motor neuronal cell death induced by G93A or A4V mutant hSOD1 gene. *Eur. J. Neurosci.* **2**, 301–309 (2005).

429. Koh, S. H. *et al.* Inhibition of glycogen synthase kinase-3 suppresses the onset of symptoms and disease progression of G93A-SOD1 mouse model of ALS. *Exp. Neurol.* **205**, 336–346 (2007).

430. Koh, S. H., Baek, W. & Kim, S. H. Brief review of the role of glycogen synthase kinase-3β in amyotrophic

lateral sclerosis. *Neurol. Res. Int.* **2011**, 205761 (2011).

431.   Maas, J. W. *et al.* Apoptosis of central and peripheral neurons can be prevented with cyclin-dependent kinase/mitogen-activated protein kinase inhibitors. *J. Neurochem.* **70**, 1401–1410 (1998).

432.   Hisanaga, S. & Endo, R. Regulation and role of cyclin-dependent kinase activity in neuronal survival and death. *J. Neurochem.* **115**, 1309–1321 (2010).

433.   Zhu, J., Li, W. & Mao, Z. Cdk5: mediator of neuronal development, death and the response to DNA damage. *Mech. Ageing Dev.* **132**, 389–394 (2011).

434.   Xu, X. *et al.* Prevention of β-amyloid induced toxicity in human iPS cell-derived neurons by inhibition of Cyclin-dependent kinases and associated cell cycle events. *Stem Cell Res.* **10**, 213–227 (2013).

435.   Arrasate, M., Mitra, S., Schweitzer, E. S., Segal, M. R. & Finkbeiner, S. Inclusion body formation reduces levels of mutant huntingtin and the risk of neuronal death. *Nature* **431**, 805–810 (2004).

436.   Gao, X., Gao, C., Liu, G. & Hu, J. MAP4K4: An emerging therapeutic target in cancer. *Cell Biosci.* **6**, 1–9 (2016).

437.   Shuo, M. & Steven T, R. Enzastaurin. *Curr. Opin. Oncol.* **19**, 590–595 (2007).

438.   Watkins, V., Hong, S. & Lin, B. Enzastaurin safety review: Data from phase I and phase II trials. *J. Clin. Oncol.* **24**, 13077–13077 (2006).

439.   Bourhill, T., Narendran, A. & Johnston, R. N. Enzastaurin: A lesson in drug development. *Crit. Rev. Oncol. Hematol.* **112**, 72–79 (2017).

440.   Huang, T., Karsy, M., Zhuge, J., Zhong, M. & Liu, D. B-Raf and the inhibitors: From bench to bedside. *Journal of Hematology and Oncology* vol. 6 30 (2013).

441.   Sayas, C. L. *et al.* Distinct functions for mammalian CLASP1 and -2 during neurite and axon elongation. *Front. Cell. Neurosci.* **13**, 5 (2019).

442.   Khanna, R. *et al.* Opening Pandoras jar: A primer on the putative roles of CRMP2 in a panoply of neurodegenerative, sensory and motor neuron, and central disorders. *Future Neurol.* **7**, 749–771 (2012).

443.   Villarroel-Campos, D. & Gonzalez-Billault, C. The MAP1B case: An old MAP that is new again. *Dev. Neurobiol.* **74**, 953–971 (2014).

444.   Guo, T., Noble, W. & Hanger, D. P. Roles of tau protein in health and disease. *Acta Neuropathologica* vol. 133 665–704 (2017).

445.   Schellino, R., Boido, M. & Vercelli, A. JNK Signaling Pathway Involvement in Spinal Cord Neuron Development and Death. *Cells* **8**, 1576 (2019).

446.   Kuta, R. *et al.* Depending on the stress, histone deacetylase inhibitors act as heat shock protein co-inducers in motor neurons and potentiate arimoclomol, exerting neuroprotection through multiple mechanisms in ALS models. *Cell Stress Chaperones* **25**, 173–191 (2020).

447.   Nishizuka, Y. Studies and perspectives of protein kinase C. *Science* **233**, 305–312 (1986).

448.   Zhu, D. *et al.* Inhibition of protein kinase C promotes neuronal survival in low potassium through an Akt-dependent pathway. *Neurotox. Res.* **6**, 281–289 (2004).

449.   Tanaka, S. & Koike, T. Activation of protein kinase C delays apoptosis of nerve growth factor-deprived rat sympathetic neurons through a Ca(2+)-influx dependent mechanism. *Neurosci. Lett.* **313**, 9–12 (2001).

450. Wiese, S. *et al.* Specific function of B-Raf in mediating survival of embryonic motoneurons and sensory neurons. *Nat. Neurosci.* **4**, 137–142 (2001).

451. Kolch, W. To be or not to be: a question of B-Raf? *Trends Neurosci.* **24**, 498–500 (2001).

452. Frebel, K. & Wiese, S. Signalling molecules essential for neuronal survival and differentiation. *Biochem. Soc. Trans.* **34**, 1287–1290 (2006).

453. Song, L., De Sarno, P. & Jope, R. S. Central role of glycogen synthase kinase-3beta in endoplasmic reticulum stress-induced caspase-3 activation. *J. Biol. Chem.* **277**, 44701–44708 (2002).

454. Ham, J., Eilers, A., Whitfield, J., Neame, S. J. & Shah, B. c-Jun and the transcriptional control of neuronal apoptosis. *Biochem. Pharmacol.* **60**, 1015–1021 (2000).

455. Ham, J. *et al.* A c-jun dominant negative mutant protects sympathetic neurons against programmed cell death. *Neuron* **14**, 927–939 (1995).

456. Yao, Z. *et al.* A novel human STE20-related protein kinase, HGK, that specifically activates the c-Jun N-terminal kinase signaling pathway. *J. Biol. Chem.* **274**, 2118–2125 (1999).

457. Dan, I., Watanabe, N. M. & Kusumi, A. *The Ste20 group kinases as regulators of MAP kinase cascades*. *Trends in Cell Biology* vol. 11 220–230 (Trends Cell Biol, 2001).

458. Chuang, H. C., Wang, X. & Tan, T. H. MAP4K Family Kinases in Immunity and Inflammation. *Adv. Immunol.* **129**, 277–314 (2016).

459. Tang, X. *et al.* Netrin-1 mediates neuronal survival through PIKE-L interaction with the dependence receptor UNC5B. *Nat. Cell Biol.* **10**, 698–706 (2008).

460. Ahn, E. H., Kang, S. S., Qi, Q., Liu, X. & Ye, K. Netrin1 deficiency activates MST1 via UNC5B receptor, promoting dopaminergic apoptosis in Parkinson's disease. *Proc. Natl. Acad. Sci.* **117**, 24503–24513 (2020).

461. Paudel, Y. N., Angelopoulou, E., Piperi, C., Othman, I. & Shaikh, M. F. Implication of HMGB1 signaling pathways in Amyotrophic lateral sclerosis (ALS): From molecular mechanisms to pre-clinical results. *Pharmacol. Res.* **156**, 104792 (2020).

462. Davies, H. *et al.* Mutations of the BRAF gene in human cancer. *Nature* **417**, 949–954 (2002).

463. Agianian, B. & Gavathiotis, E. Current Insights of BRAF Inhibitors in Cancer. *J. Med. Chem.* **61**, 5775–5793 (2018).

464. Uenaka, T. *et al.* In silico drug screening by using genome-wide association study data repurposed dabrafenib, an anti-melanoma drug, for Parkinson's disease. *Hum. Mol. Genet.* **27**, 3974–3985 (2018).

465. Sieber, J. *et al.* GDC-0879, a BRAFV600E Inhibitor, Protects Kidney Podocytes from Death. *Cell Chem. Biol.* **25**, 175-184.e4 (2018).

466. Di Giorgio, F. P., Carrasco, M. A., Siao, M. C., Maniatis, T. & Eggan, K. Non-cell autonomous effect of glia on motor neurons in an embryonic stem cell-based ALS model. *Nat. Neurosci.* **10**, 608–614 (2007).

467. Zhao, C. *et al.* Mutant C9orf72 human iPSC-derived astrocytes cause non-cell autonomous motor neuron pathophysiology. *Glia* **68**, 1046–1064 (2019).

468. Madill, M. *et al.* Amyotrophic lateral sclerosis patient iPSC-derived astrocytes impair autophagy via non-cell autonomous mechanisms. *Mol. Brain* **10**, 22 (2017).

469. Osaki, T., Uzel, S. G. M. & Kamm, R. D. Microphysiological 3D model of amyotrophic lateral sclerosis (ALS) from human iPS-derived muscle cells and optogenetic motor neurons. *Sci. Adv.* **4**, eaat5847 (2018).

470.   Birey, F. *et al.* Assembly of functionally integrated human forebrain spheroids. *Nature* **545**, 54–59 (2017).

471.   Mertens, J. *et al.* Directly Reprogrammed Human Neurons Retain Aging-Associated Transcriptomic Signatures and Reveal Age-Related Nucleocytoplasmic Defects. *Cell Stem Cell* **17**, 705–718 (2015).

472.   Bolognesi, B. *et al.* The mutational landscape of a prion-like domain. *Nat. Commun.* **10**, 4162 (2019).

473.   Poewe, W. *et al.* Parkinson disease. *Nat. Rev. Dis. Prim.* **3**, 17013 (2017).

474.   McKnight, S. & Hack, N. Toxin-Induced Parkinsonism. *Neurologic Clinics* vol. 38 853–865 (2020).

475.   Ahfeldt, T. *et al.* Pathogenic Pathways in Early-Onset Autosomal Recessive Parkinson's Disease Discovered Using Isogenic Human Dopaminergic Neurons. *Stem Cell Reports* **14**, 75–90 (2020).

476.   Pagliuca, F. W. *et al.* Generation of functional human pancreatic β cells in vitro. *Cell* **159**, 428–439 (2014).

477.   Paulo, J. A. *et al.* Quantitative mass spectrometry-based multiplexing compares the abundance of 5000 S. cerevisiae proteins across 10 carbon sources. *J. Proteomics* **148**, 85–93 (2016).

478.   McAlister, G. C. *et al.* MultiNotch MS3 enables accurate, sensitive, and multiplexed detection of differential expression across cancer cell line proteomes. *Anal. Chem.* **86**, 7150–7158 (2014).

479.   Huttlin, E. L. *et al.* A tissue-specific atlas of mouse protein phosphorylation and expression. *Cell* **143**, 1174–1189 (2010).

480.   Savitski, M. M., Wilhelm, M., Hahne, H., Kuster, B. & Bantscheff, M. A scalable approach for protein false discovery rate estimation in large proteomic data sets. *Mol. Cell. Proteomics* **14**, 2394–2404 (2015).

481.   Beausoleil, S. A., Villén, J., Gerber, S. A., Rush, J. & Gygi, S. P. A probability-based approach for high-throughput protein phosphorylation analysis and site localization. *Nat. Biotechnol.* **24**, 1285–1292 (2006).

482.   Tyanova, S. *et al.* The Perseus computational platform for comprehensive analysis of (prote)omics data. *Nat. Methods* **13**, 731–740 (2016).

483.   Subramanian, A. *et al.* Gene set enrichment analysis: A knowledge-based approach for interpreting genome-wide expression profiles. *Proc. Natl. Acad. Sci. U. S. A.* **102**, 15545–15550 (2005).

484.   Wiredja, D. D., Koyutürk, M. & Chance, M. R. The KSEA App: a web-based tool for kinase activity inference from quantitative phosphoproteomics. *Bioinformatics* **33**, 3489–3491 (2017).

485.   Mitne-Neto, M. *et al.* Downregulation of VAPB expression in motor neurons derived from induced pluripotent stem cells of ALS8 patients. *Hum. Mol. Genet.* **20**, 3642–3652 (2011).

486.   Alves, C. J. *et al.* Gene expression profiling for human iPS-derived motor neurons from sporadic ALS patients reveals a strong association between mitochondrial functions and neurodegeneration. *Front. Cell. Neurosci.* **9**, 289 (2015).

487.   Esanov, R. *et al.* C9orf72 promoter hypermethylation is reduced while hydroxymethylation is acquired during reprogramming of ALS patient cells. *Exp. Neurol.* **277**, 171–177 (2016).

488.   Kapeli, K. *et al.* Distinct and shared functions of ALS-associated proteins TDP-43, FUS and TAF15 revealed by multisystem analyses. *Nat. Commun.* **7**, 12143 (2016).

489.   Sivadasan, R. *et al.* C9ORF72 interaction with cofilin modulates actin dynamics in motor neurons. *Nat. Neurosci.* **19**, 1610–1618 (2016).

490.   Rodriguez-Muela, N. *et al.* Single-Cell Analysis of SMN Reveals Its Broader Role in Neuromuscular Disease. *Cell Rep.* **18**, 1484–1498 (2017).

491. Gendron, T. F. *et al.* Poly(GP) proteins are a useful pharmacodynamic marker for *C9ORF72* -associated amyotrophic lateral sclerosis. *Sci. Transl. Med.* **9**, eaai7866 (2017).

492. Tang, Y., Liu, M.-L., Zang, T. & Zhang, C.-L. Direct Reprogramming Rather than iPSC-Based Reprogramming Maintains Aging Hallmarks in Human Motor Neurons. *Front. Mol. Neurosci.* **10**, 359 (2017).

493. Tsuburaya, N. *et al.* A small-molecule inhibitor of SOD1-Derlin-1 interaction ameliorates pathology in an ALS mouse model. *Nat. Commun.* **9**, 2668 (2018).

494. Bossolasco, P. *et al.* Motor neuron differentiation of iPSCs obtained from peripheral blood of a mutant TARDBP ALS patient. *Stem Cell Res.* **30**, 61–68 (2018).

495. Vogt, M. A. *et al.* TDP-43 induces p53-mediated cell death of cortical progenitors and immature neurons. *Sci. Rep.* **8**, 8097 (2018).

496. Osborn, T. M., Beagan, J. & Isacson, O. Increased motor neuron resilience by small molecule compounds that regulate IGF-II expression. *Neurobiol. Dis.* **110**, 218–230 (2018).

497. Luisier, R. *et al.* Intron retention and nuclear loss of SFPQ are molecular hallmarks of ALS. *Nat. Commun.* **9**, 2010 (2018).

498. Sun, X., Song, J., Huang, H., Chen, H. & Qian, K. Modeling hallmark pathology using motor neurons derived from the family and sporadic amyotrophic lateral sclerosis patient-specific iPS cells 11 Medical and Health Sciences 1109 Neurosciences. *Stem Cell Res. Ther.* **9**, 1–14 (2018).

499. Shlevkov, E. *et al.* A High-Content Screen Identifies TPP1 and Aurora B as Regulators of Axonal Mitochondrial Transport. *Cell Rep.* **28**, 3224-3237.e5 (2019).

500. Vandoorne, T. *et al.* Differentiation but not ALS mutations in FUS rewires motor neuron metabolism. *Nat. Commun.* **10**, 4147 (2019).

501. Tung, Y.-T. *et al.* Mir-17~92 Confers Motor Neuron Subtype Differential Resistance to ALS-Associated Degeneration. *Cell Stem Cell* **25**, 193-209.e7 (2019).

502. Bellmann, J. *et al.* Viral Infections Exacerbate FUS-ALS Phenotypes in iPSC-Derived Spinal Neurons in a Virus Species-Specific Manner. *Front. Cell. Neurosci.* **13**, 480 (2019).

503. Catanese, A. *et al.* Retinoic acid worsens ATG10-dependent autophagy impairment in TBK1-mutant hiPSC-derived motoneurons through SQSTM1/p62 accumulation. *Autophagy* **15**, 1719–1737 (2019).

504. Akiyama, T. *et al.* Aberrant axon branching via Fos-B dysregulation in FUS-ALS motor neurons. *EBioMedicine* **45**, 362–378 (2019).

505. Genin, E. C. *et al.* Mitochondrial defect in muscle precedes neuromuscular junction degeneration and motor neuron death in CHCHD10S59L/+ mouse. *Acta Neuropathol.* **138**, 123–145 (2019).

506. Keskin, I. *et al.* The molecular pathogenesis of superoxide dismutase 1-linked ALS is promoted by low oxygen tension. *Acta Neuropathol.* **138**, 85–101 (2019).

507. Wong, C.-O. & Venkatachalam, K. Motor neurons from ALS patients with mutations in C9ORF72 and SOD1 exhibit distinct transcriptional landscapes. *Hum. Mol. Genet.* **28**, 2799–2810 (2019).

508. Jeon, G. S. *et al.* Pathological Modification of TDP-43 in Amyotrophic Lateral Sclerosis with SOD1 Mutations. *Mol. Neurobiol.* **56**, 2007–2021 (2019).

509. Tyzack, G. E. *et al.* Widespread FUS mislocalization is a molecular hallmark of amyotrophic lateral sclerosis. *Brain* **142**, 2572–2580 (2019).

510. Seminary, E. R. *et al.* Motor Neuron Generation from iPSCs from Identical Twins Discordant for Amyotrophic Lateral Sclerosis. *Cells* **9**, 571 (2020).

511. Oliveira, D. *et al.* Different gene expression profiles in iPSC-derived motor neurons from ALS8 patients with variable clinical courses suggest mitigating pathways for neurodegeneration. *Hum. Mol. Genet.* **29**, 1465–1475 (2020).

512. Kim, B. W., Jeong, Y. E., Wong, M. & Martin, L. J. DNA damage accumulates and responses are engaged in human ALS brain and spinal motor neurons and DNA repair is activatable in iPSC-derived motor neurons with SOD1 mutations. *Acta Neuropathol. Commun.* **8**, 7 (2020).

513. Bardelli, D. *et al.* Reprogramming fibroblasts and peripheral blood cells from a *C9ORF72* patient: A proof-of-principle study. *J. Cell. Mol. Med.* **24**, 4051–4060 (2020).

514. Ababneh, N. A. *et al.* Correction of amyotrophic lateral sclerosis related phenotypes in induced pluripotent stem cell-derived motor neurons carrying a hexanucleotide expansion mutation in C9orf72 by CRISPR/Cas9 genome editing using homology-directed repair. *Hum. Mol. Genet.* **29**, 2200–2217 (2020).

515. Rajpurohit, C. S. *et al.* Mechanistic Insights of Astrocyte-Mediated Hyperactive Autophagy and Loss of Motor Neuron Function in SOD1L39R Linked Amyotrophic Lateral Sclerosis. *Mol. Neurobiol.* **Online**, Ahead of Print (2020).

516. Kim, K. Y. *et al.* Downregulated miR-18b-5p triggers apoptosis by inhibition of calcium signaling and neuronal cell differentiation in transgenic SOD1 (G93A) mice and SOD1 (G17S and G86S) ALS patients. *Transl. Neurodegener.* **9**, 23 (2020).

517. Jensen, B. K. *et al.* Synaptic dysfunction induced by glycine-alanine dipeptides in C9orf72-ALS/FTD is rescued by SV2 replenishment. *EMBO Mol. Med.* **12**, e10722 (2020).

518. Bräuer, S., Günther, R., Sterneckert, J., Glaß, H. & Hermann, A. Human spinal motor neurons are particularly vulnerable to cerebrospinal fluid of amyotrophic lateral sclerosis patients. *Int. J. Mol. Sci.* **21**, 3564 (2020).

519. Blokhuis, A. M., Groen, E. J. N. N., Koppers, M., Van Den Berg, L. H. & Pasterkamp, R. J. Protein aggregation in amyotrophic lateral sclerosis. *Acta Neuropathol.* **125**, 777–794 (2013).

520. Smith, H. L., Li, W. & Cheetham, M. E. Molecular chaperones and neuronal proteostasis. *Semin. Cell Dev. Biol.* **40**, 142–152 (2015).

521. Kieran, D. *et al.* Treatment with arimoclomol, a coinducer of heat shock proteins, delays disease progression in ALS mice. *Nat. Med.* **10**, 402–405 (2004).

522. Kalmar, B. *et al.* Late stage treatment with arimoclomol delays disease progression and prevents protein aggregation in the SOD1G93A mouse model of ALS. *J. Neurochem.* **107**, 339–350 (2008).

523. Song, Y. *et al.* Molecular chaperone Hsp110 rescues a vesicle transport defect produced by an ALS-associated mutant SOD1 protein in squid axoplasm. *Proc. Natl. Acad. Sci. U. S. A.* **110**, 5428–33 (2013).

524. Nagy, M., Fenton, W. A., Li, D., Furtak, K. & Horwich, A. L. Extended survival of misfolded G85R SOD1-linked ALS mice by transgenic expression of chaperone Hsp110. *Proc. Natl. Acad. Sci.* **113**, 5424–5428 (2016).

525. Leak, R. K. Heat shock proteins in neurodegenerative disorders and aging. *J. Cell Commun. Signal.* **8**, 293–310 (2014).

526. Meares, G. P., Zmijewska, A. A. & Jope, R. S. HSP105 interacts with GRP78 and GSK3 and promotes ER stress-induced caspase-3 activation. *Cell. Signal.* **20**, 347–358 (2008).

527.   Cowan, C. A. *et al.* Derivation of Embryonic Stem-Cell Lines from Human Blastocysts. *N. Engl. J. Med.* **350**, 1353–1356 (2004).

528.   Rigamonti, A. *et al.* Large-scale production of mature neurons from human pluripotent stem cells in a three-dimensional suspension culture system. *Stem Cell Reports* **6**, 993–1008 (2016).

Chapter 8

Appendix A

Compendium of ALS iPSC-derived Neuronal Studies

This table includes published reports utilizing neurons derived from ALS patient iPSCs.

For brevity, studies exclusively using non-neuronal derivatives of ALS-iPSCs, FTD-C9ORF72 patient iPSC derivatives, control iPSCs transiently exposed to ALS mutant alleles/proteins, or ALS-hESCs were excluded, unless otherwise indicated.

The listed ALS-associated variants, functional assays and methodologies are focused to those used in the iPSC-derived neurons, but may include techniques used in additional models relevant to the study (mouse, Drosophila, neuro2a/NSC-34,HEK293T cells, postmortem samples, etc.).

Any omission or error is unintentional and solely the responsibility of the primary author.

ALS-Associated Variant	MN Functional Assay (Stressor, Technique)	ALS Phenotypes and Therapeutic Findings	Reference
SOD1[L144F]	• MN production (7-15 days culture maturation, IF- Hb9, Isl1/2, TUJ1, ChAT, and GFAP).	• First report showing ALS patient iPSCs could generate MNs and astrocytes.	Dimos et al., 2008[339]
SOD1[L144F] SOD1[G85S]	• MN production/differentiation efficiency (3 days culture maturation, IF- Hb9, Isl1/2, TUJ1, CHAT, Ki67). • MN electrophysiology (no stimulus, kainate, KCL, tetrodotoxin treatment, Ca^{2+} dye imaging, whole-cell-voltage-clamp, or current-clamp recording)	• Control and SOD1-ALS patient iPSCs had comparable differentiation efficiencies into MNs. • MNs were electrically active. • Donor sex and identity were areas of variability.	Boulting et al., 2011[344]
VAPB[P56S]	• MN production/differentiation efficiency (4-7 weeks culture maturation, IF- Isl1/2, MAP2, Hb9-GFP reporter). • NMJ formation (4 weeks coculture with C2C12 myoblasts, α-bungarotoxin incorporation, IF) • Protein aggregation (7 weeks culture or 5µM, 24hrs MG132 proteasome inhibition stimulus, WB, IF) • VAPB levels (qPCR, WB)	• VAPB iPSC-derived MNs could be produced and formed functional NMJs. • VAPB iPSC-derived MNs did not have basal cytoplasmic VAPB[+] inclusions (in contrast with overexpression systems). No difference in stimulated VAPB or ubiquitinated proteins between ALS/control. • VAPB iPSC-derived MNs had decreased levels of VAPB (mRNA not changed).	Mitne-Neto et al., 2011[485]
TDP-43[M337V]	• MN production/differentiation efficiency (4-6 weeks culture maturation, IF-Hb9, TUJ1, SMI-32, CHAT). • MN electrophysiology (whole-cell-voltage-clamp or tetrodotoxin, current-clamp recording) • Soluble and detergent resistant protein levels (TDP-43, WB) • MN survival assays (unstressed, 10 days longitudinal Hb9-GFP fluorescence microscopy, or 48hrs stressed, MAPK inhibitor U0126, PI3K inhibitor LY294002, ER stressor tunicamycin, LDH release)	• TDP-43 iPSC-derived MNs could be produced and were electrically active. • TDP-43 mutant MNs had increased levels of soluble and detergent resistant TDP-43. • TDP-43 mutant MNs had increased risk of death in basal longitudinal studies and increased vulnerability to PI3K inhibitor.	Bilican et al., 2012[354]
TDP-43[M337V] TDP-43[G298S] TDP-43[Q343R]	• MN production/differentiation efficiency (IF- Isl1, Hb9, SMI-32, CHAT, MAP2). • NMJ formation (2 weeks coculture with C2C12 myoblasts, α-bungarotoxin incorporation, IF)	• TDP-43 iPSC-derived MNs could be produced, formed NMJs, and were electrically active. • TDP-43 mutant MNs had shorter neurites, decreased expression of genes encoding cytoskeletal intermediate filaments and enriched transcripts related to	Egawa et al., 2012[359]

ALS-Associated Variant	MN Functional Assay (Stressor, Technique)	ALS Phenotypes and Therapeutic Findings	Reference
	• MN electrophysiology (whole-cell-patch-clamp or current-clamp recording) • Neurite analysis (Hb9-GFP FACs and fluorescent microscopy) • Gene expression analyses (qPCR, microarray) • Detergent insoluble protein levels (basal and arsenite-induced TDP-43, WB) • Intracellular localization (IF) • MN survival assay (arsenite-induced oxidative stress, IF)	RNA binding, RNA granules, splicing/spliceosomal complex, nuclear transport. • TDP-43 mutant MNs had increased detergent insoluble TDP-43 (bound to splicing factor SNRPB2) and increased TDP-43 cytoplasmic localization, forming preinclusion-like aggregates. • TDP-43 mutant MNs exhibited enhanced death with arsenite exposure. • Anacardic acid protected against degenerative phenotypes.	
SOD1[L144F] TDP-43[M337V]	• MN production • MN survival assay (14 days TF withdrawal, IF-Isl1, TUJ1, MAP2).	• ALS patient MNs had enhanced death with TF withdrawal. • Primary hit from mESC-MN survival screen (kenpaullone) promoted ALS patient MN survival.	Yang et al., 2013[360]
SOD1[A4V] SOD1[N139K] TDP-43[A315T] FUS[G1566A] sALS	• MN production/functional characterization (2 weeks-3 months culture, IF- Isl1, Hb9, SMI-31, MAP2, CTIP2, whole-cell-patch-clamp recording, tetrodotoxin, calcium imaging) • Intracellular localization and aggregation (IF- TDP-43, Phospho-TDP-43, Lamin-A, with above neuron IF markers)	• sALS and fALS iPSC-derived MNs could be produced and were electrically active. • 3/16 sALS derived MNs formed de novo phospho-TDP-43 intranuclear aggregates (1 matched to patient post-mortem sample) • HTS identified TDP-43 aggregation inhibitors, including CDK inhibitors, JNK inhibitors, triptolide, cardiac glycosides, digoxin, lanatoside C and proscillaridin A.	Burkhardt et al., 2013[421]
C9ORF72	• Neuronal production/ characterization (IF- TUJ1, Hb9, Southern blot analysis for C9ORF72 expansion, probe nanostring RNA detection for c9ORF72 mRNA) • Intranuclear GGGGCC RNA foci detection (FISH) • Cytoplasmic RNA foci and RAN peptide detection (FISH, IF- TUJ1, C9RANT) • GGGGCC RNA foci binding partner analysis (proteome array, RNA FISH- IF, RNA coIP, EMSA) • Gene expression analyses (microarray)	• C9ORF72 patient iPSC-derived neurons exhibited reduced C9ORF72 RNA levels and displayed intranuclear GGGGCC repeat containing RNA foci. These RNA foci interacted with RNA binding protein ADARB2 (not TDP-43, FUS, P62, Pur-α, or hnRNPA1). • C9ORF72 patient iPSC-derived neurons had cytoplasmic RAN translation peptides. • C9ORF72 patient iPSC-derived neurons had unique and aberrant gene expression. • C9ORF72 mutant neurons were more susceptible to glutamate-mediated excitotoxicity.	Donnelly et al., 2013[377]

ALS-Associated Variant	MN Functional Assay (Stressor, Technique)	ALS Phenotypes and Therapeutic Findings	Reference
	• MN survival assay (glutamate-mediated excitotoxicity, IF)	• Novel ASOs targeting GGGGCC repeat expansion sequence mitigated all toxic phenotypes (suggests RNA expansions are directly toxic).	
C9ORF72	• MN production/ characterization (IF- TUJ1, SMI-32, ChAT, Hb9, Southern blot analysis for C9ORF72 expansion, electrophysiology with patch-clamp recordings) • MN survival assay (4-7 weeks culture, IF- SMI-32, TUJ1) • Gene expression analysis (C9ORF72 transcript, RNA-seq, qRT-PCR, 5'RACE, protein levels, WB) • GGGGCC RNA foci detection and colocalization (FISH, IF-SMI-32) • RAN protein (DPR) detection	• C9ORF72 patient iPSC-derived MNs were produced with pathological expansions, proper morphology, markers, and electrical activity, but no basal survival difference between control MNs. • C9ORF72 patient iPSC-derived MNs did not have reduced C9ORF72 expression (RNA/protein), instead altered use of mutant allele. • C9ORF72 mutant MNs displayed intranuclear GGGGCC repeat containing RNA foci, which colocalized with hnRNPA1 and Pur-α (not TDP-43 or FUS). No detection of RAN products (DPRs). • C9ORF72 mutant MNs had altered expression of genes involved in membrane excitability/synaptic transmission, displayed hypoexcitability. • ASO mediated knockdown of C9ORF72 transcript not toxic, suppressed RNA foci formation and reversed gene expression alterations (supporting gain of toxicity).	Sareen et al., 2013[378]
TDP-43[M337V]	• MN production • Astrocyte production/functional characterization (IF- vimentin, NF1A, GFAP, S100B, EAAT1, glutamate uptake assay) • MN-astrocyte co-culture synapse formation (3-week culture, IF- PSY, PSD-95, stimulated calcium waves) • Gene expression analyses (qRT-PCR- TDP-43, HDAC6) • Protein levels (soluble and insoluble, WB- TDP-43) • Cellular localization (IF- TDP-43) • Astrocyte survival assay (10-day culture, constitutive EGFP	• TDP-43 patient and control astrocytes were produced with comparable efficiencies, functional glutamate clearance, and formation of mature synapses. • TDP-43 patient astrocytes had equivalent TDP-43 mRNA levels, increased cytosolic TDP-43 mislocalization (phenocopied by ectopic expression in control astrocytes), increased soluble TDP-43 protein, but no increase in detergent resistant TDP-43. • TDP-43 patient astrocytes had increased risk of death (hazard ratio) compared to controls.	Serio et al., 2013[355]

ALS-Associated Variant	MN Functional Assay (Stressor, Technique)	ALS Phenotypes and Therapeutic Findings	Reference
	reporter, longitudinal fluorescent microscopy) • MN-astrocyte survival assay (10-day culture, Hb9-GFP reporter longitudinal fluorescent microscopy	• TDP-43 patient astrocytes were not toxic to control MNs. • TDP-43 patient MNs cultured alone displayed cell-autonomous survival deficits, and surprisingly co-culture with either control or TDP-43 mutant patient astrocytes rescued the survival deficit. • Data indicate the absence of a non-cell autonomous astrocyte phenotype in TDP-43-ALS.	
TDP-43^{M337V} TDP-43^{A90V}	• Neuronal production/functional characterization (IF-TUJ1, electrophysiology with whole-cell voltage clamp and current clamp recordings) • Neuron survival assays (sorbitol osmotic/oxidative stress, sodium arsenite and tBOOH oxidative stress, and staurosporine apoptosis) • Cellular localization (IF-TDP-43) • Soluble vs insoluble protein (basal and staurosporine induced- TDP-43, WB) • Gene expression analysis (qRT-PCR)	• TDP-43 mutant neurons were produced with TUJ1 staining, normal action potentials, but decreased spontaneous synaptic currents. • With staurosporine exposure, TDP-43 mutant neurons exhibited enhanced TDP-43 cytoplasmic mislocalization, reduced soluble and insoluble TDP-43, reduced microRNA-9 levels, and increased death.	Zhang et al., 2013[361]
SOD1^{A4V} SOD1^{D90A} SOD1^{G85S} FUS^{M511FS} FUS^{H517Q} C9ORF72	• MN electrophysiology (14 days to 4 weeks culture, basal and treated with bicuculline or strychnine, +/-Hb9-FP FACs, multielectrode array, whole-cell patch-clamp recordings) • MN survival assay (30 days culture, IF- Isl1, TUJ1)	• ALS patient iPSC-derived MNs displayed hyperexcitability and reduced delayed-rectifier potassium current amplitudes. • Genetic correction of SOD1^{A4V} allele rescued hyperexcitability. • Retigabine, a Kv7 channel activator, blocked hyperexcitability and improved SOD1^{A4V} MN survival.	Wainger et al., 2014[346]
SOD1^{A4V} C9ORF72	• MN production/functional characterization (IF-TUJ1, Isl1/2, Hb9, spinal cord integration) • MN electrophysiology- basal, tetrodotoxin, kainate, linopiridine, whole cell voltage-clamp or current-clamp recording) • MN survival assay (30-day culture, IF- Isl1, TUJ1, TUNEL apoptosis) • MN morphology (soma size, neurite extension)	• MNs produced with normal markers, electrical activity, and spinal cord integration. • SOD1 mutant MNs had increased apoptotic death, reduced soma size, and fewer/shorter neuritic processes with time in culture (genetic correction rescued phenotypes). • MG132 induced insoluble SOD1 in mutant MNs (not gene-corrected controls). No basal insoluble SOD1.	Kiskinis et al., 2014[345]

ALS-Associated Variant	MN Functional Assay (Stressor, Technique)	ALS Phenotypes and Therapeutic Findings	Reference
	• Zing-finger SOD1 allelic correction • Soluble vs insoluble protein (basal and MG132 induced-SOD1, WB, IF) • Gene expression analyses (RNA-seq, qRT-PCR) • Mitochondrial structure and function (EM, MitoTracker and live imaging). • ER stress/UPR evaluation (siRNA, qRT-PCR, splicing assay, 15-day salubrinal rescue, DTT treatment)	• SOD1 mutant MNs had dysregulated transcripts related to cytoskeletal organization, mitochondrial structure, and function. Corresponded to vacuolar mitochondria (EM) and decreased mitochondria movement. • SOD1 mutant MNs had increased ER stress/UPR induction transcripts and gene expression, linked to electrical activity (hyperexcitable). (control MNs also had inherently high ER stress signatures- suggested inherent MN vulnerability). • SOD1 mutant survival deficit and electrical activity rescued by salubrinal. • C9ORF72 MNs shared subset of SOD1 dysregulated transcripts.	
SOD1[A4V] SOD1[D90A]	• MN production/function (IF-Isl1, Hb9, TUJ1, ChAT, electrophysiology, NMJ formation) • TALEN mediated gene correction (SOD1) and expression (SOD1, NF-L) • Gene expression levels (SOD1, NF- qRT-PCR, WB) RNA stability assay • Mutant protein localization and aggregation (Immuno-EM, IF-NF) • MN survival assay (10-20 days culture, LDH release, IF-cleaved caspase 3, TUNEL) • Neurite analysis (7-20-day culture, phase contrast microscopy, IF- p-NF-H, ChAT)	• SOD1 mutant MNs differentiate efficiently, with proper MN markers, electrical activity, and NMJ formation. • SOD1 mutant MNs exhibited small SOD1 aggregates, NF aggregation, neurite degeneration (bead-like swellings) and increased apoptotic cells with 20 days culture. • mutant SOD1 bound to NF-L mRNA 3'UTR, decreased NF-L mRNA stability and levels, altered NF subunit proportion in MNs. • Phenotypes mimicked by mutant SOD1 expression in hESC, prevented by gene correction in SOD1 mutant iPSC MNs, and prevented by NF-L expression.	Chen et al., 2014[351]
TDP-43[M337V] TDP-43[G298S] TDP-43[A315T]	• Axonal trafficking (Cy3 tagged Neurofilament-L mRNA, live fluorescent imaging over 17 days in culture)	• TDP-43 patient MNs had decreased anterograde transport and increased retrograde transport compared to controls by days 9-13. • Axonal trafficking also impaired in Drosophila and primary cortical neurons, and TDP-43 is a component of trafficked mRNP granules.	Alami et al., 2014[164]

ALS-Associated Variant	MN Functional Assay (Stressor, Technique)	ALS Phenotypes and Therapeutic Findings	Reference
TDP-43^{M337V}	• MN survival assay, hazard ratio over 200hrs (IF- Hb9-FP, MAP2)	• TDP-43 patient derived MNs exhibited elevated risk of death compared to WT derived MNs. • Treatment with novel compounds stimulating autophagy (identified from in silico screen) reduced hazard ratio in TDP-43 mutant derived MNs (nonsignificant), significantly reduced hazard in mutant derived astrocytes.	Barmada et al., 2014[356]
TDP-43^{M337V} C9ORF72	• MN production (5-6 weeks culture, IF- TUJ1, Hb9, genotyping, repeat primed PCR, RNA foci FISH) • MN survival (10 weeks culture, IR-DIC, LDH release, nuclei morphologic analysis). • MN electrophysiology (2-10 weeks culture, basal or stimulated with glutamate or GABA, whole-cell, voltage, or current-clamp recordings).	• ALS patient derived MNs were produced with comparable efficiencies and viabilities to controls. • ALS patient derived MNs displayed initial hyperexcitability, followed by loss of action potential output and synaptic activity resulting from decreased voltage activated Na^+/K^+ currents.	Devlin et al., 2015[353]
FUS^{P525L}	• MN production (8-day culture after dissociation, IF- Hb9, Isl1/2, TUJ1) • Cellular localization (IF- FUS)	• FUS patient MNS were efficiently produced and displayed increased FUS mislocalization into the cytoplasmic aggregates (notably not observed in patient fibroblasts)	Liu et al., 2015[365]
FUS^{R521C} FUS^{R495QfsX527}	• MN/cortical neuronal differentiation (45-day culture, IF- SMI32, MAP2, Ctip2, SatB2, FopP2) • Cellular localization/inclusion bodies (0 to 100 days differentiation, IF- FUS, meFUS) • Cortical neuron survival (60-80-day culture, 4-day treatment +/ 5μM sodium arsenite, IF- MAP2)	• FUS patient cortical neurons displayed basal cytoplasmic FUS mislocalization (Day 0 iPSC stage in the malignant frameshift mutation) which increased with aging in a manner correlated with the severity of disease mutation (Day 60 both benign and malignant mutant FUS neurons displayed cytoplasmic mislocalization, not controls, and meFUS became observable in both mutants at day 80). • Formation of FUS inclusions was also mutation and age dependent, with the malignant frame shift demonstrating basal inclusions by day 40, and the benign mutation and controls displaying these by day 60 (not significantly different). • FUS mislocalization and granule formation not specific to layer V	Japtok et al., 2015[366]

ALS-Associated Variant	MN Functional Assay (Stressor, Technique)	ALS Phenotypes and Therapeutic Findings	Reference
		cortical neurons (also in layer II/III neurons). • Malignant FUS line also had decreased viability with age and with arsenite stress (trend with benign mutant but not significant). • Data support a 2hit pathogenesis (1st hit mislocalized FUS from nucleus, 2nd hit from aging, cellular stress/persistent stress, inclusion formation)	
<u>Patient Mutations</u> FUS^{R514S} FUS^{R521C} TDP-43^{A382T} <u>Mutation Introduced</u> FUS^{P525L}	• MN production/differentiation efficiency (6-day culture after dissociation, IF/qRT-PCR- Hb9, Isl1, ChAT) • TALEN directed introduction of mutant allele • Cellular localization • Stress granule detection (basal and stressed with sodium arsenite, sorbitol treatment, heat shock, IF- FUS, TIAR, PABP)	• ALS patient MNs were efficiently produced comparable to control MNs. • FUS mutants displayed varying levels of basal FUS cytoplasmic mislocalization (strongest in P525L), which were increased with stress induction, causing mislocalization and recruitment into stress granules in a manner proportional to the basal cytoplasmic localization caused from each mutation.	Lenzi et al., 2015[367]
C9ORF72	• Neuron production (IF- Isl1, VGlut, MAP2, Hb9, TUJ1, SMI-32, SYT1, SYP, ChAT, NMDAR) • Cellular localization (RNA-FISH- IF, IF- G4C2 RNA, Nup205, Ubiquitin, LaminB) • Nuclear/cytoplasmic ratio (50-70-day culture, IF- Ran) • Nucleocytoplasmic transport (tdTomato reporter with classical NLS and NES, fluorescence recovery after photobleaching) • ASO treatment	• C9ORF72 patient neurons were comparably produced, and exhibited G_4C_2 RNA puncta that co-localized with RanGAP1and Nup205 (component of the nuclear pore complex) (RanGAP, as well as proteins that enhance nuclear import or suppress nuclear export, identified as a genetic modifier of C9ORF72 HRE toxicity in Drosophila) • C9ORF72 patient neurons had decreased N/C ratio of endogenous ran in mature MAP2$^+$ or ChAT$^+$ neurons, and overexpression of RanGAP1-GFP rescued the disrupted N/C Ran gradient • C9ORF72 patient neurons also had impaired nuclear import (reduced nuclear recovery of nucleocytoplasmic reporter protein and a decreased N/C ratio for TDP-43) • Strand sense ASO reduced RNA foci and rescued disrupted N/C Ran and TDP-43 gradient, suggesting nucleocytoplasmic	Zhang et al., 2015[250]

ALS-Associated Variant	MN Functional Assay (Stressor, Technique)	ALS Phenotypes and Therapeutic Findings	Reference
		transport deficits are due to C9ORF72 RNA sense-strand toxicity.	
Patient Mutation FUS^R521C Mutation Introduced FUS^P525L	• MN production (day 34, IF-Isl1/2) • TALEN directed introduction of mutant allele • Cellular localization (basal, sodium arsenite induced, IF-FUS, Pur-α)	• FUS mutant MNs had basal cytoplasmic FUS mislocalization (P525L) and arsenite-enhanced mislocalization that colocalized with Pur-α in stress granule aggregates (both mutations, lesser extent P521C) • In HeLa, NSC-43, mouse spinal cord neurons, or Drosophila models, Pur-α physically interacted with mutant FUS, co-localized with mutant FUS in stress granules, associated with ribosomes, and promoted translation inhibition by phosphorylation of eIF2α. Decreased levels of Pur-α ameliorated mutant-FUS effects and increased levels exacerbated them.	Di Salvio et al., 2015[401]
sALS	• MN production (differentiation day 20, IF- MAP2, ChAT, Hb9-GFP reporter, qRT-PCR/qPCR-Hb9, ChAT) • Gene expression analyses (microarray)	• sALS patient MNs were produced with comparable efficiencies to controls and had differentially expressed genes related to synapse organization, aging, mitochondria and oxidative phosphorylation, intracellular transport, and cell death.	Alves et al., 2015[486]
SOD1^D90A SOD1^R115G FUS^R521C FUS^R521L FUS^R495QfsX527	• MN production (DIV 32, 1-week culture after plating, IF-TUJ1, Isl1, MAP2, ChAT, SMI-32) • Basal MN viability and apoptosis detection (IF- cleaved caspase 3, LDH release, MTT) • MN electrophysiology (7-week culture, whole-cell patch-clamp, current-clamp) • Gene expression analyses (qRT-PCR- SCNA1, SCNA3, SCNA5, SCNB3, SCNB4, Kv1.1, Kv1.3, Kv1.7, Kv2.2, Kv3.1, ATF4, BiP, GrP94, CHOP)	• ALS patient MNs had comparable differentiation efficiencies and basal viability to control MNs. • ALS patient MNs were hypoexcitable due to reduced Na^+/K^+ ratios by elevated K^+ channel expression (FUS) and attenuated Na^+ channel expression (FUS, SOD1). • ALS patient MNs had elevated ER stress levels and increased caspase activation • Treatment with the FDA approved K^+ channel blocker, 4AP, restored ion-channel imbalances, increased neuronal activity and decreased ER stress and caspase activation.	Naujock et al., 2016[348]
C9ORF72 with promoter hypermethylation	• MN production (IF- Isl1, TUJ1, Hb9-GFP lentiviral reporter) • DNA methylation detection (methylation sensitive HhaI	• 5-methylcytosine (5mC) levels (occurs in 30% C9ORF72 ALS patients, represses repeat transcription, and hypothesized to	Esanov et al., 2016[487]

ALS-Associated Variant	MN Functional Assay (Stressor, Technique)	ALS Phenotypes and Therapeutic Findings	Reference
	restriction digest-qPCR, quantitative bisulfite pyrosequencing) • DNA hydroxymethylation detection (MspI/HpaII restriction digest-qPCR)	be protective) are reduced by reprogramming and re-acquired during neuronal specification. • 5-hydroxymethylcytosine (5hmC) (a stable intermediate before demethylation, indicates active demethylation) increases following reprogramming and is highest in iPSCs and MNs.	
FUS^{R521C} FUS^{R495QfsX527} FUS^{Asp502ThrfS*27}	• MN production (21- and 42-day culture, IF-TUJ1, NF-H, Hb9, Isl1, ChAT, MAP2) • Stress induction by γ-irradiation. • Cellular localization (IF-FUS) • Stress granule detection (IF-TIA1, FUS) • DNA damage (IF- γH2A.X)	• FUS patient MNs had detectable DNA damage, increased mislocalization of FUS into cytoplasmic/neuritic stress granules. • The amount of cytoplasmic mutant FUS mislocalization positively correlated with onset of patient disease. • The degenerative in vitro phenotypes could be enhanced with age in culture and irradiation.	Higelin et al., 2016[368]
C9ORF72	• MN production/differentiation (IF- TUJ1, ChAT) • RNA foci detection (2 week- 4 months culture, FISH) • RAN DPR detection (2 weeks culture Poly-GP ELISA, 2-4 months culture Poly-GR dot blot) • DNA damage detection (4 months culture, IF/WB- γH2AX, p53, p-p53, ATR, GADD45, comet assay, TUNEL) • Gene function analysis (p53 RNAi knockdown, p53 loss of function, p53 dominant negative, hSOD1 expression, catalase, Trolox antioxidant, lentiviral DPR expression, GR-expression in HEK293T interactome analysis) • Oxidative damage detection (8 weeks – 4 months culture, MitoSOX red, dihydrorhodamine 123)	• C9ORF72 patient MNs had comparable differentiation efficiencies, detectable RNA foci, RAN translation products, increased DNA damage and oxidative stress (age-dependent) compared to controls. • Exogenous expression of DPR poly-GR$_{80}$ in control derived MNs recapitulated these phenotypes. Poly-GR$_{80}$ bound to mitochondrial ribosomal proteins, compromised mitochondrial function. • Pharmacological or genetic reduction of oxidative stress partially rescued DNA damage and toxicity (mutant MNs or Drosophila models).	Lopez-Gonzalez et al., 2016[379]
FUS^{H517D}	• MN production/differentiation (20 days culture, IF- Isl1, Hb9, TUJ1, MAP2, SMI-32, GLUR1, VGLUT1) • Gene expression analysis (MN progenitor cells, exon array, qRT-PCR, WB)	• FUS patient MNs were generated with comparable efficiency to controls, expressed similar levels of FUS, but had cytoplasmic mislocalization that colocalized with stress granules.	Ichiyanagi et al., 2016[369]

ALS-Associated Variant	MN Functional Assay (Stressor, Technique)	ALS Phenotypes and Therapeutic Findings	Reference
	• Cellular localization (IF- FUS) • Stress granule induction (0.5mM, 60mins sodium arsenite or 44°C heat shock, IF-G3BP) • Neuronal survival, neurite length (unstressed, 1mM 1hr sodium arsenite, 1mM 24hrs glutamate, Hb9-venus lentiviral expression, IF- TUJ1, cleaved caspase 3)	• FUS patient MNs were more susceptible to arsenite or glutamate induced decreases in neuritic length. • FUS patient MN progenitors had aberrant alternative splicing and gene expression, with enriched transcripts related to neuron differentiation, vesicle organization, cell adhesion.	
SOD1[A4V]	• MN production/differentiation (IF- ChAT, SMI-32, Hb9-GFP reporter) • Gene expression analyses (microarray, qRT-PCR)	• MNs differentiated from patient iPSCs resembled fetal MNs rather than adult MNs. • Gene networks/pathways associated with spinal MN maturation and aging were enriched for pathogenic fALS genetic variants and were disrupted in sALS spinal MNs.	Ho et al., 2016[399]
FUS[R521G]	• MN production/differentiation (35 days post neural induction) • Gene expression analysis (RNA-seq)	• FUS patient MNs were generated with comparable gene expression profiles to controls. • FUS mutant dependent gene expression changes were largely unique, with some overlaps with genes downregulated with loss of FUS, loss of TAF15, and simultaneous loss of FUS and TAF15 (indicates FUS and TAF15 have functional redundancy and FUS mutation is partial loss of function). • Additional data from adult mouse brains indicated TAF15 bound RNAs enriched with GGUA motifs, TAF15 and FUS exhibited similar binding patterns in introns, enriched in 3'UTRs, and altered genes distinct from TDP-43.	Kapeli et al., 2016[488]
C9ORF72	• MN production/differentiation/characterization (8 weeks culture, IF- Hb9, Isl1, TUJ1, ChAT, Synaptophysin, expansion size southern blotting, repeat primed PCR, whole-cell patch clamp, unstimulated, kainate, KCl, Ca^{2+} dynamics, Fluo-4 AM) • Cortical neuron production (70-100 days culture) • RNA foci detection (FISH)	• C9ORF72 patient MNs were efficiently produced, with intranuclear RNA foci and RAN DPRs. • C9ORF72 patient MNs had increased ER Ca^{2+}, increased UPR/stress genes, increased proapoptotic genes/apoptotic factors, decreased antiapoptotic genes, stress granules, decreased mitochondrial membrane	Dafinca et al., 2016[380]

ALS-Associated Variant	MN Functional Assay (Stressor, Technique)	ALS Phenotypes and Therapeutic Findings	Reference
	• RAN DPR detection (dot blot) • ER Ca^{2+} levels (10μM thapsigargin, 0-250 seconds, Ca^{2+} dynamics, Fluo-4 AM) • Stress granule detection (IF, WB- p62, PABP, TIA-1) • ER/UPR/apoptotic levels (WB- BiP, Bcl-2, Bcl-X_L, BAK, BIM, cytochrome c, XBP1 splicing analysis, IF- cleaved caspase 3) • Mitochondrial structure/function (MitoTracker Red, EM)	potential, and abnormal mitochondria morphology.	
C9ORF72	• MN production (IF- Hb9, ChAT, MAP2) • RAN protein (DPR) detection (IF) • Co-culture with lentiviral CMV-GFP control MNs, 22 days culture • Conditioned media application	• C9ORF72 patient MNs were efficiently produced with evidence of sense strand DPRs (GA, GR, GP). PA and PR not detected. • Evidence of GA and GR DPR transmission in C9ORF72 patient and control MN co-culture. • C9ORF72 patient MN conditioned media applied to control MNs revealed GA and GR transmission. • Trans-well, microfluidic chamber, co-culture, and conditioned media experiments from NSC32 cells, cortical neurons, and astrocytes revealed DPRs transmitted to both neurons and glia, with exosome independent transmission, anterograde/retrograde transmission, and exosome dependent pathways.	Westergard et al., 2016[385]
C9ORF72	• MN production (IF- Isl1, HB9, TUJ1, MAP2) • Actin dynamics (GFP-actin, Live cell imaging) • Gene expression analyses (WB- p-Cofilin, pLIMK1/2) Function analyses (shRNA)	• C9ORF72 patient MNS were efficiently produced, had reduced actin movement velocity compared to healthy controls, increased p-Cofilin (actin binding protein) and pLIMK1/2 (phosphorylates cofilin) (comparable to C9ORF72 shRNA knockdown), and enhanced Rac1 (rescued by Arf6 shRNA knockdown). • Data suggest C9ORF72 regulates actin dynamics via regulation of GTPase activity of Arf6 and Cofilin phosphorylation, suggesting partial loss of function mechanism.	Sivadasan et al., 2016[489]

ALS-Associated Variant	MN Functional Assay (Stressor, Technique)	ALS Phenotypes and Therapeutic Findings	Reference
SOD1[L144FVX] SOD1[G93S] TDP-43[M337V] TDP-43[G298S] TDP-43[Q343R] C9ORF72 sALS	• MN production/functional characterization (X day culture after plating, IF- Hb9, ChAT, SMI-32, TUJ1, NMJ formation with myoblast coculture αbungarotoxin, electrophysiology voltage clamp, current clamp with glutamate, kainate, or GABA) • CRISPR/Cas9 mediated gene correction (SOD1) • MN survival assay (7-day old MNs cultured additional 7 days) • Misfolded protein (IP-WB, SOD1) • Gene/protein expression analysis (WB, ELISA, p-Src, p-c-Abl, single-cell RNA-seq) • Autophagy evaluation (WB, ELISA, siRNA)	• Patient MNs comparably differentiated, expressed MN markers, formed NMJs, and were electrically active. • SOD1 mutant MNs had accumulated misfolded SOD1 and increased death with time in culture. • HTS for MN survival promoting compounds identified Src/c-Abl inhibitors as protective. Confirmed in 2[ndary] dose response curves and with siRNAs. • Hit compound bosutinib reduced phosphorylated Src/c-Abl (which was increased in mutant MNs), decreased misfolded SOD1, reversed aberrant transcriptions associated with TCA cycle and electron transport chain, and protected survival in all fALS and some sALS MNs. Also effective in SOD1 mouse. • Autophagy blockers inhibited protective effects of bosutinib, suggesting effects partly through autophagy.	Imamura et al., 2017[352]
FUS[R521H] FUS[P525L]	• MN production/differentiation (28 days culture, Day 38 of differentiation, IF- Hb9, Isl1, TUJ1, ChAT, Synapsin, SMI-32) • CRISPR/Cas9 gene correction, recombinase-mediated cassette exchange • Cellular localization (IF-FUS) • MN electrophysiology (7 weeks of differentiation, whole-cell voltage-clamp, current clamp) • Axonal transport (mitochondrial movement, MitoTracker, ER vesicle movement, ER tracker, live cell imaging) • Mitochondrial structure (EM) Overlay with ER (IF- PDI, TOM20), phosphatidylcholine production. • Gene function (HDAC inhibitor treatment- tubastatin A, ACY-738, ASOs) levels (WB, ELISA)	• FUS patient MNs had comparable differentiation efficiency, but hypoexcitability. No abnormal mitochondrial morphology, but reduced ER-mitochondrial overlay • FUS patient MNs had cytoplasmic FUS mislocalization, and progressive axonal transport defects (both mitochondrial and ER vesicles movement). Phenotypes rescued by genetic correction and reproduced by mutant expression in hESCs (suggest mutant gain of function). • Inhibiting HDAC6 increased α-tubulin acetylation, ER-mitochondrial overlay and restored axonal transport defects. Did not change FUS mislocalization.	Guo et al., 2017[239]

ALS-Associated Variant	MN Functional Assay (Stressor, Technique)	ALS Phenotypes and Therapeutic Findings	Reference
SOD1[E100G] FUS[H517Q]	• MN production/functional characterization (4-20 days culture after plating, IF- Isl1, TUJ1, MAP2, ChAT, electrophysiology, GCaMP) • CRISPR/Cas9 mediated gene correction (SOD1, FUS) • MN survival assay (low density, 20-day old MNs cultured additional 14 days, basal or treatment with JNK, ERK, p38, CDK, p53, WNT, IF- Isl1, TUJ1, cleaved caspase 3) • Gene expression analyses (ER stress- qRT-PCR CHOP, ATF3, XBP1 splicing, RNA-seq, WB-JNK, pJNK, ERK, pERK, p38, p-p38) • Cellular localization (IF- JUN) • Soluble vs insoluble protein (MG132 induced, SOD1, WB)	• Mutant SOD1 patient MNs had mature markers and electrical activity. • Mutant SOD1 patient MNs had increased apoptotic death with time, reduced soma size, decreased neurite lengths, increased ER stress, and increased MG132 induced insoluble SOD1 (phenotypes corrected with gene editing) • Mutant MNs had activated transcripts associated with p53, WNT, AP1, UPR (gene network - ERK and JNK signaling), and survival phenotype rescued with ERK, p38, JNK, WNT, and p53 inhibition). • MNs expressed nuclear JUN more than non-MNs- MN specific degenerative pathway. • Mutant FUS MNs also had activated ERK and p38 (not JNK), indicating ALS mutations converge on MAPK pathways.	Bhinge et al., 2017[347]
SOD1[G298S] SOD1[G85S] TDP-43[M337V] C9ORF72	• MN production (IF- Isl1, SMN) • Lentiviral Overexpression (SMN) • MN survival (3-day culture, plus rescue treatment MLN4924, C3)	• Individual MNs derived from the same ALS patient, in the same culture, had diverse SMN levels. • SMN overexpression and a Nedd8-activating enzyme inhibitor (which increased SMN expression) promoted survival of ALS patient MNs.	Rodriguez-Muela et al., 2017[490]
SOD1[A272C] FUS[G1566A]	• MN production (differentiation day 12, IF- Isl1, Hb9, MAP2) • CRISPR/Cas9 mediated gene correction • Gene expression analyses (RNA-seq, qRT-PCR)	• ALS patient MNs and isogenic corrected controls were produced with comparable efficiency. • SOD1 patient MNs had upregulated transcripts related to nervous system activity and signal transduction, downregulated transcripts associated with ER homeostasis, calcium homeostasis, and extracellular matrix.	Wang et al., 2017[350]
C9ORF72	• Astrocyte production (IF-GFAP) • MN production (IF-Hb9, TUJ1) • MN survival with astrocyte conditioned media (5-day culture, IF- Hb9)	• ALS patient astrocyte conditioned media decreased the viability of MNs derived from control and ALS patients iPSCs. • ALS patient astrocyte conditioned media impaired autophagic flux in HEK293T cells (lowered LC3II	Madill et al., 2017[468]

ALS-Associated Variant	MN Functional Assay (Stressor, Technique)	ALS Phenotypes and Therapeutic Findings	Reference
		levels, accumulated p62 puncta, and accumulated SOD1)	
C9ORF72	• Neuron production (TUJ1, Hb9) • PolyGP DPR detection (meso scale discovery electro-chemiluminescence detection with polyGP capture and detection antibodies) • C9ORF72 ASO treatment (treated differentiation day 45, collected every 5 days for 20 days, qRT-PCR, DPR detection)	• C9ORF72 patient neurons had detectable polyGP in cell lysates and in culture media. The amounts of extracellular polyGP correlated positively with intracellular amounts. • ASO targeting intron 1 of C9ORF72 decreased repeat containing transcripts, intracellular polyGP, and extracellular polyGP. • Additional data showed that polyGP is detected in patient CSF and from G_4C_2 mice +/- ASO treatment. PolyGP levels decreased with ASO-mediated decreases in RNA foci, RAN protein burden. • Cumulatively suggest CSF polyGP levels may serve as a pharmacodynamic marker (not prognostic) in ALS, and that monitoring poly(GP) before/during ASO-based clinical trials is a feasible approach to gauge target engagement.	Gendron et al., 2017[491]
VCP[R191Q] VCP[R155C]	• MN production (17-day culture, IF- SMI-32, ChAT, RNA-seq, whole-cell patch-clamp, +/- glutamate, KCL) • Astrocyte production (IF-GFAP, GLAST, RNA-seq, cytosolic Ca^{2+} responses to ATP but not KCl) • MN survival assay (assayed in NPCs, d3 MNs, d17 MNs, IF, longitudinal imaging, hazard ratio) Apoptosis (IF- cleaved caspase 3, nuclear pyknosis) • Synapse morphology (d17 MNs, IF- SYT1, ChAT, Homer1) • TDP-43 cellular localization (IF) • ER stress (WB- BiP, pEIF2α/eIF2α) • ER calcium stores (thapsigargin induced signal) • ER stress MN survival assay (d3 MNs, 48hrs tunicamycin, PI) • Mitochondrial-ER contact (EM)	• MNs and astrocytes were functionally produced. • VCP patient MNs had impaired basal cellular viability (d17), decreased electrical activity/coordination, and disrupted synapse formation (reduced presynaptic and post-synaptic puncta and dysregulated transcripts related to synapse structure and assembly). • VCP mutant MNs also had early phenotypes of increased cytosolic TDP-43 (d3) mislocalization, increased levels of ER stress, reduced calcium stores, increased tunicamycin induced death, altered ER morphology and mitochondrial-ER contact. • VCP mutant MNs had decreased mitochondrial membrane potential and evidence of oxidative stress (greater levels of superoxide	Hall et al., 2017[403]

ALS-Associated Variant	MN Functional Assay (Stressor, Technique)	ALS Phenotypes and Therapeutic Findings	Reference
	• Mitochondrial function (TMRM membrane potential dye, response to rotenone, superoxide production) • Astrocyte survival (d14, d28, endpoint and longitudinal analysis) • Astrocyte-MN co-culture	production and depleted glutathione levels). • VCP patient astrocytes had an increased hazard ratio compared to controls (end point analysis did not show difference, potentially due to proliferation obscuring phenotype). No increased vulnerability to tunicamycin and only transient changes in mitochondrial health and ROS production. • Control astrocyte co-culture with VCP patient MNs rescued MN survival deficit while VCP mutant astrocytes failed to promote survival. • Indicates VCP mutations have MN-autonomous and non-autonomous disease mechanisms	
C9ORF72	• MN production (1-month culture) • Cellular localization (IF- U2 snRNP compounds SNRPB2, SF3a, U1 snRNP components, DDX39B, FUS, HNRNPA1)	• C9ORF72 patient MNs showed U2 snRNP cytoplasmic mislocalization and depletion from nuclear speckle domains. • HeLa cells treated with PR peptides also showed U2 snRNP cytoplasmic mislocalization. • GR and PR DPR peptides specifically associated with U2 snRNP in nuclear extracts and blocked spliceosome assembling and splicing in vitro • U2-dependent exons are preferentially mis-spliced in C9ORF72 patient RNA-seq data. • Data suggest DPRs directly cause mislocalization/splicing dysfunction in C9ORF72 ALS.	Yin et al., 2017[391]
SOD1[G90A] FUS[H517Q] FUS[R522R] (synonymous mutation)	• Detection of aging associated features (IF- Lamin B1 folding/blebbing, γH2AX DNA damage, heterochromatin markers/nuclear organization H3K9me3, LAP2α, HP1γ, qRT-PCR- telomere length, senescence markers- p16ink4a) • MN production (equivalent protocol for donor fibroblasts and iPSCs- IF- Isl1, Hb9, ChAT, MAP2, Synapsin I)	• Aging-associated features from patient fibroblasts were reset by reprogramming to iPSCs. • Fibroblasts and iPSCs were comparably produced into mature MNs. • ALS fibroblast derived MNs maintained aging-associated features, iPSC-derived MNs did not. • ALS iPSC-derived MNs displayed TF-withdrawal induced reduction in soma size and survival rate.	Tang et al., 2017[492]

ALS-Associated Variant	MN Functional Assay (Stressor, Technique)	ALS Phenotypes and Therapeutic Findings	Reference
	• MN electrophysiology (whole-cell patch-clamp, voltage-clamp, current-clamp) • MN survival (14, 21, or 35-day culture, TF withdrawal, neuronal soma size and survival)	(Fibroblast derived MNs not tested).	
SOD1[H46R] SOD1[H43R] TDP-43[M337V] TDP34[Q343R] FUS[H517D] Sporadic ALS (58 lines total)	• MN production/differentiation/maturation (30-day culture, IF-Hb9, TUJ1, SMI-32, ChAT) • MN survival and neurite length analysis (20-70-day cultures, live imaging, IF) • Apoptosis (LDH release, caspase 3 cleavage, IF) • Protein mislocalization and aggregation (IF- TDP-43, pTDP-43, FUS, G3BP) • Transcriptional analysis (qRT-PCR, Affymetrix array) • Mitochondrial activity, lipid peroxidation analysis	• fALS and sALS patient induced MNs displayed reduced survival, increased apoptosis, reduced neurite length, and pathological protein accumulation with time. • Phenotype-case clustering illustrated a high correlation between derived in vitro disease progression with patient clinical classifications. • Multi-phenotypic HTS with FDA approved drugs identified ropinirole- rescued degenerative phenotypes (in non-SOD1 models). Protection mediated by dopamine receptors, modulated mitochondrial function, and fatty-acid related pathways.	Fujimori et al., 2018[357]
FUS[R521H] FUS[P525L]	• MN production (>7 days culture, IF- Isl1, TUJ1, MAP2, ChAT) • Oxidative stress (glucose oxidase treatment) • CoIP (FUS, PARP1, LigIII, XRCCI) • Proximity ligation assays • Cellular localization (IF- FUS) • DNA damage/repair (1hr glucose oxidase treatment, recovery 30-180mins, LA-PCR H_2O_2 treatment, TUNEL apoptosis, Comet assay- alkaline or neutral) • DNA ligation assays • CRISPR/Cas9 gene correction (FUS) • FUS ASO mediated knockdown (21-day old control MNs treated for 7 days)	• Control MNs with endogenous FUS associated with PARP1, LigIII and XRCC1 in CoIP and proximity ligation assays, increased association with oxidative stress. (direct binding from in vitro studies) • FUS patient MNs had cytoplasmic mislocalized FUS (P525L), increased DNA damage, defective/delayed DNA break repair, and reduced DNA nick ligation efficiency (rescued by gene correction). • FUS mutation defects due to 2 mechanisms- decreased nuclear presence (P525L, phenocopied with ASO) as well as dominant negative activity (R521H) in nucleus (indicated by ectopic expression, and enhanced phenotype over ASO knockdown. • Data suggest a model where FUS is required for PARP1 dependent recruitment of XRCC1/LigIII complex at oxidative DNA damage sites. Unrepaired single strand DNA damage due to FUS	Wang et al., 2018[370]

ALS-Associated Variant	MN Functional Assay (Stressor, Technique)	ALS Phenotypes and Therapeutic Findings	Reference
		mutations (as well as secondary double strand breaks) contribute to neurodegeneration.	
Patient Mutations FUS^{R521C} FUS^{R521L} FUS^{R495QfsX527} Mutation Introduced FUS^{P525L}	• MN production/functional characterization (14-30 days culture, IF- TUJ1, MAP2, Hb9, ChAT, SMI-32, Isl1, electrophysiology) • FUS pathology (IF- cytoplasmic translocation and inclusions, detergent insoluble WB- FUS, Ub) • Axonal analyses (21-110-day culture, microfluidic chambers, phase contrast, IF) • Mitochondrial, lysosomal trafficking (9-30-day culture, MitoTracker, LysoTracker, live cell imaging) • DNA double strand break analyses (basal, etoposide, arsenite, laser microirradiation, IF- γH2AX, FUS-reporter, live cell imaging)	• FUS mutant MNs were comparably produced, with no basal survival deficit, hypoexcitability, increased detergent insoluble FUS, Ub, with cytoplasmic translocation and aggregation (also methylated). • With extended culture, FUS mutant MNs developed axonal swellings, lost distal extensions, progressed to lost proximal axon integrity, with increased caspase 3 positive cells and decreased % cells (indicates dying back progressive neurodegeneration). • Prior to structural deficits, FUS mutant MNs had arrested distal mitochondria and lysosomes, reduced mitochondrial length, lost mitochondrial membrane potential in distal axons, but normal lysosome size. • Prior to FUS mislocalization, FUS mutant MNs had increased DNA double stranded breaks, and impaired recruitment to induced DNA breaks, which was rescued by restoring nuclear import or preventing export. • Inhibiting DNA repair protein PARP1 in control MNs phenocopied FUS mutations and inhibiting PARG (degrades PARP1) in FUS MNs restored phenotypes (only at the proximal soma. proximal induced DNA damage led to mislocalized FUS inclusions and PARP1/PARG inhibition induction/rescue of these phenotypes. distal action or even distal axonal inhibition (nocodazole) did not lead to fus mislocalization/DNA damage phenotypes (suggest not pure axonopathy). • Suggests a vicious cycle where FUS mutations impair nucleo-cytoplasmic shuttling and DNA damage repair (PARP-dependent),	Naumann et al., 2018[371]

ALS-Associated Variant	MN Functional Assay (Stressor, Technique)	ALS Phenotypes and Therapeutic Findings	Reference
		and DNA damage enhances FUS pathology. These are early upstream events in aggregate formation and neurodegeneration	
TDP-43[S393L] TDP-43[G294V]	• MN production (5-day culture, IF- TUJ1, MAP2, SMI-32) • Metabolic activity (PrestoBlue) • LDH release • DNA damage (IF- γH2AX) nuclear stress (IF- hnRNP K, NCL, B23) • TDP-43 localization/pathology (IF- pTDP-43) • Mitochondrial, lysosomal distal and proximal axonal trafficking analyses (2- and 4-weeks culture, MitoTracker, LysoTracker, microfluidic chambers, live imaging) • MN survival assay and neurofilament analysis (5 day to 32-day culture, IF- TUJ1, MAP2, SMI-32)	• TDP-43 patient MNs had comparable differentiation efficiency, metabolic activity, mitochondrial membrane potential. No evidence of DNA damage, nuclear stress, or TDP-43 mislocalization. • Aged TDP-43 patient MNs had reduced survival and disrupted/beady neurofilament morphology with time in culture. Also reduced mitochondrial and lysosomal axonal transport speed and displacement. • D-sorbitol treatment rescued TDP-43 MN mitochondrial and lysosomal motility.	Kreiter et al., 2018[358]
TDP-43[G294V] FUS[P525L] (From Naumann and Kreiter, 2018 studies)	• Mitochondrial, lysosomal distal and proximal axonal trafficking analyses (3-week culture, MitoTracker, LysoTracker, microfluidic chambers, live imaging)	• High content profiling and analysis of dynamic axonal organelle trafficking. • Assembled multiple phenotypic signatures discriminating between healthy and disease states, chemical perturbation, etc.	Pal et al[240]
Mutation Introduced FUS[P525L]	• CRISPR/Cas9n mediated mutant allele introduction, with either a long linker (LL) or short linker (SL) GFP reporter • MN production (3-week culture, IF- MAP2, SMI-32, Isl1, Hb9) • Cytoplasmic localization (basal, 1hr 0.5mM arsenite induced, IF- FUS, eGFP) • Gene expression analyses (q-RT-PCR, WB- FUS) • Autophagy analyses (WB-LC3II) • Apoptosis/neurite analysis (IF-cleaved caspase 3, TUJ1)	• Mutant FUS MNs had comparable differentiation efficiency to controls. Had basal FUS+ stress granule puncta that were increased with arsenite (Also FUS[wt]-SL-GFP. FUS mRNA in iPSCs not changed). • mTOR/autophagy targets identified through in a FUS-iPSC stress granule modifier HTS. • Degenerative stress granule puncta in FUS-MNs ameliorated by autophagy induction with rapamycin. Also decreased apoptosis and improved neurite branching. • BBB penetrant, clinical approved drugs identified from another FUS-iPSC stress granule HTS, paroxetine and promethazine, showed a trend of ameliorating	Marrone et al., 2018[372]

ALS-Associated Variant	MN Functional Assay (Stressor, Technique)	ALS Phenotypes and Therapeutic Findings	Reference
		arsenite induced SG phenotypes in neurons.	
SOD1^{A4V} C9ORF72	• MN production/differentiation/ maturation (southern blot and repeat primed PCR for expansion, MN markers IF-TUJ1, Hb9, VACHT, electrophysiology whole-cell patch clamp and multielectrode array, NMJ formation, myotube contraction) • MN survival assays (basal, glutamate stimulated, TF withdrawal, DPR addition, Hb9-RFP time lapse microscopy) • CRISPR/Cas9 gene editing (C9ORF72) • Expression analysis (qRT-PCR, WB, RNA-seq) Function analysis (autophagy, clearance) • Cellular localization/levels (IF, density gradient fractionation, EM, membrane fraction- WB, FISH)	• MNs produced with appropriate markers, electrical activity, NMJ and muscle contraction. • C9ORF72 mutant MNs had comparable basal survival with control, increased vulnerability to TF withdrawal, glutamate excitotoxicity (due to receptor accumulation), and DPR addition (due to reduced clearance). • C9orf72 mutant MNs had reduced C9ORF72 expression. Genetic deletion of C9ORF72 in control MNs caused survival deficits and re-expression of C9ORF72 in mutant MNs rescued survival deficits (haploinsufficiency disease mechanism). • C9ORF72 localized to cytoplasmic puncta and endosomes (RAB5$^+$). C9ORF72 mutant MNs basally had more DPR puncta. • C9ORF72 deficiency and mutation reduced DRP clearance (C9ORF72 expression normally cleared DPR), decreased lysosomal numbers, altered vesicle trafficking. • HTS for survival rescue-PIKFYVE inhibition (Apilimod). This inhibition, restored C9ORF72, or activated RAB5 rescued degenerative processes in patient MNs and gain- and loss-of C9ORF72 models (indicated importance for vesicular trafficking)	Shi et al., 2018[386]
C9ORF72	• MN production/differentiation (TF-mediated lineage conversion or dox-NIL) • MN survival assay (glutamate excitotoxicity, +/- TMX2 shRNA, Hb9-RFP longitudinal tracking)	• C9ORF72 patient MNs showed enhanced vulnerability to glutamate excitotoxicity. Survival was improved by TMX2 reduction. (TMX2 was a hit modifier of C9ORF72 DPR toxicity/induced ER stress response from genome wide CRISPR/Cas9 screens in human K562 cells and mouse primary neurons).	Kramer et al., 2018[395]

ALS-Associated Variant	MN Functional Assay (Stressor, Technique)	ALS Phenotypes and Therapeutic Findings	Reference
SOD1^{L144FVX} SOD1^{G93S} TDP-43^{M337V}	• MN survival assay (7-day culture of 7-day old MNs, IF-TUJ1)	• A small molecule inhibitor of the SOD1-Derlin-1 interaction preserved the survival of SOD1^{L144FVX} patient MNs (not SOD1^{G93S} or TDP-43^{M337V} patient MNs). • Inhibitor identified through a high throughput time resolved FRET based screen. Delayed disease onset, improved survival, and number of MNs in a SOD1^{G93A} mouse model.	Tsuburaya et al., 2018[493]
sALS (with TDP-43^{G298S}, C9ORF72, FUS, etc. SNPs)	• MN production (day 35 of differentiation, IF- TUJ1, SMI-32) • Cellular localization (IF- TDP-43) • Gene expression analyses (qRT-PCR- Hb9, Isl1, ChAT, SMI-32, Synapsin I, NEFL, NEFM) • Myogenic markers (qRT-PCR-MYH1, MYHII, MYLII, MyoD) • Apoptosis detection (IF, qRT-PCR- caspase 3/7) • Autophagy analyses (qRT-PCR-ATG5, ATG7, BECN1, ULK1, ULK2, LC3) • Motor unit on a chip (7-14 days culture of derived control skeletal myoblasts and control/sALS MNs in microfluidic chambers) • Optically stimulated muscle contraction • Derived endothelial cell barrier, p-glycoprotein expression	• Developed a functional 3D motor unit "on a chip" using microfluidic based compartmentalization of light sensitive MNs and skeletal muscle bundles. • sALS patient derived MNs had decreased MNs with time, decreased neurite length, decreased expression of genes related to neurofilament formation, acetylcholine synthesis and synapse formation, and increased cytoplasmic and nuclear aggregation of TDP-43. • The sALS motor unit generated slower/fewer thick nerve fiber projections, MN degeneration, fewer muscle contractions, and muscle apoptosis (indicates ALS MNs lead to skeletal muscle myotoxicity). • Muscle contraction and apoptosis were recovered, and neuroprotection achieved by single treatment and co-treatment with rapamycin and bosutinib, which induced autophagy and degraded TDP-43 in MNs • Cotreatment of rapamycin and bosutinib through an endothelial cell BBB-like barrier decreased expression of p-glycoprotein efflux pump transporting bosutinib, beginning indications of potential ALS treatments with BBB penetration potential.	Osaki et al., 2018[469]
TDP-43^{A382T}	• MN production (10-day culture, IF- Hb9, TUJ1, SMi-32, RT-PCR-ChAT)	• Peripheral blood mononuclear cells from TDP-43 patients can be reprogrammed to iPSCs, which	Bossolasco et al., 2018[494]

ALS-Associated Variant	MN Functional Assay (Stressor, Technique)	ALS Phenotypes and Therapeutic Findings	Reference
	• Cellular localization (IF- TDP-43)	then produce MNs with comparable efficiencies to control healthy patient cells. • TDP-43 patient MNs did not display nuclear TDP-43 localization.	
SOD1[A4V]	• MN production (IF- TUJ1, MAP2, Isl1/2) • Lentiviral transduction of optopatch genes driven by CamKIIa promoter, tagged with EGFP/mOrange2 reporter • MN electrophysiology (basal and with optogenetic stimulus, fluorescence and patch clamp recordings, 10 days after lentiviral transduction, 22-28 days post plating) • Numerical simulations	• Optimized an all-optical electrophysiology pipeline for high throughput functional characterization of hiPSC-derived neuronal cultures. • SOD1 patient MNs showed elevated spontaneous activity under weak or no stimulus (hyperexcitability) and lower firing activity (hypoexcitability) and increased likelihood of entering depolarization block with strong optogenetic stimulus. • These data, simulations, and literature review suggest deficits are due to slowly activating K^+ channels.	Kiskinis et al., 2018[414]
TDP-43[G298S]	• Cortical neuron production (characterized in Alami et al., differentiated for 39 days as in Shi et al.) • Gene expression analyses (qRT-PCR- activated caspase3, TRP53, BBC3, BAX, BCL2)	• TDP-43 patient derived cortical neurons had increased apoptosis markers and 44hrs treatment with a p53 inhibitor reduced these upregulated genes and increased cortical neuron numbers. • Expression of TDP-43 and TDP-43[A315T] resulted in aberrant neurogenesis and p53-mediated apoptosis in neural progenitor cells/immature neurons in the developing mouse telencephalon (required RRMI RNA binding domain) • Data identify that activation of a pro-apoptotic gene expression is a mechanism through which TDP-43 accumulation and mutations induce cell death in murine neural progenitors and human cortical neurons, and this can be rescued.	Vogt et al., 2018[495]
SOD1[N139K] TDP-43[M337V] C9ORF72	• MN survival assay (4-week culture, IF- TUJ1, Isl1, ChAT) • Mutant protein puncta (IF-SOD1, TDP-43, OPTN) • Stress granule formation (IF-G3BP) • Insoluble protein (filter trap assay)	• ALS patient MNs did not show a difference in the number of MNs compared to controls after 4 weeks culture. • ALS patient MNs did not show increased SOD1, TDP-43, or OPTN puncta or stress granule formation.	Seminary et al., 2018[349]

ALS-Associated Variant	MN Functional Assay (Stressor, Technique)	ALS Phenotypes and Therapeutic Findings	Reference
	• Gene expression analyses (qRT-PCR/WB- HspB1, HspB8, and BAG3, phospho-HSF1) • Heat shock (42°C 1hr)	• SOD1 and C9orf72 MNs trended toward increased levels of insoluble SOD1 protein, and TDP-43 motor neurons trended towards increased insoluble TDP32 protein. • ALS MNs did not have endogenous activation of the heat shock response but could induce this response with heat shock.	
C9ORF72	• MN production (IF- Isl1/2, ChAT, TUJ1, GluR2, NR2B) • Gene/protein expression analyses in response to VDFL (qPCR- IGF-II, ELISA) • MN survival (30-day culture- DIV60 compared to DIV30- IF)	• Treatment with vardenafil (VDFL) increased IGF-II mRNA expression and IGF-II secretion into the media in both control and C9ORF72 patient derived MNs • VDFL improved survival of C9ORF72 MNs. VDFL identified as an inducer of IGF-11 expression in a compound screen of mouse primary spinal cord cultures. Important because IGF11 is increased in resistant MNs. VDFL reduced glutamate induced mouse MN death, penetrated rat BBB, increased IGF-II mRNA in rat/mouse spinal cords, and delayed motor symptom onset and prolonged SOD1G93A mice. Data support the hypothesis that genes differentially expressed in ALS can be targeted by pharmaceuticals to increase MN resilience.	Osborn et al., 2018[496]
SOD1[A4V] FUS[R521G] VCP[R155C] VCP[R191Q]	• MN production/differentiation (IF- TUJ1, ChAT, SMI-32) • Gene expression analyses (RNA-seq- iPSCs (Day 0), NPCs (7), pMNs (14), immature MNs (21), electrophysiologically active MNs (35), qRT-PCR) • Cellular localization (IF- SFPQ)	• VCP patient MNs had comparable differentiation to controls, had premature 3'UTR shortening, intron retention during differentiation (also seen in SOD1 and FUS MNs, coinciding with downregulation of splicing factors and 3' end processing). • The most significant intron retention was in the SFPQ transcript and VCP mutant MNs (and sporadic ALS patient samples) had aberrant localization (lower nuclear abundance of SFPQ).	Luisier et al., 2018[497]
TDP-43[G298S]	• Nuclear morphology (IF- Lamin B)	• TDP-43 patient MNs had abnormal nuclear lamina	Chou et al., 2018[363]

ALS-Associated Variant	MN Functional Assay (Stressor, Technique)	ALS Phenotypes and Therapeutic Findings	Reference
	• Cellular localization (IF-phenylalanine-glycine (FG) repeat-containing Nucleoporins (FG-Nups)) • Neuro2a cell line detergent-insoluble TDP-43 proximity dependent biotin identification, LC-MS/MS • TDP-43 construct transfections • ALS patient biopsies, patient fibroblasts, mouse primary cortical neurons, TDP-43-Drosophila models	morphology and mislocalized FG-Nups. • Neuro2A proteomic interactome data identified detergent-insoluble TDP-43 aggregates enriched in components of the nuclear pore complex and nucleocytoplasmic transport machinery. • Aggregated/disease-linked TDP-43 mutations in Neuro2a cells, mouse cortical neurons caused sequestration/mislocalization of nucleoporins, interfered with nuclear protein import and RNA export. • Nuclear pore pathology present in sALS, TDP-43- and C9ORF72 ALS patient biopsies. • Suppressing nuclear export rescued TDP-43 neurotoxicity in mouse cortical neurons/Drosophila.	
C9ORF72	• MN production/differentiation (1-3 weeks culture, IF- Tau$^+$, Isl1/2, Chat) • CRISPR/Cas9 gene correction of C9ORF72 • Protein levels (WB- C9ORF72) • RNA foci detection (FISH) • RAN protein (DPR) detection (dot blot) • MN survival assay (1-week culture, single cell longitudinal counts, cell counts, 24hour AMPA exposure on 1 week old or 3-week-old cultures) • MN electrophysiology (whole-cell patch clamp) • Gene expression analyses (RNA-seq, qRT-PCR, WB)	• C9ORF72 patient MNs were produced with comparable differentiation efficiency, baseline survival, electrophysiology, and amount of C9ORF72 protein levels compared to healthy and isogenic controls. • C9ORF72 patient MNs had intranuclear RNA foci, increased GA, GP, GR RAN DPR proteins, increased expression of GluA1 AMPA receptor (AMPAR) subunit, increased Ca^{2+}-permeable AMPAR expression, and enhanced selective MN vulnerability to AMPA excitotoxicity. (phenotypes not in cortical derived neurons and abolished with gene edited expansion deletion). • Postmortem patient spinal cord tissue had increased GluA1	Selvaraj et al., 2018[381]
C9ORF72	• MN/cortical neuron production (day 30 of MN differentiation, day 55-65 cortical neuron differentiation, IF- ChAT, TUJ1) • RNA foci detection (FISH) • PolyGP DPR detection (ELISA)	• C9ORF72 patient MNs and cortical neurons were produced with comparable efficiencies to control lines and had detectable RNA foci and polyGP DPR. • Small molecule inhibitors that stabilize RNA G$_4$C$_2$ RNA G-quadruplex conformations	Simone et al. 2018[382]

ALS-Associated Variant	MN Functional Assay (Stressor, Technique)	ALS Phenotypes and Therapeutic Findings	Reference
	• Gene expression analysis (qRT-PCR	(identified from a FRET-based screen reduced RNA foci burden and levels of polyGP DPRs in C9ORF72 patient MN/cortical neurons without causing toxicity or reducing C9ORF72 transcripts (specific to G-Quadruplex structure) (also reduced DPRs and improved survival in G_4C_2-expressing Drosophila).	
TDP-43[G298S] sALS	• MN production (21 day differentiation, analysis 1-10 days after) non-MN production (treatment with cyclopamine to inhibit SHH) • Cellular localization (ICC, immuno-EM, TDP-43) • Neurofilament inclusions (ICC, EM- NF-H, NF-M, NF-L) • Mitochondria density and velocity (MitoTracker-ORG, with TALEN-mediated HR of neurofilament NFL-EGFP into ALS iPSCs, live cell imaging, IF, EM) • MN survival (4 day old MNs, 0.6uM MG132, 24hrs treatment, LDH release, Caspase3%)	• Comparable MN differentiation efficiency of control, TDP-43, and sALS lines (VERY high efficiency, ~90% Hb9$^+$) • TDP-43 localized to nucleus in sALS and WT MNs, some cytoplasmic mislocalization in TDP-43 mutants (ICC). However, Immuno-EM showed TDP-43 translocation and small aggregates in almost all TDP-43 and sALS MNs, not WT. • ALS MNs had more NF inclusions than WT MNs, and MNs had more than nonMNs. Levels also increased with time in culture. • Mitochondria accumulated and clustered in NF inclusions, had decreased axonal transport velocity. Neurite mitochondrial density was lower in ALS MNs than WT MNs (nonMNs not affected) • Insertion of TDP-43[G298S] into H9-HES cells recapitulated NF and mitochondrial phenotypes. • MG132 treatment led to TDP-43 translocation, even in WT MNs. With MG132 treatment, ALS MNs had more NF inclusions, accumulated mitochondria, more LDH release and CC3 than control MNs (nonMNs, ALS or WT, were not as affected)	Sun et al., 2018[498]
C9ORF72	• Neuronal production (IF- Isl1) • PolyGP DPR detection (ELISA) • Cellular localization (IF- Ran-protein/nucleocytoplasmic transport reporters, MAP2, DAP1)	• C9ORF72 patient neurons had basal [polyGP] DPRs, increased cytoplasmic/nuclear transport abnormalities, and enhanced glutamate-mediated death. These phenotypes were significantly	Cheng et al., 2019[387]

ALS-Associated Variant	MN Functional Assay (Stressor, Technique)	ALS Phenotypes and Therapeutic Findings	Reference
	• Neuronal survival (4hrs 10μM glutamate toxicity) • Protein function analyses (DDX3X lentiviral overexpression, cDNA transfection)	reduced with exogenous DDX3X expression. (DDX3X identified from a CRISPR/Cas9 KO screen as a modifier of C9ORF72 DPR production. It acts as an RNA helicase that suppresses RAN translation of the C9ORF72 repeats)	
Mutation Introduced FUS[P525L]	• MN production (Hb9) • Cellular localization/stress granule incorporation (IF-FUS, G3BP1, TIAR) • Protein function analysis (lentiviral knockdown- MBNL1)	• Mutant FUS MNs were efficiently produced (~50% Hb9^{+}) and had cytoplasmic mislocalized FUS incorporated into stress granules, and knockdown of muscleblind reduced FUS[+] stress granules by 50% • Muscleblind identified as a modifier of FUS toxicity in a Drosophila genetic stress. Data in Drosophila, HEK293T, primary cortical neurons, and NSC-32 cells support knockdown of muscleblind suppressed FUS associated neuronal defects, toxicity, FUS mislocalization and incorporation into stress granules, and restored SMN nuclear localization (SMN also modified FUS toxicity)	Casci et al., 2019[373]
FUS[P525L]	• MN production (IF- MAP2, Isl1) • Cellular localization (IF- FUS) • Protein levels (WB- RAD23B, LIG4, MSH2) • Gene function (ASO mediated FUS knockdown)	• FUS patient MNs were produced with comparable efficiency to control MNs, had cytoplasmic FUS accumulation, and decreased levels of DNA damage repair proteins RAD23B, LIG4, MSH2 • (these proteins were identified as dysregulated in a RT2-PCR array of CRISPR/Cas9 FUS-KO and FUS-shRNA HEK293 lines) • ASO mediated FUS knockdown in control MNs also resulted in reduced RAD23B, LIG4, MSH2 proteins, comparable to FUS patient MN results, consistent with a loss of function mechanism.	Wang et al. 2019[374]
C9ORF72	• MN production (IF-MAP2) • Gene function analysis- shRNA, CRISPR/Cas9 AFF2 deletion. • Gene expression analysis (qRT-PCR, allele-specific pyrosequencing)	• C9ORF72 patient cortical neurons had RNA foci, DPRs, and TF withdrawal induced cytoplasmic TDP-43 and axonal degeneration. • Knockout of AFF2/FMR2 (identified as a suppressor of	Yuva-Aydemir et al., 2019[383]

ALS-Associated Variant	MN Functional Assay (Stressor, Technique)	ALS Phenotypes and Therapeutic Findings	Reference
	• RNA foci detection (FISH) • DPR detection (IF- poly-GP, GR) • Cellular localization (2-3 weeks TF withdrawal stress, IF-TDP-43) • Axonal degeneration (2-3 weeks TF withdrawal, IF- TUJ1)	polyGR toxicity in Drosophila screen) decreased expression of mutant expansion-containing C9ORF72 allele, reduced RNA foci, DPRs, TDP-43 pathology and rescued axonal regeneration.	
FUS^{R495QfsX527} FUS^{D502Tfs*27}	• MN production (IF- NF-H) • Myotube differentiation (IF-PAX7, MYOG, MHC, desmin, α-actinin, RyR1, DHPrα) • Gene expression analysis (qRT-PCR- AChRα1) • Coculture- myotube and MNs (3 weeks). • Cellular localization (IF- FUS)	• Myotubes from FUS patient MNs had endplate maturation defects, • Co-culture of FUS patient MNs and myotubes aggravated endplate maturation defects, decreased differentiation (MYOD, MYOG, AChRa1) (intrinsic FUS toxicity in both MNs and myotubes). • FUS mislocalized to cytoplasm in patient derived MNs, not myotubes. • Skeletal muscle biopsy of FUS patients displayed muscle atrophy, endplate denervation, FUS mislocalization, and impaired enrichment in subsynaptic nuclei. • Knock-in FUS ALS mouse model showed postsynaptic NMJ defects in newborn homozygous mice (rescued by FUS WT selective cell-autonomous expression in skeletal muscle. Neonatal lethality not rescued). Adult het had smaller NM endplates, denervated before axon loss. FUS collaborated with ERM to stimulate transcription of acetylcholine receptors receptor genes. • Conclude FUS regulates acetylcholine receptor gene expression in subsynaptic myonuclei, muscle-intrinsic toxicity of ALS-mutant FUS contributes to dying back motor neuropathy.	Picchiarelli et al., 2019[242]
SOD1^{A4V}	• Mitochondrial motility (MitoDsRed, 48hours, time-lapse automatic imaging, CellProfiler particle analysis and tracking, kymography)	• SOD1 patient MNs had defective mitochondrial motility that was reversed by inhibitors to F-actin (latrunculin), TPP1 (AAF-CMK), and aurora kinase B (Hesperadin) Targets identified from a rat hippocampal neuron mitochondrial transport screen.	Shlevkov et al., 2019[499]

ALS-Associated Variant	MN Functional Assay (Stressor, Technique)	ALS Phenotypes and Therapeutic Findings	Reference
FUS^{R521H} FUS^{P525L}	• MN production (28-32-day old MNs (19-23 days after plating), RNA-seq, IF- TUJ1, ChAT, Isl1, SMI-32, Synapsin, whole-cell patch clamp, current-clamp, voltage-clamp electrophysiology) • Metabolic profiling/flux (radioactive substrate tracing- $^{13}C_6$-glucose or $^{13}C^3$-lactate incorporation into pyruvate/ TCA metabolites, liquid chromatography MS, oxygen consumption rate (OCR)) • Mitochondrial morphology (transmission EM) function (OCR)	• FUS patient MNs were produced with comparable efficiency to controls, appropriate MN markers (transcriptomic and IF), and electrical activity (spontaneous and evoked action potentials). • MN differentiation rewired metabolic routes (shift from glycolytic metabolic state in iPSCs to oxidative metabolic state in MN) • MN used lactate to fuel this increased oxidative metabolism, shifting pyruvate into TCA cycle. • FUS patient MNS did not have altered mitochondrial morphology (intermembrane space, cristae patterns, overall shape), altered mitochondrial function, or altered flux through metabolic pathways.	Vandoorne et al., 2019[500]
TDP-43^{G298S} TDP-43^{N352S} FUS^{R521G}	• Stress granule induction (100µM 120mins sodium arsenite, 250nM 120mins thapsigargin, 5µg/ml 12hrs puromycin, IF- G3BP1) • Cellular localization (puromycin 24hrs, recovery washout 24hours, IF- TDP-43, G3BP1) • Protein expression levels (stress granule enriched fractions, WB)	• ALS patient MNs exhibited inducible stress granules. These accumulations were inhibited by hit compounds from a high throughput stress granule screen. (arsenite-induced, G3BP1-GFP in HEK293T and NPC cells) • ALS patient MNs also had puromycin-induced cytoplasmic TDP-43 puncta (often colocalized with G3BP1 stress granule in TDP-43 mutants, not FUS). Planar hit compounds could prevent cytoplasmic TDP-43 puncta.	Fang et al., 2019[362]
SOD1^{D90A} SOD1^{R115G} TDP-43^{G294V} TDP-43^{S393L} FUS^{R521C} FUS^{R521L} FUS^{R521H} FUS^{R495QfsX527} FUS^{P525L} C9ORF72	• MN production/differentiation (28-32 days culture, IF- TUJ1, SMI-32, qRT-PCR- TUJ1, SMI-32, MAP2, ChAT) • Ca^{2+} dynamics/glutamate receptor properties (basal, thapsigargin, S-AMPA, NMDA, ATPA, and DHPG stimulated, Ca^{2+} imaging, qRT-PR)	• ALS patient MNs were produced into MNs with comparable IF staining, slight differences in qRT-PCR expression of MN markers. • C9ORF72 patient MNs had more frequent spontaneous transients (Ca^{2+} imaging), increased voltage gated calcium channels and kainate receptor expression. • TDP-43 patient MNs had elevated basal intracellular Ca^{2+} levels and AMPA-induced signal amplitudes. • FUS patient MNs had increased AMPA and kainate receptor expression (qRT-PCR)	Bursch et al., 2019[394]

ALS-Associated Variant	MN Functional Assay (Stressor, Technique)	ALS Phenotypes and Therapeutic Findings	Reference
		• SOD1 patient MNs had decreased amplitude of Ca^{2+} response to thapsigargin, increased metabotropic glutamate receptors.	
$SOD1^{L144F}$	• MN production/maturation (IF-Isl1, SMI-32, ChAT, FOXP1) • CRISPR/Cas9 gene correction • MN survival assay (28 days TF withdrawal, day 32-60 of culture) (24-48hrs ER stressor CPA treatment hESC-MN system) • Gene expression analyses (qRT-PCR, WB- mir-17~92, PTEN, NEDD4-2, NDFIP1) Overexpression rescue (lentivirus) • Cellular localization (IF- PTEN)	• SOD1 patient MNs had comparable differentiation efficiency, enhanced degeneration with 28 days TF withdrawal. • 14 days after TF withdrawal (and 14 days before severe survival loss) mir-17~92 decreased, increased PTEN, NEDD4-2, NDFIP1, and enhanced $PTEN^{nucleus/cytosol ratio}$ • Lentiviral mir-17~92 overexpression rescued survival defects and expression changes. • $SOD1^{G93A}$ mouse studies showed reduced mir-17~92 in LMC-MNs before disease onset (confirmed in hESC system). Intrathecal AAV-mir-17~92 overexpression improved motor deficits and survival.	Tung et al., 2019[501]
FUS^{P525L}	• MN production (IF- Isl1, MAP2, TUJ1, ChAT, SMI-32, RNA-seq) • Cellular localization (eGFP) • Monosynaptic rabies tracing • HIV1/ZIKV infection • Microfluidic chambers • Stress granule formation (IF-FUS-eGFP, TIAR, G3BP1 (confirmed with arsenite stress in supplement) • LDH release, MTT assay	• FUS MNs differentiated comparably and had increased FUS cytoplasmic mislocalization (as characterized in Marrone et al and Bursch et al) • FUS^{P525L} spinal neurons had decreased defense against rabies infection (shown by increased monosynaptic rabies tracing in early infectivity (2 weeks), exacerbated FUS^+ cytoplasmic foci/stress granule formation, and enhanced degeneration with long-term infection (decreased monosynaptic rabies tracing with time 4weeks) • FUS^{P525L} spinal neurons also had decreased survival with HIV1 and ZIKV infections. HIV (but not ZIKV) also induced cytoplasmic FUS accumulation (like rabies) • Data suggest viral infections exacerbate effects of fALS mutations and could enhance neural connectivity spread of disease.	Bellmann et al., 2019[502]
$TBK1^{T77WfsX4}$ $TBK1^{E643Del}$	• MN production (14-day culture, IF- ChAT, MAP2)	• TBK1 patient MNs had reduced TBK1 levels, decreased ATG10,	Catanese et al., 2019[503]

ALS-Associated Variant	MN Functional Assay (Stressor, Technique)	ALS Phenotypes and Therapeutic Findings	Reference
TBK1^{Y185X}+ FUS^{R524G} FUS^{R521C} FUS^{R495QfsX527} C9ORF72	• MN survival (DIV 35 and DIV42 compared to DIV14, IF-ChAT, Caspase 3) • Phospho-antibody array • Intracellular accumulation (IF-SQSTM1) • Aggresome detection (High-pressure freezing transmission electron microscopy, PROTEOSTAT aggresomes dye, IF- Ubiquitin, HDAC6) • Screening (DIV14 MNs, 24hr treatment, rapamycin positive control, 0.1% DMSO negative control) • Autophagy analyses • Gene/protein expression analyses (Human Autophagy RT2 Profiler™ PCR Array, RT-PCR, WB)	decreased phosphorylation of AKT/MTOR pathway targets, impaired autophagosome maturation (accumulated immature phagophores due to failure in the elongation phase), had accumulated cytosolic SQSTM1$^+$ aggresomes, and decreased viability with long term culture. • Screening of nuclear receptor ligands in TBK1 MNs identified the retinoid 4-hydroxy(phenyl)retinamide (4HPR) as an inducer of SQSTM1$^+$ aggresomes. • 4HPR exacerbated SQSTM1 accumulation, exacerbated TBK1 mutant autophagic impairment, and decreased TBK1 mutant MN survival. • 4HPR also enhanced SQSTM1 accumulation in C9ORF72 MNs (not FUS), decreased ATG10, and increased aggresome formation (autophagy impairment at later stage than in TBK1 mutant). • Data suggest that the retinoid worsens autophagic flux in MNs carrying TBK1 and C9orf72 (but not FUS) ALS-related mutations, leading to the accumulation of SQSTM1 aggresomes and the loss of ATG10, but interfering with autophagy at distinct steps of the pathway. increasing autophagic flux is therefore not a therapeutic solution for ALS if 'autophagy bottlenecks' are not also solved at the same time.	
Patient Mutation FUS^{H517D} SOD1^{H46R} TDP-43^{M337V} Mutation Introduced FUS^{H517D} FUS^{P525L}	• MN production (10-day culture, IF-TUJ1, MAP2, ChAT, SMI-32, Isl1) • Gene introduction/correction (TALEN, CRISPR/Cas9) • Stress granule induction (1 mM NaAsO2 treatment, 30 mins, IF-FUS, G3BP) • Axon branching analyses (Hb9-venus reporter, progenitor cells plated as spheres, neurites radially projected, 10 days post	• FUS mutant MNs were produced with comparable efficiency and displayed increased FUS cytoplasmic localization to induced stress granules. • FUS mutant MNs had aberrant /increased axon branching (no difference in length) and increased levels of axonal Fos-B, whose mRNA bound to FUS. • Fos-B siRNA mediated reduction or compound inhibition	Akiyama et al., 2019[504]

ALS-Associated Variant	MN Functional Assay (Stressor, Technique)	ALS Phenotypes and Therapeutic Findings	Reference
	plating, live cell monitoring, IF-MAP2, TAU1) • RNA profiling (microarray) of isolated axons from microfluidic devices • Gene expression/function analyses (qRT-PCR, smFISH in neurons- Fos-B, RNA pull down assays, siRNA/overexpression)	ameliorated the observed aberrant axon branching and overexpression in control MNs showed deteriorated axon morphologies • Abnormal axonal branching also seen in SOD1 and TDP-43 mutant MNs, but only TDP-43 also had Fos-B dysregulation	
C9ORF72	• Cellular localization (day 55 of differentiation, IF- ADAR2, MAP2) • Whole transcriptomic analyses (RNA-Seq) • Gene function analyses (siRNA-ADAR1, ADAR2, lentiviral ADAR2 lacking a nuclear localization signal)	• C9ORF72 patient MNs had comparable levels of ADAR2 (responsible for adenosine (A) to inosine (I) editing of double-stranded RNA), but it was mislocalized out of the nucleus. ADAR2 mislocalization also occurred in patient samples and C9ORF72 mice, and resulted in vast RNA A to I editing aberrations, including in ALS related transcripts and the EIF2 signaling pathway (phenocopied by loss of ADAR2 with siRNA or overexpression of ADAR2 lacking a nuclear localization signal).	Moore et al., 2019[390]
CHCHD10^{S59L}	• MN production (day 35 of differentiation, IF- TUJ1, Isl1) • Mitochondrial structure (day 35 of differentiation, ultrastructural analysis with transmission electron microscopy) • Caspase activation (0.5µM staurosporine, 24hrs or 50–100µM glutamate for 48hrs, DEVDase activity measurement)	• CHCHD10^{S59L} mutant motor neurons were comparably produced to controls and had similar baseline viability. MNs did display altered mitochondria and were more sensitive to staurosporine or glutamate-induced caspase activation than control cells. • Mice with CHCHD10$^{S59L\ mutation}$ knocked-in displayed a fatal mitochondrial myopathy with mtDNA instability, NMJ denervation, MN degeneration, and TDP-43 cytoplasmic aggregates at end stage.	Genin et al., 2019[505]
SOD1^{A4V} SOD1^{H46R} SOD1^{E78_R79ins}^{SI} SOD1^{N86S} SOD1^{D90A} SOD1^{G93A} SOD1^{L117V} SOD1^{D125Tfs*24} SOD1^{G127Gfs*7}	• Mixed MN and astrocyte production (11-13 days after plating, IF- TUJ1, Isl1/2, SMI-32) • 1-19% O_2 tension, 24hrs, analysis of disordered and total SOD1 (ELISA) • Non-reducing western blotting • Proteasome activity (Proteasome-Glo) detergent	• Culturing SOD1 MNs under low O_2 tensions caused reductive bond cleavage and increased disordered and aggregated SOD1, which was not attributable to reduced proteasome activity or gross perturbations in GSH/GSSG redox signaling.	Keskin et al., 2019[506]

ALS-Associated Variant	MN Functional Assay (Stressor, Technique)	ALS Phenotypes and Therapeutic Findings	Reference
FUS^{Q23L} C9ORF72 TBK1^{A417X} TBK1^{M598V} TBK1^{I450Kfs*14} TBK1$^{p.690-713del}$	soluble vs insoluble protein (+/- proteasome inhibition) • Analysis of reduced and oxidized glutathione		
<u>Mutation Introduced</u> FUS^{P525L}	• CRISPR/Cas9n mediated mutant allele introduction, with either a long linker (LL) or short linker (SL) GFP reporter • MN production (3-week culture, IF- MAP2, SMI-32, Isl1, Hb9) • Apoptosis (IF- cleaved caspase 3) • Cellular localization, accumulation/autophagy analysis (basal, arsenite induced, autophagy inhibited (3MA or chloroquine), proteasome inhibited (MG132), capillary electrophoresis/IF- FUS, p62, LC3, lysosomes) • Protein-protein interactions (LC-MS/MS, CoIP WB, capillary electrophoresis gene expression analyses ALS-RBPs) • In vitro phase separation assay • Lentiviral RBP knockdown, LDH release	• Mutant FUS MNs had comparable differentiation efficiency to controls, had FUS cytoplasmic mislocalization that correlated with apoptosis (FUS^{P525}SL > FUS^{P525L}LL ≈ FUS^{WT}SL > FUS^{WT}LL) • Mutant FUS MNs also had increased FUS, p62 accumulation, and LC3 levels (phenocopied by inhibiting proteasome or autophagy) suggesting impaired protein degradation processes • CoIP/LC-MS/MS identified ALS associated RBP binding interactions were disrupted with cytoplasmically localized mutant FUS. (hnRNPA1, hnRNPA2B1, TAF15, EWSR1) not TDP-43). • Aberrant solid phase transition was also increased with mutant FUS and aggravated by lack of binding RBPs (which can normally prevent solid phase aggregation). • FUS mutant MNs had decreased RBP protein levels (not mRNA) were also reduced and knockdown of RBP levels alone reduced viability in non FUS mutant neurons. • Inducing autophagy (torkinib, PQR309) reduced accumulated cytoplasmic mutant FUS and restored RBP homeostasis in MNs and decreased motor dysfunction in Drosophila.	Marrone et al., 2019[375]
FUS^{Asp502Thrf*27}	• MN production (42-day culture, IF, SMLM imaging-dSTORM technique, exchange-paint technique, EM- FUS, Homer1, Bassoon) • Subcellular fractionation of synaptosomes	• FUS localized to nucleus and closer to the postsynaptic marker Homer1 in control human neurons and in immature rat MNs. In mature rat synapses (DIV 14/21 in rat MNs, FUS localized closer to the presynaptic marker Bassoon.	Deshpande et al., 2019[376]

ALS-Associated Variant	MN Functional Assay (Stressor, Technique)	ALS Phenotypes and Therapeutic Findings	Reference
		• FUS patient MNs had mislocalized cytosolic localization, and increased neuritic and synaptic accumulation of mutant FUS, aggregated with both presynaptic protein Bassoon and postsynaptic Homer1.	
C9ORF72 SOD1[A272C] SOD1[A4V]	• Transcriptomic and proteomic data sets obtained from NeuroLINCs, bioinformatic analyses	• Analyses of publicly available multiOMIC data sets suggest C9ORF72 patient derived MNs and post-mortem patient MNs from C9 or sALS had elevated transcripts/proteins related to ECM, cell adhesion, inflammation, and immunity, and TGFβ targets. • SOD1 MNs had opposite transcriptomic signatures to C9 patient MNs (upregulated ECM, cell adhesion, etc.) and did not correlate with C9ORF72 MNs. Some overlap between SOD1[A4V] and sALS postmortem samples (repressed TCA cycle, oxidative phosphorylation RNA processing, ribosomal biogenesis) • Overall indicate distinct transcriptional signatures between sALS and C9ORF72 ALS compared to SOD1 ALS.	Wong et al., 2019[507]
C9ORF72	• Astrocyte production/functional characterization (IF- vimentin, NFIA, S100B, GFAP, Ca2+ wave propagation, glutamate up-take) • RNA foci (FISH) • Urea soluble Poly-GP, GA, PA DPR detection (WB) • TDP-43 localization (IF) Levels (WB) • MN production (heterogeneous cultures and highly enriched) • Astrocyte-MN co-culture (IF-caspase 3, SMI-32) • Electrophysiology (3-10-week culture, whole-cell patch clamp, voltage-clamp) • Gene expression analyses (RNA-seq of astrocytes)	• C9ORF72 mutant astrocytes were produced with comparable efficiency and function to controls, predominantly nuclear TDP-43, but RNA foci and Poly-GP DRP. • C9ORF72 mutant astrocytes did not cause control MNs to lose viability (even after 10 weeks culture) but significantly altered MN electrophysiological properties (age-dependent loss of firing, loss of voltage activated currents). • Highly enriched C9ORF72 patient MNs did not have any electrophysiological phenotype by themselves. Instead, the presence of the C9ORF72 mutation in astrocytes alone was sufficient to induce electrophysiological	Zhao et al., 2019[467]

ALS-Associated Variant	MN Functional Assay (Stressor, Technique)	ALS Phenotypes and Therapeutic Findings	Reference
		dysfunction in either control of C9ORF72 MNs. Mutant astrocytes drive non-cell autonomous MN pathology. • RNA seq of C9ORF72 patient astrocytes revealed upregulated genes related to ionotropic glutamate receptor signaling, complement activation, and nuclear export. Downregulated genes involved synapse assembly, cell adhesion, regulation of sodium and potassium ion import.	
C9ORF72	• MN production • Gene/protein expression analyses (2 week or 3-month culture, qRT-PCR/WB- Ku80, pATM, p53, PUMA, BAX, cleaved caspase 3, IF- Ku80, pATM, cleaved caspase 3 ChAT) • RNA foci detection (FISH) • PolyGR detection (ELISA) • CRISPR/Cas9 gene deletion (C9ORF72, Ku80) • Lentiviral shRNA/small deliverable RNA Ku80 knockdown • DNA double stranded break analysis (comet assay)	(Ku80 is an essential DNA repair protein identified as a modifier of Drosophila polyGR toxicity in a genetic screen). • C9ORF72 patient MNs had RNA foci, polyGR, and elevated expression of Ku80 in 3-month-old cultures (not in astrocytes, and not in 2-week MN cultures) • 3-month-old mutant lines also had elevated downstream proapoptotic proteins (p-ATM, p53, PUMA, BAX, and cleaved caspase 3). • Genetic deletion of the C9ORF72 repeats or partial loss of Ku80 suppressed pATM, p-p53, and cleaved caspase 3 apoptotic pathway increases (no effect on polyGR levels, or any increase in DNA double stranded breaks)	Lopez-Gonzalez et al., 2019[384]
SOD1^{L144F} TDP-43^{M337V} TDP-43^{G298S}	• MN survival assays (12-20days TF withdrawal or 48hrs ER stress, thapsigargin/tunicamycin, IF- Isl1/2, TUJ1) • Protein function analyses (siRNA/shRNA mediated knockdown- MAP4K4, JNK1-3, cJUN, MAP4K4 inhibitors) Protein levels- WB, dot blot • Apoptosis, neurite analysis (TF withdrawal, IF, WB- Isl1/2, TUJ1, cleaved caspase 3, TUNEL, pJNK, JNK, p-cJUN, cJUN) • Autophagy/mutant protein aggregation (TF withdrawal, WB- SOD1, Ubiquitin, LC3, p62, FOXO1)	• ALS MNs had enhanced death, apoptosis, neuritic degeneration, and impaired autophagy-mediated aggregate clearance. • MAP4K4 (a molecular target of kenpaullone, a neuroprotective compound identified from a mESC-MN survival screen, Yang et al., 2013) is activated in ALS MNs and in stress conditions. Its reduction (RNAi/compounds) cell-autonomously improved degenerative phenotypes by blocking the JNK3-cJUN mediated apoptotic pathway and by stimulating FOXO1 mediated autophagy.	Wu et al., 2019[400]

ALS-Associated Variant	MN Functional Assay (Stressor, Technique)	ALS Phenotypes and Therapeutic Findings	Reference
TDP-43[M337V] TDP-43[G298S] TDP-43[Q343R] TDP-43[A315T]	• MN production/purity/ maturation (Hb9-GFP reporter for hESC MNs, NCAM[+]/ EpCAM- FACS for iPSC-derived MNs, 10 days culture, IF-TUJ1) • Gene expression analyses (RNA-seq, qRT-PCR, splicing assays, WB). • Protein binding partners (TDP-43 IP and RNA IP- fRIP) • Protein function (siRNA- TDP-43, STMN2, knock-in TDP-43 WT/mutant allele, CRISPR/Cas9 STMN2 deletion) • Neurite analysis (basal growth and regrowth after axotomy, Sholl analysis, microfluidic chambers) • Protein mislocalization, soluble vs insoluble levels (basal and MG132 proteasome inhibition induced, IF- TDP-43, WB)	• Hundreds of transcripts identified as regulated by TDP-43 knockdown in hESC-MNs. • TDP-43 knockdown in hESC-derived MNs decreased STMN2, caused cryptic exon inclusion (direct TDP-43 protein binding of STMN2 RNA). Increased WT or mutant TDP-43 also decreased STMN2, cryptic exon inclusion. • Patient iPSC-derived TDP-43 mutant MNs had decreased STMN2 expression. • TDP-43 mutant patient derived MNs did not display basal TDP-43 cytoplasmic mislocalization or differences in soluble/insoluble TDP-43. MG132 induced nuclear loss and insoluble TDP-43, reduced STMN2 expression, and caused cryptic exon inclusion. • Depletion of TDP-43 or STMN2 induced neurite outgrowth defects and axonal regrowth defects. • JNK inhibition (SP600125) rescued STMN2 levels and neurite defects.	Klim et al., 2019[198]
TDP-43[G298S] TDP-43[N352S] TDP-43[N390S] TDP-43[A382T]	• Fibroblast trans-differentiation to MNs (IF- TUJ1, Hb9, MAP2) • Gene expression analyses (RNA-seq, qRT-PCR, in-situ, WB- TDP-43, STMN2). • Protein binding partners (TDP-43 iCLIP) • Neurite analysis (with ASOs to TDP-43 or STMN2, basal growth and regrowth after axotomy, microfluidic chambers)	• TDP-43 mutant transdifferentiated MNs had reduced STMN2 levels. • TDP-43 knockdown or mutation in neuronal cell line reduced STMN2. • TDP-43 directly bound STMN2 mRNA and suppressed premature polyadenylation (causing cryptic exon inclusion). • ALS postmortem samples (SOD1[A4V], C9ORF72, C9ORF72+ FTD, sALS, sALS+FTD) had reduced STMN2 and altered transcript processing. • Depletion of TDP-43 or STMN2 did not affect basal axonal outgrowth but reduced axonal regeneration after axotomy (rescued by STMN2 expression).	Melamed et al., 2019[364]
SOD1[G17S]	• MN production (2-week culture, IF- ChAT) • Cellular localization (IF- C and N terminal TDP-43, p-TDP-43, SOD1, ChAT)	• SOD1 patient MNs had C-terminal TDP-43 cytoplasmic mislocalization, and p-TDP-43 colocalized with SOD1 inclusions. • Data from SOD1[G93A] mice and SOD1[G86S] patient spinal cord	Jeon et al., 2019[508]

ALS-Associated Variant	MN Functional Assay (Stressor, Technique)	ALS Phenotypes and Therapeutic Findings	Reference
		showed pathological increases in SOD1, C-terminal TDP-43 and p-TDP-43 inclusions (not N-terminal TDP-43). Studies in NSC-34 cells and primary cortical neurons indicated transfected mutant SOD1 induced biochemical TDP-43 alterations.	
VCP^{R155C} VCP^{R191Q}	• MN production (as described in Hall et al) • Cellular localization (IF- FUS) • SFPQ intron retention and cytoplasmic mislocalization (Cellular fractionation and qPCR, single molecule FISH)	• VCP patient derived MNs had decreased nuclear-to-cytoplasmic FUS ratio (found in VCP mouse spinal cord and sALS patient spinal cord tissue but not SOD1 mouse). • FUS protein bound to aberrantly retained intron 9 within the SFPQ transcript, and VCP patient MNs had cytoplasmic mislocalized SFPQ intron-retaining transcripts (SFPQ previously identified as one of the most significantly retained intron in ALS mutations, Luisier et al)	Tyzack et al., 2019[509]
$TDP-43^{M337V}$ $TDP-43^{I383T}$ C9ORF72	• MN production (30-day culture, IF- SMI-32, ChAT, TUJ1, Isl1) • live Ca2+ imaging Fura 2-AM • Response to depolarization (50mM KCl) Glutamate excitotoxicity • ER-ca2+ release/levels (carbamylcholine perfusion, 10μM thapsigargin) • Cellular localization (IF- TDP-43) • Gene expression analyses (28-30-day old cultures, RNA-seq, qPCR, WB)	• Both C9ORF72 and TARDBP MNs showed delayed buffering/recovery of cytosolic Ca2+, glutamate hyperexcitability, and altered Ca2+ responses after depolarization (low levels/ hypoexcitability in TARDBP, high levels/ hyperexcitability in C9ORF72 MNs) No TDP-43 mislocalization. • Calcium responses in C9ORF72 could be linked to lower ER ca2+ release (essential for ER-mitochondria transfer of Ca2+ ions/ATP production), upregulated Ca2+-permeable AMPA and NMDA subunits and impaired mitochondrial Ca2+ buffering due to imbalanced MICU1 and MICU2 on the mitochondrial Ca2+ uniporter.	Dafinca et al., 2020[393]
sALS C9ORF72 $SOD1^{A4V}$ $SOD1^{N139K}$	• MN production (IF- Isl1, TUJ1, ChAT) • MN survival/neurite analysis (Number at 4 weeks of differentiation, IF- ChAT) • Insoluble protein detection (WB- SOD1, TDP-43, OPTN, p62)	• MNs from sALS patient and his nonALS twin brother exhibited comparable viability, levels of insoluble and autophagy proteins (not consistently changed with glutamate stress).	Seminary et al., 2020[510]

ALS-Associated Variant	MN Functional Assay (Stressor, Technique)	ALS Phenotypes and Therapeutic Findings	Reference
	• Autophagy (WB-LC3-II/I) • +/- Glutamate stress (100μM for 96hrs at 4 weeks of differentiation)		
VAPB^{P56S}	• Derived iPSCs and MNs from 5 ALS patients and 3 controls • Copy number variation, whole exome sequencing • Expression levels (RT-qPCR, WB, VAPB) • Cell death (propidium iodide staining) • Mitochondrial activity (oxygen consumption rate- basal, ATP-linked, protein leak-linked, maximal) • RNA sequencing	• Described 5 ALS patients with same mutation but different clinical phenotypes • Copy number variation and whole exome sequencing analyses did not reveal previously described modifiers of pathogenicity. • All ALS patient MNs had reduced VAPB mRNA and protein expression. • MNs from ALS patient iPSCs with severe clinical presentations had more death than MNs from ALS patients with mild clinical phenotypes. These mild ALS patient MNs had had the same cell death as control MNs. • Severe ALS MNs had decreased oxygen consumption rate parameters, which was partially rescued in milder patient MNs. • RNA seq of severe ALS MNs vs control MNs showed upregulated terms related to synaptic signaling and organization, while downregulated terms included protein translation, protein targeting to the ER and rRNA biogenesis. • Identified differentially expressed genes that were shared by the mild ALS patients, suggesting modulatory/mitigating processes by maintaining protein localization to ER and translation initiation.	Oliveira et al., 2020[511]
Patient mutation SOD1^{A4V} Mutation Introduced SOD1^{G93A}	• CRISPR/Cas9 mutation addition (G93A) • MN production/differentiation (18-31 days culture, IF- Isl1, Hb9, ChAT) • DNA damage and recovery (30-day old cultures induced with, 1hr 10μM etoposide, washout/recovery up to 24hrs, IF-γH2A.X)	• SOD1 mutant MNs had comparable MN differentiation and capacity for DNA damage break repair. • Studies of ALS post-mortem tissue indicated accumulated DNA damage (single stranded, OHdG), significant DNA damage response (ATM activation, nuclear BRCA1, c-Abl), activated p53 and cleaved caspase 3, and	Kim et al., 2020[512]

ALS-Associated Variant	MN Functional Assay (Stressor, Technique)	ALS Phenotypes and Therapeutic Findings	Reference
		hypomethylated promoters of DNA repair genes.	
C9ORF72	• Neuron production (at least 4-week culture, IF- Isl1, TUJ1, NeuN) • CRISPR/Cas9 C9ORF72 correction • PR DPR detection (IF) • Protein levels (60-day cultures, WB-, Ku-70, RAD52, pRAD52, IF- RAD52, pRAD52) • Promoter methylation (bisulfite pyrosequencing, cytosine methylation)	• C9ORF72 patient MNs were efficiently produced, had PR expression, and inefficient DNA damage repair (increased levels of a DNA damage marker (γH2AX), a NHEJ marker (Ku-70), and a single strand annealing marker (pRAD52)(1 line did not have pRAD52 phenotype, likely due to promoter hyper-methylation). • DPR expression (PR, GR, and GA) in cell lines was sufficient to inhibit DNA double strand break repair efficiency, decreasing NHEJ, single strand annealing, and microhomology mediated end joining, not HR. PR inhibited double strand break repair in part by binding to NPM1.	Andrade et al., 2020[388]
C9ORF72	• Protein distribution (50-day MN culture, subcellular nucleo-cytoplasmic fractionation, super-resolution imaging, structured illumination microscopy, serial confocal imaging, expansion microscopy, IF, WB- eRF1) • Protein synthesis rate (50-day MN culture, Click-it HPR, puromycin, SUnSET) • Nonsense mediated decay (NMD) (50-day MN culture, IF-pUPF1, WB-SMG1) • Function analysis (eRF1 knockdown, UPF1 reduction) • RNA foci detection (FISH)	• eRF1 identified from HEK293 proteome-wide nucleocytoplasmic analysis as differentially distributed in C9ORF72 mutation. • C9ORF72 patient MNs had apparent nuclear enrichment of eRF1, puncta actually in cytosol in highly complex LMNB$^+$ nuclear envelope invaginations (also postmortem tissue) • C9ORF72 patient MNs had reduced protein synthesis and increased, hyperactivated NMD (dependent on eRF1- knockdown diminished NMD activity, increased cytosolic C9-RNA foci. • eRF1 overexpression is a strong genetic modifier of C9ORF72 toxicity in flies. Downstream NMD eRF1 effector UPF1 overexpression also ameliorated eye degeneration). • Data suggest a model where eRF1 mediates a UPF1 driven nonsense mediated degradation of expanded C9ORF72 transcript	Ortega et al., 2020[392]
C9ORF72	• MN production (10 days culture, IF- Hb9, TUJ1, SMI312, qRT-PCR- Hb9, ChAT, expansion detection with southern blot, repeat primed PCR)	• C9ORF72 MNs derived from fibroblasts or peripheral blood cells displayed comparable differentiation ability, RNA foci, predominantly nuclear TDP-43,	Bardelli et al., 2020[513]

ALS-Associated Variant	MN Functional Assay (Stressor, Technique)	ALS Phenotypes and Therapeutic Findings	Reference
	• RNA foci detection (FISH) • Cellular localization (IF- TDP-43, p-TDP-43) • Stress granule detection (0.5mM sodium arsenite, 1hr, IF-TIAR)	and arsenite-induced stress granules.	
C9ORF72	• MN production (2-3-week culture, IF- Isl1, MAP2, SMI-32, qRT-PCR- MAP2, SMI-32, ChAT, electrophysiology whole-cell patch clamp, current clamp) • CRISPR/Cas9n C9ORF72 gene correction (repeat primed PCR, southern blot, qRT-PCR, capillary electrophoresis) • Gene expression analyses (RNA-seq) • Axonal lysosomal trafficking (LysoTracker, microfluidic chambers, live imaging) • Apoptosis detection (14-day culture, IF- cleaved caspase 3) • Poly-GP DPR detection (ELISA, IF) • Protein levels (capillary electrophoresis) • Stress granule detection (0.5mM sodium arsenite, 1hr, IF- eIF3)	• C9ORF72 MNs had comparable differentiation efficiency but were hypoexcitable. • Transcriptomic analyses showed C9ORF72 MNs had enrichment of terms related to programmed cell death, DNA damage checkpoint, microtubule organization and motor activity, with some overlap with KO lines • C9ORF72 mutant MNs had decreased axonal trafficking and increased apoptosis, exacerbated by KO (suggest LOF aggravated GOF) • C9ORF72 had polyGP detection which was not observed in WT or isogenic controls. Interestingly, C9ORF72 + KO lines (which had the most degeneration) had less DPR suggesting exaggerated GOF with LOF is partly DPR independent. • LOF exacerbation of GOF affected stress granule formation (SGs increased in C9 mutant, increased even more in C9+KO) • LOF exacerbation of GOF altered HSP levels (decreased DNAJA4, HSPA1A, HSPA1B in C9 mutant compared to gene corrected controls, even further decreased with C9 + KO). Reducing HSP synthesis in C9ORF72 MNs also caused axonal defects and apoptosis.	Abo-Rady et al., 2020[389]
C9ORF72	• CRISPR/Cas9 (double-nicking approach to reduce off target) and HR Isogenic correction of C9ORF72 • MN differentiation/analysis (DIV 20, DIV 30- IF- Olig2, Islet1, Hb9, SMI-32, ChAT) • C9ORF72 gene expression and methylation status (qRT-PCR, WB, methylation sensitive	• The isogenic correction of C9ORF72 had no effect on pluripotency markers or MN differentiation ability • Correction restored normal C9ORF72 gene expression (from lower mRNA in C9 mutant (no basal difference in protein levels), restored the reduced methylation at the C9ORF72 locus (hypermethylated in mutant),	Ababneh et al., 2020[514]

ALS-Associated Variant	MN Functional Assay (Stressor, Technique)	ALS Phenotypes and Therapeutic Findings	Reference
	restriction enzyme-quantitative RT-PCR) • RNA foci detection (FISH) • Dipeptide translation products (dot blot- GA, GP, GR) • MN survival (DIV30, basal conditions, IF- cleaved caspase 3) • Stress granule formation (sodium arsenite, 1.5hrs, IF-G3BP) • RNA seq (DIV 30 MNs)	reduced intron retention, and abolished pathological phenotypes in MNs (sense and antisense RNA foci, dipeptide proteins, basal apoptosis, induced stress granules) • RNA-seq and enrichment analyses demonstrated an over-representation of ALS relevant pathways such as calcium ion dependent exocytosis, synapse organization and neurotransmitter transport in upregulated genes.	
SOD1[L39R]	• MN production (20-21 DIV, IF-Olig2, Nestin, MAP2, TH-) • Astrocyte production (5 weeks, IF- GFAP, Sb100) • Stress granule analysis (ICC-G3BP1, 50 DIV astrocytes) • ER stress (IF- Calcineurin A, ER tracker) • Apoptosis (IF-AIF1, cleaved caspase 3/7) • Lysosome tracker, colocalization of autophagy proteins (IF- LC3 I/II, P62, LAMP1) • Astrocyte-MN conditioned media survival (6 day treatment, 1:1 with MN media, MTT assay) • Detection of ROS, mitochondrial membrane potential (live cell imaging) • Whole-cell-patch-clamp	• SOD1 ALS astrocytes had more G3BP1, more apoptotic markers, increased number of lysosomes, colocalization of autophagy proteins. • MNs treated with patient conditioned media had less viability, higher apoptosis markers, altered neuritic morphology, higher levels of ROS, disrupted mitochondrial membrane potential, high colocalization of autophagy proteins, and altered electrophysiological firing, than those treated with control astrocyte conditioned media. (normal astrocyte conditioned media also conversely exerted rescue • Demonstrates non-cell-autonomous protective and degenerative effects of astrocyte secretomes.	Rajpurohit et al., 2020[515]
SOD1[G17S]	• MN production (IF- Hb9, CHAT) • Gene expression (qRT-PCR)	• SOD1 ALS MNs had decreased miRNA-18b-5p, increased expression of Hif1a, Mef2C, BAX, decreased expression of Mctp1, Rarb, Bcl2, higher intracellular calcium, decreased neurite length, and increased LDH release • Overall work with NSC-34 lines demonstrate that SOD1 mutations decrease miR-18b-5p, which sequentially regulates Hif1a, Mef2C, miR-206, Mctp1, and Rarb to trigger apoptosis by inhibition of calcium signaling.	Kim et al., 2020[516]

ALS-Associated Variant	MN Functional Assay (Stressor, Technique)	ALS Phenotypes and Therapeutic Findings	Reference
<u>Mutation Introduced</u> FUS^{P525L}	• MN production (21-day culture, FUS-GFP reporter) • DNA damage response (24hr treatment DMSO, 4μM RGFP109, 0.1μM tubastatin A, 2μM SAHA, laser irradiation linear cuts, live imaging)	• Mutant FUS failed to be recruited to laser-irradiated DNA damage sites (WT showed normal recruitment). 24hr Treatment with HDAC1/3 inhibitor, pan HDAC inhibitor, or HDAC6 inhibitor restored mutant FUS recruitment. • Data from spinal cord dorsal root ganglion cells indicate HDAC inhibitors could induce/co-induce HSPs.	Kuta et al., 2020[446]
C9ORF72	• i3 C9ORF72 cortical neuron production • Gene and protein expression analyses (21 days culture cortical neuron, 32 day differentiated MN cell pellet, IF, qPCR, WB- SV2)	• C9ORF72 patient cortical neurons had reduced synaptic vesicle associated protein 2 (SV2) compared to isogenic controls (IF, WB, qPCR) while levels of synaptophysin remained unchanged. Trend to reduced SV2 in unpurified C9ORF72 MN lysates. • DPR GA$_{50}$ expression in primary cortical or motor neurons also revealed synaptic dysfunction- GA aggregates localized to neuritic regions, were mobile throughout the length of the neurites (without impeding mitochondrial, lysosomal or RNA transport), were toxic to both neurons, compromised synaptic release, increased Ca2+ influx, and reduced SV2. Restoring SV2 rescued synaptic dysfunction and cellular toxicity.	Jensen et al., 2020[517]
SOD1^{R115G} TDP-43^{S393L} FUS^{R521C} sALS CSF	• MN differentiation (9 day patterning from NPCs, then replate, IF- TUJ1, SMI-32) • CSF treatment (6 day treatment, applied to MN cultures 10days after plating) • Protein aggregation and cytoplasmic mislocalization (IF-TDP-43, FUS, SOD1, SMI-32) • Golgi fragmentation (IF-GM130)	• CSF (ALS and control) caused a decrease in the relative number of neuronal cells (per total cells) compared to non-treated cells. No difference between ALS and control CSF or ALS and control MNs. Authors show CSF also increases NPC numbers, so this finding is due to the increased NPC, rather than neuronal cell death. • CSF (ALS and control) did not affect neuronal network, and did not cause ALS protein aggregation, or cytoplasmic mislocalization. • ALS CSF (but not control CSF) induced Golgi fragmentation in	Bräuer et al., 2020[518]

ALS-Associated Variant	MN Functional Assay (Stressor, Technique)	ALS Phenotypes and Therapeutic Findings	Reference
		healthy patient derived MNs, and more so than nonMNs. (interestingly CSF addition did not change Golgi fragmentation in ALS MNs, but these already had higher rates of fragmentation basally). • Conclude that sALS CSF induces Golgi fragmentation (early pathological sign) in human iPSC-derived MNs and this affected MNs more than nonMNs- novel way to model early features of sALS.	

Chapter 9

Appendix B

Supplementary Data and Figures

Supplementary Video Files 1-4.

Automated live cell imaging of iPSC-derived MN cultures treated with DMSO (1), 1μM Thapsigargin (2), 1μM Tunicamycin (3), or 1μM MG132 (4). Images taken every 6 hours, for 48 hours.

Supplementary Data Set 1

ER stress and protection proteomics and phosphoproteomics dataset. Proteins and phospho-peptides quantified are displayed with their corresponding Log_2Fold Expression Change with each treatment, compared to respective control.

Supplementary Data Set 2

HSPA4L knockout proteomics and phosphoproteomics dataset. Proteins and phospho-peptides quantified are displayed with their corresponding Log_2Fold Expression Change compared to untargeted WT control.

Chapter 10

Appendix C

Investigating the role of HSPA4L in ALS patient MNs challenged with proteostatic stress

10.1 Attributions

10.2 Introduction

Amyotrophic Lateral Sclerosis (ALS) is a paralyzing and fatal neurological disorder characterized by the progressive degeneration of cortical and spinal motor neurons (MNs)[1]. A variety of complex genetic and environmental factors contribute to MN degeneration in ALS, making drug discovery particularly challenging. However, despite diverse etiological triggers, the dysregulation of protein homeostasis pathways appears to be a convergent point along the path to ALS MN degeneration, with mutations in protein quality control components causing genetic forms of disease and intracellular protein aggregates universally appearing in all cases of ALS[519]. It is thus possible that improving the capacity of MNs to handle proteostasis malfunctions and manage increasing aggregate burdens may have broad therapeutic utility.

Studies demonstrating that ALS phenotypes can be attenuated by increased levels of protein quality control components, such as heat shock proteins (HSPs) and molecular chaperones, provide support for this hypothesis[520]. In a particularly successful study, Kieran et al. demonstrated that treatment with arimoclomol, a co-inducer of HSPs, significantly delayed disease progression in a SOD1^{G93A} mouse model of ALS, with marked improvement in protein aggregation, muscle function, and life expectancy[521]. This rescue effect notably occurred even when arimoclomol was administered after symptom onset, demonstrating the feasibility of arimoclomol to benefit ALS patients, whose motor deficits are observable by the time of clinical diagnosis[522]. With such promising preclinical results, arimoclomol is now currently being evaluated in Phase II/III clinical trials to determine the safety and effectiveness in SOD1 fALS patients (ClinicalTrials.gov Identifier: NCT00706147), supporting the proposition that increasing cellular proteostasis management may be a worthwhile therapeutic avenue.

More selective upregulation of a singular heat shock protein- HSPA4L- has also recently been reported to attenuate ALS degenerative phenotypes. Increasing the levels of HSPA4L was shown to completely rescue axonal

transport defects produced by mutant SOD1 protein in squid axoplasm[523], protect against photoreceptor neuronal degeneration in multiple genetic Drosophila ALS models (unpublished data, Spyros Artavanis-Tsakonas, Harvard Medical School), as well as significantly extend motor function and life expectancy of two different ALS transgenic mouse models[524]. Since HSPA4L functions to regulate protein disaggregation in the cytosol, it is possible that increasing HSPA4L expression levels helps break apart the pathological proteins that aggregate and accumulate in MNs and consequently may prevent MN degeneration in ALS patients. Given the high failure rate of drug candidates that have only been tested in mouse models, it was critical that these hypotheses be validated in human cells to determine the tractability of this protein as a potential new therapeutic target.

Towards this end, this study aimed to establish the protective function of HSPA4L in ALS patient MNs. We first performed a baseline characterization of the expression levels of HSPA4L in 10 control and ALS patient cultures and demonstrated that HSPA4L RNA and protein levels were indeed modulated in stress and disease conditions. We then performed knockout experiments to test the hypothesis that loss of this potentially protective protein would increase susceptibility to stress. Instead, we found that CRISPR/Cas9 genetic deletion of HSPA4L did not alter patient MN viability in response to proteostatic stress, but rather resulted in global proteomic changes related to cell cycle and division processes, spindle organization, microtubule activity and DNA damage repair. Finally, attempts to increase HSPA4L expression to test the hypothesis that elevated levels would confer protection against ALS patient MN degeneration were met with a large degree of technical difficulty. We describe our attempts to overexpress HSPA4L with both viral vectors and DNA plasmids, and additionally describe a small molecule mediated screen for pharmacological modulators of HSPA4L that may aid the future interrogation of this protein in ALS patient MN survival.

10.3 Results

10.3.1 HSPA4L expression is modulated in stress and disease.

To begin evaluating the role of HSPA4L in ALS, we first tested the expression levels of HSPA4L in ALS patient iPSCs and derived MNs. We performed both western blot and qPCR analyses of 6 control and 2 ALS lines (TDP-43^{G298S} and SOD1^{L144F}) and found no significant differences in HSPA4L protein or mRNA expression across unmatched lines (Figure 10.1A-B). Comparison of an ALS line (SOD1^{A4V}) with its isogenic corrected partner line however did show an increase in HSPA4L expression in the ALS mutant (Figure 10.1C-E), in both the iPSC stage as well as in differentiated MNs. These data seem to suggest an increased and persisting stress response in the ALS mutant compared to control, which we speculate may be protective to combat slow, genetically caused molecular damage.

HSPA4L expression analysis with proteostatic stress, however, revealed a different trend. HSPA4L mRNA levels were variably upregulated after treatment with thapsigargin and tunicamycin, while protein levels remained constant or decreased with proteostatic stressors (with the extent of decrease being cell line dependent)(Figure 10.1F-I). Given the strength of these toxic stressors, as well as the accelerated nature of the assay, the decreased HSPA4L levels may be reflective of MNs already on the pathway to death. The variability of HSPA4L levels with different stressors- upregulated in persisting, genetically caused mutations versus downregulated with rapid strong stimuli- are at least consistent with previous literature evaluating the levels of heat shock proteins and stress response chaperones in neurodegenerative diseases. The type of stress, as well as the time point of stress activation, is among the many confounding factors when making generalizations about HSP levels in stress and disease[525]. Nonetheless, these data support that HSPA4L is modulated in stress and disease conditions.

Figure 10.1. HSPA4L expression levels are modulated in stressed and diseased conditions.

A) qRT-PCR analysis of HSPA4L expression in control and ALS hPSC lines. $\Delta\Delta$Ct values are graphed, normalizing target gene qPCR Ct values (HSPA4L) to housekeeping gene Ct values (GAPDH) and comparing this normalized Ct value to control conditions such that the fold change over 1016A control = 1. $N_b > 3$, $n_t = 3$.

B) Western blot and quantification of HSPA4L expression in control and ALS hPSC lines. $N_b > 2$.

C) qRT-PCR ($N_b = 4$, $n_t = 3$) and (D) western blot analysis ($N_b = 4$) of HSPA4L expression in ALS 39B-SOD1^{A4V} and isogenic corrected control iPSCs.

E) Western blot and quantification of HSPA4L expression in ALS 39B-SOD1^{A4V} and isogenic corrected control MNs. $N_b = 4$.

F) Time course of HSPA4L mRNA expression with 1μM thapsigargin or tunicamycin. $\Delta\Delta$Ct values are graphed, normalizing target gene qPCR Ct values (HSPA4L) to housekeeping gene Ct values (GAPDH) and comparing this normalized Ct value to control DMSO conditions at each time point such that the fold change DMSO$_{time}$ =1. $N_b = 3$, $n_t = 3$.

G) Time course of HSPA4L protein levels with 1μM thapsigargin or tunicamycin. $N_b = 3$.

H) qRT-PCR analysis of HSPA4L expression levels in control and ALS MN cultures after 48hours of 1μM thapsigargin or tunicamycin. $\Delta\Delta$Ct values are graphed, normalizing target gene qPCR Ct values (HSPA4L) to housekeeping gene Ct values (GAPDH) and comparing this normalized Ct value to control DMSO conditions per line such that DMSO$_{line}$ =1. $N_b = 3$, $n_t = 3$.

I) Western blot analysis of HSPA4L expression levels in control and ALS MN cultures after 48hours of 1μM thapsigargin or tunicamycin. $N_b > 2$.

A) HSPA4L Basal Expression iPSCs (RNA)

B) HSPA4L Basal Expression iPSCs (Protein)

C) HSPA4L Basal Expression iPSCs (RNA)

D) HSPA4L Basal Expression iPSCs (Protein)

E) HSPA4L Basal Expression MNs (Protein)

F) Time Course of HSPA4L Expression with ER/UPR stress (RNA)

G) Time Course of HspA4L Expression with ER/UPR stress (Protein)

H) HspA4L Expression with 48hrs ER/UPR stress (RNA)

I) HspA4L Expression with 48hrs ER/UPR stress (Protein)

10.3.2 Genetic loss of HSPA4L does not affect MN survival or ER stress induction after proteotoxic challenge and instead results in proteomic changes related to cell cycle processes, spindle organization, microtubule activity and DNA damage repair

To further interrogate the role of HSPA4L in patient cells, we next generated a CRISPR/Cas9 genetic knockout of HSPA4L to test the hypothesis that loss of this potentially protective protein would confer an increased MN susceptibility to stressors. To create this knockout, 3 single guide RNA (sgRNA) plasmids were designed with sequence homology to the 3rd exon of HSPA4L, as this exon is included in all splicing isoforms and an early mutation is most likely to result in complete protein loss. Expression of the 3 guide RNA sequences was driven by the human U6 promoter, while the remaining expression vector contained a Cas9 nuclease and GFP driven from a CMV promoter. These 3 sgRNA plasmids were then nucleofected into control patient iPSCs. After 1 week, the nucleofected-iPSCs were FACs sorted for sgRNA-GFP expression and plated at single cell density for clonal isolation and PCR-genotyping. 23/96 clones were successfully targeted and one clone (HSPA4L knockout #42) containing a 5 base-pair, frame-shift deletion was subsequently expanded, confirmed to be karyotypically normal, mycoplasma free, and successfully depleted of HSPA4L levels using sanger sequencing (Figure 10.2A), next generation whole exome sequencing (data not shown), western blot (Figure 10.2B), and global proteomics (Figure 10.2H).

To investigate whether genetic loss of HSPA4L would increase MN vulnerability to proteostatic stress, the HSPA4L knockout clone #42, as well as a nontargeted clone #18 and the parental iPSC line were next differentiated into MNs and challenged with increasing doses of thapsigargin and tunicamycin. Dose response curves of both ER stressors showed that the HSPA4L knockout MNs did not, in fact, have an increased susceptibility to stress compared to the nontargeted control and parental line (Figure 10.2C-D), supporting instead the null hypothesis.

Previous literature investigating the loss of HSP105, a highly homologous protein to HSPA4L, substantiated these survival results- showing that loss of HSP105 similarly did not affect cell viability after ER stress but instead changed the mode of death to a caspase 3 independent pathway[526]. To investigate if HSPA4L knockout would similarly divert the mode of death after ER stress, we evaluated the upregulation of UPR signaling in MNs derived from the HSPA4L knockout clone #42 treated with thapsigargin or tunicamycin. However, we found that the HSPA4L knockout clone #42 maintained increased levels of activated cleaved caspase 3 (Figure 10.2F), as well

as activated BiP and CHOP in response to ER stress (Figure 10.2E-G), indicating a distinct functional difference between HSPA4L and HSP105.

Since loss of HSPA4L did not alter cell survival, UPR induction or mode of death, we hypothesized that there may be compensation occurring within the cell to handle HSPA4L depletion. To investigate this and further understand how the cellular proteome was changed with HSPA4L loss, global proteomic analyses were performed on MN cultures derived from the HSPA4L knockout clone #42, in collaboration with Dr. Alban Ordureau from the Harper lab at Harvard Medical School. A total of 71,517 peptides and 22,729 phospho-peptides were quantified, corresponding to 7,803 unique proteins and 3,284 unique phospho-proteins (Figure 10.2H). Intriguingly, the majority of significantly dysregulated hits in the HSPA4L knockout were related to cell cycle and division processes, spindle organization, microtubule activity and DNA damage repair (Figure 10.2H-I). Specifically, aurora kinase B was among the top upregulated hits in the HSPA4L knockout.

Figure 10.2. Knockout of HSPA4L does not affect MN viability or the induction of apoptotic UPR signaling with proteostatic stress.

A) Sequence confirmation of a HSPA4L CRISPR knockout iPSC clone (#42) containing a 5bp frame-shift deletion. A non-targeted clone (#18) and the parental iPSC line (1016A) are normal at the HSPA4L locus.

B) Western blot analysis of HSPA4L in the knockout #42 and control iPSC lines. N_b=3.

C) Isl1/2$^+$ MN differentiation efficiency of controls and HSPA4L knockout #42. N_b=3, N_t=10.

D) Dose response curves of thapsigargin and tunicamycin in HSPA4L knockout #42 and control MNs. N_b=3, N_t>5.

E) qRT-PCR analysis of BIP and CHOP upregulation in control and HSPA4L knockout #42 MNs exposed to 8hrs or 48hrs of 1μM thapsigargin or tunicamycin. ΔΔCt values are graphed, normalizing target gene qPCR Ct values (BIP and CHOP) to housekeeping gene Ct values (GAPDH) and comparing this normalized Ct value to control DMSO conditions at each time point such that the fold change DMSO$_{time}$ =1. N_b=3, n_t=3.

F) Western blot analysis and (G) quantification of BIP upregulation and caspase 3 cleavage in HSPA4L knockout #42 and control MNs exposed to 8hrs or 48hrs of 1μM thapsigargin or tunicamycin. N_b=3.

H) Volcano plot showing all proteins quantified in HSPA4L knockout #42 proteomic analysis. Significant hits are colored green, selected terms are annotated.

I) Gene ontology terms for the significantly upregulated or downregulated proteins in HSPA4L knockout #42.
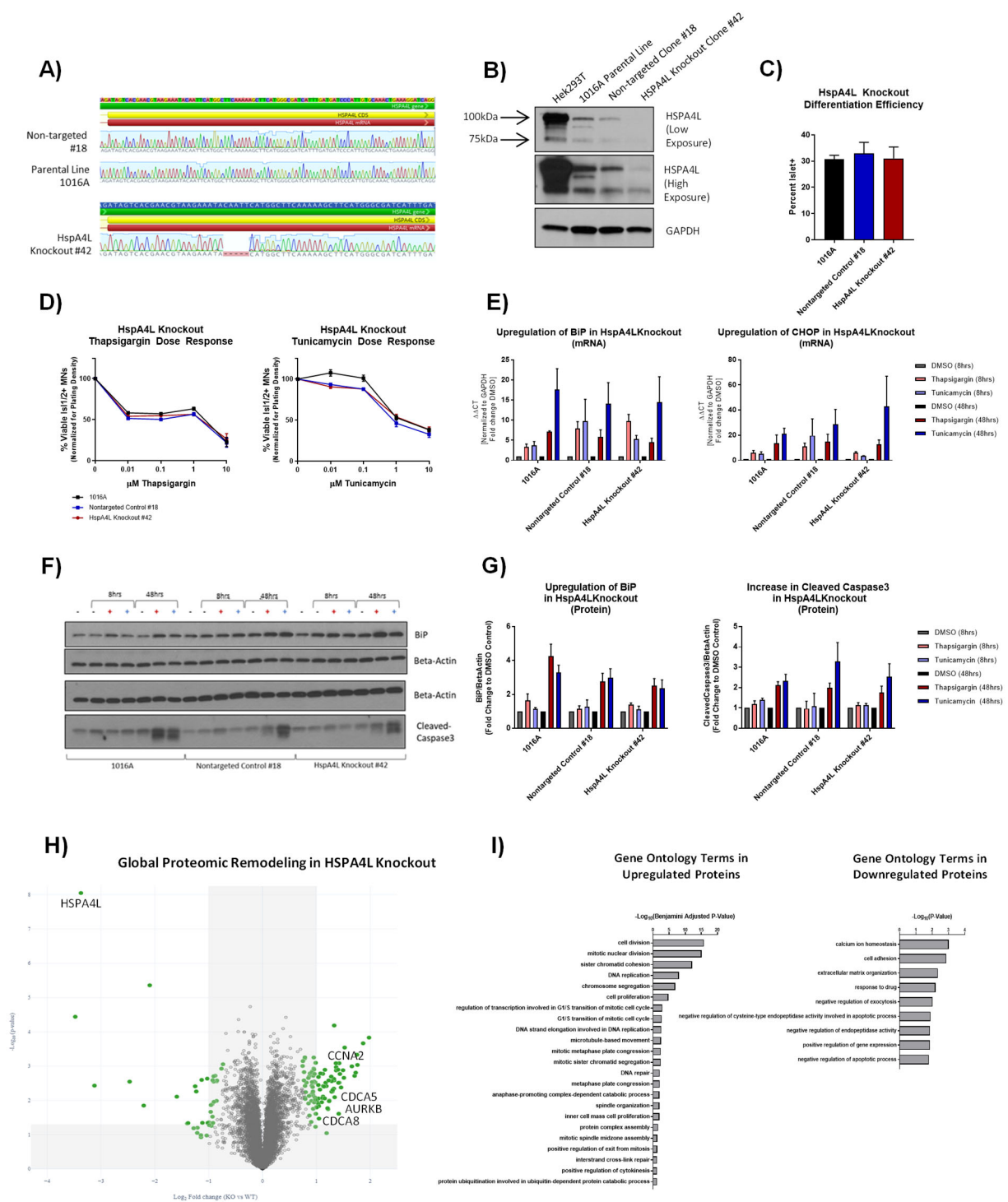
**10.3.3 Interrogating HSPA4L overexpression- trials and tribulations.**

While loss of HSPA4L function did not have an obvious phenotype in patient MNs challenged with proteostatic stress, it was still possible that increasing HSPA4L levels would confer a protective effect. To test this hypothesis, overexpression in patient derived MNs was attempted with both lentiviral vectors and plasmid expression. lentiviral overexpression was attempted first, a total of 5 independent times, with no success. 1 lentivirus was produced by Systems Biosciences (SBI)(Figure 10.3A), 1 lentivirus was produced by Boston Children's Hospital Viral Core (BCH, vector from CCSB-Broad expression library) (Figure 10.3D), 2 viruses were produced in house using both SBI and CCSB-Broad viral backbones (data not shown), and 1 virus failed in production by the company ORIGENE. No virus produced conferred overexpression of HSPA4L, regardless of lentiviral vector (SBI or CCSB-Broad) or production source, while all control viruses worked efficiently, as indicated by GFP[+] reporter (Figure 10.3A-G).

Viral expression of HSPA4L was therefore no longer pursued after these failed attempts, and transient overexpression via nucleofection of a small GFP linked HSPA4L expression vector was attempted next. This technique did result in modest, transient expression of HSPA4L in patient MNs (Figure 10.3H-I), yet HSPA4L overexpression in SOD1[A4V] ALS patient derived MNs did not ultimately produce any bulk survival difference compared to control GFP plasmid nucleofection, either when quantifying total viable nuclei (Figure 10.3J-K) or viable Isl1/2[+] nuclei in the culture (Figure 10.3L). It is likely that this bulk analysis lacks the resolution to show a survival or protective effect conferred by the small population of HSPA4L expressing cells amongst un-nucleofected cells. Measuring enrichment of cells only expressing higher HSPA4L-GFP levels would therefore be more informative, yet this was additionally challenging due to the delay in GFP reporting between control and overexpression plasmids coupled with the transient nature of plasmid-driven expression. We propose that single cell GFP[+] tracking with time-lapse imaging may be the best step forward to interrogate MN viability effects with plasmid based HSPA4L overexpression.

Figure 10.3. Lentiviral-mediated overexpression of HSPA4L was unsuccessful and plasmid-based overexpression did not confer bulk survival effects.

A) Vector map of Systems Biosciences (SBI) HSPA4L overexpression lentivirus plasmid. HSPA4L expression is driven by an EF1α promoter, with a T2A ribosomal skip into GFP.

(B) Western blot analysis of HSPA4L from Hek293T cells 72hrs after transduction with empty-vector lentiviral particles or SBI-HSPA4L lentiviral particles (MOI >100). No death seen by viruses (not shown).

(C) FACS plot for GFP$^+$ iPSCs 96hrs after transduction with either empty vector lentiviral particles or SBI-HSPA4L lentiviral particles (MOI >100).

(D) Vector map of CCSB-Broad HSPA4L overexpression lentivirus plasmid. HSPA4L expression is driven by a CMV promoter and contains a V5 tag.

(E) Western blot analysis of HSPA4L from Hek293T cells transduced with control CMV-GFP lentiviral particles or CCSB-HSPA4L lentiviral particles, generated by Boston Children's Hospital Viral (MOI >200). No death seen by viruses (not shown).

(F) Fluorescent image of Hek293T cells 72hrs after transduction with Boston Children's Hospital control CMV-GFP lentivirus.

(G) qRT-PCR for HSPA4L expression in Hek293Ts transduced with control CMV-GFP lentiviral particles or CCSB-HSPA4L lentiviral particles, generated by Boston Children's Hospital Viral (MOI >200).

H) Vector map of a small expression vector pEF-GFP (Addgene plasmid # 11154). HSPA4L coding sequence was cloned into the vector at the EcoR1 and Sma1 sites to be expressed with an EGFP reporter by the EF1α promoter.

I) Western blot analysis of HSPA4L overexpression in nucleofected ALS (39B-SOD1^{A4V}) MN cultures.

J) Representative TUJ1 immunofluorescent images showing comparable survival of ALS 39B-SOD1^{A4V} MNs nucleofected with control or HSPA4L expression vectors.

K) Percent viable nuclei from ALS 39B-SOD1^{A4V} MN cultures, at various plating densities, following nucleofection with either control or HSPA4L expression vectors. N_b=2, n_f=6.

L) Percent viable MNs from ALS 39B-SOD1^{A4V} MN cultures, at various plating densities, following nucleofection with either control or HSPA4L expression vectors. N_b=2, n_f=6.

A) CD526A-hspA4L 9794 bp

B)

	Untransduced Control	Empty Vector Lentivirus	SBI-HSPA4L Lentivirus
HSPA4L			
GAPDH			

C) Untransduced | Empty Vector Lentivirus | SBI-HSPA4L Lentivirus

D) pLX304-Blast-V5

E)

	Untransduced Control	BCH CMV-GFP Control Lentivirus	BCH CCSB-HSPA4L Lentivirus
HSPA4L			
GAPDH			

F) BCH CMV-GFP Control Lentivirus

G)

H) pEF-GFP 5054 bp

I)

	Unnucleofected	Control-GFP	HSPA4L-GFP
HSPA4L			
GAPDH			

J) Control-GFP | HSPA4L-GFP

K) Total Cell Survival

L) MN Survival

220

10.3.4 A small molecule mediated screen for HSPA4L modulators.

Since genetically overexpressing HSPA4L was met with so much challenge, we next wanted to see if we could identify pharmacological modulators of HSPA4L as a surrogate method for overexpression. Under my direct supervision, an undergraduate researcher, Kelly Zhang, performed a pilot antibody-based compound screen in HEK-293T cells for HSPA4L modulators, with assistance from Dr. Feo Price and Erica Wolin. 88 SelleckChem compounds were tested at 1μM, in triplicate, for either 4 or 8 hours, and imaged using a high-content, automated fluorescent microscope (Operetta). The average HSPA4L intensity was calculated for each cell, per well, and 8 hits were identified based on a Z score calculated using the mean and standard deviation of HSPA4L intensity (Figure 10.4A). These hits included 3 IGF/PI3k/Akt/mTOR inhibitors (GSK1904529A, BX-912, GDC-0941), 2 TNF-a inhibitors (2-Methoxyestradial, lenalidomide), an androgen biosynthesis inhibitor (TAK-700), ginkgolide B, and most intriguingly, an aurora kinase inhibitor (VX-680) previously reported to promote motor neuron survival[360]. To further interrogate the hits, an HSPA4L intensity cut off was set to quantify %HSPA4L$^+$ cells. Fold change of HSPA4L$^+$ cells was then calculated compared to DMSO wells (Figure 10.4B). Given that our CRISPR/Cas9 genetic knockout of HSPA4L resulted in an upregulation of aurora kinase B, as well as this data demonstrating that an aurora kinase inhibitor increased HSPA4L levels, we hypothesize that there may be a functional cooperation between these two cellular proteins.
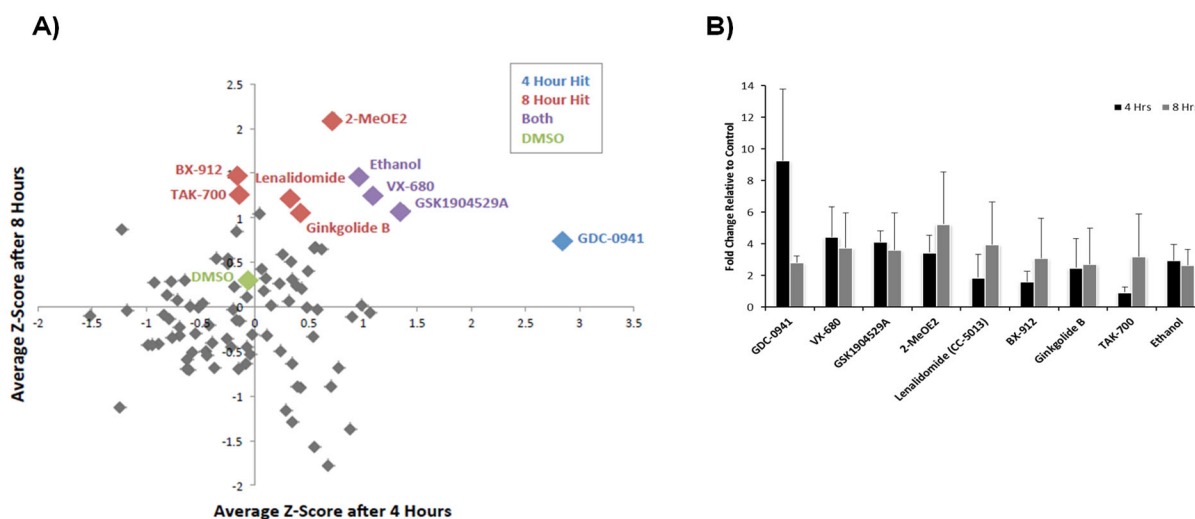
Figure 10.4. Compound modulators of HSPA4L expression.
  A) Z-score scatter plot of a pilot Hek293T screen for compound modulators of HSPA4L expression levels. 88 compounds tested, in triplicate, for either 4 or 8 hours. Z scores calculated for each compound based on the mean and standard deviation HSPA4L intensity (Kelly Zhang).
  B) Fold change of HSPA4L$^+$ cells in hit-compound treated conditions compared to DMSO control. Error bars: +STDEV (Kelly Zhang).

10.4 Conclusions

In this study, we investigated the function of HSPA4L in ALS patient MNs and identified compound modulators of this protein. We demonstrated that HSPA4L RNA and protein levels were modulated in stress and disease conditions, using qPCR and western blot analyses of healthy and ALS patient iPSC and MN cultures, treated with and without cellular stressors. We additionally demonstrated that CRISPR/Cas9 genetic deletion of HSPA4L did not alter MN susceptibility to proteostatic stress, but rather resulted in global proteomic changes related to cell cycle and division processes, spindle organization, microtubule activity and DNA damage repair. Finally, we attempted to increase HSPA4L expression with viral vectors and DNA plasmids to test the hypothesis that this protein would confer protection against ALS MN degeneration, and describe a small molecule mediated antibody-based screen for pharmacological modulators of HSPA4L. These experiments may ultimately aid the future interrogation of this protein in ALS patient MN survival.

10.5 Materials and Methods

10.5.1 hPSC culture

All human pluripotent stem cell (hPSC) culture was performed with approval by the institutional review board and the Harvard Committee on the Use of Human Subjects. Table 10.1 lists all hPSC lines used in this chapter.

Table 10.1. Human pluripotent stem cell lines used.

Cell Type	Line ID	Diagnosis	Mutation	Age of Onset	Age of Biopsy	Gender	Lab	Publication
hES	HuES-3 Hb9-GFP	Healthy Reporter	/			M	Eggan	Di Giorgio et al., 2007[466]
hES	HuES8	Healthy	/			M	Melton	Cowan et al., 2004[527]
iPSC	BJ sIPS	Healthy	/		neonate	M	iPS Core	Rigamonti et al., 2016[528]
iPSC	1016A	Healthy	/		20s	M	Melton	Pagliuca et al., 2014[476]
iPSC	18A	Healthy	/		48	F	Eggan	Boulting et al., 2011[344]
iPSC	15B	Healthy	/		48	F	Eggan	Boulting et al., 2011[344]
iPSC	47d	ALS	TDP-43^{G298S}	43	43	M	Eggan	Alami et al., 2014[164]
iPSC	29d	ALS	SOD1^{L144F}		82	F	Eggan	Boulting et al., 2011[344]
iPSC	39b	ALS	SOD1^{A4V}	43	43	F	Eggan	Kiskinis et al., 2014[345]
iPSC	39b-Corrected	Isogenic Control	/	43	43	F	Eggan	Kiskinis et al., 2014[345]

Cell cultures were maintained at 37°C with 5% CO_2 in a ThermoFisher Scientific biological incubator. hPSCs were cultured with supplemented StemFlex medium (ThermoFisher Scientific) on Matrigel-coated (BD Biosciences) tissue culture plates. Cells were fed every other day and passaged at ~80% confluency using 5 minutes of room temperature 0.5mM EDTA (Life Technologies) and mechanical disruption with a cell lifter. All cultures were tested monthly for mycoplasma contamination and confirmed genotypically correct and karyotypically normal.

10.5.2 Motor neuron differentiation and dissociation

hPSCs were differentiated into MNs as described in Maury, et al, 2014[341]. Briefly, confluent (60-90%) hPSC cultures were detached from Matrigel (BD Biosciences) coated plates and dissociated into single cells using Accutase (Stem Cell Technologies) at 37°C for ~5 minutes. Accutase was quenched and single cells were seeded for differentiation in suspension at a density of 1×10^6 cells/mL in complete mTeSR media (Stem Cell Technologies) supplemented with 10ng/mL FGF2 (Peprotech) and 10µM ROCK-inhibitor Y-27632 (Stemgent). 24 hours after seeding, cells were filtered through a 100µm cell strainer (VWR) and additional, equal volume complete mTeSR media (Stem Cell Technologies) was added. 48 hours after seeding (differentiation day 0), mTeSR media was replaced with N2B27 MN differentiation media. This media was composed of a v:v mixture of DMEM/F12 and Neurobasal media (Life Technologies), supplemented with 1% N2 (Life Technologies), 2% B27 (Life Technologies), 1% Pen-Strep (Life Technologies), 1% Glutamax (Life Technologies), 0.1% beta-mercaptoethanol (βME, Life Technologies), and 20µM ascorbic acid (Sigma Aldrich). Day 0 and day 1 of differentiation, N2B27 MN differentiation media was supplemented with 10µM SB-431542 (R&D Systems), 100nM LDN-193189 (ReproCELL), and 3µM CHIR-99021 (ReproCELL). Day 2 and Day 4, differentiation media was supplemented with 10µM SB-431542, 100nM LDN-193189, 3µM CHIR-99021, 1µM retinoic acid (Sigma Aldrich), and 1µM smoothened agonist (DNSK International, LLC). Day 5, differentiation media was supplemented with 1µM retinoic acid, and 1µM smoothened agonist, Day 7 with 1µM retinoic acid, 1µM smoothened agonist, and 20ng/mL brain derived neurotrophic factor (BDNF, R&D Systems). Day 9, differentiation media was supplemented with 1µM retinoic acid, 1µM smoothened agonist, 20ng/mL BDNF, and 10µM DAPT (R&D Systems). Day 11 and 13, differentiation media was supplemented with 1µM retinoic acid, 1µM smoothened agonist, 20ng/mL BDNF, 10µM DAPT, and 20ng/mL glial derived neurotrophic factor (GDNF, R&D Systems).

Day 15 of differentiation, embryoid bodies (EBs) were collected, washed once with 1x phosphate buffer solution (PBS) without calcium and magnesium (VWR), and dissociated with 0.25% Trypsin-EDTA (Life Technologies) and 50µg/mL DNase1 (Worthington Biochemical) for 5 minutes at 37°C with movement. Trypsin was quenched with fetal bovine serum (FBS, Sigma Aldrich), and centrifuged at 400g for 5 minutes. The cell pellet was then resuspended in dissociation buffer, consisting of 5% fetal bovine serum (FBS, Sigma Aldrich), 25mM glucose, 1% Glutamax, in 1x PBS without calcium and magnesium, and mechanically triturated using a p1000 pipet. Dissociated single cells were pelleted by centrifugation (400g, 5 minutes) and resuspended in complete MN media, consisting of Neurobasal media supplemented with 1% N2, 2% B27, 1% Pen-Strep, 1% Glutamax, 1% Non-essential amino acids (Life Technologies), 0.1% βME, 20µM ascorbic acid, 20ng/mL BDNF, GDNF, and CNTF (ciliary neurotrophic factor, R&D Systems), and 10µM UFDU (v:v Uridine (Sigma Aldrich):Fluorodeoxyuridine (Sigma Aldrich)). Resuspended dissociated single cells were filtered through a 40µm cell strainer, counted with a 1:1 trypan blue dilution using an automated cell counter, and plated at the desired density on tissue culture treated plates coated with 1X borate buffer (Life Technologies), 25µg/mL poly-ornithine (Sigma Aldrich), 5µg/mL mouse laminin (Life Technologies), and 10µg/mL fibronectin (VWR).

10.5.3 RNA isolation, reverse transcription, and quantitative PCR

Total RNA was isolated from $2x10^6$ cells with Trizol (Life Technologies) according to manufacturer's instructions. Briefly, cells were washed once with 1x PBS, on ice, and lysed with 250µL Trizol Reagent and mechanical disruption using a cell lifter. 50µL of chloroform was added to the Trizol-cell extract, and samples were centrifuged at 12,000g at 4°C for 15 minutes. The aqueous phase was collected into a clean Eppendorf tube and 125µL isopropanol, 15µg GlycoBlue Coprecipitant (Life Technologies) were added. Samples were incubated for 10 minutes at room temperature, and then centrifuged at 12,000g at 4°C for 10 minutes. The RNA pellet was washed twice with 250µL 75% ethanol, air-dried, and resuspended in 30µL of 1x DNase1 buffer (Life Technologies). 1µL of amplification grade DNase 1 was then added and incubated for 15 minutes at room temperature to degrade contaminating genomic DNA. 1µL of 25mM EDTA was added to each sample and incubated at 65°C for 10 minutes to quench the reaction.

Total RNA concentrations were analyzed using a nanodrop, and equal amounts of sample RNA were used to synthesize cDNA using the iScript Reverse Transcription Supermix for RT-qPCR (Bio-Rad). Per reaction, 4µL of

5X iScript RT supermix was combined with 0.5-1µg of total RNA, with water to a final volume of 20µL. Sample reactions were then run through the following thermocycler conditions- 5 minutes at 25°C, 20 minutes at 46°C, and 1 minute at 95°C.

Quantitative PCR (qPCR) was then performed on cDNA samples using Fast SYBR Green (Life Technologies). Per reaction, 5µL of 2X Fast SYBR Green Master Mix was combined with 1µL (50ng) of cDNA sample, 1µL of 10µM forward and reverse primer solution, and 3µL water. The following primer pairs were designed for target transcripts using Primer3Plus and validated using NCBI Blast and Geneious software (GAPDH forward 5'-TGACTTCAACAGCGACACCCA-3', GAPDH reverse 5'-CACCCTGTTGCTGTAGCCAAA-3'; HSPA4L forward 5'-GGATGTGCGTTACAGTGTGC-3', HSPA4L reverse 5'- TTGAGAATGGGGCAGGATGG-3'; BiP forward 5'-TCTTCAGGAGCAAATGTCTTTGT-3', BiP reverse 5'-CATCAAGTTCTTGCCGTTCA-3'; CHOP forward 5'-AGGGCTAACATTCTTACCTCTTCA-3', CHOP reverse 5'-GATGAAAATGGGGGGTACCTATG-3'). Technical triplicate reactions were set up for each sample and target primer in MicroAmp Optical 384-well Reaction Plates (Life Technologies), and reactions were run and analyzed on a Quant Studio 12K Flex Real-Time PCR system (ThermoFisher Scientific) following the standard Fast SYBER Green protocol. Melt curves of each target primer pair were analyzed to ensure amplification and quantification of a single PCR product. Differential gene expression was then determined using the ΔΔCT method and visualized as fold change values.

10.5.4 Protein extraction and western blotting

Protein from $2x10^6$ cells was harvested on ice after 1 PBS wash using the Pierce RIPA lysis and extraction buffer (25 mM Tris-HCl, pH 7.6, 150 mM NaCl, 1% NP-40, 1% sodium deoxycholate, 0.1% SDS, Life Technologies) containing fresh protease and phosphatase inhibitors (Life Technologies). Collected samples sat on ice for an additional 30 minutes and were pulled through a 28G insulin syringe for complete lysis. Protein concentrations were then determined using the Pierce BCA Protein Assay Kit (ThermoFisher Scientific). Equal amounts of protein samples (5-20µg) were diluted in RIPA buffer and βME-Laemmli buffer (Bio-Rad Laboratories) to equal volumes and boiled for 7 minutes at 95°C. Denatured samples were then loaded and run on Criterion TGX (Tris-Glycine eXtended) precast gels (Bio-Rad) for ~15 minutes at 80V, and then ~45 minutes at 150V. Migrated proteins were transferred from the gels to PVDF membranes using the Trans-Blot Turbo Transfer System (Bio-Rad)

and run settings of 2.5A, 25V, for 7 minutes. Equal loading and complete transfer were checked with Ponceau S (Sigma Aldrich) staining for 30 minutes, shaking. After removing Ponceau, membranes were blocked with 5% nonfat milk diluted in 1x TBS-T for 45 minutes, shaking. Blocked membranes were incubated with primary antibodies overnight at 4°C, with shaking, with the following primary antibodies: HSPA4L (Sigma Aldrich AV53693, 1:1000), GAPDH (Life Technologies AM4300, 1:5000), GRP78 BiP (Abcam ab21685, 1:1000), CHOP (Cell Signaling Technology 2895T, 1:1000), Cleaved Caspase-3 (Cell Signaling Technology 9664S, 1:1000), β-Actin (Cell Signaling Technology 3700S, 1:5000.

Primary antibody solutions were removed after overnight incubation, and membranes washed 3 times with 1x TBS-T for 5 minutes. Membranes were then incubated for 1 hour, shaking, with species-matched secondary antibodies conjugated to horseradish peroxidase (Goat anti-Rabbit IgG (H+L) HRP, Life Technologies 31460, 1:5,000; Goat anti-Mouse IgG (H+L) HRP, Life Technologies 31430, 1:5000) diluted in 5% milk. Following 3 TBS-T washes, chemiluminescent signal was produced using the SuperSignal West Dura Extended Duration Substrate (ThermoFisher Scientific) and membrane signal was detected on film. All films were scanned using an EPSON scanner without automatic intensity contrast adjustments. Scanned images were cropped and measured for pixel intensity using FIJI/ImageJ. Figure quantifications display fold changes normalized for background film intensity and loading control protein.

10.5.5 Proteostatic stressor assays

For gene expression analyses, dissociated MNs were plated in complete MN media at a density of 2×10^6 cells/well of 6-well plates coated with borate, poly-ornithine, laminin, and fibronectin. 3 days after plating, media was removed and MN cultures were treated with 1μM thapsigargin, tunicamycin, or DMSO for 8hrs or 48hrs. Samples were collected at the appropriate timepoints for RNA and protein expression analyses as indicated in Section 10.5.3 RNA isolation, reverse transcription, and quantitative PCR and Section 10.5.4 Protein extraction and western blotting.

For survival assays, dissociated MNs were plated in complete MN media at a density of 50,000 cells/well in the inner 60 wells of 96-well plates coated with borate, poly-ornithine, laminin, and fibronectin. Outer wells were filled with water to avoid evaporation effects. 3 days after plating, ¾ of the media was removed and replaced with fresh complete MN media. 6 days after plating, all media was removed, and MN cultures were treated with

increasing doses of thapsigargin (Sigma Aldrich) or tunicamycin (Sigma Aldrich). MNs were incubated with stressor media for 48 hours and fixed with 4% paraformaldehyde (PFA, VWR) prior to quantitative analysis of Isl1/2 (Abcam), TUJ1 (Biolegend) primary antibody staining with species-specific, fluorophore-conjugated secondary antibodies (Life Technologies) and Hoechst (Life Technologies), as described in Section 10.5.6 Immunofluorescent staining and image analysis. All cell counts were expressed as a percentage of surviving DMSO-control cells.

10.5.6 Immunofluorescent staining and image analysis

Cells were fixed for 15 minutes at room temperature with 4% paraformaldehyde (PFA, Sigma Aldrich) in PBS, achieved by adding equal volume 8% PFA to equal volume culture media. Fixed cells were gently washed once with PBS, then blocked with 10% normal goat serum, 0.1% Triton X-100 in 1x PBS for 30 minutes at room temperature. Blocked cells were then incubated for 1 hour at room temperature with primary antibodies anti-Isl1/2 (Abcam ab109517, 1:2000) and anti-TUJ1 (Biolegend 801202, 1:2000). Following primary antibody incubation, cells were gently washed with PBS once, and incubated for 1 hour at room temperature with $2\mu g/mL$ Hoechst (Life Technologies H3569) and species-matched, fluorophore-conjugated secondary antibodies (Life Technologies Alexa-488, -546, -555, or -647, 1:1000) diluted in 10% normal goat serum, 0.1% Triton X-100, in PBS. Immunofluorescent labeled cells were gently washed twice with PBS before image acquisition.

High content screening systems (Operetta (PerkinElmer) or ImageXpress (Molecular Devices)) were used for all image acquisition. Images were acquired automatically using a 10x or 20x objective, a solid-state laser light source, and a sCMOS (scientific complementary metal-oxide-semiconductor) camera, corresponding to 9-12 evenly distributed fields per well of each 96-well plate. Using these parameters, at least 2,000 cells were imaged per well of each 96-well plate, with typically >5,000 cells/well with normal assay conditions. Quantitative analyses of these images were then performed using the Columbus/Harmony image analysis software (PerkinElmer). Manually designed scripts were written to define a viable cell population, which consisted of intact, Hoechst-stained nuclei larger than $\sim 45\mu m^2$ (range 37-55) in surface area and with intensities lower than the threshold brightness of pyknotic nuclei. From this viable cell population, the neuron-specific βIII-Tubulin marker (TUJ1 antibody, Biolegend) was used to define the neuronal population (~95% of all cells, Figure 2.2B) and neurite morphologies. From the viable population, nuclear Isl1/2 antibody staining was used to define the MN population, using intensity thresholds that

accurately reflect positive nuclear staining. With these set parameters, total numbers of nuclei, viable neurons, and viable MNs were then quantified automatically across the plate, ensuring unbiased measurements for all test conditions. Images were visually inspected during analysis and script generation, and after analysis to ensure data validity. All cell counts were then expressed as a percentage of surviving DMSO-control cells.

10.5.7 CRISPR/Cas9 mediated HSPA4L gene knockout

CRISPR gRNAs were designed to target the 3rd exon of the HSPA4L locus as this exon is present in all splicing isoforms and an early coding deletion is most likely to result in complete loss of functional protein. 3 guide RNA sequences were selected to target this locus using Dr. Feng Zhang's online CRISPR design tool (http://crispr.mit.edu/) that computationally assessed proximity to a 5'-NGG PAM and the predicted likelihood of minimal off target binding events. Sense and antisense oligonucleotides with homology to these 3 gRNA sequences were then purchased from IDT (CRISPR 1 forward: 5'-caccgATGGCTTCAAAAAGCTTCAT-3', CRISPR 1 reverse: 5'-aaacATGAAGCTTTTTGAAGCCATc-3'; CRISPR 2 forward: 5'-caccgCATGGCTTCAAAAAGCTTCA-3', CRISPR 2 reverse: 5'-aaacTGAAGCTTTTTGAAGCCATGc-3'; CRISPR 3 forward: 5'-caccgAACGTAAGAAATACAATTCA -3', CRISPR 3 reverse: 5'-aaacTGAATTGTATTTCTTACGTTc -3') and were cloned into the pX458 vector to be expressed from the human U6 promoter along with S. pyogenes Cas9 and GFP (Addgene 48138).

Briefly, the sgRNA oligonucleotides were first phosphorylated and annealed. 1μL of 100μM sense oligo and 1μL of 100μM antisense oligo were combined with 1μL 10X T4 Ligation Buffer (New England Biolabs), 0.5μL T4 PNK (New England Biolabs) and 6.5μL ddH$_2$0 to a final reaction volume of 10μL. This reaction mixture was run on a thermocycler at 37°C for 30 minutes, 95°C for 5 minutes, and then cooled to 25°C with a temperature ramp-down of 5°C per minute. The phosphorylated and annealed sgRNA oligos were then diluted 1:250 in water, and 2μL of diluted oligos were added to 100ng of the pX330 CRISPR/Cas9 vector backbone in a digestion-ligation reaction consisting of 2μL 10X FastDigest Buffer (New England Biolabs), 1μL FastDigest BbsI (New England Biolabs), 0.5μL T7 DNA ligase (New England Biolabs), 1μL 10mM DTT, and 1μL 10mM ATP into ddH$_2$0 to a final reaction volume of 20μL. This digestion-ligation reaction was run on a thermocycler at 37°C for 5 minutes, 23°C for 5 minutes, for 6 cycles. Competent bacteria were then transformed with the resulting sgRNA-CRISPR/Cas9 expression plasmids and sequence confirmed for MAXI prep.

To generate a HSPA4L knockout hiPSC line, control hiPSCs (1016A) were nucleofected with the HSPA4L targeting sgRNA-CRISPR/Cas9 expression plasmids. 1 hour prior to nucleofection, 1016A hiPSCs cultures were first pretreated with 10µM ROCK-inhibitor Y-27632 (Stemgent). Following pretreatment, hiPSC colonies were dissociated into single cells using Accutase, and ~5x10^6 cells were resuspended in 100µl of P3 Nucleofection mix (LONZA) containing 5µg of each of the 3 HSPA4L sgRNA-CRISPR/Cas9 expression plasmids. This cell-nucleofection resuspension mix was loaded into a nucleofection cuvette (LONZA) and nucleofected with the hes9 H9 pulse code CB 150. 1mL mTeSR media containing 10µM ROCK-inhibitor Y-27632 (Stemgent) was quickly added to the 100µL cell-nucleofection fix and cells were replated on Matrigel coated plates. Media was changed the following day to basal mTeSR media and 48 hours after nucleofection, hiPSCs were FACs sorted for GFP and plated at 10,000, 20,000, and 50,000 cells/10cm plate for clonal isolation and expansion. Genotyping of single clones was performed using the Wizard Genomic DNA Purification Kit (Promega) and the following primer pairs (HSPA4L forward: 5'-GGTGGATAATTTGGGAGGCAAG-3', HSPA4L reverse: 5'-AGATCTCCTGGCATTCACTAAAA-3'), as described in Section 10.5.8 DNA extraction and PCR. Genotype was confirmed with at least 3 expanded iPSC passages and MN differentiations.

10.5.8 DNA extraction and PCR

Genomic DNA was extracted using the Wizard Genomic DNA Purification Kit (Promega). Approximately 2x10^6 cells were lysed using 600µL of nuclei lysis solution and mechanical trituration by pipetting. 3µL of RNase solution was added to the nuclear lysate and incubated for 15 minutes at 37°C. 200µl Protein Precipitation Solution was then added, vortexed briefly, and centrifuged for 4 minutes at 16,000g. DNA containing supernatant was then transferred to a fresh Eppendorf tube containing 600µl isopropanol. Sample solutions were mixed gently by inversion until white thread-like strands of DNA were visible. Samples were centrifuged for 1 minute at 16,000g, and the DNA pellet was washed with 70% ethanol before centrifuging again (1 minute, 16,000). The DNA pellet was air dried for 15 minutes and resuspended with 100µl DNA rehydration solution for 1 hour at 65°C or overnight at 4°C. Total DNA concentrations were analyzed using a nanodrop.

To extract DNA from agarose gels, the Wizard SV PCR and Gel clean up Kit (Promega) was used. Per 10mg of excised gel slice, 10µl Membrane Binding Solution was added, vortexed and incubated at 50–65°C until completely dissolved. The melted gel mixture was then transferred to the Minicolumn assembly, incubated at room

temperature for 1 minute, and centrifuged at 16,000g for 1 minute. Flowthrough was discarded, and the minicolumn was washed twice with Membrane Wash Solution and 1 minute 16,000g centrifugation. Washes were discarded and the minicolumn was centrifuged for 1 minute at 16,000g to dry the membrane. Extracted DNA was finally eluted from the column by incubating the column membrane with 50ul DNase free water and centrifuging for 1 minute at 16,000g. Total DNA concentrations were analyzed using a nanodrop.

Polymerase chain reaction (PCR) was performed using the Phusion Hot Start Flex 2X Master Mix (New England Biolabs). Reactions were set up according to manufacturer's instructions- 50-100ng of genomic DNA sample was added to 12.5µL Phusion Hot Start Flex 2x Master Mix and 2.5µL 10µM forward and reverse primer solution. Water was added to a final reaction volume of 25µL. Thermocycler conditions were the following- 1 cycle of 98°C for 30 seconds; 30 cycles of 98°C for 10 seconds, 45-72°C for 30 seconds (depending on melting temperature of primer pairs determined by NEB Tm calculator), 72°C for 30 seconds/kb; and 1 cycle of 72°C for 10 minutes. PCR products were run at 135V on a 1% agarose gel containing ethidium bromide and bands were observed using a ChemiDoc XRS+ (Bio-Rad).

10.5.9 Sequencing

Sequencing of DNA plasmids and PCR products was outsourced to and performed by Psomagen. We provided 80-150ng/µL of plasmid samples, 25-50ng/µL of PCR products, along with 5pmol/µL forward and reverse primers, to allow for 10µL per sequencing reaction. Resulting sequencing files were analyzed with Geneious software using NCBI gene data.

10.5.10 Karyotyping

G-banded karyotyping was outsourced to and performed by Cell Line Genetics or WiCell Cytogenetics. Live cell cultures between 40-60% confluency were prepared in T25 flasks filled with media and shipped overnight to either company for analysis. 20 metaphase spreads were analyzed for each line.

10.5.11 Mycoplasma Testing

Routine testing for mycoplasma contamination in cell cultures was performed monthly using either the LookOut Mycoplasma PCR Detection Kit (Sigma Aldrich) or the MycoAlert PLUS Mycoplasma Detection Kit

(Lonza). For the LookOut Mycoplasma PCR Detection Kit, 1mL of media supernatant was collected from 90% confluent cell cultures, boiled for 5 minutes at 95°C, and centrifuged briefly to pellet cellular debris. 2µL of boiled samples were added to 23µL of Rehydration Buffer containing JumpStart Taq DNA polymerase (Sigma Aldrich). Negative controls included 2µL of DNA-free water, and positive controls included non-infectious DNA fragments of *Mycoplasma orale* provided in reaction tubes. Reactions were then run using the following thermocycler conditions: 1 cycle of 94°C for 2 minutes; 40 cycles of 94°C for 30 seconds, 55°C for 30 seconds, and 72° C for 40 seconds. Cooled samples (4-12°C) were loaded on a 1.2% agarose gel containing ethidium bromide and migrated bands were visualized using a ChemiDoc XRS+ (Bio-Rad). Negative controls and samples showed a single distinct band at 481bp. Positive controls and samples had an additional band at 259bp.

For the LookOut Mycoplasma PCR Detection Kit, 1mL of media supernatant was collected from 90% confluent cell cultures, centrifuged for 5 minutes at 200g, and 100µL transferred to an optically clear luminescent-compatible 96-well plate. 100µL of MycoAlert PLUS Reagent was added to each sample and incubated for 5 minutes prior to collecting an initial luminescence reading. 100µL of MycoAlert PLUS Substrate was then added to each sample, incubated for 10 minutes, and then read again for a final luminescence reading. A ratio of final luminescence reading/initial luminescence > 1.2 was interpreted as positive for mycoplasma contamination.

10.5.12 Sample collection for global proteomic and phosphoproteomic analyses

$3x10^6$ dissociated MNs were plated on borate/poly-ornithine/laminin/fibronectin coated 6-well tissue culture plates. 3-day old MN cultures were washed 3 times with chilled PBS, on ice, and total protein was collected using 200µL/well of freshly prepared lysis buffer containing 6M urea (Life Technologies), 50mM EPPS (Sigma Aldrich), 1% triton X-100 (Sigma Aldrich), 5mM tris (2-carboxyethyl) phosphine (ThermoFisher Scientific), 20mM chloroacetamide (Sigma Aldrich), with 1x protease and phosphatase inhibitors (Life Technologies). Mechanical disruption with a cell lifter was used to collect the protein lysates into Eppendorf tubes which were then flash frozen in liquid nitrogen and stored at -80°C until mass spectrometry analysis.

10.5.13 Global proteomic and phosphoproteomic analyses

Proteomics - Sample preparation and digestion

Protein concentrations from sample lysates were determined using the Bradford assay (ThermoFisher Scientific). Proteins denatured in 1% SDS were subjected to disulfide bond reduction with 5mM tris (2-carboxyethyl) phosphine (room temperature, 15 minutes) and alkylation with 20mM chloroacetamide (room temperature, 20 minutes). Methanol-chloroform precipitation was then performed, adding 400μL of 100% methanol to the 100μg/100μL protein sample, vortexing 5 seconds, and then adding 100μL of 100% chloroform and vortexing 5 seconds. 300μL of water was added to the sample, vortexed 5 seconds, and centrifuged for 1 minute at 14,000g to generate distinct phase separations. The aqueous phase and organic phases were removed, leaving behind the protein disk that was washed twice with 400μL 100% methanol, and centrifuged at 21,000g for 2 minutes at room temperature. containing 0.1% RapiGest and digested at 37°C for 2 h with LysC protease at a 200:1 protein-to-protease ratio. Trypsin was then added at a 100:1 protein-to-protease ratio and the reaction was incubated for 6 h at 37°C.

Tandem mass tag labeling of each sample was performed by adding 10 ul of the 20 ng/μL stock of TMT reagent along with acetonitrile to achieve a final acetonitrile concentration of approximately 30% (v/v). Following incubation at room temperature for 1 h, labeling efficiency of a small aliquot was tested, and the reaction was then quenched with hydroxylamine to a final concentration of 0.5% (v/v) for 15 min. The TMT-labeled samples were pooled together at a 1:1 ratio. The sample was vacuum centrifuged to near dryness, resuspended in 5% formic acid for 15 min, centrifuged at 10000×g for 5 minutes at room temperature and subjected to C18 solid-phase extraction (SPE) (Sep-Pak, Waters).

Proteomics – TMT-labeled phosphopeptide enrichment

Phosphopeptides were enriched using Pierce Fe-NTA phosphopeptide enrichment kit (Thermo Fisher Scientific, A32992) following the provided protocol. In brief, combined TMT-labeled dried peptides were enriched for phosphopeptides, while the unbound peptides (flow through) and washes were combined and saved for total proteome analysis. The enriched phosphopeptides were dried down and fractionated according to manufacturer's instructions using High pH reversed-phase peptide fractionation kit (Thermo Fisher Scientific, 84868) for a final 6 fractions and subjected to C18 StageTip desalting prior to MS analysis.

Proteomics - Off-line basic pH reversed-phase (BPRP) fractionation

Unbound TMT-labeled peptides (flow through from phosphor-peptide enrichment step) and washes were dried down and resuspended in 100μl of 10 mM NH_4HCO_3 pH 8.0 and fractionated using BPRP HPLC[477]. Briefly, samples were offline fractionated over a 90 min run, into 96 fractions by high pH reverse-phase HPLC (Agilent LC1260) through an aeris peptide xb-c18 column (Phenomenex; 250 mm x 3.6 mm) with mobile phase A containing 5% acetonitrile and 10 mM NH_4HCO_3 in LC-MS grade H_2O, and mobile phase B containing 90% acetonitrile and 10 mM NH_4HCO_3 in LC-MS grade H_2O (both pH 8.0). The 96 resulting fractions were then pooled in a non-continuous manner into 24 fractions (as outlined in Supplemental Fig. 5 of Paulo et al., 2016[477]) and 12 fractions (even numbers) were used for subsequent mass spectrometry analysis. Fractions were vacuum centrifuged to near dryness. Each consolidated fraction was desalted via StageTip, dried again via vacuum centrifugation, and reconstituted in 5% acetonitrile, 1% formic acid for LC-MS/MS processing.

Proteomics - Liquid chromatography and tandem mass spectrometry

Phosphopeptide mass spectrometry data were collected using an Orbitrap Fusion Lumos mass spectrometer (Thermo Fisher Scientific) coupled to a Proxeon EASY-nLC1200 liquid chromatography (LC) pump (Thermo Fisher Scientific). Peptides were separated on a 100 μm inner diameter microcapillary column packed in house with ~35 cm of Accucore150 resin (2.6 μm, 150 Å, ThermoFisher Scientific) with a gradient consisting of 5%–16% (0-78 min), 16-22% (78-98min), 22-28% (98-110 min) (ACN, 0.1% FA) over a total 120 min at ~500 nL/min. For analysis, we loaded 1/2 of each fraction onto the column. Each analysis used the Multi-Notch MS^3-based TMT method[478]. The scan sequence began with an MS^1 spectrum (Orbitrap analysis; resolution 120,000 at 200 Th; mass range 400−1400 m/z; automatic gain control (AGC) target $1×10^6$; maximum injection time 50 ms). Precursors for MS^2 analysis were selected using a Top10 method. MS^2 analysis consisted of collision-induced dissociation (quadrupole ion trap analysis; Turbo scan rate; AGC $2.0×10^4$; isolation window 0.7 Th; normalized collision energy (NCE) 35; maximum injection time 150 ms) with MultiStage Activation (MSA) for neutral loss of 97.9763. Monoisotopic peak assignment was used, and previously interrogated precursors were excluded using a dynamic window (150 s ± 7 ppm). Following acquisition of each MS^2 spectrum, a synchronous-precursor-selection (SPS) MS^3 scan was collected on the top 10 most intense ions in the MS^2 spectrum[478]. MS^3 precursors were fragmented by high energy collision-induced dissociation (HCD)

and analyzed using the Orbitrap (NCE 65; AGC 1.5×10^5; maximum injection time 250 ms, resolution was 50,000 at 200 Th).

Proteomic mass spectrometry data were collected using an Orbitrap Fusion Lumos mass spectrometer (Thermo Fisher Scientific) coupled to a Proxeon EASY-nLC1200 liquid chromatography (LC) pump (Thermo Fisher Scientific). Peptides were separated on a 100 μm inner diameter microcapillary column packed in house with ~35 cm of Accucore150 resin (2.6 μm, 150 Å, Thermo Fisher Scientific) with a gradient consisting of 5%–22% (0-125 min), 22-28% (125-140min) (ACN, 0.1% FA) over a total 150 min run at ~500 nL/min. For analysis, we loaded 1/10 of each fraction onto the column. Each analysis used the Multi-Notch MS^3-based TMT method[478], to reduce ion interference compared to MS^2 quantification. The scan sequence began with an MS^1 spectrum (Orbitrap analysis; resolution 120,000 at 200 Th; mass range 350−1400 m/z; automatic gain control (AGC) target 5×10^5; maximum injection time 50 ms). Precursors for MS^2 analysis were selected using a Top10 method. MS^2 analysis consisted of collision-induced dissociation (quadrupole ion trap analysis; Turbo scan rate; AGC 2.0×10^4; isolation window 0.7 Th; normalized collision energy (NCE) 35; maximum injection time 35 ms). Monoisotopic peak assignment was used, and previously interrogated precursors were excluded using a dynamic window (150 s ± 7 ppm), and dependent scan was performed on a single charge state per precursor. Following acquisition of each MS^2 spectrum, a synchronous-precursor-selection (SPS) MS^3 scan was collected on the top 10 most intense ions in the MS^2 spectrum[478]. MS^3 precursors were fragmented by high energy collision-induced dissociation (HCD) and analyzed using the Orbitrap (NCE 65; AGC 3×10^5; maximum injection time 150 ms, resolution was 50,000 at 200 Th).

Proteomics - Data analysis

Mass spectra were processed using a Sequest-based (v.28, rev. 12) in-house software pipeline[479]. Spectra were converted to mzXML using a modified version of ReAdW.exe. Database searching included all entries from the UniProt Human Reference Proteome database (2017 - SwissProt and TrEMBL). Sequences of common contaminant proteins (for example, trypsin, keratins and so on) were appended and the database was concatenated with one composed of all size-sorted protein sequences in reverse order. Searches were performed using a mass tolerance of 20 p.p.m. for precursors and a fragment-ion tolerance of 0.9 Da, and a maximum of two missed cleavages per peptide was allowed. TMT tags on lysine residues and peptide N termini (+229.163 Da) and carbamidomethylation of cysteine residues (+57.021 Da) were set as static modifications (except when testing for labeling efficiency, in which case the

TMT modifications are set to variable), while oxidation of methionine residues (+15.995 Da) was set as a variable modification. Peptide-spectrum matches (PSMs) were adjusted to a 1% false discovery rate (FDR) and PSM filtering was performed using a linear discriminant analysis, as described previously[479], while considering the following parameters: Xcorr and Diff Seq. Delta Score, missed cleavages, peptide length, charge state, and precursor mass accuracy. Using the Picked FDR method[480], proteins were filtered to the target 1% FDR level. Moreover, protein assembly was guided by principles of parsimony to produce the smallest set of proteins necessary to account for all observed peptides. For TMT-based reporter ion quantitation, we extracted the summed signal-to-noise (S:N) ratio for each TMT channel and found the closest matching centroid to the expected mass of the TMT reporter ion (integration tolerance of 0.003 Da). Proteins were quantified by summing reporter ion counts across all matching PSMs using in-house software, as described previously[479]. PSMs with poor quality, MS_3 spectra with more than 8 TMT reporter ion channels missing, or isolation specificity less than 0.7 (or 0.6 for phosphorylation dataset), or with TMT reporter summed signal-to-noise ratio that were less than 150 (100 for phosphorylation dataset), or had no MS_3 spectra were excluded from quantification.

For phosphorylation dataset search, phosphorylation (+79.966 Da) on Serine, Threonine or Tyrosine and deamidation (+0.984 Da) on Asparagine or Glutamine were set as additional variable modifications. Phosphorylation site localization was determined using the AScore algorithm[481]. AScore is a probability-based approach for high-throughput protein phosphorylation site localization. Specifically, a threshold of 13 corresponded to 95% confidence in site localization.

Protein quantification values were exported for further analysis in Microsoft Excel and Perseus[482] and statistical test and parameters used are indicated in the corresponding Supplementary Data Set 2. Briefly, Welch's t-test analysis was performed to compare two datasets, using s0 parameter (in essence a minimal fold change cut-off) and correction for multiple comparison was achieved by the permutation-based FDR method, both functions that are built-in in Perseus software. For whole cell proteome analysis, each reporter ion channel was summed across all quantified proteins and normalized assuming equal protein loading of all samples. For phospho-peptide dataset, peptide abundance was normalized to the protein abundance when available.

10.5.14 Gene ontology analyses

Gene ontology enrichment analyses were performed using the Database for Annotation, Visualization, and Integrated Discovery (DAVID) v6.8. Differentially expressed genes that reached a false discovery rate q-value significance threshold <0.05 were analyzed for enrichment compared to the total protein list quantified, using default stringency parameters.

10.5.15 Lentivirus transduction

Two HSPA4L overexpression lentiviruses were used in these studies- one purchased and produced by Systems Biosciences (CD526A-1, 1.48×10^9 infectious units/ml) and one purchased from Dharmacon (CCSB-Broad Lentiviral Expression Library) and packaged by the Boston Children's Hospital Viral Core (2.3×10^7 genomic copies/ml). ~70% confluent Hek293T cells or hiPSCs were transduced with either lentivirus in serum free media using increasing multiplicities of infection, ranging from MOI 0.1 – MO1 >200. 8 hours after transduction, fresh media with serum was added to the cells, and 24 hours later media was changed completely. 48 hours to 120 hours post transduction, cells were collected and analyzed for overexpression using a variety of techniques including western blotting (Described in Section 10.5.4 Protein extraction and western blotting), FACs sorting for GFP, fluorescent microscopy, and qRT-PCR (Described in Section 10.5.3 RNA isolation, reverse transcription, and quantitative PCR).

10.5.16 Expression vector cloning, nucleofection and survival assay

A smaller, non-viral plasmid expressing HSPA4L was generated by cloning the HSPA4L-T2A-GFP fragment from the Systems Biosciences lentiviral vector (CD526A-1) into the pEF-GFP expression plasmid (Addgene 11154). 10μg of the HSPA4L Systems Biosciences vector was first digested with 10μL Xba1 and 10μL Sal1 restriction enzymes (New England Biolabs) in 5μL Cutsmart Buffer (New England Biolabs) in water to a final reaction volume of 50μL. This digestion reaction was incubated at 37°C for 1 hour, inactivated at 65°C for 20 minutes, and the digested product (3,391bp) containing HSPA4L-T2A-GFP was gel purified using the Wizard SV Gel and PCR Clean-Up System (Promega) as described in Section 10.5.8 DNA extraction and PCR.

2 nested PCR reactions were then performed from the pEF-GFP expression plasmid to generate an EF1α-expression plasmid fragment that had 5' and 3' end homology to the digested HSPA4L-T2A-GFP fragment. The

following primer pairs were used for these nested PCR reactions (pEF-GFP forward 1: 5'-CAGACATGGTGGCGAATTCGCTAGCTCTAATTCCTCACGACACC-3', pEF-GFP reverse 1: 5'-GGATCTCGCTAGAGCTGAATCTAAGTCGAGGCCGCACTCCTCAGG-3'; Nested forward 2: 5'-GGTCAATGCCAACCACAGACATGGTGGCGAATTCG-3', Nested reverse 2: 5'-GGACCCGGCTCCACCGGATCTCGCTAGAGCTGAAT-3'), using 5ng of pEF-GFP expression plasmid for the first PCR reaction, 5ng of the first PCR reaction for the second PCR reaction, and following the Phusion Hot Start Flex 2X Master Mix (New England Biolabs) reaction set up and thermocycler conditions described in Section 10.5.8 DNA extraction and PCR using. A Gibson reaction was then used to ligate 50ng of the PCR-amplified EF1α-expression plasmid fragment with 115ng gel-purified, restriction digested HSPA4L-T2A-GFP. NEBalpha competent bacteria were transformed with this Gibson reaction, and successful integration and generation of the cloned EF1α-HSPA4L expression plasmid was confirmed with diagnostic restriction enzyme tests and DNA sequencing of the mini/maxi preps.

To transiently overexpress HSPA4L in ALS derived MNs, 2million dissociated cells were nucleofected with 1.2pmols of the cloned EF1α-HSPA4L expression plasmid in 100μL P3 nucleofection mix using the Neuron pulse code EM 110. Nucleofected MNs were plated at 150K, 100K, and 75K per well of a 96well borate/poly-ornithine/laminin/fibronectin coated plate. 6 hours later the nucleofection mix was removed and 96 hours after nucleofection, cells were fixed and analyzed for viability by staining with Hoechst, Isl1/2 and TUJ1 as described in Section 10.5.6 Immunofluorescent staining and image analysis.

Representative images displayed in figures were cropped using FIJI/ImageJ. All automatic contrast settings in Harmony/Columbus were first disabled. Images were then selected for each condition, saved from the database, and imported into FIJI/ImageJ. A region of interest (ROI) was generated and used for each image per condition, allowing the preservation of equal image scale. Cropped images were then saved as final high-resolution TIFs.

10.5.17 Compound screen for HSPA4L modulators

HEK293T cells were plated into 96-well plates at a density of 20,000 cells/well. Cells were treated for 4 or 8 hours with 88 SelleckChem compounds at 1μM, in triplicate. Compounds were diluted to 10μM in DMSO using the Matrix Hydra DT automated liquid handling platform (Thermo Fisher), and 10uL of the diluted compounds were added to 90uL of media. Positive control wells included 0.5% ethanol and negative control wells contained DMSO

vehicle. Following the appropriate incubation period, plates were fixed in 4% PFA using the EL406 Combination Washer Dispenser (Biotek Instruments), and stained/imaged with anti-HSPA4L (1:250, Santa Cruz, sc-133253), 2µg/mL Hoechst (Life Technologies H3569) as described in Section 10.5.6 Immunofluorescent staining. Hits were identified based on a Z-score that determined how many standard deviations the measured HSPA4L intensity differed from the mean HSPA4L intensity, such that Z = (HSPA4L Intensity$_{compound\ treated}$ – HSPA4L Intensity$_{All\ compounds}$)/ Standard Deviation HSPA4L Intensity$_{All\ compounds}$. Compounds with a Z-score above 1.25 in 2 out of 3 replicates were considered hits.

10.5.18 Statistical Analyses

All statistical analyses were performed in Microsoft Excel, with the StatPlus plugin. Comparisons between 2 groups were analyzed with a two-tailed, unpaired student's t-test.